Dissertation submitted in fulfilment of the degree of

MASTER OF SCIENCE IN ENGINEERING

Department of Mechanical Engineering
University of Cape Town

August 2013

THERMAL AND CHEMICAL ANALYSIS OF CARBONACEOUS MATERIALS: DIESEL SOOT AND DIESEL FUEL REACTOR DEPOSITS

Irénée Kaminuza

Supervised by

Chris Woolard

Plagiarism declaration

1. I know that plagiarism is wrong. Plagiarism is using another's work and to pretend that it is one's own.
2. This dissertation is my own work.
3. I acknowledge that pretending that someone else's work, or part of it, is my own is wrong, and declare that this is my own work.
4. I have used the IEEE 2006 referencing style as the convention for citation and referencing. Each significant contribution to, and quotation in, this dissertation from the work, or works of other people has been attributed and referenced.

Irénée Kaminuza

Acknowledgements

"Gratitude is not only the greatest of virtues, but the parent of all others."-Cicero

I would like thank the following persons or organisations for aiding me throughout my MSc studies:

1. First and foremost, I would like to thank my sponsors, Sasol Technology Fuels Technology, and Canon Collins Trust, as funding is the lifeblood of every student. I was fortunate to have such generous patronage from both sponsors during my MSc degree and I thank them for investing in my future.
2. I would like thank my supervisor, Dr Chris Woolard, for recruiting me and introducing the world of petroleum science engineering at the Sasol Advanced Fuels Laboratory (SAFL). I appreciated his guidance and empathy. I also thank him for welcoming me to his home for the end of year functions and for introducing Journal Club to the chemists in the research group. It was a great way to learn and engage with others. I really appreciate the amount of time and dedication he put into assisting me in interpreting my data. Furthermore I would like to express my gratitude towards him for arranging me funding during this past year.
3. I would like to express a great deal of appreciation towards Dr. Stefan De Goede for being an exemplary mentor throughout my MSc. Like Dr Woolard, Stefan is an incredibly busy man, which is why I felt privileged as he spent a great deal of his time assisting me. From providing me with relevant literature material, organising my samples, exposing me to several analytical facilities, reading and offering input into the written aspect of my thesis, organising formal and informal discussions or just emailing me to inquire about my progress, Stefan went well and beyond the call of duty.
4. A big thank you goes to Mrs Miranda Waldron and Dr François Cummings of the Electron Microscope Unit at UCT for helping me to image my samples. Their warmth and assistance is greatly appreciated.
5. I would like to thank Ms Shanielle Botha for her help with the GC-MS.
6. Mr Ross Burnham deserves a big thank you. His help around the laboratory is much appreciated. He acquainted me with many of the analytical equipment
7. To Mr Victor Burger and Mr Gerhard Lourens, I thank you for your help around the laboratory. Thank you for demystifying an engineering workshop.
8. Ms Beverley Glass deserves a mention. Her assistance with quotes and bursary payments is appreciated. In addition I want to thank her for the office humour and for being a wonderful colleague and friend.
9. Deep appreciation goes to Ms Jeanri Coetzee for being such a great help around the laboratory. I appreciate the trouble she went through in organising quartz crystal

microbalance experiments for me and for keeping the laboratory in order. I would also like to thank her for her incredible friendship. I will miss her.

10. To Uyuenendiwannyi Mandavha, thanks for being a wonderful friend and colleague, my days at SAFL were brightened because of you.
11. To Mr Keenan Heynes and Mr Wesley Neutt. I really appreciate the energy and enthusiasm you brought to the lab and assisting me tremendously during vacation work at SAFL. For the first time as SAFL the flow reactor worked properly, and it was due to you guys. Thank you for your friendship.
12. I would like to thank Mr Lucky Mokwena from the Central Analytical Facility (CAF) at the University of Stellenbosch for performing GC-MS on some of my soot samples while the GC-MS at SAFL was faulty.
13. A word of thanks goes to Mr Fletcher Hiten (from the CAF) for performing ESI-MS on my fuel samples as well as ICP-MS on my soot sample.
14. I would like to thank Ian Scott, Gary McFarlane, Rudi Russouw, Warren Randall, Chris Scully, Washington Mudenha, Timothy King, Marlan Perumal, Dylan Smit, Dirren Govender, Leanne Robertson, René Laryea-Goldsmith, Gareth Floweday, Aiden Ehrenreich, Mariam Ajam, Andrew Winstanly, Hundzukani Vukeya and Toby Rockstroh for being wonderful friends and colleagues.
15. Thanks also go out to my friends outside my research group for lifting my spirits during the tough times. A special mention goes to Juliette Dusabe, Natalie Hendrickse, Jason Cottle, Graham Morrison, Khanyisa Mubunda, Lisa Williams, Bianca Kriel, Ncediwe Ndlulwa and Sabina Yusuf Shaik. Thank you for your assistance throughout this journey.
16. To Stacey-Leigh Titus, my fantastic dance partner, I truly appreciated your encouragement and support particularly during the last stretch of my thesis.
17. Finally I would like to thank my family for their support. To my parents, I thank them for their genes and for providing me with a warm and loving living environment. I want to thank my siblings, Patrick, Celestine and Fabrice, for providing me with the motivation to do better and grow. I also want to thank them for their friendships.

Table of Contents

List of figures

List of tables

List of abbreviations

AMU	atomic mass unit
avg	average
B20	diesel which contains 20% fatty acid methyl ester (v/v)
B100	100% FAME (biodiesel)
CCD	charge-coupled device
CDPF	catalysed diesel particulate filter
CFPP	cold filter plugging point
DCA	deposit control additive
DOC	diesel oxidation catalyst
DPF	diesel particulate filter
DRIFTS	diffuse reflectance infrared Fourier- transform spectrometry
DSC	differential scanning calorimetry
DTG	differential thermogravimetry
dyno.	dynamometer
EBSD	electron backscattered detection
EDS	energy dispersive spectroscopy
EGA	evolved gas analysis
EGR	exhaust gas recirculation
EI	electron ionisation
EMU	Electron Microscope Unit
EN590	European Union automotive diesel fuel quality specification
eng	engine
ESI-MS	electrospray ionisation - mass spectrometry
ESI (+) MS	positive electrospray ionisation - mass spectrometry
EU	European Union
FAME	fatty acid methyl ester
FTIR	Fourier transform infrared spectroscopy
GC-MS	gas chromatography - mass spectrometry
GIF	Gatan image filter
HACA	hydrogen abstraction – carbon addition
HFRR	high frequency reciprocating rig
HPDI	high pressure diesel injector
HPLC	high performance liquid chromatography
HRTEM	high-resolution transmission electron microscopy
HSP	Hansen solubility parameter
ICP-MS	inductively coupled plasma – mass spectrometry
Jet A-1	civil aviation turbine fuel used outside the United States of America

MALDI-MS	matrix-assisted laser desorption/ionisation – mass spectrometry
max.	maximum
m/z	mass to charge ratio
NMR	nuclear magnetic resonance
NOx	nitrogen oxides
PAH	polyaromatic hydrocarbon
POME	palm oil methyl ester
PM	particulate matter
QCM	quartz crystal microbalance
RME	rapeseed methyl ester
RME20	rapeseed methyl esters, blended with 80% EN590 diesel (v/v)
rpm	revolutions per minute
SAFL	Sasol Advanced Fuels Laboratory
SEM	scanning electron microscopy
SFAC	Sasol Fuels Application Centre
SL-Bocle	sliding load Bocle
SME	soybean methyl ester
SME20	soybean methyl esters, blended with 80% EN590 diesel (v/v)
SMORS	soluble macromolecular oxidatively reactive species
SOF	soluble organic fraction
SOx	sulfur oxides
syn air	synthetic air
TEM	transmission electron microscopy
TGA-MS	thermogravimetric analysis - mass spectrometry
TIC	total ion count
TIGF	teflon impregnated glass fibre
TOD	thermo-oxidative deposit
TOS	thermo-oxidative stability
TPO	temperature programmed oxidation
UCT	University of Cape Town
USEPA	United States Environmental Protection Agency
wt%	mass (or weight) *per cent*

Abstract

Methods for the characterisation of fuel-derived carbonaceous materials were assessed. These methods were applied to two such materials, *viz.* diesel soot and diesel fuel deposits.

Diesel soot

Diesel soot, sampled from a commuter bus, was characterised using an array of analytical techniques. Physical and chemical characterisation of diesel soot was conducted with particular interest in the component of soot known as the soluble organic fraction (SOF). The SOF represents adsorbed chemical species and is traditionally obtained via Soxhlet extraction of soot using an organic solvent. Chemical speciation of the SOF was performed using GC-MS analysis.

Five solvents (hexane, cyclohexane, toluene, methanol and acetone) were compared with dichloromethane, the most extensively used solvent for the extraction of soot with respect to their ability to extract a variety of species, including polyaromatic hydrocarbons (PAHs) and potential endocrine disrupting molecules, *e.g.* phthalates.

Extraction results suggest that the SOF quantity depends significantly on the extraction solvent. For the soots analysed, SOF ranged between 1.0 and 4.8 wt%, depending on the solvent used. Moreover, it was shown that polar solvents extracted a greater SOF than non-polar solvents. For PAH extraction the order of efficiency was acetone > methanol > > toluene > hexane > cyclohexane while for esters, including endocrine disrupting phthalates, the order in efficiency was methanol > dichloromethane >acetone > toluene > > hexane > cyclohexane> n-hexane. A suggestion is made that to maximise SOF, sequential extraction should be made.

Thermogravimetric analysis revealed a discrepancy between VOF and SOF which was ascribed to the presence of sulfurous and sulfuric acid which were not extracted by the organic solvents investigated

Fuel deposits

Fuel was degraded in three reaction vessels, *viz*. a continuous flow reactor, open glass flasks and closed metal reactors (bombs) in an attempt to synthesise carbonaceous deposits, analogous to those found in diesel injectors. The degradation of four diesel fuels, *viz*. an EN590 reference diesel, a commercial diesel and two B20 biodiesel blends (rapeseed and soybean methyl esters blended with EN590 diesel), was investigated in the thermo-oxidative temperature regime, *i.e.* below 300°C.

The depositing propensity of the fuels was investigated using a quartz crystal microbalance (QCM). Data from the QCM indicated that the test fuels had different deposition propensities under stress conditions of 140ºC for 15 h with headspace air. The deposition for the test fuels was as follows: 1.3 µg/cm^2 (EN590 diesel), 6.4 µg/cm^2 (B20, RME), 11.9 µg/cm^2 (B20, SME) and 0.1 µg/cm^2 (commercial diesel). These trends were in agreements with TEM and TGA-MS results of both flask reaction and reactor bomb deposits where the biodiesel blends exhibited greater degradation than EN590 diesel and commercial diesel. The low deposition propensity of commercial diesel was ascribed to the presence of additives such as deposit control additives.

The test fuels degraded to different extents under flask reactor conditions (140ºC, 15 h and 50 mℓ flowing synthetic air). Mixtures of gums and carbonaceous deposits were produced. Thermogravimetric analysis, with mass spectrometric analysis of the evolved gases (TGA-MS), of mixture deposits showed that the carbonaceous deposits therein had lower thermal oxidative stability (combustion of deposits was complete by 550ºC) than diesel injector deposits (complete combustion occurs around 750ºC), reported elsewhere. The higher oxidative reactivity of flask reactor deposits was attributed to their association with oxygen moieties and amorphous structure, as shown by transmission electron microscopy (TEM). ESI-MS and FTIR confirmed the formation of oxygen-containing species and high molecular weight species. The formation of high molecular weight species was found to be consistent with the formation of a low volatility component as observed by TGA.

Experiments in closed metal reactors also produced gums and carbonaceous deposits. TEM micrographs showed that these deposits were amorphous and lacked regular interference patterns, typical of graphitic structures with the exception of deposits formed from SME20 at 240^{o}C in a closed bomb. In both reactor systems, biodiesel blends degraded to a greater extent than petroleum diesels. TGA-MS demonstrated a strong correlation between differential thermogravimetry and CO_2 evolution. Each fuel formed deposits with a variety of H:C ratios. Components that burnt at higher temperatures had lower H:C ratios.

No discernible deposits were formed in the flow reactor under the conditions studied. It was consequently recommended that flow reactors be modified with recirculation loops to better mimic common rail diesel injector systems.

1 Introduction

"Begin, be bold, and venture to be wise."-Horace

1.1 Subject and motivation for this study

This dissertation is a study in two parts which concerns the characterisation of two fuel-derived carbonaceous materials: diesel soot and diesel fuel deposits. This study not only makes use of conventional analytical techniques such as Soxhlet extraction and electron microscopy but also less applied techniques such as thermogravimetric analysis (TGA) with identification of the evolved gases by mass spectrometry (MS).

1.1.1 Diesel particulate matter (PM)

Diesel particulate matter (PM) or soot is a nano-structured, carbonaceous, solid material that results from incomplete combustion of hydrocarbon fuels that is found in in diesel engine exhaust emissions [1]. There is increasing interest in diesel PM by toxicologists, environmental scientists, local governments and the automotive industry because it can contain potentially high levels of carcinogenic compounds such as polyaromatic hydrocarbons (PAHs) as well as other molecules, predominately phthalates, some of which have been implicated as endocrine disruptors [2, 3, 4]. While PAHs are primarily a by-product of fuel combustion in the engine, phthalates are typically derived from engine lubricating oil [4, 5]. During engine exhaust gas cooling PAHs and other molecules, which adsorb onto the soot matrix, become associated with the soluble organic fraction (SOF) of soot, *i.e*. the component of soot that is solvent extractable.

A number of studies have partially addressed the characterisation of the soluble organic fraction (SOF) of diesel soot. Most are concerned with PAHs rather than potential endocrine disruptors. Few studies address the influence of the extraction solvent has on the quantity and types of molecules that are extracted. In the case of endocrine disruptors, no studies have been conducted which address the effect the solvent type has on the extraction of such molecules from soot.

Consequently, the objectives of this study were:

1. to investigate the influence of solvent nature, particularly polarity, on the nature (quantity and composition) of the fraction extracted from soot,
2. to ascertain the efficiency of different solvents at extracting PAHs and potential endocrine disruptors
3. to apply thermogravimetric techniques to the characterisation of soot.

1.1.2 Diesel deposits

Fuel instability, *i.e.* the tendency of a fuel to undergo physical and chemical transformations prior to combustion, is of concern to fuel and vehicle manufacturers [6]. Fuel stability is often referred to as the resistance to decomposition at elevated temperatures which leads to the formation of solid deposits [7]. During diesel engine operation, fuel instability can lead to the formation of carbonaceous deposits and gums in various parts of the fuel system, *e.g.* fuel filters and injectors, as the fuel is exposed to elevated temperatures and pressures as well as an oxygenated environment [8]. Deposits can lead to increased maintenance costs, decreased reliability, decreased fuel economy, increased exhaust emissions and in severe cases engine failure [6].

Many studies on diesel fuel deposits have used two approaches to sampling deposits: either simulations are performed, using test bed engines, until deposits are formed on vehicle components, primarily injectors [9], or deposits are sampled from those formed in field vehicles [10]. The synthesis of deposits via degradation of diesel fuel using laboratory reactors is an approach that currently hasn't been well explored although a significant literature exists for the application of such techniques to jet fuel [11, 12] where deposits, similar to those found in aviation fuel systems, have been produced. This study also serves as one of the first to produce deposits from biodiesel blends in the thermo-oxidative (130-300^{o}C) regime rather than the oxidative regime (<120^{o}C).

The following objectives were set for the study of diesel deposits:

1. to ascertain the depositing propensity of a set of test diesel fuels (a commercial diesel, an EN590 diesel (reference fuel), EN590 diesel (80% by volume) with rapeseed methyl ester (biodiesel) and EN590 diesel (80% by volume) with soybean methyl ester (biodiesel) using a quartz crystal microbalance (QCM) reactor,
2. to synthesise fuel deposits by degrading diesel fuel within the thermo-oxidative regime (130-300°C) in three reactors, which are often used for thermo-oxidative stability (TOS) studies, *viz.* a continuous flow reactor, open glass flasks and closed metal reactors, using the four different diesel fuels to enable comparison between deposits of different diesel fuels,
3. to assess the morphology of these deposits using electron microscopy and compare them to deposits found in vehicles and test bed engines,
4. to analyse the deposits with thermogravimetric analysis coupled with mass spectrometry, and
5. to use electrospray ionisation mass spectrometry (ESI-MS) and Fourier transform infrared (FTIR) spectroscopy to investigate the formation of deposit precursors.

1.2 Limitations and scope of the study

1.2.1 Diesel particulate matter

Only one source of diesel particulate matter (PM) is reported in this study: the exhaust pipe of a commuter bus, although methods were developed using a wide range. The intention of this study was not to assess the impact of different engine conditions on soot properties, but rather to develop methodologies for the characterisation of soot.

A commuter bus provided sufficient sample size to enable characterisation using all analytical techniques. Table 1.1 features the techniques that were used to examine diesel PM.

Table 1.1: Techniques employed for the characterisation of diesel PM

Analytical technique	Feature of PM studied
Scanning electron microscopy (SEM)	Soot morphology and structure
Transmission electron microscopy (TEM)	Soot particle size, morphology, crystallinity and structure
Soxhlet extraction	Soluble organic fraction (SOF) size
Gas chromatography – mass spectrometry (GC-MS)	SOF chemical speciation
Thermogravimetric analysis (TGA) with evolved gas analysis (EGA)	Oxidative reactivity, SOF quantification

1.2.2 Diesel deposits

Because the emphasis was on the development of characterisation methods, a restricted set of stressing conditions were adopted for each set of reactor experiments. Fuel was degraded using four reactors, *viz*. a continuous flow reactor, open glass flasks, closed metal reactors and a quartz crystal microbalance (QCM). Four fuels were used: a commercial diesel, an EN590 reference diesel and two 20% biodiesel blends, *i.e.* a first blend of 20% (v/v) of rapeseed methyl ester (RME) with 80% (v/v) EN590 diesel and a second blend of 20% (v/v) of soybean methyl ester (SME) with 80% (v/v) EN590 diesel. Testing in all reactors was conducted at temperatures ranging from 140-250°C, which are temperatures that lie within the thermo-oxidative regime (130-300°C) in the presence of dissolved or excess air. The fuel deposits were analysed using electron microscopy (TEM) and thermogravimetric analysis with evolved gas detection by mass spectrometry (TGA-MS) while fuel precursor deposits, restricted to those obtained from flask reactions, were evaluated using ESI-MS. Because limited deposit samples were obtained with some reactors, *e.g.* flow reactor, less comprehensive characterisation was performed. This applied particularly to analytical techniques that require large quantities of samples.

1.3 Plan of development

This thesis is constructed in two parts, each addressing characterisation of a different fuel-derived carbonaceous material: diesel soot and thermo-oxidative deposits. It commences with Chapter 2, a literature review, covering both types of materials. Chapter 3 encompasses the materials used and methods that were involved to characterise diesel PM. In part 2 of Chapter 3, the synthesis conditions and characterisation protocols for diesel fuel deposits are highlighted. Chapter 4 addresses the application of a variety of characterisation methods to soot. Chapter 5 investigates the deposit forming propensity of the four test fuels, using data obtained from a quartz crystal microbalance. Chapters 6, 7 and 8 address the characterisation of fuel-derived deposits. These deposits were produced in open flask reactors, closed bomb reactors and a continuous flow reactor. Chapter 9 provides general conclusions while Chapter 10 covers general recommendations for future studies.

2 Literature Review

"The only true wisdom is in knowing you know nothing." -Socrates

2.1 Diesel fuel

Diesel is a liquid fuel that powers compression ignition engines [13] which is widely used in Europe where it fuels 53% of passenger vehicles and, increasingly, elsewhere in the world. Its use has been rising because compression ignition engines' superior efficiency, translates into higher fuel economy [14]. Typically, a 25-40% better fuel efficiency is obtained in comparison to an equivalent spark ignition (petrol) engine [13, 15].

2.1.1 Source and composition of diesel fuel

2.1.1.1 Petroleum diesel

Petroleum diesel is derived from a middle distillate, distilled from crude oil at temperatures between approximately 160°C and 360°C. It is a complex mixture of hydrocarbons, with carbon numbers ranging from C_9 to C_{20} [16]. Typical classes of compounds that are found in diesel include *iso* and *n*-paraffins, aromatics, naphthenes (*i.e.* cycloalkanes) and mixed aromatic cycloalkanes, *e.g.* tetralin [16, 17].

Aromatic compounds form an important class of molecules which are primary soot precursors. Of these precursors, most significant are those where the aromatics are composed of multiple aromatic rings. These compounds are termed polycyclic aromatic hydrocarbons (PAHs), some of which, *e.g.* benzo(α)pyrene, have been shown to be carcinogens [17, 18].

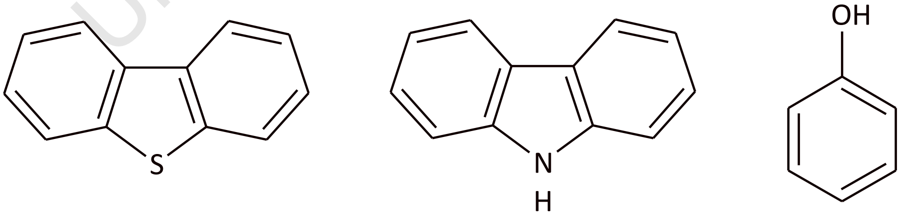

Figure 2.1: Heteroatomic species found in diesel fuel. Left to right: dibenzothiophene, carbazole and phenol

Although diesel fuel is primarily composed of hydrocarbons, there are a small quantity of molecules which have other elements (other than carbon) included in their backbone. These classes of molecules are known as heteroatomic molecules and they contain the elements sulfur (*e.g.* in dibenzothiophene), nitrogen (*e.g.* in carbazole) and oxygen (*e.g.* in phenol). These are illustrated in Figure 2.1. Even though these heteroatomic molecules occur in minor quantities in diesel fuel, they have a significant influence on the properties of the fuel [17].

A number of grades of diesel may be produced [19]. A number of region-specific classification systems exist for diesel fuel. The USA, for example, classifies diesel into three categories denoted 1-D, 2-D and 4-D. Further sub-classifications, *e.g.* based on sulfur content, may exist [16, 20]. The European Union (EU) has its own automotive diesel fuel quality specification, EN590, which also contains sub-classifications which differ in cold filter plugging point (CFPP) values [21].

2.1.1.2 Biodiesel

Declining crude reserves and a rise in petroleum diesel fuel prices have led to the introduction of biodiesel fuel into the market [22]. The most common type of biodiesel is composed of fatty acid methyl esters (FAMEs) [22]. FAMEs are derived from the reaction of vegetable oil or animal fat triglycerides with methanol in the presence of a catalyst. A generic trans-esterification reaction is shown in Figure 2.2. The main vegetable oil sources, which are used to make biodiesel, include rapeseed oil, sunflower oil, palm oil and soybean oil. Non-edible feedstocks include jatropha, mahua, karanja, castor, microalgae, camelina and vegetable waste oils [22].

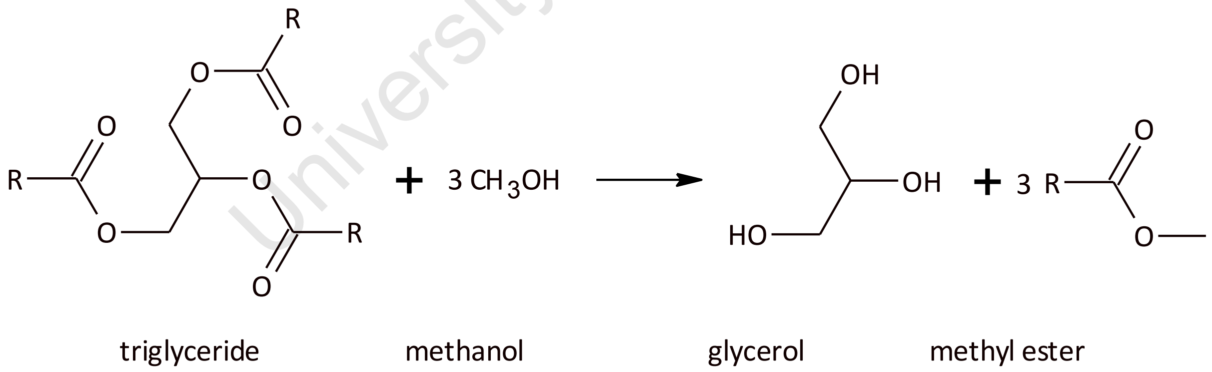

Figure 2.2: Trans-esterification reaction used to produce FAME

2.2 Fuel and engine oil additives

Pump diesel fuel is composed not only of base fuels but also contain many additives [23]. These are added to the base fuel primarily to enhance the quality of the fuel as well as to meet specifications [23]. A wide variety of additives such as detergents, lubricity and cold flow improvers are available [23]. Lubricity additives form an important class of additives primarily because they have helped alleviate the adverse effects of hydrotreatment (a process that is employed in the production of low sulfur fuels) [24]. Removal of sulfur compounds in fuels negatively affects the lubricating abilities of the fuel and usage of unadditised ultra low sulfur diesel (< 20 ppm) can result in drivability and pump failures which arise from excessive wear on components comprising fuel injector pumps [25]. Together with the base fuel, these additives may contribute to the formation of diesel emissions.

Aside from fuel, engine oil may also contribute to soot. It is estimated that about 10% of lubricating oils produced are fully synthetic [26]. These synthetic oils which are composed of saturated olefin oligomers lack lubricating properties and consequently lubricity additives are added into the oils to meet specification [26].

The chemical nature of lubricity additives for both engine oil and diesel fuel is similar. The most common feature of lubricity additives is that they “consist of a polar functional group attached to an oleophilic part” [24]. The polar functional groups of the additives are typically carboxylic acid esters (ester), carboxylic acids and carboxylic acid amides (amide) [24]. These are illustrated below:

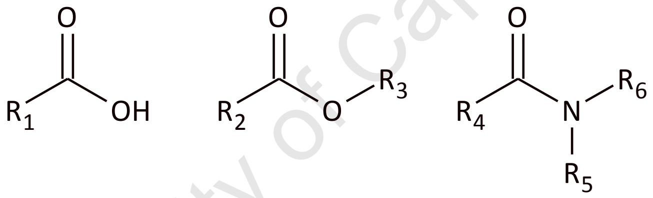

Figure 2.3: Functional groups of lubricity additives. Left to right: carboxylic acid, carboxylic acid ester and carboxylic acid amide

2.3 Diesel PM emissions

Although diesel engines enjoy a number of advantages over spark ignition engines, diesel engines come with a few drawbacks. Chief among these is that diesel engines emit approximately 10 times more particulate matter (PM) than spark ignition engines. PM is defined by the USEPA as the material collected on a glass fibre filter from the vehicles exhaust gas that has been diluted and cooled to 52°C or below. It is a carbonaceous soot matrix with adsorbed hydrocarbons and inorganic compounds, such as sulfates, and imbedded metallic ash [27].

Not only is PM a potent air polluter but studies have also shown that it can be harmful to human health [27]. Upon inhalation, soot particles may aggravate underlying pulmonary and cardiac problems which may ultimately cause death. Soot particles that are smaller than 100 nm in size (ultra-fine particles) cannot be filtered by the respiratory tract. Long term exposure can lead to cancer and/or asthma [28, 29].

2.3.1 Components of diesel PM

2.3.1.1 Carbonaceous soot

Carbonaceous soot is the largest component of diesel PM and forms the matrix of exhaust PM onto which several species are adsorbed [27]. Soot is primarily composed of fixed carbon with varying degrees of hydrogen [30]. Soot particles exist as agglomerates (cluster or chain-like aggregates) with primary particles 15-30 nm in diameter [27, 31]. The basic building units of the fixed carbon are graphene segments which are polyaromatic structures [32].

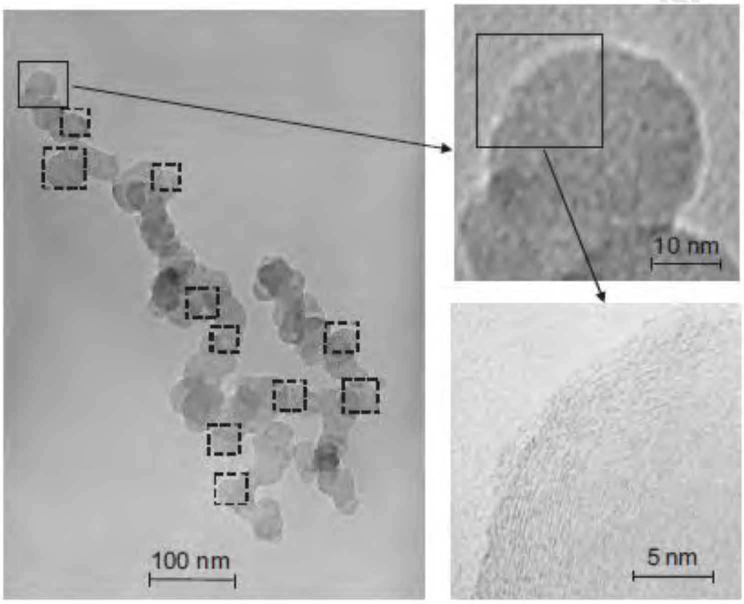

Figure 2.4: TEM images depicting the shape and internal structure of a primary soot particle (spherule) as component of a larger agglomerate, reproduced from [33]

The TEM micrograph in Figure 2.4 shows a typical soot agglomerate as well as the primary particle. The primary particle is nearly spherical in nature while the agglomerate is inherently irregular in shape [33]. The irregularities of the agglomerates further extend to their size as well as their apparent compactness [34].

2.3.1.2 Adsorbed hydrocarbon species

Soot acts as matrix for several adsorbed hydrocarbons which when extracted form a component known as the soluble organic fraction (SOF). The chemical speciation and quantity of the SOF depends on a number of factors including engine performance, mode of operation, fuel and lubricating oil quality [35]. Traditionally, the SOF is composed of paraffins, aromatic species and oxygenated compounds. The quantity of SOF has been shown to vary significantly between 5 and 60% of total PM mass [35].

2.3.2 Composition of the SOF and its effects on biological systems

2.3.2.1 Polyaromatic hydrocarbons (PAHs)

The adverse effects of the SOF on biological systems have been known for over 30 years. By 1981 several studies had shown that soot extracts from light-diesel engines could cause mutations in bacteria and mammalian cells [36].

Yu and Hites conducted comprehensive gas chromatography-mass spectrometry (GC-MS) on several diesel soot extracts to identify possible mutagenic species [36]. Despite analysing the SOF of diesel soot using several different solvents, Yu and Hites presented only GC-MS spectra of the hexane/toluene and toluene fractions as previous had demonstrated that these fractions were the most mutagenic. The hexane/toluene fraction was found to be composed entirely of polyaromatic hydrocrabons (PAHs) while the toluene fraction was composed of oxygenated PAHs and and ketones [36].

A range of studies to characterise diesel soot SOF and, in particular PAHs, have been conducted [2, 3, 35, 37, 38, 39, 40, 41]. More than 32 PAHs have been classified in diesel engine emmisions by the US Environmental Protections Agency (USEPA). 16 of these have been added to a priority list, due to their carcinogenic potential. These compounds are listed in Table 2.1.

Table 2.1: List of 16 PAHs on the USEPA's priority list, adapted from [3]

Priority PAHs	
naphthalene	chrysene
acenaphthylene	pyrene
acenaphthene	benzo(g,h,i)perylene
fluorene	fluoranthene
phenanthrene	indeno(1,2,3-c,d)pyrene
anthracene	benzo(β)fluoranthene
dibenz(α,η)anthracene	benzo(κ)fluoranthene
benz(α)anthracene	benzo(α)pyrene

Jonker [40] performed a comprehensive study on the effectiveness of different solvents on PAH extraction [40]. It was found that a mixed solvent: toluene/methanol (1:6) was best.

2.3.2.2 Phthalates

Another important class of molecules in the SOF are phthalates. *In vivo* some phthalate molecules may act as endocrine disruptors which modify the hormone production system [4]. In 1998 the Japanese Environmental Agency identified a range of chemicals as endocrine disruptors. A significant percentage were phthalate molecules [42]. Phthalates that compose the SOF of diesel soot may have a number of sources including polymer rubber seals, where they are employed as plasticisers, and automobile lubricating oils [43]. Few studies have focussed on endocrine disruptors in diesel soot [4, 44]. They have been even less concerned with the nature of the extraction solvent.

Todovorić and Zdravkovski [4] recently developed a screening methodology for the determination of components (primarily PAHs and endocrine disruptors) in diesel PM. Soot was collected from vehicles, containing particulate matter traps, which were driven in field tests. The traps were extracted using toluene as solvent. In some cases, the extraction process was sped up by ultrasonication. The toluene extract was then concentrated for GC-MS analysis by rotary evaporation [4].

Table 2.2 lists potential endocrine disruptors and PAHs components which were identified in the exhaust PM of several diesel vehicles.

Todovorić and Zdravkovski [4] found many other classes of molecules in the SOF including alkanes, PAHs, aromatics, alcohols, alkenes, aldehydes, esters and acids.

Table 2.2: Chemical components in exhaust PM, adapted from [4]

CAS	**Name**
	Potential endocrine disruptors
106-44-5	4-methylphenol
2050-67-1	3,3'-dichloro-1,1'-biphenyl
84-66-2	diethyl phthalate
84-69-5	1,2-benzenedicarboxylic acid, bis(2-methylpropyl) ester
4376-20-9	1,2-benzenedicarboxylic acid, mono(2-ethylhexyl) ester
	PAHs
91-57-6	2-methylnaphthalene
120-12-7	anthracene
129-00-0	pyrene
91-20-3	naphthalene
85-01-8	phenanthrene

2.3.2.3 *Effect of extraction solvent on the size of the soluble organic fraction*

There is little other work in the literature which investigates the influence of the solvent on the quantity of SOF extracted. Although the variation in SOF quantity has been attributed to engine conditions and fuel, the influence of the nature of the extraction solvent on the quantity of SOF has often been ignored. The quantity of SOF is reported to vary between 5 and 60% of total PM mass [35]. Most often studies are performed using dichloromethane as solvent [31, 40]. Clague *et al.* performed a sequential extraction of dichoromethane followed by benzene to render the soot "clean", *i.e.* in a state where all but the most strongly bound organic molecules have been removed [31].

One study that addressed the impact of solvent type on SOF amount is that of Collura *et al.* [35]. They demonstrated that extraction using a single solvent yielded a lower quantity of SOF than applying two different solvents. Like Clague *et al.*, they used dichlormethane followed by an aromatic solvent. Instead of the toxic benzene, they used the less toxic toluene. Extraction using dichloromethane initially yielded a SOF value of 2.85wt % while subsequent extraction of soot with toluene yielded a further SOF value of 3.20wt % to give a total SOF of 6.05wt. %. This illustrates the importance of extraction solvent on the quantity of SOF which served as a motivation for the first part of the current investigation.

While there is little work on the influence of solvent type on the size of the SOF, even less work has been done on the effect of the solvent on the chemical speciation of the SOF.

2.4 Thermo-oxidative stability of middle distillate fuels

Thermo-oxidative deposit formation results from fuel exposure to elevated temperature in the presence of oxygen. In diesel vehicles, deposits may be found in a number of engine components such diesel injectors, fuel filters and cylinders [45, 46].

2.4.1 Diesel injector deposits

To combat relatively high PM emissions from diesel engines, stringent emission legislations have been introduced in many countries [13]. In order to meet emission legislations automotive manufacturers have had to develop improved engine technology, including fuel injection equipment [47]. Developments have meant a reduction in nozzle orifice diameters and increased injection pressures [48]. The reduction in nozzle diameters has made injectors more sensitive to deposit formation which blocks exit holes [48].

The exposure of diesel fuel to high temperatures can cause deposits in the nozzle area of injectors (see Figure 2.5). Deposit formation depends on many factors including fuel and lubricant composition, engine design and operating conditions. Deposit build-up in injectors affects the fuel flow patterns which reduces fuel economy and increases emissions of soot and unburned hydrocarbons [8].

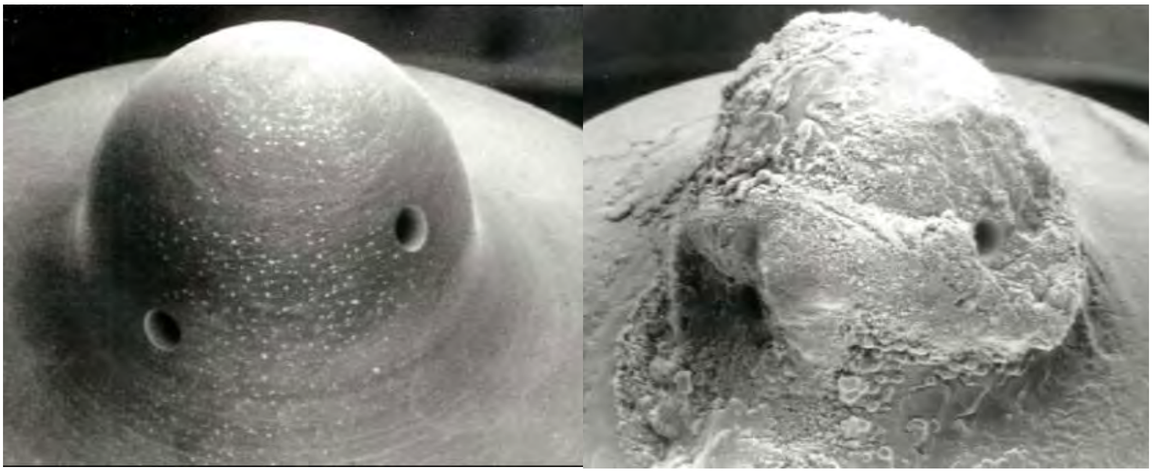

Figure 2.5: Clean (left) and fouled (right) injector, reproduced from [47]

2.4.2 Mechanism of deposit formation

Injector nozzle coking/fouling occurs near 300°C through condensation and cracking reactions [9]. The precise chemical reactions, however, remain to a large extent unknown or poorly understood because of their complexity. They are thought to involve polymerisation, auto-oxidation and thermal decomposition [9].

The high temperatures and excess air in the in the combustion cavity of the diesel engine, as well as that dissolved in the fuel, create a highly oxidising environment for fuel at the injector tip [9]. This leads to fuel undergoing free-radical chain reactions that result in the formation of hydroperoxides (see Figure 2.6 [45]).

Initiation

$$\mathrm{RH} \xrightarrow{\Delta} \mathrm{R}^{\bullet} + \mathrm{H}^{\bullet} \qquad (1)$$

Propagation

$$\mathrm{R}^{\bullet} + \mathrm{O_2} \longrightarrow \mathrm{ROO}^{\bullet} \qquad (2)$$

$$\mathrm{ROO}^{\bullet} + \mathrm{RH} \longrightarrow \mathrm{ROOH} + \mathrm{R}^{\bullet} \qquad (3)$$

Chain branching

$$\mathrm{ROOH} \longrightarrow \mathrm{RO}^{\bullet} + \mathrm{HO}^{\bullet} \qquad (4)$$

$$\mathrm{RO}^{\bullet} + \mathrm{RH} \longrightarrow \mathrm{ROH} + \mathrm{R}^{\bullet} \qquad (5)$$

$$\mathrm{HO}^{\bullet} + \mathrm{RH} \longrightarrow \mathrm{H_2O} + \mathrm{R}^{\bullet} \qquad (6)$$

Termination

$$R^\bullet + R^\bullet \longrightarrow R-R$$

$$\left.\begin{array}{l} ROO^\bullet + R^\bullet \\ \\ ROO^\bullet + ROO^\bullet \\ \\ RO^\bullet + R^\bullet \end{array}\right\} \text{acids, ketones, esters, alcohols } \textit{etc.}$$

Figure 2.6: Reactions showing oxidation of hydrocarbon by free-radical chain reactions [45]

Subsequent reactions lead to the formation of low molecular weight materials such as ketones, acids, alcohols and aldehydes [45]. High molecular weight materials form when low molecular weight species react through polymerisation reactions as illustrated in Figure 2.7. The high molecular species that are formed are observed as deposits, sludges and varnishes [45].

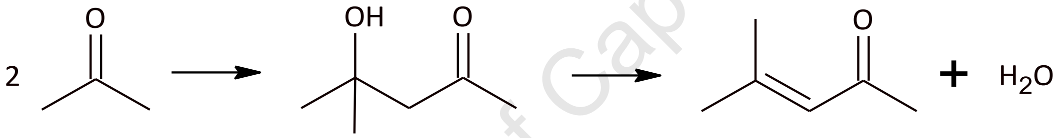

Figure 2.7: Condensation and polymerisation reactions of primary oxidation products, reproduced from [45]

2.4.2.1 Soluble macromolecular oxidatively reactive species (SMORS) mechanism

Thermo-oxidative deposits do not result only from the hydrocarbon species in middle distillate fuels. Heteroatomic species have been implicated as key contributors to poor thermo-oxidative stability of such fuels. The influence of such species may be explained by a variety of mechanisms, one of which is the soluble macromolecular oxidatively reactive species (SMORS) mechanism [49, 50, 51, 52].

SMORS, which have a molecular mass less than 900g/mol, are species formed when low molecular-weight heteroatomic molecules react to form larger molecular-weight heteroatomic species that incorporate oxygen [50, 52]. Species, heavier than 900g/mol, which form from further reaction precipitate out as deposits [49].

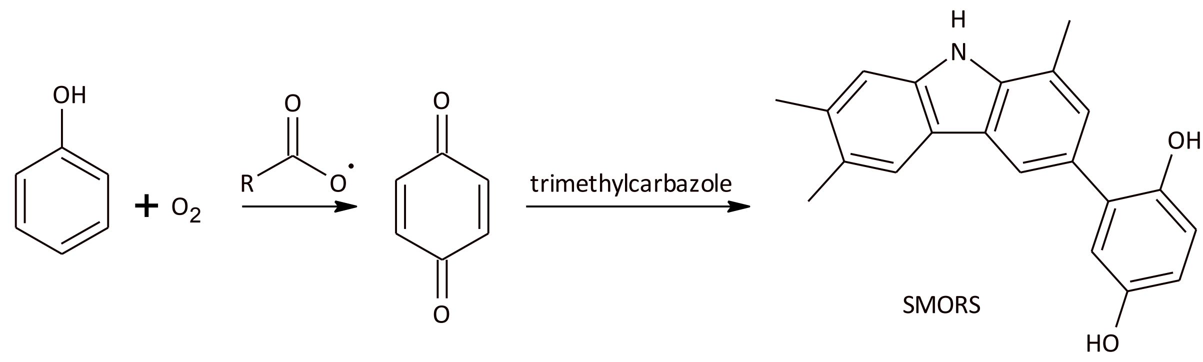

Figure 2.8: Scheme by which SMORS are formed [49]

An example reaction, showing the formation of a SMORS, is illustrated in Figure 2.8. A compound, often found in petroleum middle distillates, phenol, reacts with oxygen and a hydrocarbon peroxide (see Figure 2.6) to form a quinone which subsequently reacts with an electron-rich aromatic compound, *e.g.* trimethylcarbazole, to yield a low molecular weight SMORS.

It is important to note that the reaction scheme shown in Figure 2.8 and, indeed, the SMORS mechanism is meant to be generic and is applicable to a variety of other compounds in addition to the ones shown in Figure 2.8. Examples of other electron-rich aromatic compounds, found in petroleum diesel, which can react with the quinone, include pyrroles, anisoles, indoles, carbazoles and biphenyl anisoles [49]. Ultimately the fate of a SMORS species is such that it undergoes further coupling reactions until its molecular weight and polarity causes it to precipitate out of solution. The products that are formed are termed thermal oxidative deposits (TODs) [50].

Further insight into fuel stability and the many factors that affect it can be found in [6, 9] and [53].

2.4.2.2 Mechanism of the thermo-oxidative stability of fatty acid methyl esters (FAMEs)

Fatty acid methyl esters are known to have lower oxidative stability than petroleum diesel [54, 55, 56, 57, 58].

The oxidation of FAMEs causes both the formation of lower and greater molecular weight species. The mechanism for the former is well established but that for the latter is less certain. It is the latter that gives rise to gums and sludges [59]. This process is initiated by the formation of hydroperoxides [60]. Fang and McCormick used Fourier transform infrared (FTIR) and nuclear magnetic resonance (NMR) spectroscopy to study FAME degradation. From this they proposed several high molecular weight structures [61]. The following reaction scheme has been proposed for the thermo-oxidative reactivity of a FAME component, methyl linoleate.

It was proposed that unsaturated compounds are oxidised at allylic carbons while doubly unsaturated species such as methyl linoleate are oxidised at *bis*-allylic carbons [59].

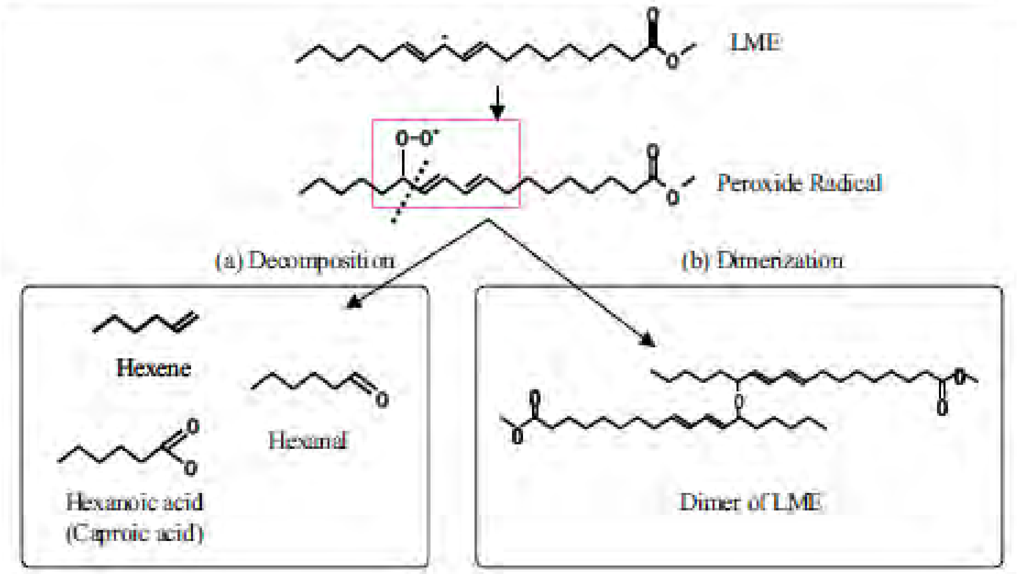

Figure 2.9: Proposed reaction scheme for the thermo-oxidative degradation of methyl linoleate [59].

2.4.3 Fuel deposit production

2.4.3.1 Engine and engine component tests

Several approaches have been taken by authors to investigate deposits formed in diesel engines. Most often a series of engine test cycles, which attempt to simulate field conditions, are performed. Deposits that have formed on engine parts such as injectors and cylinder heads during the test run are analysed [9, 62].

A second approach is to analyse deposits from sample engine components from vehicles (field tests). Studies by Barker *et al.* [46] and Venkataraman and Eser [10] adopt this approach.

2.4.3.2 *Reactor testing*

Venkataraman and Eser [10], and Mayo and Bosco [63] adopted an approach where deposits are formed by subjecting fuels to accelerated degradation tests. In accelerated degradation tests, fuels are subjected to conditions, which favour the formation of deposits and/or gums, for extended periods of time [63]. This has been widely applied in the study of jet fuel deposits. Fuel is typically degraded using a range of apparatus including closed bomb reactors (often heated in a sand bath) [49], continuous flow rigs [11, 12, 52, 64] and glass flasks [50, 63].

The advantage that reactors have over bench test cycle testing in the study of fuel degradation is that reactors provide more degrees of freedom, *i.e.* more variables can be introduced and hence enable one to test a wider range of factors. The role of temperature, air pressure, metal substrates, oxygen concentration and sulfur content in deposit formation has been well studied using the aforementioned reactors [6, 11, 12, 63]. Reactor studies are useful for development of fuel degradation mechanisms [50, 63].

2.4.3.3 *Quartz crystal microbalance*

In many of the afore-mentioned reactors, forming sufficient deposits to quantify is a challenge [65]. The minute quantity of deposits formed during mild fuel degradation tests has led to the development of tests under more extreme conditions. Unfortunately these accelerated tests are conducted at conditions (elevated temperature and/or high oxygen availability) that may not be a realistic representation of what a real fuel may experience. The chemical mechanisms, governing the reactions at accelerated conditions, may differ from the mechanisms that govern fuel degradation under real world conditions [65].

The quartz crystal microbalance (QCM), developed by Klavetter *et al.* [66] for jet fuel stability studies, is a reactor with the ability to execute real-time *in situ* measurements of deposition at temperatures that closely approximate real fuel system conditions [65]. The instrument can resolve minute quantities of surface deposits, as low as 0.1 to 0.2$\mu g/cm^2$. This inherent high sensitivity has paved the way for real-time fuel deposition tests at low temperatures [65]. Further insight into the basic operation of the QCM as well as the theory behind its workings can be found in [65] and [67].

2.4.4 Deposit characterisation techniques

A number of techniques have been used to investigate diesel deposits. The discussion that follows addresses the application of the techniques, used in this study, to thermo-oxidative deposits.

2.4.4.1 Transmission electron microscopy

Barker *et al.* [46] investigated the microstructure and degree of crystallinity of carbonaceous diesel deposits, obtained from fuel filters from engines employing high pressure common rail systems.

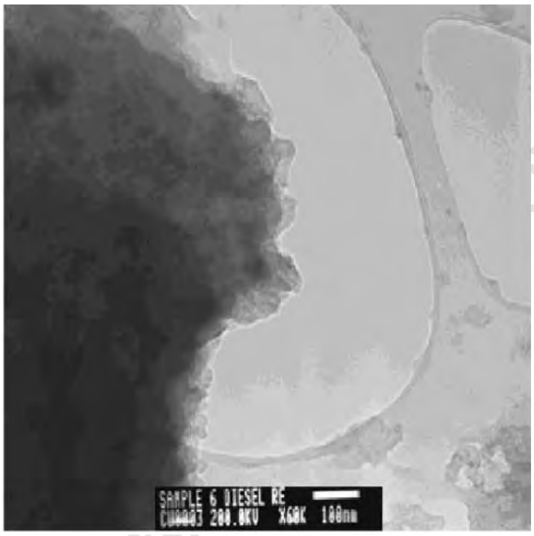

Figure 2.10: TEM at image of a deposit sample from a field filter [46]

Fuel filter deposits are not necessarily thermo-oxidative in origin and may form during storage at low temperature or as the result of microbial action.. The absence of regular interference patterns in transmission electron microscopy (TEM) micrographs of filter deposits reveal deposits that are primarily amorphous in nature (see Figure 2.10).

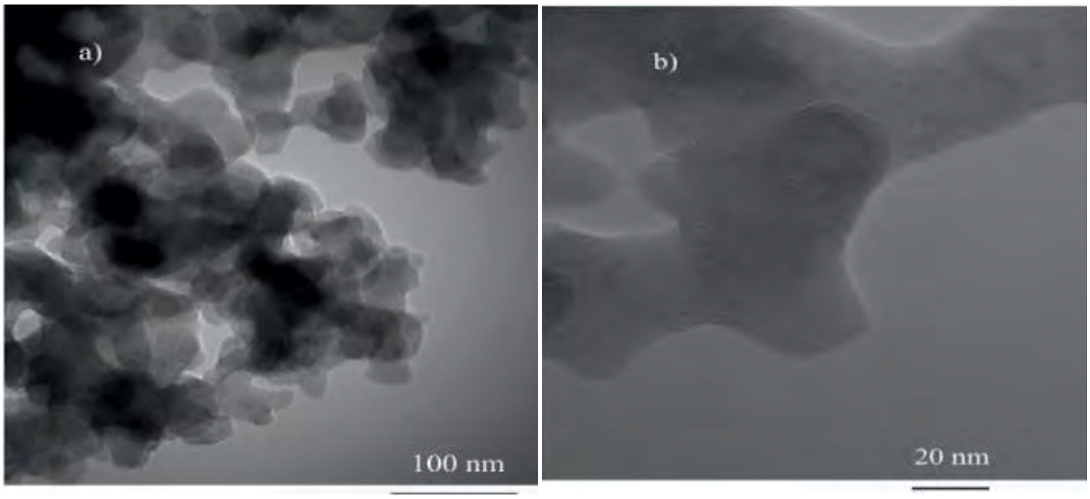

Figure 2.11: TEM image of deposits from an HPDI (high pressure diesel injector) at increasing magnifications [10]

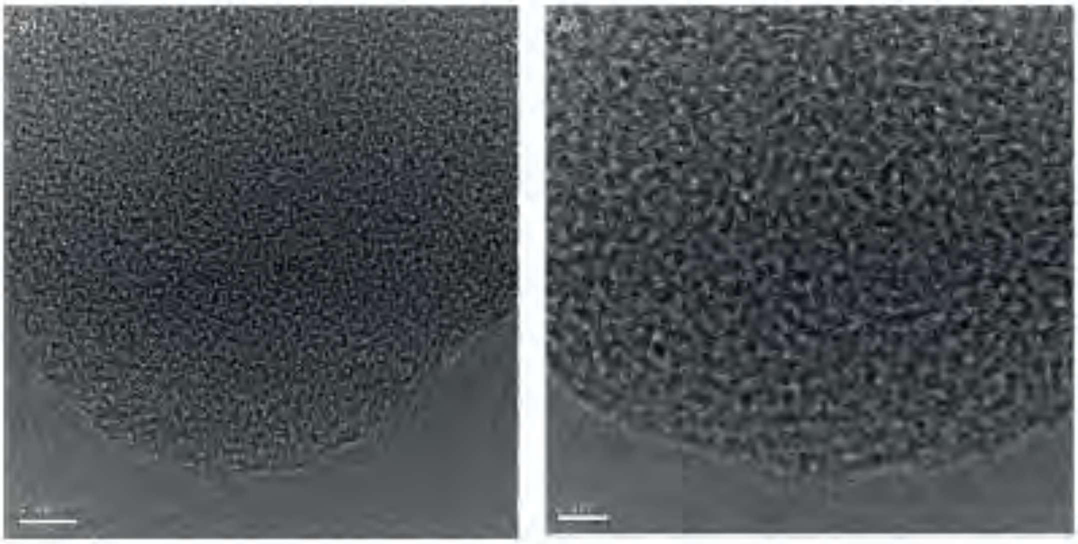

Figure 2.12: HRTEM images of particle deposits obtained from an HPDI [10]

Venkataraman and Eser [10] used TEM to observe the microstructure, crystallinity and configuration of deposits which were obtained from fuel injectors which were stripped from a diesel vehicle. TEM was conducted after scanning electron microscopy (SEM) analysis to confirm the configuration of deposits.

SEM revealed that the deposits of a diesel injector consist of agglomerated particles that form condensed structures. These can be seen in the high resolution TEM (HRTEM) micrographs in Figure 2.11. Figure 2.12 contains images of the same particle at very high magnifications which show that individual particles of HPDI deposits contain no significant regions of layer plane alignment in their internal structures. No long-range structure, *i.e.* large crystalline regions, is present.

Very few studies have investigated the morphology of diesel deposits produced using simulation apparatus such as flow reactors, fluidised sand bath and flask reactors. Where flow reactors have been used to form diesel deposits for characterisation, the deposits have often been formed at very high temperatures, *e.g.* in excess of 400°C [7, 52]. These few studies have usually been restricted to petroleum diesels or model compounds.

Venkataraman and Eser, however, did use TEM to visualise deposits, derived from degradation of a diesel model compound, *n*-hexadecane, in a flow reactor which can be seen in Figure 2.13 [10].

Agglomerates of near spherical primary particles can be seen. This suggests deposit nucleation and growth in the liquid phase. At higher magnification the internal structure of the deposit is revealed as a largely amorphous carbonaceous interior. Towards the periphery of the deposits, parallel lattices fringes can be observed. These fringes are indicative of layers of planar poly-aromatic structures [10]. The presence of these fringes in *n*-hexadecane, rather than real fuel deposits, may be because the simpler model systems have fewer interfering molecules which may disrupt ordered growth.

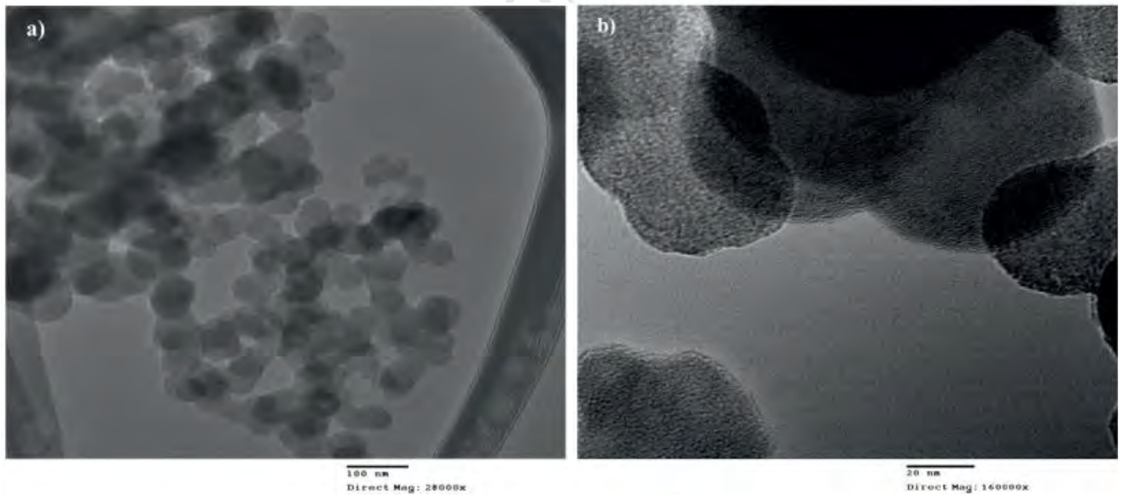

Figure 2.13: TEM images of deposits formed from thermal oxidative degradation of n-hexadecane at 10°C and 31bar for 2.5h [10]

2.4.4.2 Thermogravimetric analysis (TGA)

Thermogravimetric analysis (TGA) is a thermal analysis technique in which a sample's mass is measured as a function of temperature or time in a controlled atmosphere [68]. Although a single TGA experiment can induce a variety of physical or chemical changes in the sample, not all of them are detectable by the TGA instrument. Some of the physical phenomena identifiable by a TGA include absorption, sublimation, adsorption, desorption and vaporisation. While TGA is predominantly used for the investigation of physical phenomena several chemical phenomena can be investigated namely: chemisorptions, oxidative degradations, desolvations (especially dehydration) and solid-gas reactions (oxidation or reduction) [68] .

TGA has been extensively used for coal and soot classification studies. Significantly fewer studies are reported on fuel deposits [62]. Very few studies on deposits, derived from thermal-oxidative degradation of fuel using laboratory apparatus, could be found. Husnawan *et al.* [62] used TGA to demonstrate its potential use for the evaluation of the thermal stability of in-cylinder deposits, formed on a single-cylinder direct injection diesel engine cylinder head from a compression ignition engine fueled running on diesel fuel emulsions containing 0%, 5%, 10% and 15% water and 20% palm oil methyl ester (POME) with conventional diesel. They used simultaneous TGA-DSC in an air atmosphere [62] at a heating rate of 10°C/min to 950°C, where after they were held isothermally until a constant mass was achieved. The remaining residue was identified as ash and consists of inorganic salts and oxides.

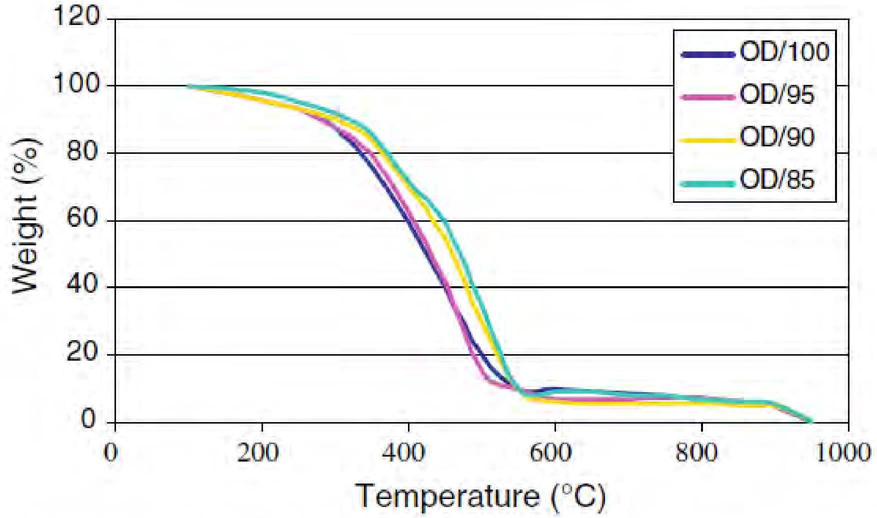

Figure 2.14: TG analysis for the oxidation of cylinder deposits in air [62]. The numbers in the legend reflect the combined diesel and biodiesel content of the fuels

Figure 2.14 depicts the weight loss profiles of the different deposits. To better expound the TGA results, Husnawan *et al.* used differential scanning calorimetry (DSC) thermograms (see Figure 2.15) which were obtained simultaneously with TGA [62].

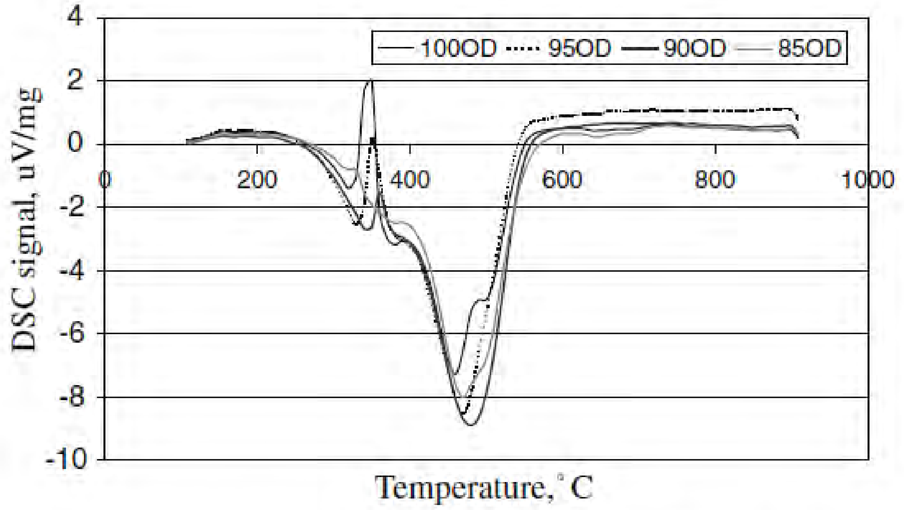

Figure 2.15: Oxidative DSC profiles of diesel carbon deposit derived from diesel-water emulsions with varying amounts of water [62]

It should be noted that the deposits investigated by Husnawan *et al.* [62] are in-cylinder deposits and are thus formed at much higher temperatures than injector and filter deposits.

2.4.4.3 TGA coupled to evolved gas analysis (EGA)

Venkataraman and Eser used TGA-MS to analyse both diesel injector deposits and deposits of the thermo-oxidative degradation of *n*-hexadecane [10]. They analysed HPDI (high pressure diesel injector) deposits obtained from the tip of an injector nozzle of a vehicle, with an unknown driving history. Figure 2.16 depicts the CO_2 and H_2O profiles from TGA-MS analysis of HPDI deposits. The CO_2 profile indicates that oxidation commenced around 350°C and was completed by 750°C. They propose that the carbon atoms/groups to which oxygen atoms are bound are expected to be the most reactive components of the deposits and would be the earliest to oxidise. The peak between 650°C and 720°C in the CO_2 profile is attributed to oxidation of relatively ordered polyaromatic structures [10].

The H_2O evolution profile comprises three distinguishable peaks: below 200°C, a second at 450°C and a third at 600°C [10]. The authors attribute the initial peak at 120°C to the removal of physisorbed water from the deposit and to a smaller extent the oxidation of physisorbed hydrocarbons on the deposits. They propose that the peak at 450°C originates from the decomposition of hydroxyl groups while the peak at 610°C derives from hydrogens associated with PAHs. They calculated an H/C ratio of approximately 0.4, which is an indicator of condensed polyaromatic rings. Venkataraman and Eser account for the absence of an H_2O peak, which would correspond to the CO_2 shoulder at 720°C, by postulating that the carbon fraction that oxidised at 720°C did not have significant amount hydrogen associated [10].

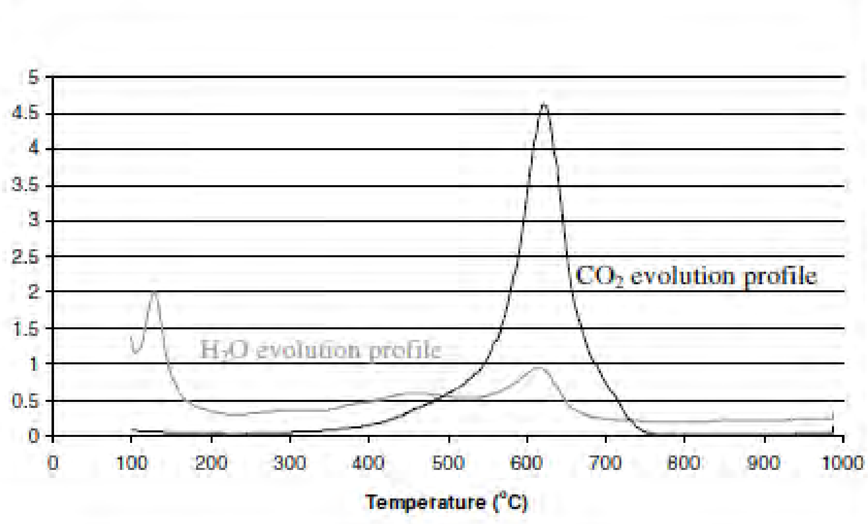

Figure 2.16: CO_2 and H_2O evolution profiles for the oxidation of carbon and hydrogen species in HPDI deposits in an air atmosphere [10]

Figure 2.17 shows the results of TGA-MS analysis on n-hexadecane degradation deposits by Venkataraman and Eser [10]. One of several noticeable differences between the CO_2 profiles of n-hexadecane deposits and HPDI deposits is that the CO_2 peak for *n*-hexadecane deposits occurred at around 740°C which is 20°C higher than the CO_2 peak of ordered structures in the HPDI deposits. Venkataraman and Eser explain the difference in the CO_2 profiles by making reference to TEM images where the n-hexadecane deposits were observed to have a greater degree of order.

To explain the observed differences in the structures of the deposits Venkataraman and Eser allude to past studies which showed that amorphous carbonaceous solids (deposits) form from large aromatic species via a coalescence mechanism [10]. In contrast carbonaceous deposits formed from smaller hydrocarbons (such as soot formed from acetylene) are composed of more ordered graphitic structures due to controlled hydrogen abstraction-carbon addition (HACA) reactions. Because diesel is a complex blend of aromatic, aliphatic and cycloalkane compounds, carbonaceous deposits derived from fuel degradation are likely to be amorphous than carbonaceous deposits from simple radicals derived from *n*-hexadecane [10].

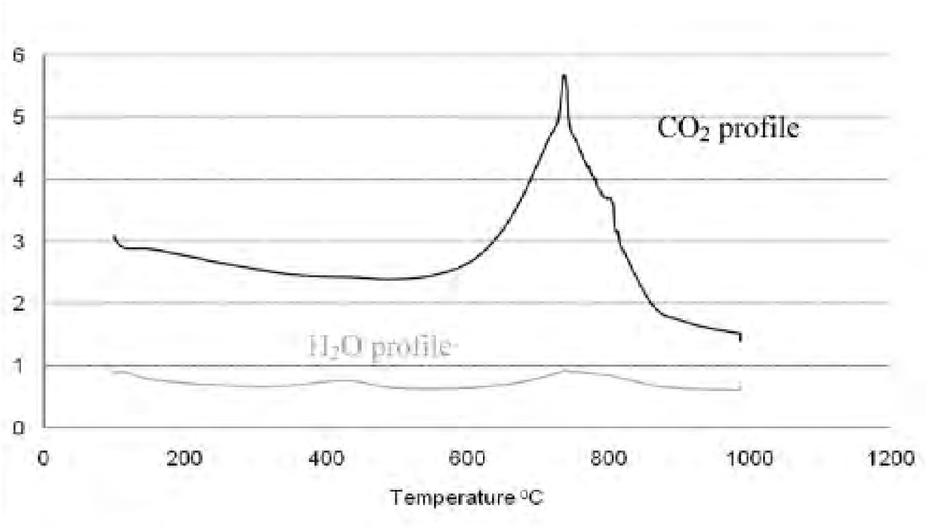

Figure 2.17: Evolved CO_2 and H_2O profiles for the oxidation in air of solid deposits formed from n-hexadecane degradation [10]

The CO_2 profile of n-hexadecane deposits reveals that CO_2 evolution occurs between 540°C and 900°C. This CO_2 profile differs from the CO_2 profile of HPDI deposits as it lacks the more reactive component of deposits oxidising around 450°C. There was a discrepancy between the CO_2 profile and H_2O profile as in both cases (HPDI and *n*-hexadecane deposit H_2O profiles) the corresponding H_2O peak around the same temperature (450°C) is observed. To explain this discrepancy, Venkataraman and Eser suggests that the CO_2 peak which evolved from the n-hexadecane deposits between 400°C and 500°C may have been hidden by the offset in the baseline of the CO_2 evolution profile [10].

The second H_2O peak occurs around 750 °C which Venkataraman and Eser attribute to hydrogen species associated with PAHs. On the CO_2 profile two spikes are witnessed at 750°C and 800°C which the authors attribute to the oxidation of capsules of volatiles trapped within the layers of ordered PAHs [10].

More widely used for the study of deposits than TGA-MS is temperature-programmed oxidation (TPO), usually performed in a carbon analyser. Here a sample is heated at a programmed rate in an oxygen/nitrogen atmosphere and the volatiles released are oxidised to CO_2 and H_2O. It has been widely used to characterise the oxidative reactivity of deposits, often in the study of catalysts [7, 69, 70].

2.4.4.4 Electrospray ionisation-mass spectrometry

Electrospray ionisation mass spectrometry (ESI-MS) has been successfully used in the analysis of both high and low molecular weight biomolecules, organometallic and inorganic complexes and polymers. A solution, containing the analyte, is introduced into a steel capillary tube which has a large potential difference applied across it (see Figure 2.18). The large potential difference between the counter electrode and capillary induces a large electric field which in turn permeates the solution at the tip of the capillary tube and converts the solution at the tip of the capillary into charged droplets [71, 72]. The solution typically consists of a 1:1 (v: v) mixture of acetonitrile and water as well as <1% acetic acid, formic acid or triflouroacetic acid. It is then evaporated. The molecules in the charged droplets are transformed into gas phase ions [73]. The ionisation process is achieved by adjusting the pH of the solution via capillary voltage manipulation to either deprotonate (in negative mode) or protonate (in positive mode) the ionisable groups [71, 73].

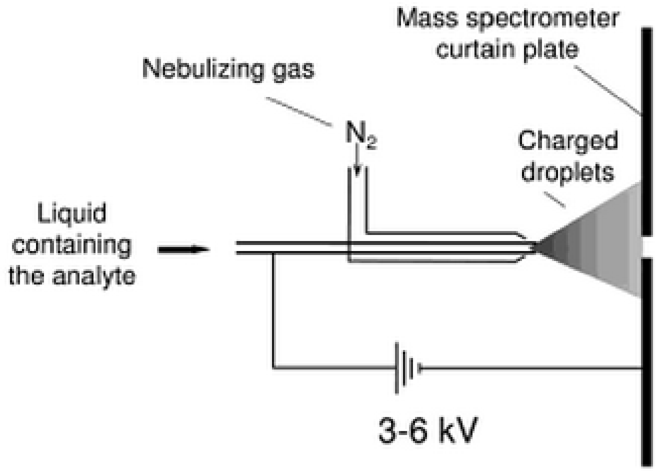

Figure 2.18: Pneumatically assisted electrospray, reproduced from [71]

Ions resulting from the electrospray process are detected by the MS as either $[M + nH]^{n+}$ (in positive mode) or for $[M - nH]^{n-}$ (in negative mode) [73]. Further insight into the fundamentals of the electrospray process as well as the interpretation of ESI-MS spectra is provided by Wanner and Höfner [71], Qian *et al.* [72] and Dass [73].

Although ESI-MS has been widely used for analysis of proteins and high molecular mass polymers, it has been sparingly used for liquid hydrocarbon fuels analysis [74]. An attributing factor is that liquid fuels. *i.e.* jet fuel, diesel and petrol are primarily composed of non-polar hydrocarbon species, while ESI-MS is biased towards polar species that can easily protonate or depronate. ESI-MS, however, has recently begun to be applied to the study of liquid hydrocarbon fuels as the technique has several advantages of over traditional fuel diagnostic techniques such as GC-MS. The major advantages are i) sample volatility in ESI-MS is not an issue and hence this allows ESI-MS the ability to detect molecules with molecular masses as high as 100MDa and ii) the electrospray ionisation process is a significantly softer ionisation mode than electron ionisation (EI), usually used in GC-MS, and as a consequence leads to little or no mass fragmentation of target molecules. The high selectivity towards polar species was exploited by Rostad *et al.* [75] who used the technique to differentiate between different fuel types based on their polar components.

Thermo-oxidative degradation of hydrocarbon fuel leads to the formation of high molecular polar species, *e.g.* acids and ketones. Commodo *et al.* [74] applied positive ESI-MS to identify polar compounds in neat unstressed jet fuel (Jet A-1) as well as polar species that formed when the fuel was thermally stressed in the presence of oxygen. Jet A-1 positive ESI-MS identified several nitrogenous homologous series in Jet A-1, including possible alkylated pyridines/or anilines, alkylated carbazoles and alkylated quinolines. Polar molecules that were detected for neat unstressed Jet-A1 were generally in the m/z 100-250 range. Two additional homologous series in the low molecular region (m/z 100-250) were observed in stressed Jet A-1 (160°C for 2 h under excess air). Furthermore stressed Jet-A1 formed homologous series in the m/z 250-400 range while no dimers $[2M+H]^+$ or trimers $[3M+H]^+$ were observed in the spectra. ESI-MS not only afforded Commodo *et al.* [74] a means in which to identify polar species in unstressed jet fuel, but also proved integral for the development of a mechanism for jet fuel degradation. In the proposed mechanism, soluble polar species in the m/z 250-400 range adopt the role of parent deposit precursors which by aggregation, polymerisation and/or clustering convert into insoluble precursors which ultimately precipitate to form solid deposits.

Rostad *et al.* [75] and Hughey *et al.* [76] used ESI-MS to investigate polar species in diesel fuel. Although both sets of authors showed that ESI-MS can be useful in identifying particular polar species in diesel fuel, their studies did not investigate polar species formed during thermal-oxidative stressing of the respective diesel fuels.

The use of ESI-MS in tracking oxidation products has had greater reception with biodiesel than petroleum diesel. Catharino *et al.* [77] used the technique to characterise biodiesel. They could determine the alcohol used in the trans-esterification process, track degradation products and screen for residual glycerine and associated glycerides. Catharino *et al.* [77] purposely chose to perform ESI-MS on biodiesel in both positive and negative modes. In negative mode ESI-MS oxidation products (mainly oxidised fatty acids) formed as a result of thermo-oxidative degradation (120°C, 8 h in excess air) of biodiesel were identified. Additionally negative ESI-MS provided identification of deprotonated fatty acids in unstressed biodiesel. Positive ESI-MS aided in the identification of protonated fatty esters of the biodiesel which was used to reveal the alcohol (methanol or ethanol) used in the trans-esterification process [77]. Ogawa *et al*. [59] used ESI-MS to track the oxidation of a number of FAME model compounds.

3 Experimental methods

"It does not do to leave a live dragon out of your calculations, if you live near him."- J.R.R. Tolkien, The Hobbit

3.1 Diesel soot

3.1.1 Source of soot

Diesel soot, used for this study, was obtained directly from the exhaust of a commuter bus (Marcopolo Senior), operated by Sibanye Bus Service, with a 4.6L MAN diesel engine.

3.1.1.1 Commuter bus operating conditions

Information available regarding the factors and conditions that led to the formation of the soot that was sampled from the commuter bus is limited. Because the bus operates in the real world, it is difficult to regulate and account all for all the factors that influence the resultant soot. The few details that are known are listed below.

The bus operates as a shuttle transporting university students from a residence to university campus and return. It operates in a 3 km loop system, with about one third of the distance spent traversing through steep inclines.

Table 3.1: Engine characteristics of the commuter bus from which soot was sampled

Engine type and manufacturer	Euro 3 D0834 LOH, by MAN
Cylinders and arrangement	4 cylinders inline
Number of valves	4 per cylinder
Displacement	4.6 ℓ
Related output	132 kW
At speed	2400 rpm
Max Torque	700 Nm
At speed	1400 rpm
Mode of operation	Four-stroke diesel engine with direct fuel injection
Injection system	Common rail
Exhaust after treatment	None
Exhaust gas technology	EGR

The engine type of the commuter bus is indicated in Table 3.1 while the properties and lubricant used by the bus can be found in Table 3.2.

Table 3.2: Lubricating oil properties, used by the commuter bus from which soot was sampled

Lubricant	Mobil Delvac 1 LE 5W-30
SAE grade	5W-30
Viscosity, ASTM D445, cSt @ 40°C	74.4
cSt @ 100°C	12.2
Sulfated Ash, wt %, ASTM D874	1.0
Pour point, °C, ASTM D97	-51
Flash point, °C, ASTM D92	234
Density @15°C kg/ℓ, ASTM D 4052	0.855

The source of the commercial diesel, used regularly by the bus, is unknown. The only available information regarding the sample is that it contains a maximum of 50ppm sulfur.

3.1.1.2 Soot sampling

Sampling from the commuter bus was achieved by using a clean metal spatula to scratch soot off the exhaust of the commuter bus. The soot was transferred to a 100mℓ media bottle and stored at ambient temperature and pressure.

3.1.2 Analytical techniques and protocol adopted

3.1.2.1 SEM

The morphology of the soot was investigated using an FEI Nova NanoSEM 30 Series with Digital Micrograph Software at the Electron Microscope Unit (EMU) at the University of Cape Town (UCT).

Dry diesel soot requires minimal sample preparation prior to observation in the SEM. For each experiment, a sample stub was coated with double coated carbon tape. Carbon tape was used to negate charge build up in the soot samples as soot is a nonconductive material. Soot was then directly applied onto the carbon tape and the sample stub was inserted into the SEM. The microstructure of the samples was observed in scanning mode as well as with back-scattered electron detection. The acquisition parameters used to obtain each micrograph are displayed on the each respective micrograph in the results section.

3.1.2.2 TEM

Transmission electron microscopy was employed to study soot microstructure in greater detail. The instrument used for this analysis was a FEI Tecnai G^2 20 TEM, equipped with a lanthanum hexaboride (LaB_6) filament and a Gatan Tridiem image filter (GIF), housed at the EMU at UCT. The protocol highlighting the sample preparation undertaken by this study for all soot samples for TEM analysis is listed below.

Sample preparation protocol:

Note: Steps 1-3 applied only to test bed engine soot while steps 4-6 applied to both the commuter bus and test bed engine soot.

1. A 25 mm diameter TIGF filter paper containing ± 4mg of soot sample was placed in a 100mℓ beaker containing 20mℓ ethanol (Kimix, Cape Town, South Africa).
2. The filter paper with adsorbed soot was ultrasonicated for 5min or until the soot de-adsorbed from the filter paper and dispersed into the ethanol solvent.
3. The stripped filter paper was removed from solution.
4. Using a dropper, a few drops of the soot and ethanol mixture from the beaker were transferred onto a 3mm carbon-coated copper grid.
5. The 3mm grid containing the sample was held under a UV light (250W xenon lamp source) until the ethanol completely evaporated.
6. The dry copper grid was then inserted into the TEM grid holder.

TEM experimental parameters

The TEM was operated at 200keV to obtain high resolution bright field images. The signal-to-noise ratio, and hence the contrast, in the images was enhanced by employing a 20eV energy slit (using the GIF) to filter out elastically scattered electrons. All images were captured using a Gatan Ultrascan 1000 digital camera with a CCD chip comprising of 1024 x 1024 array of pixels of width 15µm.

3.1.2.3 Inductively coupled plasma – mass spectrometry (ICP-MS with ICP-AES)

Analysis were performed by an external service provider – the Central Analytical Facility at the University of Stellenbosch. ICP-MS was conducted on soot to determine the quantities of trace elements while ICP-AES was measured the major elements. The instruments used for ICP-MS and ICP-AES were an Agilent 7700 ICP-MS and a Thermo iCap 6300 ICP-AES respectively. Analytical conditions were optimized for each instrument, with an instrument calibration done using NIST traceable standards. Accuracy of measurement was verified using a separate standard at the beginning of the analysis.

In each analysis a 20 mg sample of soot was microwave digested in HNO_3 and then analysed by ICP-AES and ICP-MS.

3.1.2.4 Soxhlet extraction

The SOF of the commuter bus soot was obtained via Soxhlet extraction. Sample size limitations for the test bed engine soot meant that testing the effect that the solvent has on the quantity and type of SOF during extraction was exclusively investigated using commuter bus soot. Six solvents were chosen to test the influence of the extraction solvent on the quantity of SOF. The solvents that were used are highlighted in Table 3.3 while the procedure that was adopted for the extraction of commuter bus soot is indicated thereafter.

Table 3.3: Solvents used for soot extraction

Dichloromethane
Toluene
Hexane
Acetone
Methanol
Cyclohexane

All solvents were supplied by Kimix (Cape Town, South Africa). During Soxhlet extraction, samples are typically placed inside a thimble. Initial work was done using cellulose thimbles but these were replaced with glass ones. The motivation for this may be found in Appendix D.

Extraction protocol:

1. A glass fibre extraction thimble, extractor and flask were cleaned with acetone to remove any laden particles.
2. The thimble, extractor and flask were dried in an oven at 50°C for 15min.
3. The extraction thimble was weighed using a Mettler Toledo AT 20 microbalance (±2µg).
4. Approximately 100mg of commuter bus soot was added to the thimble and the combination was reweighed.
5. The thimble, containing the soot sample, was inserted into the extraction cavity of the Soxhlet and 30mℓ solvent was added to the flask.
6. Soxhlet extraction was continued under reflux for 24 h.
7. On completion of the extraction process the thimble with sample was removed from the extraction cavity and dried in a fumehood for 1 h. Thereafter they were dried in an oven at 50°C for 48 h.
8. The dried thimble with sample was then weighed.
9. SOF was calculated as follows

$$\mathrm{SOF}(\%) = \frac{[m(t)+m(s)]_i - [m(t)+m(s)]_f}{m(s)} \times 100$$

where m = mass, t = thimble, s = sample, i = prior extraction and f = after extraction.

3.1.2.5 *Chemical speciation of the SOF*

Chemical speciation of the SOF of the soot was conducted. The extraction process adopted was the same as in section 3.1.2.4, except steps 7-9 were omitted. The solvents used were the same as those in Table 3.3. The protocol undertaken in determining the chemical speciation of the SOF from extraction commuter bus soot is highlighted below.

3.1.3 Gas Chromatography - Mass Spectrometry (GC-MS)

GC-MS enabled identification of contents in the SOF for both test bed engine and commuter bus soot extracts. Of particular interest were PAHs and phthalates (esters). The GC-MS used for this work was a Shimadzu GCMS-QP2010 Plus, with a high performance quadrupole mass spectrometer that allow detection of a mass range of 1.5 to 1090 m/z.

The solvent (SOF) obtained from Soxhlet extraction was analysed using the following protocol:

1. The extract was concentrated to approximately 1 mℓ using a rotary evaporator (water bath temperature = 50°C).
2. 2mℓ of the same neat solvent as the extraction solvent was used to rinse the walls of the rotary evaporate flask and added to the concentrated extract.
3. Half of the total (1mℓ concentrated extractant + 2mℓ rinsing solvent for rinsing the wall) concentrated extract was then transferred to a 2mℓ brown glass GC vial and the reserve was stored in another brown glass vial in a chemical fridge at 5°C.
4. The extract was analysed by GC-MS using the parameters in Table 3.4.

Table 3.4: GC and MS parameters employed in the determination of the SOF

Instrument	Shimadzu QP 2010 Plus GC-MS
Column	BPX5 MS Column (fused silica) with a temperature range: -60 °C to 360 °C and dimensions of 25m (axial length), 0.32 mm (internal diameter) and 0.25µm (film thickness).
Gas	Helium
GC injection program	
Injection temperature	270 °C
Injection mode	Splitless
Injection volume	1µℓ
GC pressure program	
Flow control mode	Linear velocity
Pressure	53.1 kPa
Total flow	38.3mℓ/min
Column flow	3.21mℓ/min
Purge flow	3.0 mℓ/min
Linear velocity (helium, carrier gas)	120.3cm/s

Column oven temperature program				
Rate	Final temperature (°C)	Hold time (min)		
-	50	0		
10	280	0		
MS program				
Start time (min)	End time (min)	Acquisition mode	Start m/z	End m/z
3.20	23.00	Scan	50	450
MS parameters				
Ion source temperature (°C)	Interface temperature (°C)	Solvent cut off time (min)		
220	280	3		

3.2 Diesel fuel deposits

This section addresses three aspects regarding carbonaceous deposits namely 1) the methods and reactors employed in the synthesis of carbonaceous deposits, 2) the materials and fuels that were used and 3) the analytical techniques that were used to analyse the synthesised deposits.

3.2.1 Materials

3.2.1.1 Fuels

Four different fuels were investigated in this study: a reference diesel (EN590 diesel), two biodiesel blends (RME blended with reference EN590 diesel (1:4 by volume) and SME blended with reference EN 590 diesel (1:4)) and a commercial diesel, obtained from local filling station. The properties of the fuels are listed in Table 3.5.

Analytical data, in Table 3.5, for these fuels samples was provided by Sasol Technology. The commercial diesel was obtained locally and thus not characterised. FAME blends were prepared by Sasol Technology. A few experiments (ESI-MS) were conducted on the neat FAMEs as well.

Table 3.5: Properties of the fuels used

	% EN 590 diesel	%RME 80:20	%SME 80:20	Commercial Diesel*
Percentage EN590 diesel	100	20	20	-
Density @ 15 °C	0.8358	0.8417	0.8419	-
Viscosity @ 40 °C	2.79	3.05	2.94	-
CFPP	-20.0	-22.0	-17.0	-
Derived cetane number	56.5	57.2	54.3	-
Flash point	84.0	85.0	88.0	-
Acid number (SCI)	0	0.09	0.02	-
Acid number	0.06	0.08	0.09	-
HFRR	327			-
S content (ppm)	<1	1.0	<1	-
I value (Br number)	<0.01	10.50	10.70	-
Carbon residue (wt. %)	0.02	0.03	0.10	-
Ash content (wt. %)	<0.01	<0.01	<0.01	-
Oxidation stability (rancimat) (h)	168.00	30.28	13.79	-
K	<0.100	<0.100	1.52	-

* Commercial Diesel: In select experiments commercial diesel was degraded to provide comparable data for the stability of diesel that is on the local market. The only known property of the fuel was its sulfur level which was below 50 ppm.

3.2.1.2 Consumable chemicals

Unless otherwise stated chemical reagents (solvents) used in this study were obtained from KIMIX (Cape Town, South Africa) and had a minimum 99.5% purity.

3.2.1.3 Gases

All gases used were obtained from Air Products^{TM}. The grades are indicated in Table 3.6.

Table 3.6: Gases used and their quality grade

Gas	Grade
Nitrogen	5.0
Synthetic air	Medical grade
Oxygen	5.0
Helium	5.0

3.2.2 Flask Reactor conditions

The conditions/parameters that were set in each reactor were done so intentionally. The rationale that was behind each of the set experimental conditions is outlined below.

Table 3.7: Flask reactor conditions

Flask Reactor		
Experimental parameter	Set point	Reason
Temperature (ºC)	140	The temperature is within the thermal oxidative region. It corresponds to the ASTM temperature of the QCM reactor [67] . Random preliminary testing showed that the temperature was sufficient to induce carbonaceous deposits in fuels. During stress tests fuel is heated and volatiles are condensed back into the flask reactor cavity by a condenser. Preliminary tests showed that at higher temperatures (>180ºC) a small fraction of volatiles escaped through the top of condenser i.e. the condenser could not effectively cool rapidly moving volatiles. In order to circumvent this issue a lower temperature (<180ºC) had to be chosen. For these reasons the temperature of 140ºC was selected for all experiments.
Synthetic air	N/A	To deliver excess oxygen during the test. This was seen as a critical parameter in influencing the carbonaceous deposit formation. A small section in the latter part of this dissertation elaborates on the significance of oxygen in driving fuel degradation.
Nitrogen	N/A	To provide a deoxygenated test environment.
Gas flow rate (mℓ/min)	50	This flow rate was used by a previous author who used the flask reactor to study jet fuel oxidation [50]. Furthermore for experiments with synthetic air, the flow rate was judged to be sufficient in providing excess oxygen conditions.
Experimental duration (h)	15	Preliminary tests (conducted at 140ºC and excess oxygen) revealed that most test fuels had not formed carbonaceous deposits by the 10th hour (<10h). As the objective of the tests was to form characterisable deposits, the experimental

		duration had to be greater than 10h. Further tests revealed that after 15h, significant deposition had occurred in the test fuels and in particularly the biodiesel blends. Additionally the 15h duration corresponds to the time used in ASTM method for the QCM [67].
Sample size (mℓ)	30	This was chosen because it corresponded to the sample size that was used by Kabana *et al* [50].

3.2.2.1 Glass flask reactor configuration

Thermo-oxidative stability of diesel fuel and biodiesel blends was investigated at accelerated conditions in an 'open system' in glass flasks. The set-up is presented in Figure 3.1. Three separate three-necked reactor flasks each with a condenser, heating mantle, gas delivery pipette and thermocouple were assembled to form the open glass flask reactor system. The direction of delivery gas, water and electrical supply are indicated.

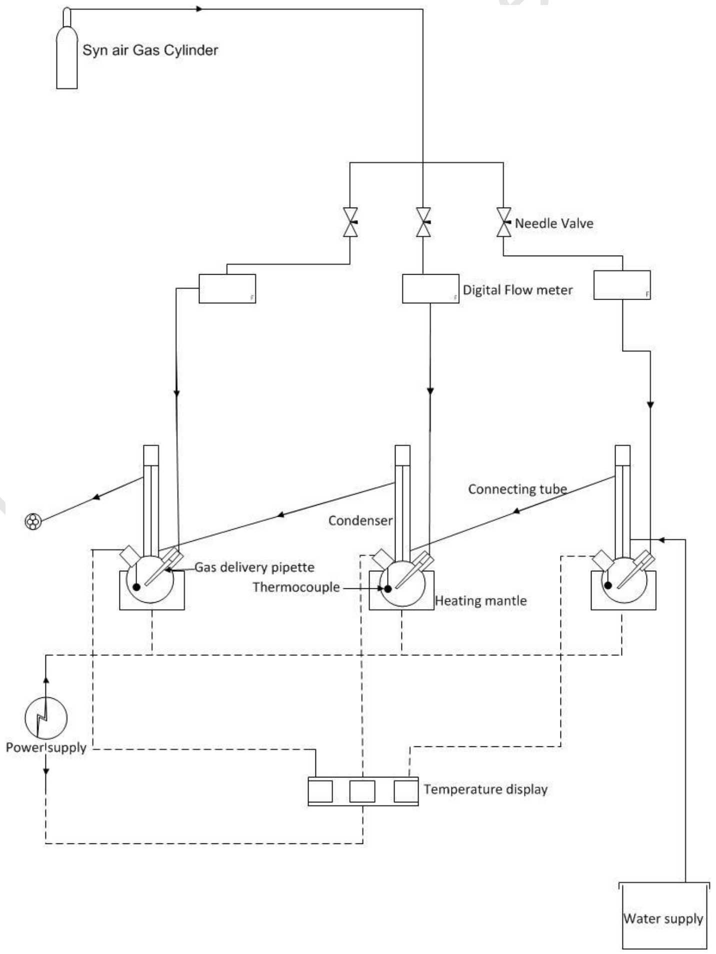

Figure 3.1: Schematic of the flask reactor setup

Table 3.8 indicates the flask reactor experimental conditions as well as tested materials.

Table 3.8: Experimental conditions used in reactor flask studies

Fuels	EN590, RME20, SME20 and commercial diesel
Sample size	30mℓ
Temperature	140°C
Experiment duration	15 h
Gas	Synthetic air @ 50ml/min
Pressure	Ambient pressure (±1 bar)
Reactor surface composition	Glass

Experimental protocol:

1. Each three-necked flask was charged with fuel.
2. The heating mantle was switched on and adjusted accordingly to reach the desired temperature.
3. Once the desired temperature was reached, the gas supply was activated using a needle valve and the flow rate was set using a digital flow meter.
4. The conditions were kept constant for the duration of the experiment.
5. At the end of each experiment the products were allowed to cool to room temperature.
6. The cooled contents were then transferred to 50mℓ media bottles which were then stored in a fridge at 5°C
7. The entire contents (fuel and deposits) in the media bottles were analysed by TEM, TGA-MS and ESI-MS.

3.2.2.2 Closed bomb reactor (fluidised sand bath)

Fuels were degraded in metallic bombs which were externally heated by being submerged in a fluidised sand bath. The reactor bombs were constructed of 316 stainless steel cylinder with 60mℓ volume capacity. Because these reactors are closed, higher temperatures, similar to what fuel may reach at the injector tip of a diesel injector (250-300°C, [78]) were used. The products of degraded fuel were filtered and analysed using TGA-MS and TEM. Figure 3.2 shows a schematic of the major components making up the sand bath system while Figure 3.3 contains detail of the reactor bomb used. This reactor bomb/vessel is clamped onto the rotor shaft sand bath and submerged in the sand during an experiment.

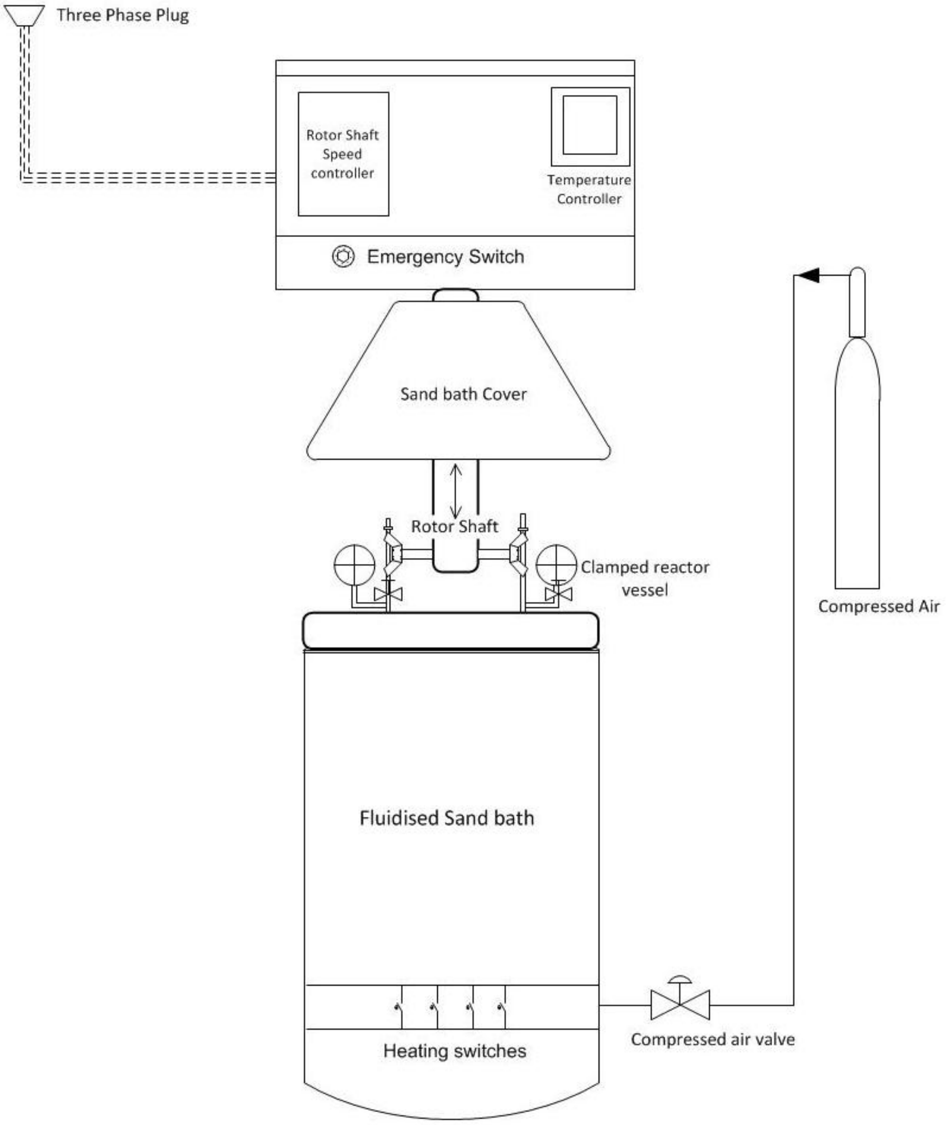

Figure 3.2: Schematic of the fluidised sand bath used to degrade fuel

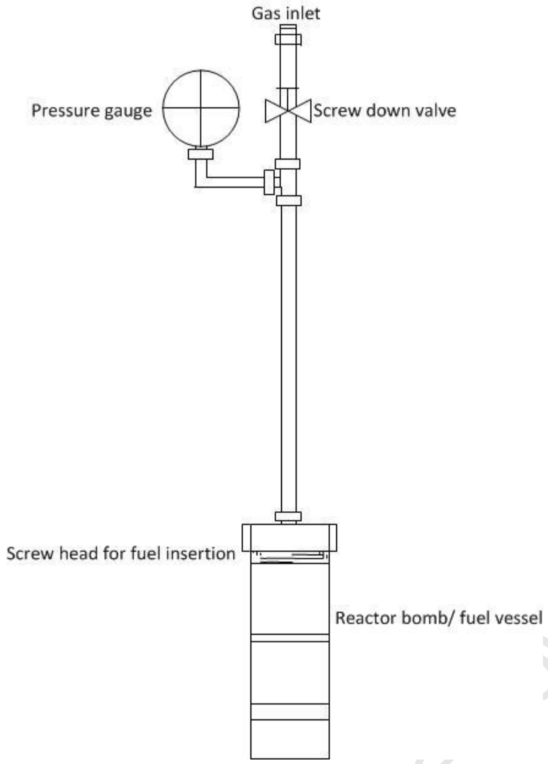

Figure 3.3: Schematic of the closed reactor bomb/vessel used to degrade fuel

Table 3.9 shows the conditions under which fuel was degraded.

Table 3.9: Degradation conditions in the fluidised sand bath experiments

Fuels	Commercial diesel, EN590, RME20, SME20
Sample size	30mℓ
Temperature	250°C
Experiment duration	24h
Gas	Oxygen
Pressure	10bar
Reactor surface composition	316 stainless steel

Experimental protocol:

1. Compressed air was introduced into the sand bath using the compressed air valve.
2. Once the sand was fluidised at a desired level, the sand bath temperature controller was turned on and the experimental temperature was set.
3. The heaters of the sand bath were switched on.

4. The reactor bombs were filled with the appropriate fuel and charged with oxygen gas to the desired pressure.
5. Once the sand bath reached the set temperature the reactor bomb was clamped onto the rotor shaft of the sand bath and then submerged in the fluidised heated sand.
6. The submerged reactor bomb was then agitated by switching on and adjusting the speed controller of the reciprocating shaft. The agitation is provided by a constant upward and downward motion of the shaft.
7. All conditions were kept constant for the duration of the experiment. Procedure for collecting deposits.
8. After the duration of the experiment each reactor bomb was removed from the fluidised sand bath and quenched in a water bucket and left to cool in the bucket for approximately 10min.
9. The reactor bombs were depressurised and opened. The products were collected on a Munktell glass fibre filter, washed with 25mℓ hexane and analysed using TGA-MS and TEM.

3.2.2.3 Continuous flow reactor

A flow reactor was employed in this study to stress diesel at elevated temperature and pressure in a flowing system. The system is composed of a vertical furnace, temperature controller, HPLC pump and chiller, which circulates coolant to the condensing unit to cool heated fuel. The temperature conditions were chosen to resemble the conditions experienced by the diesel injector tip [78]. Figure 3.4 depicts a basic schematic of the flow reactor used in this study while Table 3.10 illustrates the experimental conditions and reactor tube characteristics.

Other authors [10, 11] use single-pass fuel flow reactors. Because some of the fuel in common rail injections systems recirculates between the rail and the tank, it was decided to modify the system to enable recirculation of fuel. This also allows smaller quantities of fuel to be used for stressing.

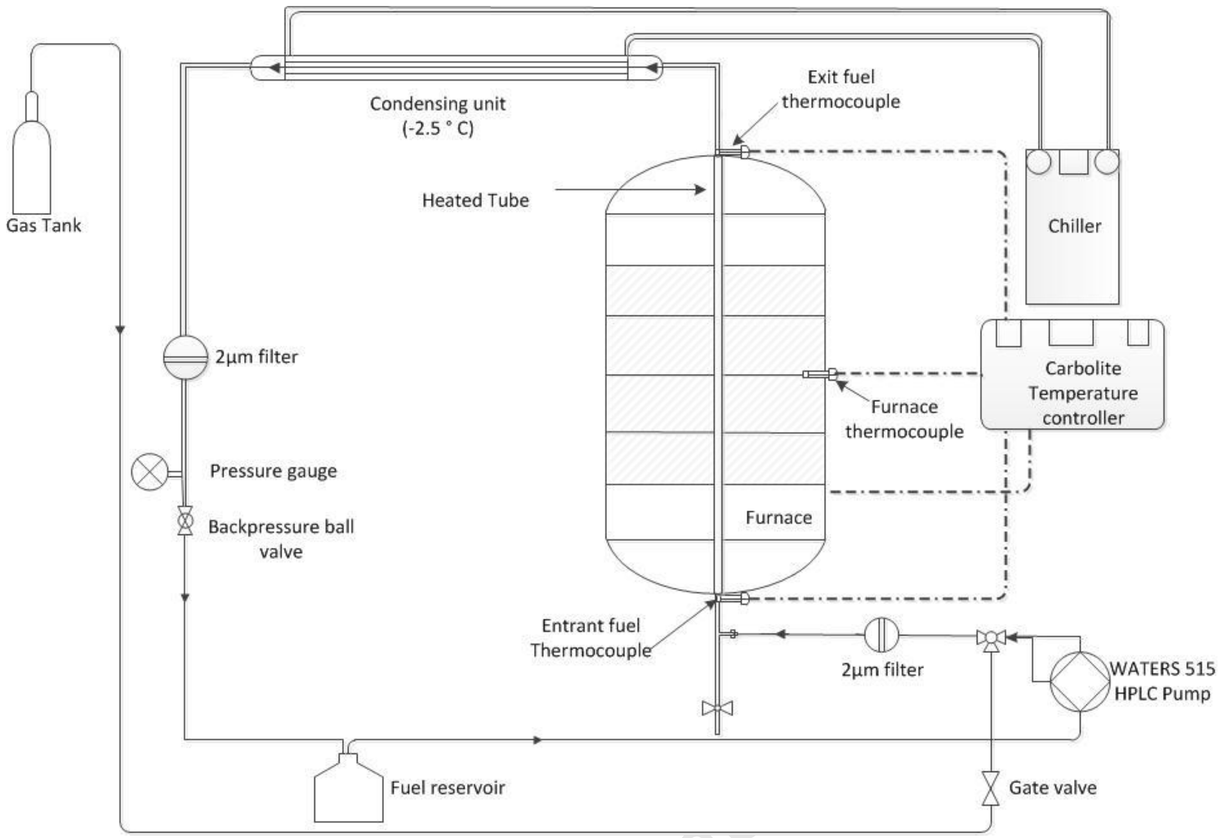

Figure 3.4: Schematic of the flow reactor set up used in this study

Table 3.10: Experimental conditions and flow reactor tube characteristics

Fuel path	Closed loop
Fuels tested	EN590 diesel, RME20, SME20, EN590 diesel doped with zinc neodecanoate (Sigma Aldrich, St Louis, USA) (10 ppm)
Sample size	2.0ℓ
Furnace temperature	250°C
Experimental duration	24h
Gas	Dissolved air
Fuel line pressure	10bar
Fuel flow rate	1mℓ/min
Time spent in heated tube	7.44min
Tube surface composition	316 stainless steel
Tube length	97cm
Internal tube diameter	1/8“

Experimental protocol:

1. The metal tube reactor was fastened into the furnace and connected to the external fuel circuit.
2. The furnace was then turned on and the desired temperature was set.
3. Once the furnace reached the set temperature, the fuel was pumped through the system by activating the HPLC pump.
4. The back pressure valve was adjusted to the desired pressure.
5. The conditions were kept constant for the duration of the experiment.
6. The reactor tube was sectioned into seven segments of equal length. 3 mm thick disks representing each segment were sliced out at the junctions between segments and washed in hexane to remove residual fuel.
7. The sectioned disks were then analysed using TGA-MS and optical microscopy.

Because the fuel residence time in the flow reactor is short, further tests were performed on fuels which had been doped with 10ppm zinc. Zinc was added because it is known to accelerate deposit formation [79, 80, 81, 82]. Doping followed the CEC F-98-08 DW10 injector fouling engine test protocol [83].

Doping protocol:

1. A zinc stock solution was prepared by dissolving 2.99g zinc neodecanote (Alfa Aesar, Karlsruhe, Germany) in 26.95g of an aromatic solvent, Fluidar 150 (Engen, Durban, South Africa).
2. This solution was then used to dose diesel fuels and blends. 10ppm (m/m) dosed fuels were prepared by adding 44.5mg of the zinc stock solution to 800g of the base fuels, to produce the fuels in Table 3.5.

3.2.2.4 Quartz crystal microbalance (QCM)

A QCM was employed by this study to provide quantitative data on the depositing propensity of diesel fuels under conditions described in Zabarnick [65] and ASTM D7739-11 [67]. The preparation, clean up and basic operation of the QCM are described in ASTM D7739-11. Below is a summary of these.

Table 3.11: Set of conditions that fuels were subjected during QCM experiments

Test conditions			
Temperature (°C)		Pressure (bar)	Time (h)
140		1	15
Fuels tested			
EN59 diesel	Commercial diesel	RME20	SME20

3.2.3 Sampling methodology for reactor deposits

The sample sizes of the deposits varied due to difference in their sampling methodologies. These methodologies were enforced by the different nature of the deposits.

3.2.3.1 Flask reactions

Degradation of RME20 and even more so SME20 in glass flasks produced viscous sludge that was difficult to filter. For this reason a representative sample of fuel plus deposits was collected from the flask reactor and was analysed using TGA-MS and TEM. Where two layers formed after stressing, a Pasteur pipette was used to remove a sample from each layer.

3.2.3.2 Sand bath reactor deposits

Sand bath reactor deposits were filtered because they were not as viscous as flask reactor deposits. At the end of a degradation test the fuel and deposit contents in each reactor bomb were filtered through a Munktell^{TM} glass fibre filter paper (1.6µm). Carbonaceous deposits, which strongly adhered to the walls of the sand bath reactor bombs, were scrapped off and transferred onto the filter with the fuel deposit filtrate. The filter and filtrate were analysed using TGA-MS and TEM.

3.2.3.3 Flow reactor deposits

Sampling from the flow reactor required sectioning the reactor tubes into 3mm disks. This was done to minimise the mass of the tubes because the TA Instruments Q5000IR mass balance has a weight range up to 100mg. The sectioned tubes consistently had a mass of 70-80mg. These were analysed directly in the TGA.

3.2.4 Techniques employed to characterise fuel deposits

3.2.4.1 TGA-MS

All thermal analysis experiments were performed using a TA Q5000IR thermogravimetric analyser (TGA) which was coupled to an MKS^{TM} Cirrus 2 mass spectrometer via a heated capillary tube. This configuration enabled simultaneous monitoring of mass loss of the sample and identification of the evolved gases. Thermal analysis was conducted on deposits from the flask, fluidised sand bath and flow reactor, under nitrogen and synthetic air atmospheres. Thermal analysis of deposits yielded gases which were detected by the MS. During oxidative thermal analysis (synthetic air atmosphere) the gases of concern were primarily CO_2 and H_2O. CO_2 profiles were used to indicate the fixed carbon content of the deposits and their oxidative stability while the water signal was used as an indicator of deposits associated with hydrogen [10].

Table 3.12 contains system conditions for the TGA which were consistent for deposits from all reactors. The TGA was calibrated for mass using mass standards and for temperature using the Curie points of nickel (358^{o}C) and iron (770^{o}C). The MS was calibrated for concentration using synthetic air. The MS instrumental information and experimental parameters are shown in Table 3.13.

Table 3.12: Experimental conditions adopted for analysis of diesel soot and deposits in the TGA

Heating rate	10°C/min
Atmosphere	Syn air or N_2
Sample purge gas flow rate	25mℓ/min
Pan type	50µl Pt

The heating rate was chosen because 10^{o}C/min is often used as default and so that the results observed here could be compared to other studies [84].

Table 3.13: MS instrument information and experimental parameters for analysis of diesel deposits

Instrument information	
Instrument	MKS^{TM} Cirrus 2 MS
Sensor identification	Standard enclosed source
Detector types	Dual Faraday and multipliers
Maximum mass	300 amu
Experimental parameters	
Source	Standard electron energy (70eV)
Detector used	Faraday
Mass scan range	12-50 amu

3.2.4.2 Fourier transform infrared spectroscopy (FTIR)

FTIR spectra were obtained using the instrument and technique detailed in Table 3.14.

Table 3.14: FTIR instrument description and experimental parameters

Instrument specifications	
Instrument type	Nicolet 6700 FTIR
Spectral range	7800-350 cm^{-1}
Optical resolution	0.09 cm^{-1}
Wavenumber precision	0.01 cm^{-1}
Experimental parameters	
FTIR mode	Absorbance
Number of sample scans	32.0
Number of background scans	32.0
Resolution	4.00
Optical velocity	0.63
Aperture	100
Detector	DTGS KBr
Beamsplitter	KBR
Source	IR

3.2.4.3 TEM

The TEM used to analyse fuel deposits was the same as that employed for the study of diesel soot. The deposits that were analysed using this technique were deposits from the flask and sand bath reactions.

Analysis of flask reactor deposits with the TEM required a representative sample. Approximately 15mℓ fuel, soluble and insoluble gum *etc.* from the bottom of the flasks were removed with a spatula and transferred to a glass vial containing 20mℓ ethanol. The ethanol deposit mixture was then centrifuged. A sample was dropped onto a copper TEM grid using a Pasteur pipette. The remainder of the procedure was in accordance with the method described in section 3.1.2.2.

For sand bath reactor deposits, the filtrate was scrapped off the filter and transferred to a vial containing ethanol, then centrifuged and transferred to a Cu grid. The rest of the procedure followed that in section 3.1.2.2.

3.2.4.4 ESI-MS

Positive ESI-MS was used to evaluate the deposit precursors that are formed during thermal-oxidative stressing of diesel fuels in a glass flask. Sample preparation for ESI-MS as well as instrumental parameters are outlined below.

Sample preparation:

1. 30 ℓ of each fuel were degraded inside a 50mℓ flask at 140°C with 50mℓ/min air flow for 15h.
2. After the thermal-oxidative stressing process, the cooled fuels were inserted into a separatory funnel and mixed with methanol (fuel: methanol 5:2 by volume).
3. The fuel-methanol mixture was shaken and left in the separatory funnel for 2 h to ensure adequate separation of the methanol fraction from the fuel.
4. The methanol layer was collected and stored in glass vials in a fridge at 5°C for later analysis.

The acquisition process involved introducing the ESI probe containing sample into a stream of acetonitrile and 0.1% formic acid. Commodo *et al.* [74] diluted their methanol extract with methanol i.e. (1:100 methanol extract/ methanol). In the paper however they concede that dilution of the sample with methanol was probably unwise and hence in this study no dilution of the methanol extract was conducted. The mass spectra of the methanol extract were collected in the range of m/z 100-1000.

Analyses where performed at the Central Analytical Facility at the University of Stellenbosch.

The instrument as well as its parameters are detailed in Table 3.15.

Table 3.15: Instrument employed in the acquisition of ESI-MS data

Instrument	Waters Synapt G2
Source	ESI positive
Cone voltage	15 V
Lock mass (reference)	Leucine enkaphalin (555.6g/mol)

3.2.4.5 Digital microscopy

Images of the compressed samples were captured using a Nikon ShuttlePix P-MFSC microscope.

4 Chemical and physical characterisation of soot

"I don't create miracles. I create results."-Lionel Suggs

4.1 The effect of extraction solvent on the quantity of the SOF

Soxhlet extraction was conducted on commuter bus soot using six solvents to gauge their relative ability to extract adsorbed species from diesel soot. The average SOF obtained during five separate experiments for each of the solvents is depicted by Figure 4.1. The raw data may be found in Table 12.1 in Appendix A. The solvents in Figure 4.1 are arranged such that the commonly used extraction solvent, dichloromethane, is on the left with all other solvents in decreasing order of polarity.

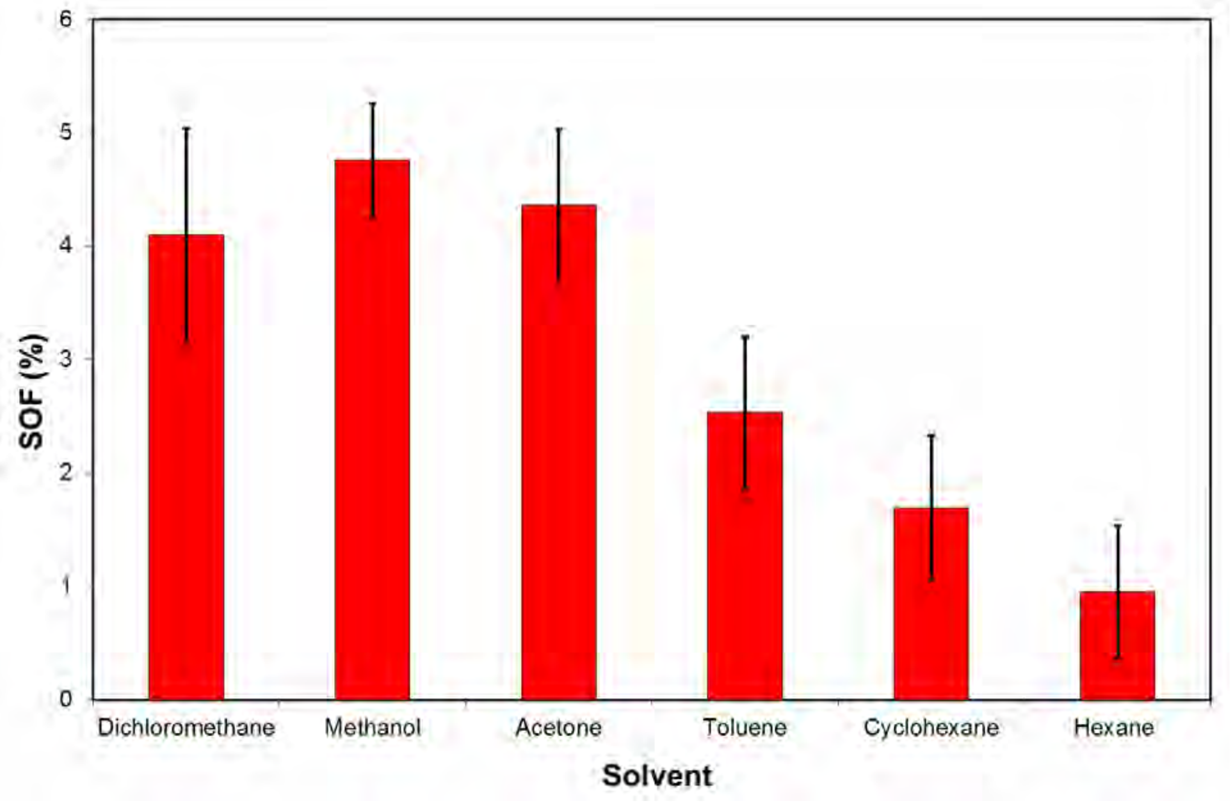

Figure 4.1: The mean SOF values obtained by Soxhlet extraction of commuter bus soot with six different solvents. Each bar graph represents the average of 5 discrete experiments. The error bars indicate the 95% confidence interval.

Figure 4.1 highlights that the solvent choice during extraction affects the measured quantity of SOF. Methanol which provided the highest SOF (4.76wt. %) was nearly five times more effective than hexane (0.95wt. %) at extracting the soluble portion of commuter bus soot. The

SOF component of commuter bus soot, used for testing, is low compared to the range of 5-60wt. % reported by Collura *et al.* [35]. Hydrocarbon solvents (toluene, cyclohexane and hexane) were particularly poor at extraction.

4.2 Chemical speciation of SOF derived diesel soot

Dichloromethane is the most extensively used solvent for the extraction of diesel soot that is reported in the literature. Although several authors [40, 85] have investigated the use of alternative solvents at extracting soot, their primary objective was ascertaining the proficiency of the solvents at extracting PAHs from soot matrix and not SOF in general.

In this study the effectiveness of different solvents at extracting not just PAHs but also other adsorbed molecular species was of interest. Of particular interest were phthalates which are potential endocrine disruptors [43]. Identification in the section that follows was based on a match of 70% or greater with the NIST/EPA/NIH Mass Spectral library [86]. Concentrations are reported as a percentage of the total ion count (TIC).

4.2.1 n-Hexane extract

n-Hexane was the least polar of all the solvents tested. It has already been noted that this solvents extracts the least total SOF.

It can be seen in Figure 4.2 that the main extracts are hydrocarbons (paraffins, cycloparaffins, monoaromatics, hydrocyclic aromatics and PAHs). Hydrocyclic aromatics are bicyclic compounds in which one ring is aromatic and the other is hydrogenated. Examples include indane and tetralin.

The dominant class is comprised of monoaromatics species. Nonetheless an appreciable amount of linear and branched alkanes were present. Only di-aromatic PAHs were identified, *viz.* naphthalene, 1-naphthalene, 2-naphthalene, 1,2-dimethylnaphthalene and 1,3-dimethylnaphthalene. The esters were primarily esters of aliphatic acids and diacids such as oxalic acid. A small percentage of the total (0.38%) was identified as being phthalic acid esters (best matches were di-dodecyl phthalate, di-iso-octyl phthalate and di-(2-methylpropyl)-phthalate)). The sulfates/sulfite/sulfone compounds were primarily esters of sulfurous acid. Full details may be found in Table 12.2 in Appendix A.

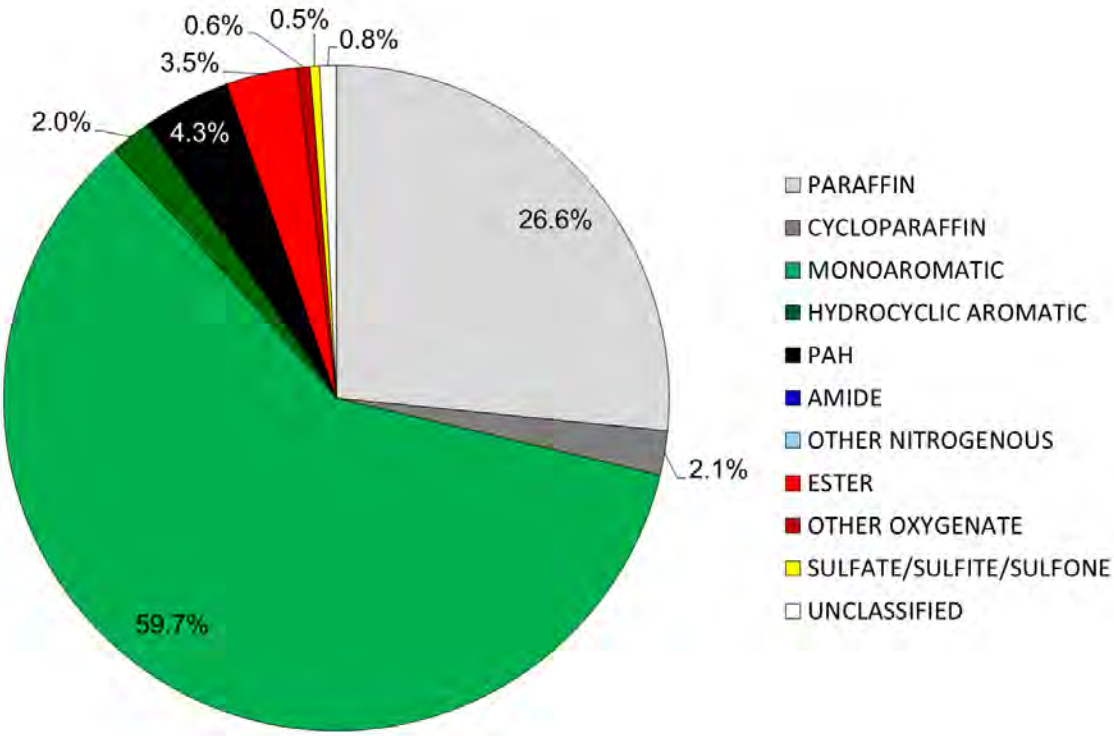

Figure 4.2: Class distribution of molecules extracted from commuter bus soot by n-hexane, as determined by GC-MS

4.2.2 Cyclohexane extract

The cyclohexane extract was also primarily hydrocarbon in nature. The distribution across chemical classes is very similar to the n-hexane extract (see Table 12.3 and Figure 4.3).

An increase in PAHs and related hydrocyclic aromatics was observed but the difference is small, given the variability in the extraction technique and the fact that the distribution is reported for one extraction. The increase may well be an artefact of the co-elution of monoaromatics. Again only bicyclic PAHs were observed. The esters were again primarily aliphatic in nature. Only one phthalate (0.07%) was identified.

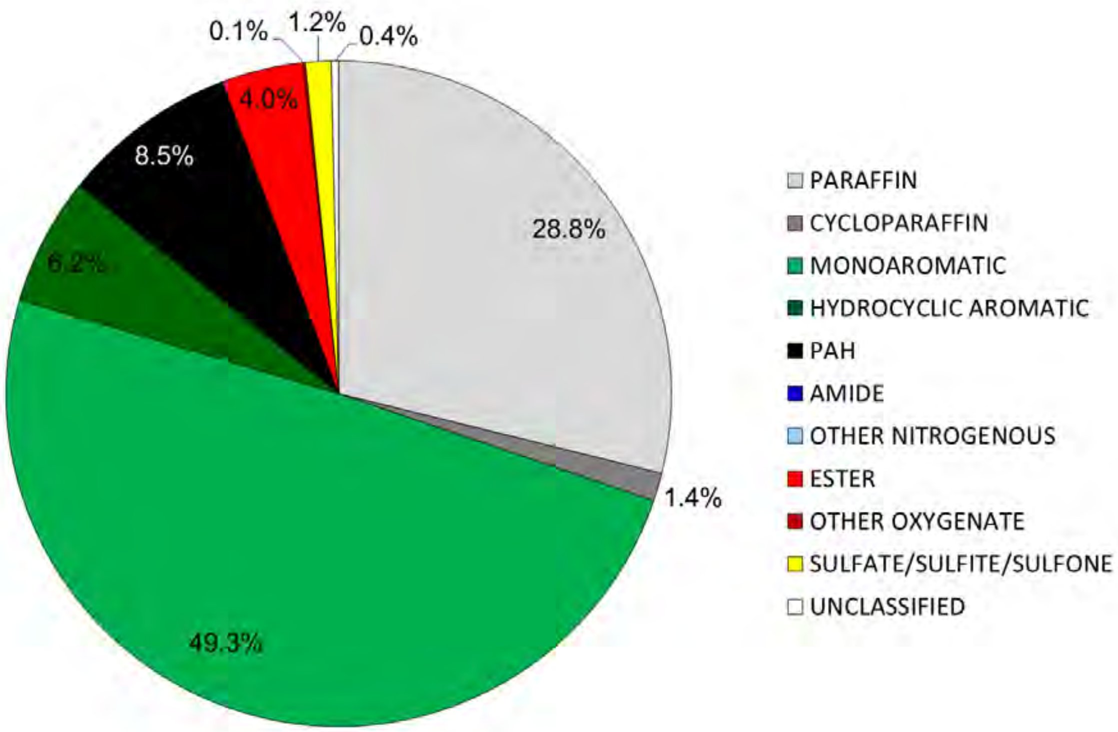

Figure 4.3: Class distribution of molecules extracted from commuter bus soot by cyclohexane, as determined by GC-MS

4.2.3 Toluene extract

The chemical classes and their proportions in the toluene extract from the commuter bus soot are displayed in Figure 4.4. The raw data may be found in Table 12.4 in Appendix A. A sizeable portion of the extract from the commuter bus soot is composed of aromatic compounds, which should be expected since toluene is an aromatic solvent. This is in contrast to the other solvents.

The amount of paraffins extracted is reduced. This may partly be because some of the lighter paraffins are now obscured by monoaromatics in the chromatogram. It should be observed (Figure 4.1) that switching from n-hexane to toluene more than doubles the SOF. It is suggested that the bulk of this increase is due to the more effective extraction of aromatics species (mono- and bi-cyclic). Again the PAHs are naphthalene derivatives. Although the quantity of esters has appeared to decrease compared to n-hexane and cyclohexane, this is the result of the increase in the aromatics extracted causing the relative percentage of esters to drop. The total quantity of esters extracted has not changed significantly. 0.3% of the total constitutes phthalate esters.

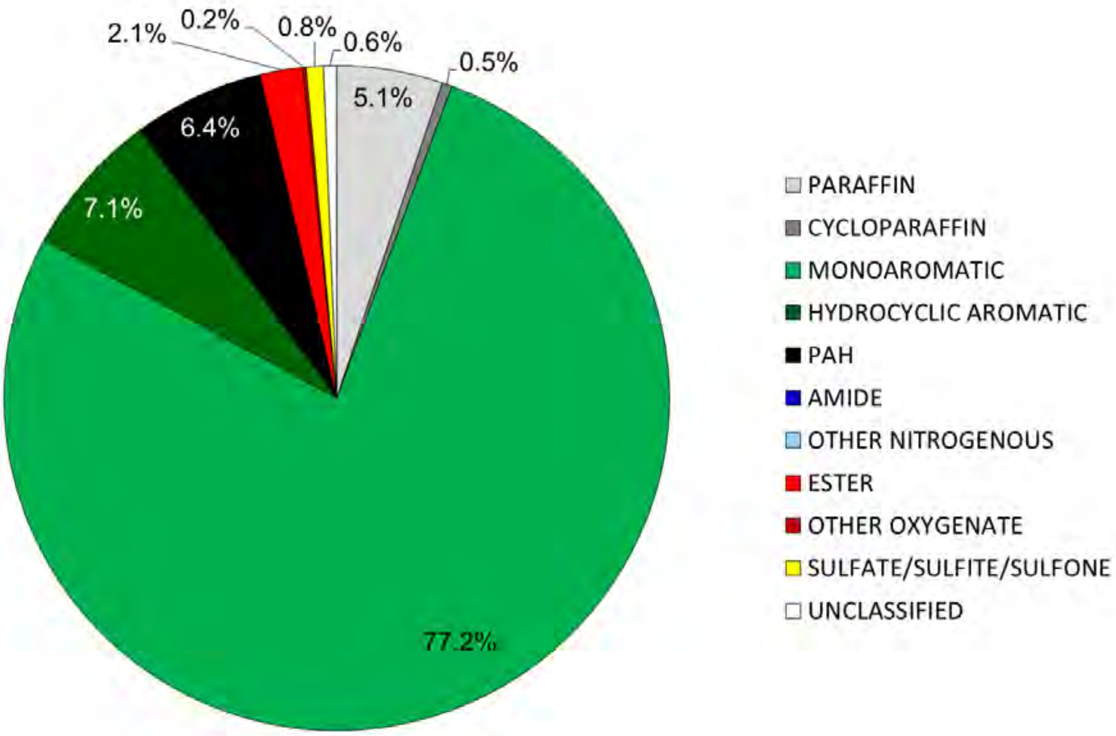

Figure 4.4: Class distribution of molecules extracted from commuter bus soot by toluene, as determined by GC-MS

4.2.4 Acetone extract

As was the case with the previous solvents aromatics constitute the largest portion of the acetone extracts (see Figure 4.5).

It can be seen that the extraction of PAHs is enhanced by acetone. The level of extraction is enhanced even over that of toluene. These PAHs are naphthalene derivatives. Most noticeably, the percentage of species which are esters has increased significantly over the hydrocarbon solvents. In absolute terms, this increase is greater than a simple comparison of Figure 4.4 and Figure 4.5 might suggest. The increase in ester extraction is 8-fold. A significant fraction (2.4% of the total extract) are phthalate esters with the remainder being primarily oxalic acid esters.

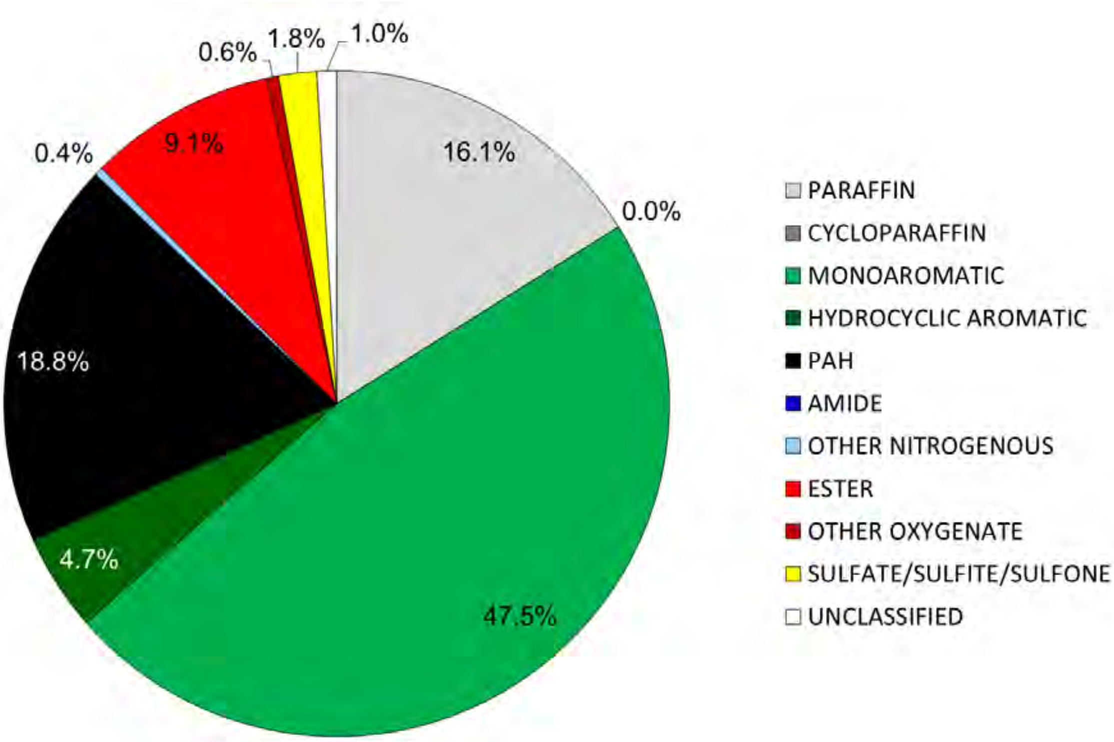

Figure 4.5: Class distribution of molecules extracted from commuter bus soot by acetone, as determined by GC-MS

4.2.5 Methanol extract

When methanol was used as extraction solvent, aromatic compounds no longer constituted the most extracted class. Esters constituted the greatest fraction of the extracts. This was not too surprising since methanol is capable of forming hydrogen bonds with and thus shown a preference for analytes containing hydrogen donating (e.g. hydroxyl) or accepting (*e.g.* nitro, carboxy or ester) functional groups [87]. The quantity of esters has increased 4-fold over that extracted by acetone (compare Figure 4.5 and Figure 4.6).

12.4% of the total were phthalate esters. One ester (identified as possibly being di-dodecyl phthalate) constituted 7.1%. Again the PAHs were bicyclic in nature.

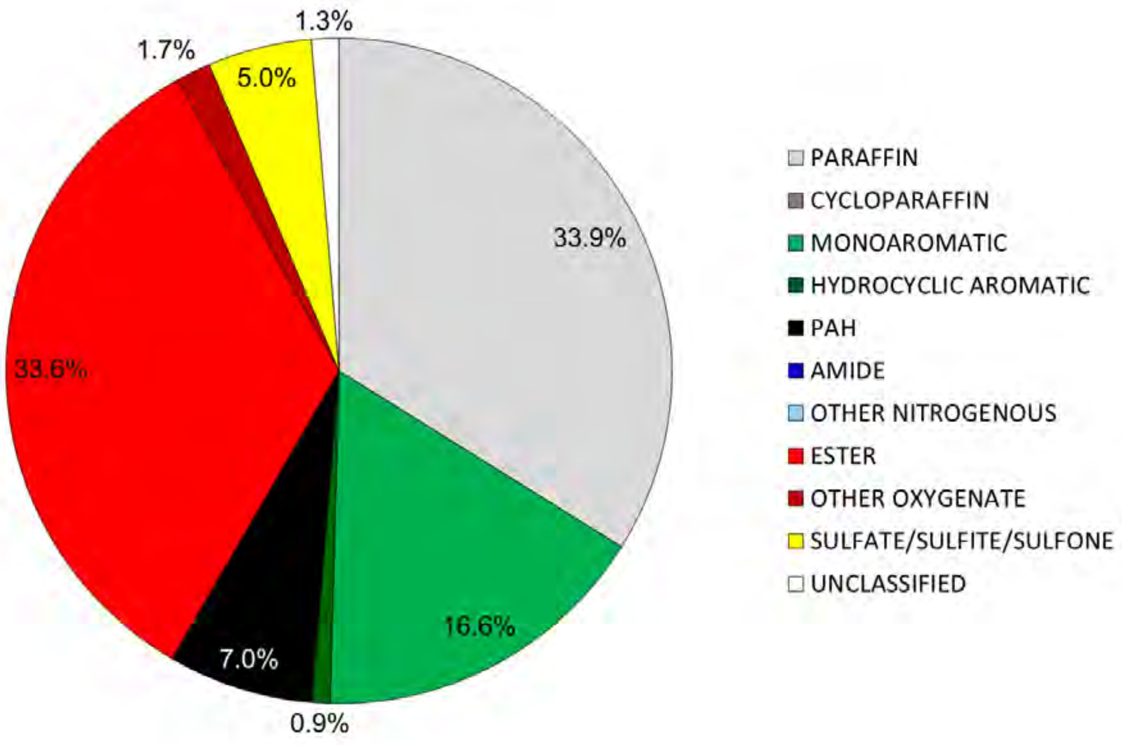

Figure 4.6: Class distribution of molecules extracted from commuter bus soot by methanol, as determined by GC-MS

4.2.6 Dichloromethane extract

Esters also constitute a large fraction of the extract when dichloromethane was used as solvent (*see* Figure 4.7). No aromatics were observed but this was because MS detector issues caused an unsteady baseline which made the positive identification of early eluting aromatics difficult.

The data in Table 12.7 reveals that a significant number of peaks with retention time (3.5 – 6 min) could not be classified (matches were all < 50%). These retention times are consistent with aromatic species (compare the tables in Appendix A for the other solvents). The unclassified peaks in this region constituted 19% of the total.

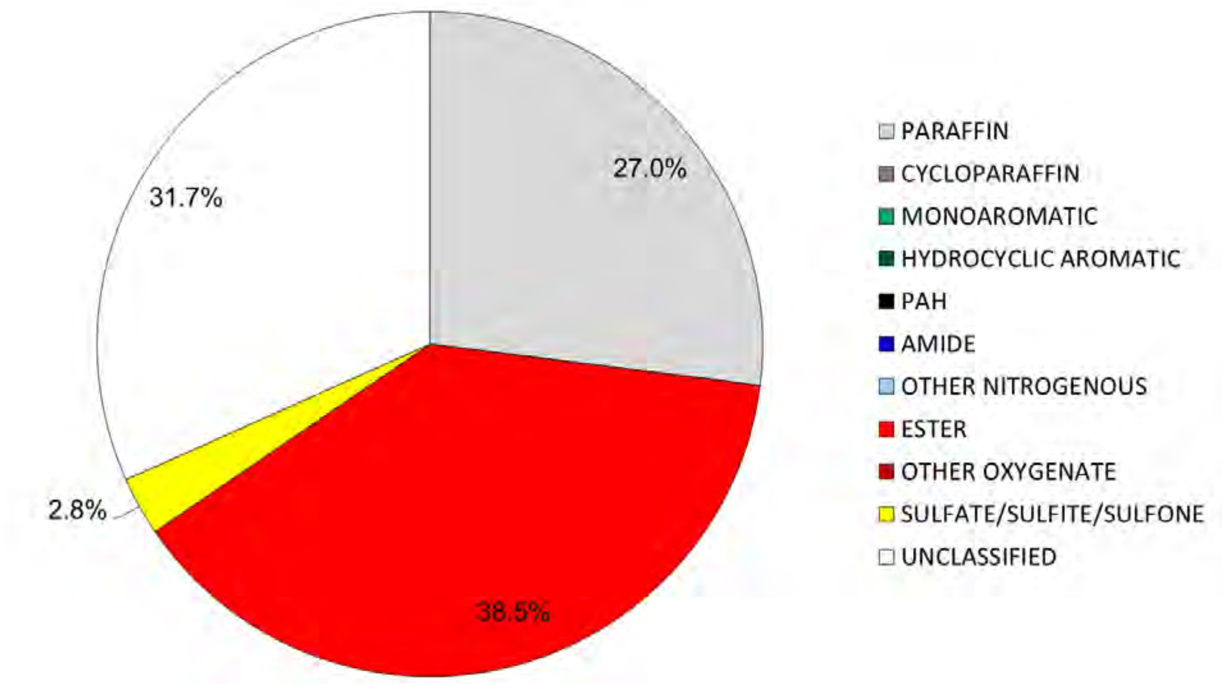

Figure 4.7: Class distribution of molecules extracted from commuter bus soot by dichloromethane, as determined by GC-MS (own analysis)

Of the species that were identified, esters constituted by far the largest class. 5.05% were phthalate esters. It is possible that some of the late eluting unclassified species (13-16 min) are also phthalate esters. Because the MS could not be fixed, samples of the dichloromethane extract were sent to the University of Stellenbosch for analysis. The instrument parameters used at the University of Stellenbosch may be found in Appendix A.

Again the importance of esters can be seen (see Figure 4.8). Aromatics are still absent but perusal of the data supplied by the University of Stellenbosch reveals that data for short retention times, at which aromatics might be expected to elute, were missing. Unfortunately the effectiveness of dichloromethane for the extraction of aromatic compounds could not be addressed in this study because of equipment failures.

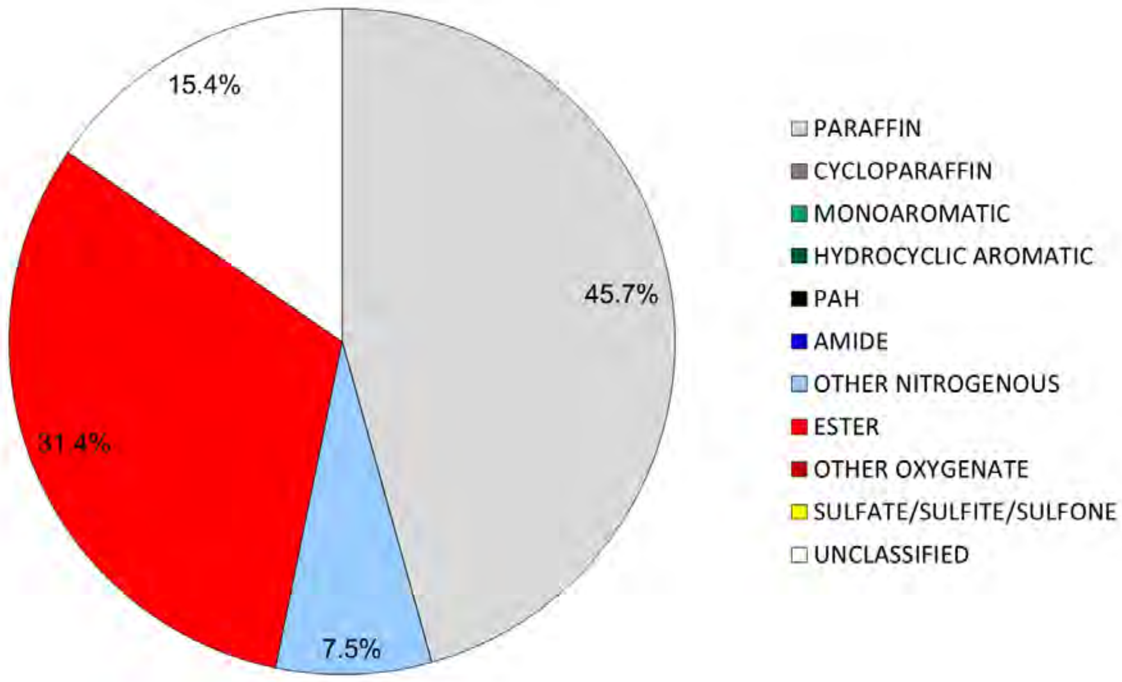

Figure 4.8: Class distribution of molecules extracted from commuter bus soot by dichloromethane, as determined by GC-MS (University of Stellenbosch analysis)

4.3 Thermogravimetric analysis of soot

Thermogravimetric analysis is often used to characterise soot, including assessing the volatile fraction. Samples were heated at 10^{o}C/min to allow comparison with other studies.

Commuter bus soot was analysed in the TGA to primarily obtain the volatile organic fraction (VOF) which could enable comparison with the SOF obtained via Soxhlet extraction. The VOF comprises mainly of fuel and lubricant oil components which are physisorbed on the soot matrix [88].

In thermal analysis experiments (inert atmosphere) the VOF of soot is often calculated from temperatures around 150°C (water free) to 380°C. A cut off temperature of 380°C is chosen because most diesel fuels and lubricating oils evaporate from 200 and 380°C [88].

Any further mass loss that occurs beyond 380°C under inert atmosphere is due to thermal decomposition of adsorbed oxygenated groups anchored on the surface of the carbonaceous matrix and/or decomposition of less stable groups of the carbonaceous matrix [89]. The oxygen that advances mass loss of soot under inert atmosphere at temperatures beyond 380°C is derived from various oxygenated groups including lactones, cyclic anhydrides, cyclic ethers, carbonyls and quinones [89].

Several samples of commuter soot were thermally interrogated in the TGA under the inert atmosphere. The mean VOF (150-380°C) of five random samples was 9.3 ± 0.7wt %. This value is more than double the SOF (4.76 ± 0.28wt %) that was obtained via Soxhlet extraction with methanol solvent. Although it is expected that the VOF is greater than the SOF, the two values are usually close. It is also apparent from the TGA thermograms that the soot samples contained absorbed moisture.

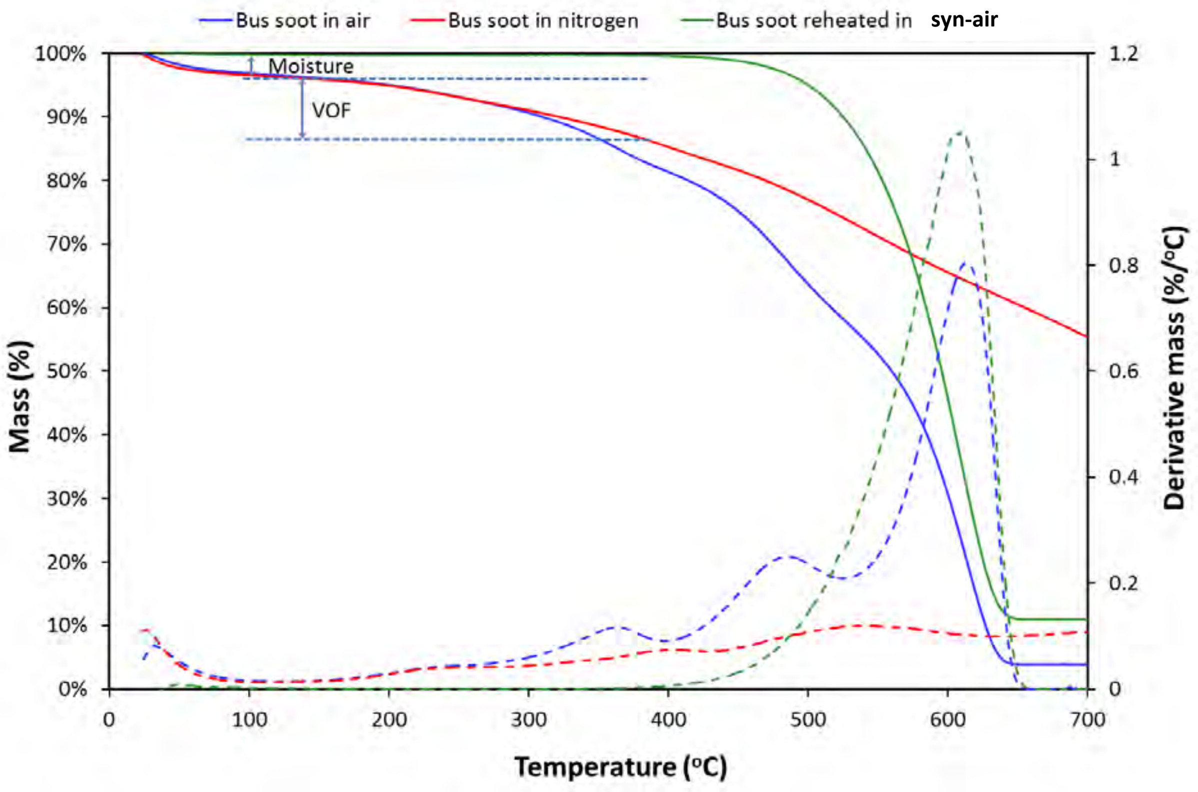

Figure 4.9: TGA thermograms of commuter bus soot when exposed to nitrogen and air. Solid lines = mass loss; dashed lines = derivative

The sample was first heat treated under (10°C/min) nitrogen to 700°C to remove any physisorbed species (figure 4.9, red curve) and subsequently heat treated (10°C/min) in synthetic air to 700ºC to investigate the combustion of the carbonaceous soot (green curve). The combustion curve for original soot is provided in blue. It can be seen that the evaporative curve (in nitrogen, red) contains three peaks (395, 535 and 549°C) and a shoulder at 235°C. The oxidative curve (blue) contains the same shoulder but the first two peaks have shifted to lower temperatures (360, 480 and 615°C). However, the extent of mass loss associated with each event is greater. Where the sample had been preheated to 700°C in nitrogen, only the last oxidative peak remained (green dotted curve). It is worth noting that the shoulder at 235°C is present in both the blue and green curves, this suggests that part of the VOF lies below its auto-ignition temperature. Previous authors [89, 90, 91] have also witnessed multiple combustion phases in wet soot and they attribute the phenomena to combustion of carbonaceous material which have dissimilar physical structure and surface chemical nature. The CO_2 evolution peak was observed to get large as temperature rose as was seen in the current study [91].

Lastly the ash content which represents residual and non-combustible component of particulate matter was investigated with oxidative TGA. The ash content (conventionally determined in a single run, where a sample of soot is thermally interrogated in an oxidising medium to a temperature where all combustible material has reacted) in commuter bus soot was particularly high i.e. 12.5±1.2 wt% (mean and standard deviation was calculated from five random samples, N.B the curves of the five respective samples are not indicated). The sampling process of commuter bus soot (scratching soot from the exhaust pipe of the commuter bus) serves to elucidate the relatively high content of ash in commuter bus soot. During the sampling of commuter bus soot, metal components (from the exhaust), were invariably collected with the soot sample. The final ash level is higher for the dried soot as a percentage because of the loss of 40% volatiles during the pre-treatment in nitrogen.

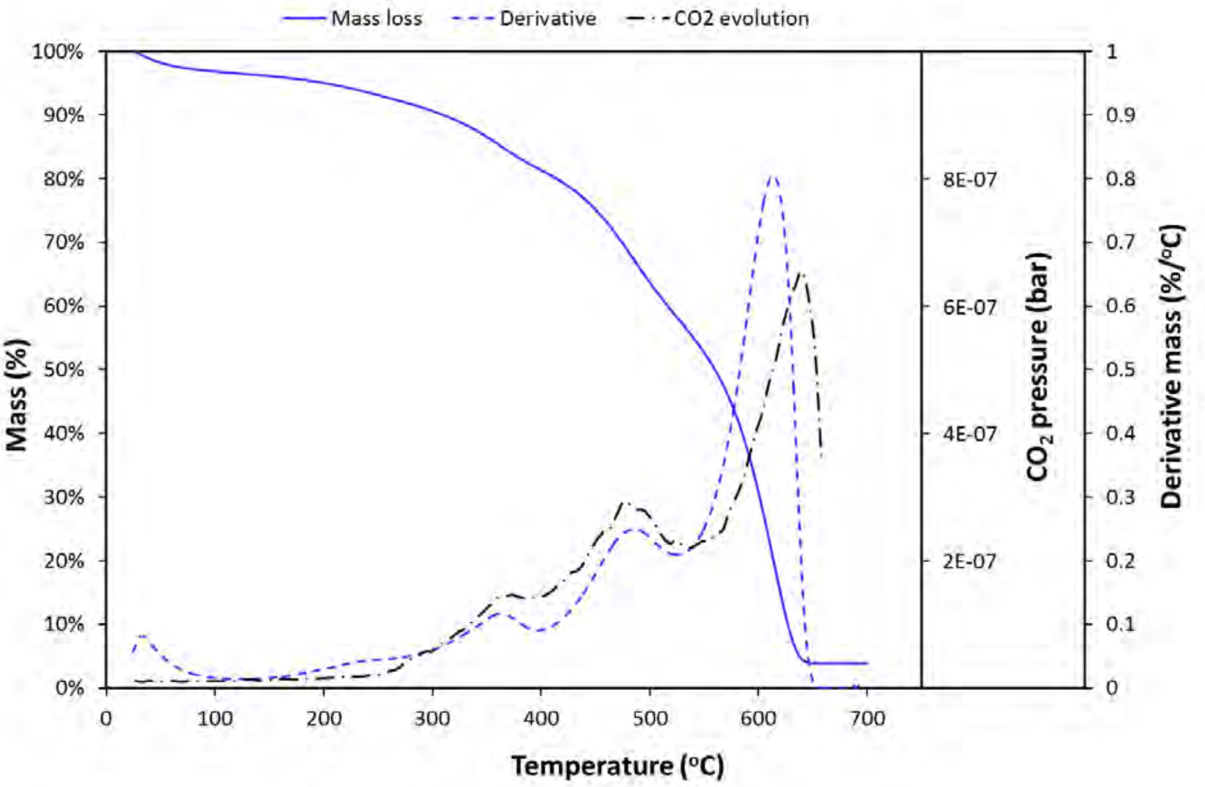

Figure 4.10: CO_2 and mass loss curves of as received commuter soot which was heated from ambient to 700°C at 10°C/min in flowing synthetic air

Figure 4.10 illustrates that the various mass loss peaks in the oxidative DTG curve in Figure 4.9 are all associated with CO_2 evolution. This is indicative of combustion, rather than only devolatilisation of the soot. The H_2O evolution curve increased monotonically from the onset of combustion.

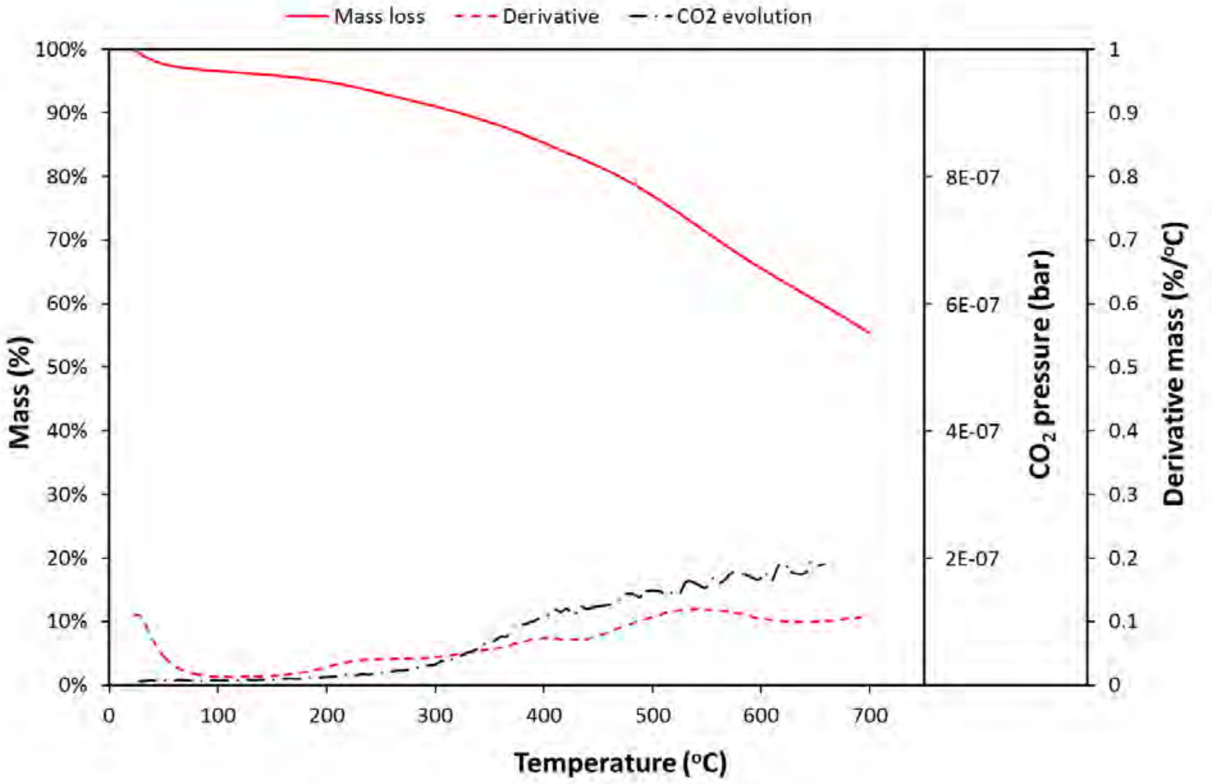

Figure 4.11: CO_2 and mass loss curves of as received commuter soot which was heated from ambient to 700°C at 10°C/min in flowing nitrogen. Full scale on the CO_2 axis is 1 x 10^{-6}bar

Figure 4.11 performs the same analysis as Figure 4.10 but for the case where the soot is heated in nitrogen. It can be seen that the mass loss is again associated with CO_2 evolution. This is indicative of the fact that the mass loss when soot is heated in dry nitrogen is not just the result of the evaporation of independent volatile compounds but also involves pyrolysis reactions in which CO_2 is eliminated.

4.4 Electron microscopy of diesel bus soot

Electron back-scattered detection (EBSD) is a mode of SEM which detects electrons that are diffracted by atomic layers in crystalline materials. Although EBSD is primarily used to provide information regarding crystal structure and crystallographic information, it provides high contrast images which are useful for identifying the presence of elements with high electron density, *e.g.* metals. This is because the intensity of backscattered electrons is an increasing function of the electron density in the scattering element.

Analysis of Figure 4.12 reveals that there is a difference between the two images, namely a significant number of bright spots in the EBSD image. The bright spots are indicative of regions of high electron densities while the darker grey regions represent areas of low electron density. Metals which are electron rich atoms deliver more backscattered electrons to the backscattered detector and in the image are responsible for bright regions. In contrast atoms with low electron density such as carbon atoms deliver a lower count of backscattered electrons to the detector and as such appear as dark regions. Careful observation of the bright regions of Figure 4.12 reveal these to have an angular nature, indicative of crystalline particles.

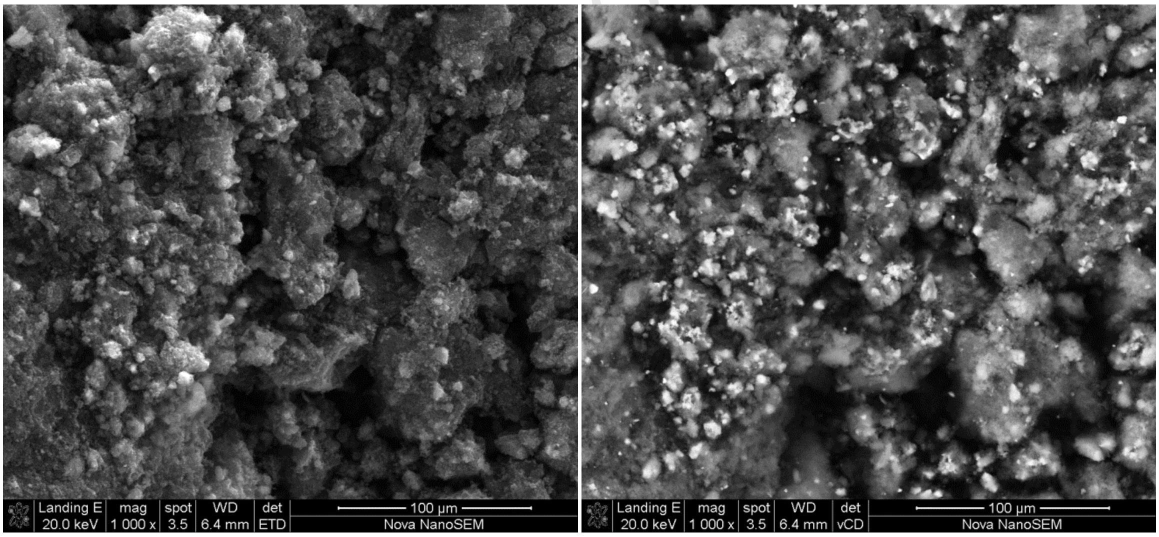

Figure 4.12: Electron micrographs of commuter bus soot in a) scanning mode and b) EBSD mode

EDS revealed that the metals responsible for these bright spots in commuter bus soot are primarily iron, calcium, aluminium and silicon. The iron is likely from the exhaust while the calcium is likely from the lubricant. Calcium naphthenates are often added as detergency additives. The aluminium and silicon are likely from dirt or sand in the exhaust although polysiloxanes may be added to lubricants.

A representative soot sample was digested in hydrofluoric acid and the resultant solution was analysed for metals using ICP-MS. The results, presented in Table 4.1, are consistent with the EDS results. Also observed were Zn and P which are also found in lubricant additives. Zinc dithiophosphate is typically added as an anti-wear agent. It also has a minor anti-corrosion and anti-oxidant role.

Table 4.1: ICP-MS elemental analysis of commuter bus soot (excluding carbon and oxygen)

Element	**Concentration (%)**
Na	0.08
K	0.04
Mg	0.03
Ca	0.22
Fe	3.15
Zn	0.04
Al	0.12
P	0.12
Si	0.16

The elements P, Fe, Ca and Zn were reported in soot by Clague *et al* [31].

4.5 Comparison of the extraction potential and specificity of a variety of solvents

The polarity of the extraction solvent was found to have a significant influence on the quantity of material extracted from the soot samples under investigation. Figure 4.13 clearly indicates a positive relationship between solvent polarity, as measured by the polarity index, and the quantity of the SOF. This is consistent with the chemical nature of the SOF, present in the soot. GC-MS revealed the presence of a significant fraction of polar components in the SOF, extracted by the polar solvents. These were primarily esters. While these where extracted by the polar solvents, they were extracted to a much lesser degree by the hydrocarbon solvents: toluene, cyclohexane and n-hexane. The increased extraction by toluene relative to the alkanes can be ascribed to the affinity of toluene for other aromatic species.

Among the six solvents used in this study the polarity index decreases from methanol = acetone > dichloromethane > toluene > cyclohexane > hexane (see Table 4.2).

Table 4.2: The polarity index of the solvents used in this study, adapted from [87]. Hansen solubility parameters (HSPs) are from [92]

Solvent	**Polarity index**	**Dipole moment (D)**	**Dispersive HSP (δ_d)**	**Polar HSP (δ_p)**	**Hydrogen bonding HSP (δ_H)**	**Molar volume (cm^3/mol)**
Dichloromethane	3.1	1.60	18.2	6.3	6.1	63.9
Methanol	5.1	1.78	15.1	12.3	22.3	40.7
Acetone	5.1	2.88	15.5	10.4	7.0	74.0
Toluene	2.4	0.31	18.0	1.4	2.0	106.8
Cyclohexane	0.2	0.00	16.8	0.0	0.2	108.7
n-Hexane	0.0	0.00	14.9	0.0	0.0	131.6

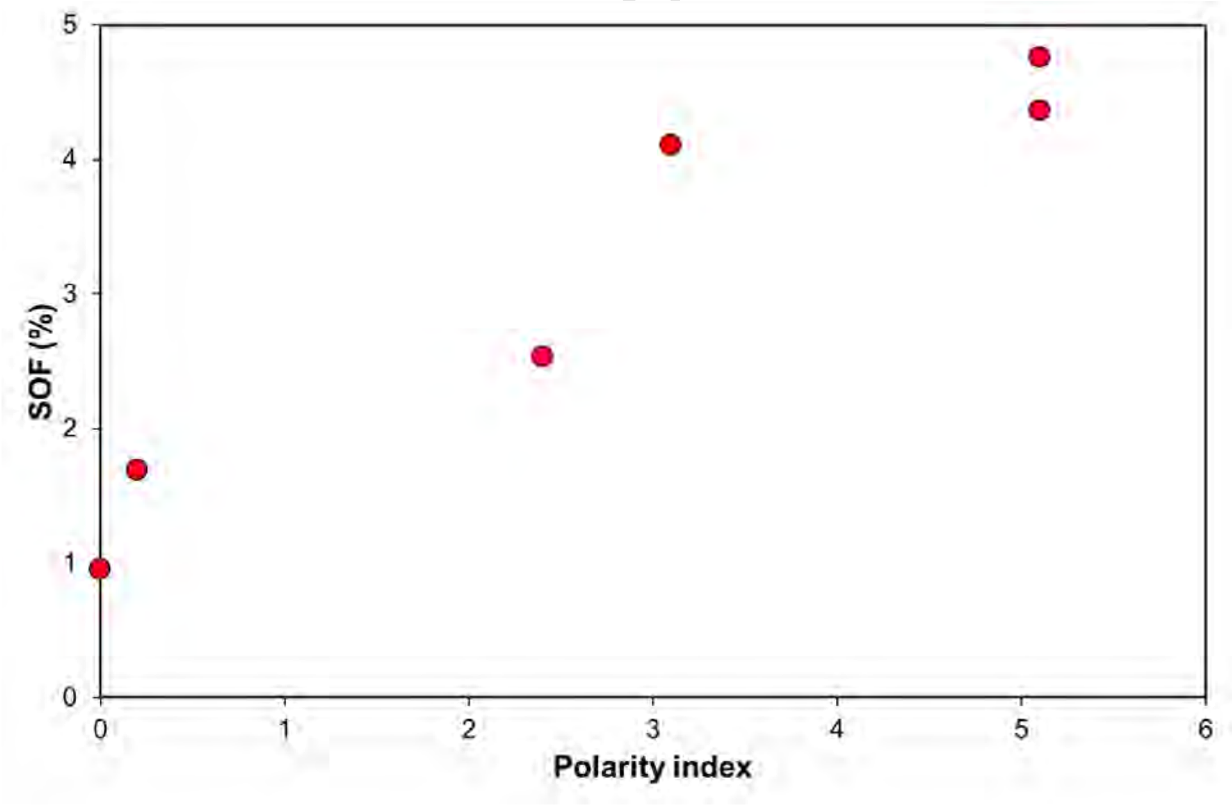

Figure 4.13: Relationship between quantity of SOF extracted and solvent polarity

The level of extracted SOF was much lower than many previous studies. Lubricating oil has been implicated as a significant contributor to diesel soot. Both engines used in this study operated using a synthetic lubricant which is much cleaner than the lubricants, based on mineral oils, which were previously used. The low levels, extracted in the current study, would suggest that the composition of the engine oil has a significant impact on the SOF.

As previously highlighted extraction of commuter bus soot with the six respective solvents yielded SOF's with varied chemical speciation. GC-MS chromatograms revealed that the solvents had varied affinities for species adsorbed onto the soot matrix. Below is table 4.3 which summaries the GC-MS data from the respective solvents. In the table the competence (indicated by percentages) of each solvent at extracting targeted chemical species is shown.

Table 4.3: Percentage of soot extracted by chemical class and extraction solvent

Solvent	**Paraffins***	**Mono-aromatics**	**Hydrocyclic aromatics**	**PAHs**	**Esters**	**Others$^{\#}$**	**Phthalates**
Dichloromethane	1.1	u.d.	u.d.	u.d.	1.6	u.d.	0.2
Methanol	1.6	0.8	0.04	0.3	1.6	0.4	0.6
Acetone	0.7	2.1	0.2	0.8	0.4	0.17	0.11
Toluene	0.14$^{\$}$	2.0	0.2	0.2	0.05	0.04	0.01
Cyclohexane	0.5	0.8	0.10	0.14	0.07	0.03	0.00
n-Hexane	0.3	0.6	0.02	0.04	0.03	0.02	0.00

* includes cycloparaffins

$^{\#}$ includes unclassified

u.d. undetermined because of equipment difficulties

$^{\$}$ likely under-estimate

It should be noted that siloxane compounds were ignored because they are likely indicators of column bleed/breakdown. However, siloxanes may also be used as anti-wear agents in lubricants and may thus be a small constituent of the SOF. Since Si makes up 0.16% of the soot (Table 4.1), the total siloxane content is unlikely to exceed 0.30%. The real level will be lower since some of the Si is undoubtedly associated with Al as dirt.

Surprisingly fewer paraffins were extracted by the paraffinic solvent, n-hexane, than the more polar: acetone, methanol and dichloromethane. While this may at first seem counterintuitive, it may be readily explained by considering the dissolution process. In order for a component to dissolve into the solvent, it must be able to reach that solvent. This requires that the binding matrix of the soot needs to be swollen so that solvent may migrate into the soot and the components may migrate out. The matrix is likely aromatic and/or polar and is thus poorly swollen by n-hexane. The increased swelling by methanol, for instance, allows the paraffins to exit the soot. A similar effect has been observed when coal is swollen and extracted [92].

Toluene and acetone were the most effective for the extraction of monoaromatics and hydroaromatics. The extraction by the former is not surprising since the solubility parameters of toluene matches those of the aromatics concerned. Dissolution is usually maximised when solubility parameters match [92]. The extraction by methanol is reduced because methanol is likely too polar. Although there is a slight mismatch in solubility parameters between acetone and monoaromatics, this is offset by the small molar volume of acetone. Small molar volume solvents are more effective at swelling and dissolution [92].

The extraction of PAHs was maximised in acetone. Although these species are aromatic their delocalised π-electron distribution gives them some polar and "hydrogen-bonding" character. δ_p and δ_h are more closely aligned with those of acetone. The extraction by methanol is lower because the δ_p and δ_h are even higher and more mismatched, leading to methanol being a poorer solvent for PAHs. Similar behaviour has been observed for the extraction of polyaromatic asphaltenes from crude oil [92]. Mannistu *et al.* found better asphaltene solubility in acetone than methanol [93]. Another possible reason for the absence of PAHs in methanol extract is that PAH stability in methanol has been shown to be an issue. PAHs such as benzo[α]pyrene, acenapthene, benz[α]anthracene, fluoranthene and dibenz[a,h]anthracene photodegrade in methanol [87] on relatively short time scales which may have occurred during handling. Interestingly Jonker and Koelmans [40]were able to get good extraction using alcohols by blending these with toluene. This has the effect of creating a solvent with average solubility parameters closest to PAHs. The study of mixed solvents was beyond the scope of the current study.

Nonetheless, the total level of PAH extraction was low. This is in contrast to Todorović and Zdravkovski [4] and *Yu et al.* [36]. Yu *et al.* [36] reported that their toluene fraction was almost wholly composed of substituted and unsubstituted PAHs. Note, however, that their study was conducted in 1981. Commercial diesel fuels had less stringent fuel specifications, permitting a larger component of PAHs and aromatics in the fuel and lubricants. Lubricants have been implicated as a significant contributor to soot [31]. The commercial bus, from which soot was taken, used synthetic oil which contains next to no PAHs, unlike older lubricants which used mineral oils as a base. In a more recent study by Todorović and Zdravkovski [4] the toluene extract of soot from several modern vehicles contained far fewer PAHs. Only naphthalene, pyrene, anthracene and phenanthrene were detected. This observation suggests that lower PAHs in modern commercial fuels and lubricants, leads to fewer PAHs being detected in modern soot samples.

The intrinsic polarity of methanol and acetone renders these solvents ideally suited for ester extraction. Esters are common additives to lubricating oil, particularly synthetic lubricating oils (composed of mainly n-paraffinic molecules), to enhance the oils lubricity as well as enable the oil to form stable solutions with polar additives [26]. It is known that the bus (MAN) from which our sample was collected, ran on synthetic lubricating oil (Mobil Delvac 1 LE 5W-30). The higher solubility parameters of methanol than acetone provide a better match with those for these esters which explains the higher extraction by methanol. Over a third of the esters extracted by methanol were found to be phthalate esters. These esters are potential endocrine disruptors. Esters were also identified by Todorović and Zdravkovski [4]. The low polarity of the hydrocarbon solvents explains why very little of these esters are found in the extracts of these solvents.

Unfortunately good data could not be obtained for dichloromethane because of equipment difficulties. However, dichloromethane has been shown to extract PAHs in diesel soot by Borras *et al.* [5], Yu *et al.* [36] and Oukebdane *et al.* [85]. However, mixed aromatic/alocohol solvents were demonstrated to be better [40]. Esters also make up a large portion of the dichloromethane extract. This was confirmed by analysis both at SAFL and at the University of Stellenbosch.

4.6 Comparison of the analysis of SOF and VOF

In this study the VOF, as determined by TGA, was significantly higher than the SOF as determined by Soxhlet extraction. While this could to some extent be ascribed to uncertainties about which temperature range in the TGA best corresponds to the VOF, it may well indicate that the VOF contains volatile species not extracted by the organic solvents used. Likely candidates are sulfurous and sulfuric acid. It should be noted that the commuter bus operated on diesel that contained up to 50 ppm sulfur. It is not inconceivable that this contributed to the VOF. A number of organic sulfates, such as dibutyl sulfate, hexyl decyl sulphate and di-(2-ethyl hexyl sulphate), were observed in the polar extracts of the commuter bus soot. More polar sulphates and sulphuric acid, however, would not be observed in the extracts by GC-MS. Another possible explanation for the discrepancy is that pyrolysis of soot constituents produces a char and some volatile components [94]. The constituents, themselves, are not extractable by solvent. There is evidence for such pyrolysis in the results of this study. This can be seen in the evolution of CO_2 in Figure 4.11. Unfortunately CO (amu 28) evolution could not be monitored because N_2, the atmosphere, has the same molar mass.

Collura et *al.* [89] extracted two types of diesel soot (VSA and VSB) and found their SOF's to be 6 and 20% respectively. Thermal analysis of the two soot samples revealed that the VOF (excluding moisture) of VSA and VSB was 8 and 20% respectively. It is possible that the closer match of SOF and VOF values was because Collura et *al.* [89] performed sequential Soxhlet extraction using two different solvents on the same sample. They used dichloromethane extraction followed by toluene extraction. The data in As previously highlighted extraction of commuter bus soot with the six respective solvents yielded SOF's with varied chemical speciation. GC-MS chromatograms revealed that the solvents had varied affinities for species adsorbed onto the soot matrix. Below is table 4.3 which summaries the GC-MS data from the respective solvents. In the table the competence (indicated by percentages) of each solvent at extracting targeted chemical species is shown.

Table 4.3 indicate that while methanol is effective at extracting esters, acetone is more effective at extracting PAHs. The total sequentially extractable material is thus expected to exceed that extracted by each of the solvents, individually. It should, however, be noted that not all authors report a match between volatile and extractable content. Clague *et al.* report discrepancies of between 40 and 90% [31]. The latter discrepancy is of the order measured in this study.

In order to investigate the mismatch further, the extracted soot samples were subjected to thermogravimetric analysis. Figure 4.14 provides a comparison of the mass loss of original soot vs. acetone extracted soot under nitrogen.

It is apparent that a significant volatile fraction remains and that only about half of the VOF is present in the SOF. The difference between 9.4% and 5.3% compares well with SOF for acetone (4.3%). Similar curves were found for the other extracted soots. The VOF remaining was largest for n-hexane, as expected.

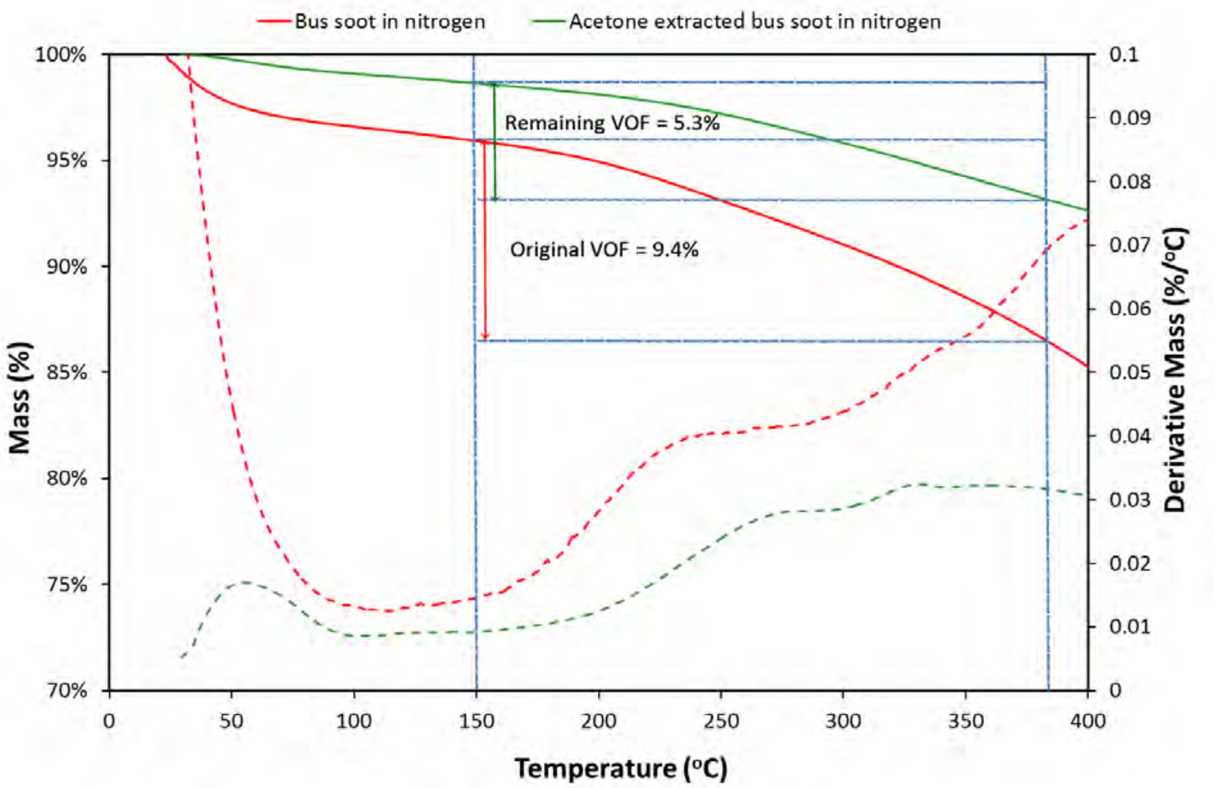

Figure 4.14: TGA thermograms of commuter bus soot in nitrogen in the original (red) condition and after acetone extraction. Mass loss curves are solid lines, derivatives are dashed

4.7 Conclusions

It is apparent that the choice of extractant matters when measuring SOF and characterising soot. It is recommended that a sequential extraction such as employed by Collura et *al.* be followed. It is suggested that methanol extraction be followed by acetone extraction. Because acetone extracts the same compounds as toluene but to a greater extent, a further extraction with toluene might not be required. A final aqueous extraction is recommended to remove aqueous-extractable components such as sulphuric acid. Where the speciation of phthalates is especially important, methanol is the preferred solvent. Although binary solvent mixtures are not recommended at this stage they could be explored. Japar *et al.* used a binary mixture of toluene and n-propanol although they did not speciate the SOF [95].

It is apparent from both samples that, when compared to analyses performed in the 1980s, the importance of PAHs as a fraction of the SOF has decreased significantly. It is suggested that it is because of improved engine operation but more significantly because of the replacement of aromatic base oils with synthetic base oils. This would imply a lowered toxicity potential from PAHs. However, the presence of potential endocrine disruptors should not be ignored.

This has often been ignored in previous studies. These are likely derived from engine oil additives. A number of other lubricant markers were observed in the soot such as Ca, Zn and P.

Because of the low SOF obtained, any contribution of non-extractable species such as sulfurous and sulphuric acid will contribute a greater fraction to the VOF than earlier studies where the organic fraction constitutes a greater fraction of the volatiles. The VOF would be better termed volatile fraction since a component is likely not organic in nature.

5 Evaluation of depositing propensity of diesel fuels

5.1 QCM measurements

A quartz crystal microbalance (QCM) was used to thermally stress diesel fuels according to ASTM D7739-11 [67] method to provide quantitative and qualitative information regarding the depositing propensity of test fuels.

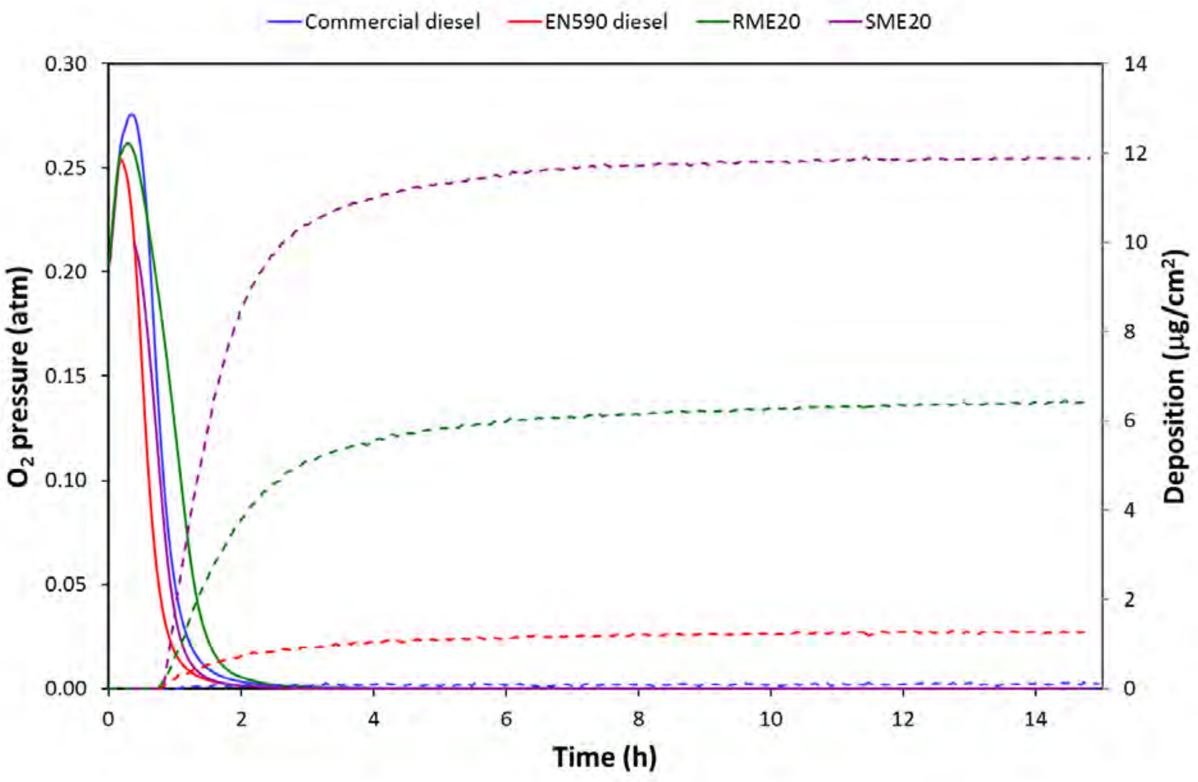

Figure 5.1: QCM traces of four diesel fuels which were exposed to reactor conditions of 140°C and 1 bar of synthetic air for 15 h. The plots indicate mass (deposit) accumulation (dashed lines) and oxygen consumption (solid lines)

Figure 5.1 shows that there were vast differences in the mass accumulation plots between the fuels. The plots show that commercial diesel had almost no mass accumulated during the 15 h test. Total pressure in the QCM was observed to rise because of fuel evaporation and a temperature increase from ambient after which it dropped until oxygen was consumed and then levelled off. In the case of the least stable fuel, SME20, the pressure then rose again slightly after passing through a minimum indicating a small degree of cracking and the formation of volatile compounds. This was not noted for the other fuels.

A plot of the natural logarithm of the oxygen pressure vs. time produced a curve had two straight portions once the fuel temperature had stabilised. This was observed for all fuels and is illustrated below for RME20.

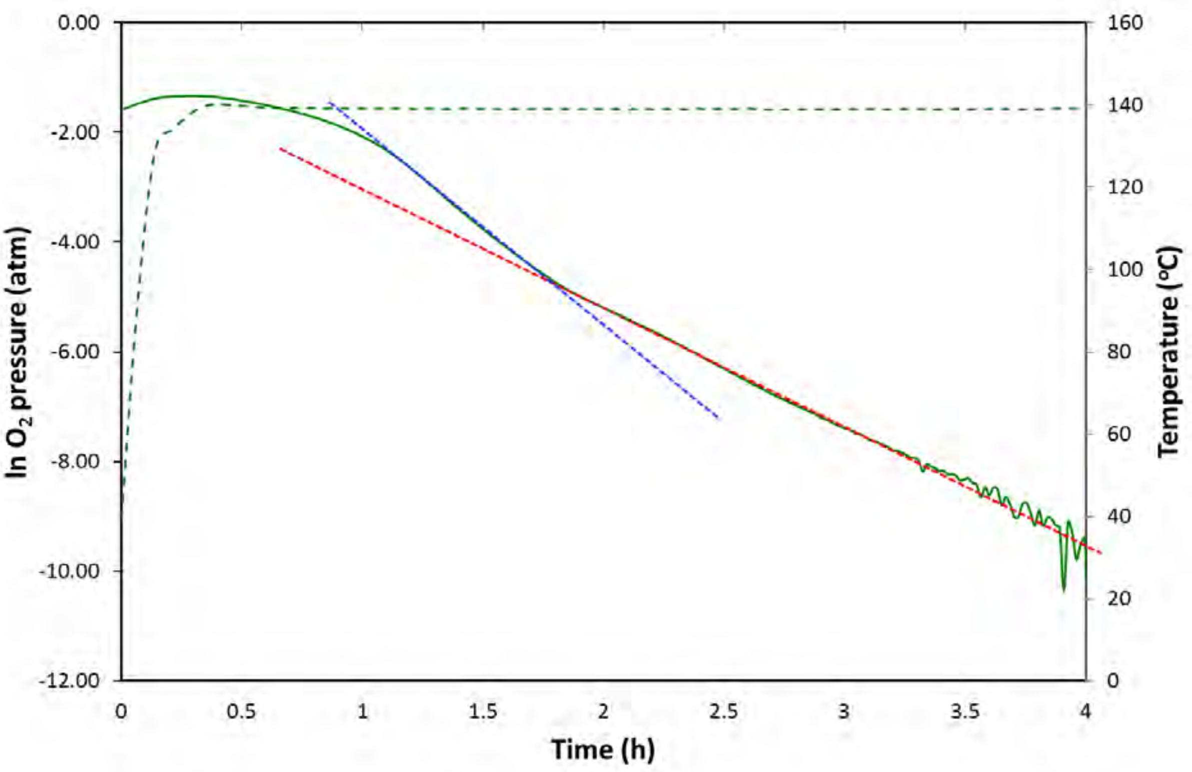

Figure 5.2: Dependence of ln p_{O2} on time for the thermo-oxidative stressing of RME20. Solid curve = natural logarithm of oxygen pressure; dashed curve = temperature

These are indicative of pseudo-first order processes in oxygen which is often observed for oxygen depletion when fuels are stressed [65]. There is a slightly delay before the onset of the first linear portion, likely the result of the need for an initial intermediate to form. Investigations into why there are two linear portions were deemed beyond the scope of this study. The slopes of the two linear regions may, however, be used to characterise the rate of oxygen uptake. Zabarnick [65] suggests that the mechanism may be a mix of auto-catalysis and ordinary first-order kinetics. Which dominates depends on the composition of the fuel [65].

All the fuels displayed full consumption of oxygen within 3h of the tests beginning. No relationship between the rate of oxygen consumption and deposit formation was observed across the four fuels tested. Deposit formation levelled off once oxygen was consumed.

Table 5.1: Summary statistics for QCM thermo-oxidative stressing

Fuel	**Time for O_2 pressure to reach 0.05 atm (h)**	**k_1 (/h)**	**k_2 (/h)**	**Deposition at 14h (μg/cm^2)**	**Initial rate of deposition (μg/cm^2/h)**	**Minimum total pressure at 140°C**	**Total pressure at 14h (atm)**
Commercial diesel	0.99	3.83	1.65	0.11	0.08	1.19	1.19
EN590 diesel	0.76	4.69	2.23	1.26	1.06	1.11	1.11
RME20	1.29	3.11	2.21	6.41	4.00	1.16	1.16
SME20	0.93	4.70	2.49	11.91	9.21	0.88	0.91

k_1 and k_2 are the negatives of the slopes of the two linear portions of the ln p_{O2} vs time curves

5.2 Discussion

The levelling off of deposit formation once oxygen is consumed is consistent with the deposit formation processes being oxygen-limited for all fuels. This has been observed previously [65]. It should be noted that the commercial diesel contains anti-oxidants, deposit control agents (DCAs) and less than 50 ppm sulfur. Less than 50 ppm sulfur indicates the fuel was hydrotreated which would remove species known to cause deposit formation in petroleum fuels. This together with the presence of DCAs would impede deposit formation. This commercial fuel is more stable than any of the jet fuels reported by Zabarnick [65]. Unlike diesel, DCAs cannot be used in jet fuel.

The EN590 diesel did not contain any anti-oxidants, unlike the commercial diesel and the FAME blends. This would explain the faster consumption as indicated by the time for the O_2 pressure to reach 0.05 atm.

The absence of a relationship between the rate of oxygen consumption and extent of deposition is likely the result of different mechanisms for deposit formation between petroleum fuels and FAMEs. Different mechanisms would follow a different sequence of subsequent steps leading to deposits. It is possible to have a fuel such as a pure alkane which rapidly consumes oxygen which forms low levels of deposits. Nonetheless, within the FAME blend pair, it was found that the faster oxidising fuel (SME20) also formed more deposits.

A review by Birgel *et al.* [9] concedes that running an engine on rapeseed methyl esters or soybean methyl esters can cause dramatic injector tip fouling. In the current study the effect of blending EN590 diesel with 20% rapeseed methyl esters and 20% soybean methyl esters on the depositing propensity of EN590 diesel can be seen. Blending EN590 diesel with 20%

rapeseed methyl esters increases deposition more than four fold. The deposition propensity of EN590 diesel almost doubles again when blended with 20% soybean methyl esters.

Two possible reasons have been proposed for the increased deposition in biodiesel blends, namely ester functional groups have been shown to moderately affect fuel stability [6] and that, because fatty acid methyl esters have an unsaturated hydrocarbon backbone, these can experience double bond migration to form conjugated dienes which when attacked by oxygen lead to crosslinking between molecules leading to deposits [96]. The tendency of FAME molecules to undergo oxidation is strongly dependent on the number of double bonds and the extent of conjugation [55, 97].

Not all methyl esters have the same propensity to decrease fuel stability, as was evidenced SME20 produced approximately double the amount of deposits as RME20 under the same conditions. This can be attributed to the fatty acid composition of the soybean oil which is composed of 50% 18:2 (carbon number: double bond) fatty acids as opposed to 13% (18:2) for rapeseed oil (see appendix B). It is this greater degree of unsaturation that renders soybean methyl esters more prone to oxidation than rapeseed methyl esters hence the higher rate of oxygen consumption since *bis*-allylic sites are extremely prone to hydrogen abstraction. This in turn leads to faster crosslinking reactions and thereby deposition. The mechanism in petroleum fuels does not follow this pathway.

While a useful predictor of storage stability of biodiesels, oxygen consumption is not necessarily a useful predictor of thermo-oxidative stability of a full set of fuels which includes fuels which do not contain FAME.

5.3 Conclusions

QCM measurements indicated under thermo-oxidative conditions that the four test fuels have different depositing propensities. The depositing propensities of test fuels increased from commercial diesel << EN590 diesel < RME20 < SME20. As demonstrated in the following chapters, this is consistent with other observations about the quantity and nature of the deposits formed.

6 Analysis of flask reactor deposits

6.1 Visual observations

Samples of the four test fuels were observed pre- and post-stressing. Distinct changes in the colour of the fuels can be seen in Figure 6.1. With some fuels the colour change was accompanied by phase separation into two layers, the denser of which was darker. This was the case with the stressed EN590 diesel and RME20 blend. It is likely that the darker bottom layers contain high molecular weight polar species that are insoluble in the stressed fuel (insoluble gum) [74]. In the case of the SME20 blend, only the dark layer was observed, suggesting that this blend was the most unstable of all. In contrast, commercial diesel formed no insoluble gum and no darker layer was present.

Mayo suggested that colour can be used as indicator of fuel stability [63]. The darker the fuel is from its initial unstressed state the greater the extent of degradation [63]. This would suggest that stability increases in the order: SME20 << RME20 < EN590 diesel < commercial diesel. This trend is consistent with QCM data, presented in Chapter 5.

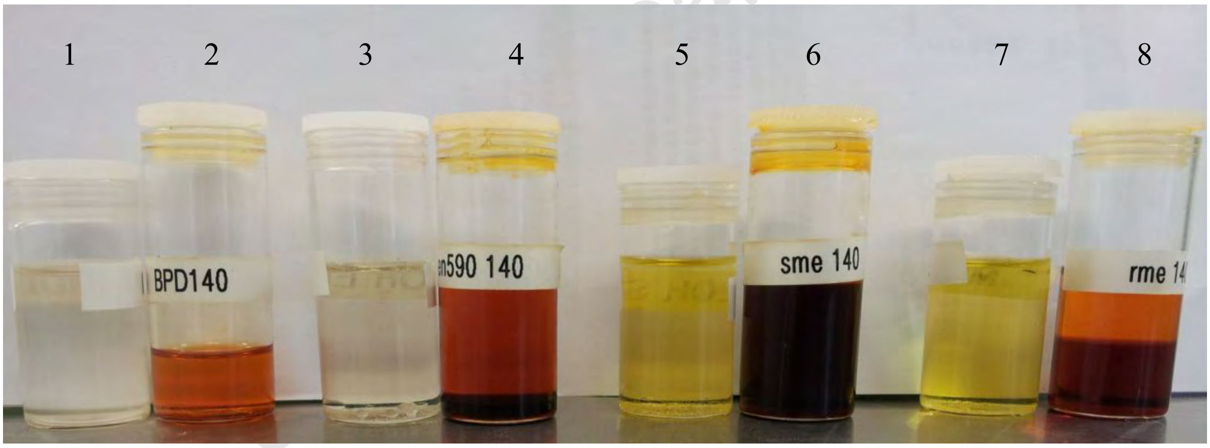

Figure 6.1: Four neat fuels and their corresponding stressed versions: 1) Neat commercial diesel, 2) stressed commercial diesel, 3) neat EN590 diesel 4) stressed EN590 diesel 5) neat SME20, 6) stressed SME20, 7) neat RME20 8) stressed RME20

6.2 Transmission electron microscopy

TEM was used to investigate the microstructure of flask reactor deposits. As far as could be ascertained, no other TEM studies in literature have investigated deposits obtained in flask reactors of diesel fuels, with or without FAME.

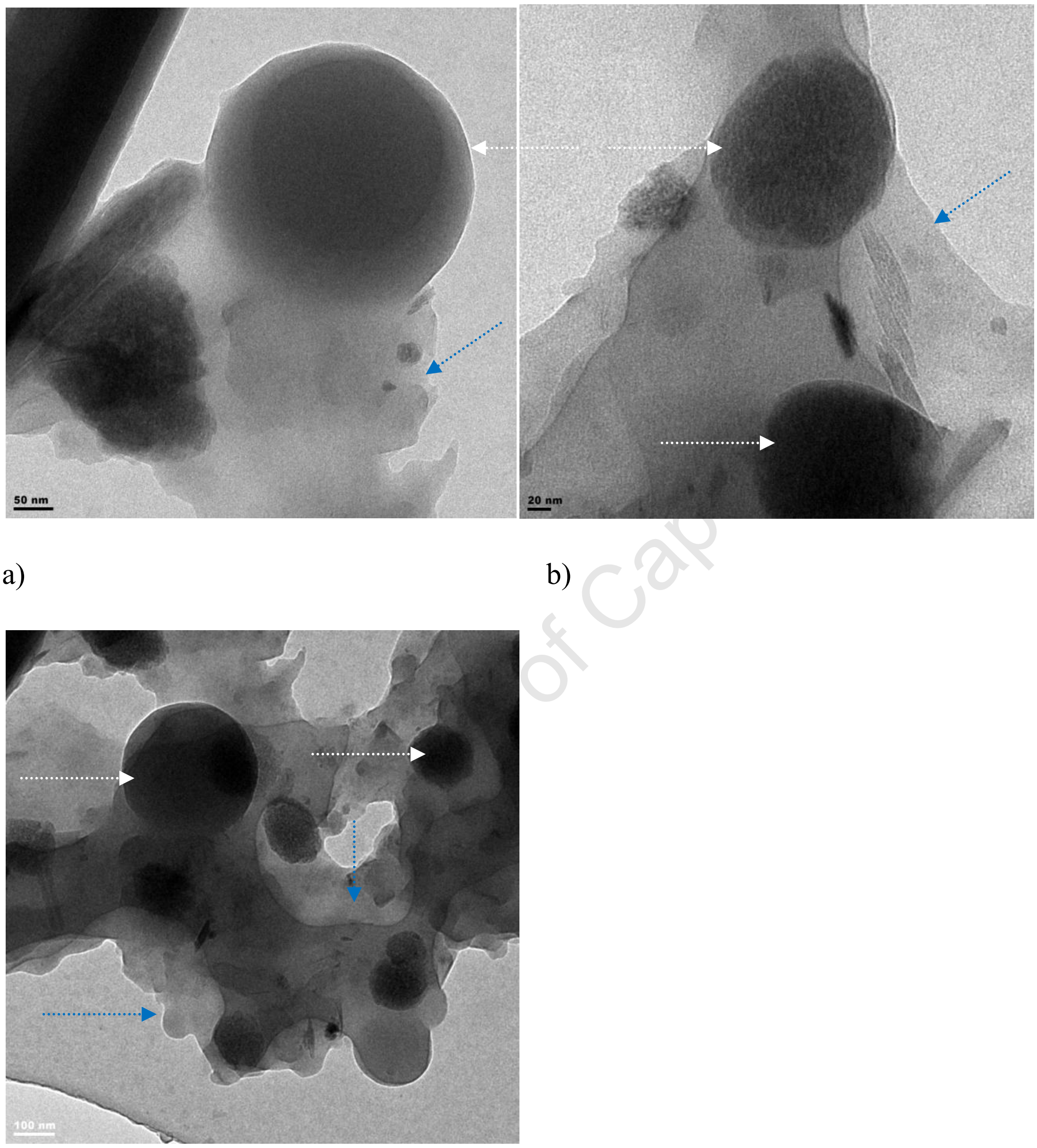

a)

b)

c)

Figure 6.2: Stressed fuel deposits investigated by TEM: a) Commercial diesel, b) EN590 diesel, c) RME20

In this study, conditions of 140°C and 15h in the flask reactor with excess oxygen led to the formation of deposits in all test fuels. All stressed fuels formed deposits which were observed using TEM, as illustrated in Figure 6.2. The micrographs reveal that the fuels formed deposits with contrasting morphologies.

Degradation of commercial diesel, EN590 diesel, and RME20 in the flask reactor yielded dark deposits and a gum-like material. This presented an interesting hybrid of materials when viewed under the TEM. The three fuels formed deposits that included spherical particles which were opaque to the TEM. These are indicated by white arrows in Figure 6.2. Interestingly such particles were also found in the commercial diesel sample, despite this fuel not separating into two layers (Figure 6.2a). This spherical material is embedded in a matrix of what appears to be a gum-like material with no structure (indicated by blue arrows). In the case of the commercial diesel, however, the quantity of spherical particles was low. For the most part, uniform layers of gum-like material were observed. The near spherical profile of the deposits is significant as it suggests that the fuel deposits are formed from nucleation and growth in a liquid phase [10]. The low number of spherical particles in the commercial diesel samples is consistent with the higher stability of this fuel as evidenced by visual inspection (Figure 6.1) and QCM data.

The spherical material may be darker because a) the material is thicker in these regions or b) it contains a higher oxygen and carbon content than the lighter areas. This is because the opacity of a TEM photo rises with increased atomic number and thickness. However, no regular structure (interference patterns) could be observed in the spherical particles. This suggests they have a highly amorphous structure.

With regards to particle size, it is apparent from Figure 6.2 that deposits of several different sizes were formed. The primary spherical particles were significantly larger than soot which has a primary particle size of 20-30nm in diameter [34]. On average, primary deposit particles had dimensions of 100nm or greater. A possible reason for this is that deposits, derived from diesel fuels (a complex mixture of aromatic, aliphatic, cycloaliphatic *etc.*), endure a much more complex formation process in comparison to carbonaceous deposits formed from simpler hydrocarbons (for example soot formed from acetylene), which typically form more ordered graphitic structures accompanied by smaller primary particles [98].

The particles sizes in this study were of the same order of magnitude as injector deposits reported by Venketaraman and Eser [10].

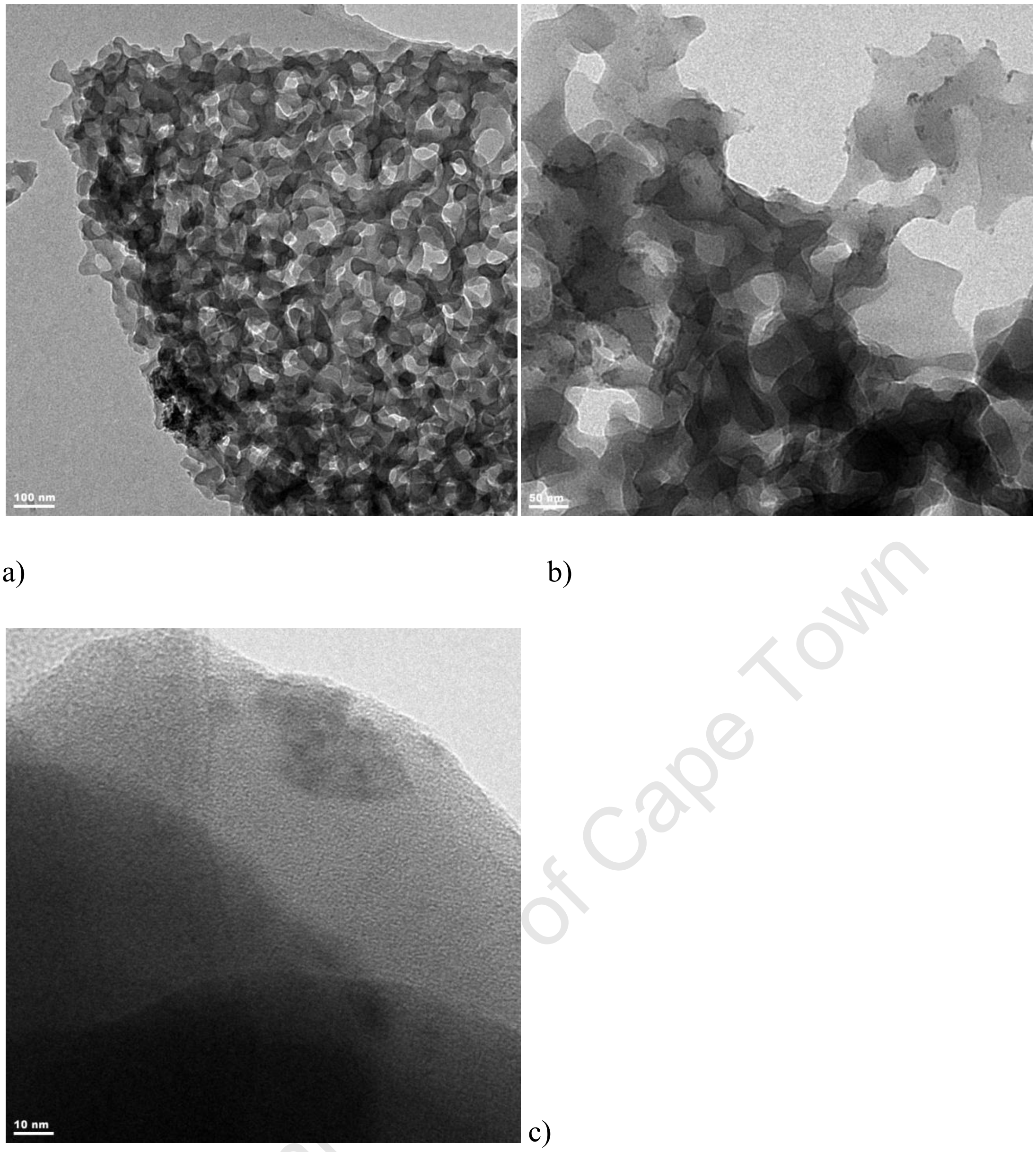

a) b)

c)

Figure 6.3: TEM images of deposits formed from SME20. The images are shown in order of increasing magnification

Of all tested fuels, SME20 produced deposits with a microstructure that displayed the most structure. This is illustrated in Figure 6.3. Nonetheless, high resolution TEM did not reveal any interference patterns, indicative of crystalline structure or plane alignment in this material. The images are indicative of amorphous structures which is consistent with the observation of diesel fuel filter deposits made by Baker *et al.* [46]. High pressure diesel injector deposits which were investigated by Venketaraman and Eser [10] were equally found to be amorphous with no graphitic plane alignment.

6.3 TGA-MS analysis of flask reactor diesel deposits

Thermogravimetric analysis was performed on stressed fuel. In the case of EN590 diesel and RME20, samples were taken from each of the top and bottom layers using a Pasteur pipette. An assessment of repeatability may be found in Appendix C.

6.3.1 Thermal analysis of unstressed and stressed diesel fuels in nitrogen

Below are thermograms of the four test fuels and their corresponding stressed versions. In the case of EN590 diesel and RME20, thermograms are provided for both stressed layers.

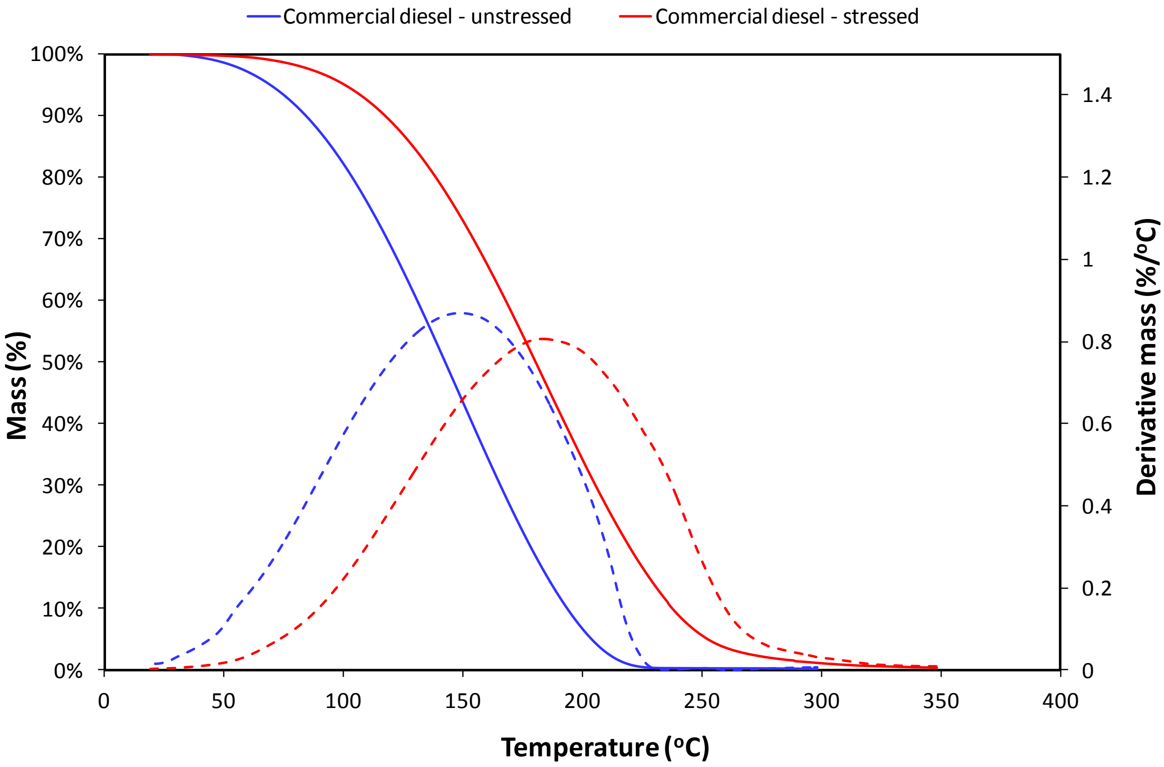

Figure 6.4: Thermograms of stressed (red) and unstressed (blue) commercial diesel. Experiments were conducted under nitrogen at a heating rate of 10°C/min. Solid lines – mass loss curves; dashed lines – derivatives

Figure 6.4 shows that the decomposition/evaporation temperature of stressed diesel has shifted to higher temperatures. The peak maximum has shifted by 34°C. This is likely due to the presence of higher molecular weight species which were formed during thermo-oxidative stressing of the fuel. Because of their higher molecular weight, such species will have higher boiling points. Alternatively such species could contain oxygen moieties which if hydrogen bonded would also have higher boiling points. It should be note that the extent of stressing (15h) was chosen to exaggerate the extent of deposition so that further analysis, *e.g.* ESI-MS, could be performed. Interestingly a shift was observed, despite very little deposit being observed in the QCM. A very small shoulder can be observed above 275°C in the DTG curve. The near Gaussian shape of the derivative suggests a Gaussian boiling point distribution.

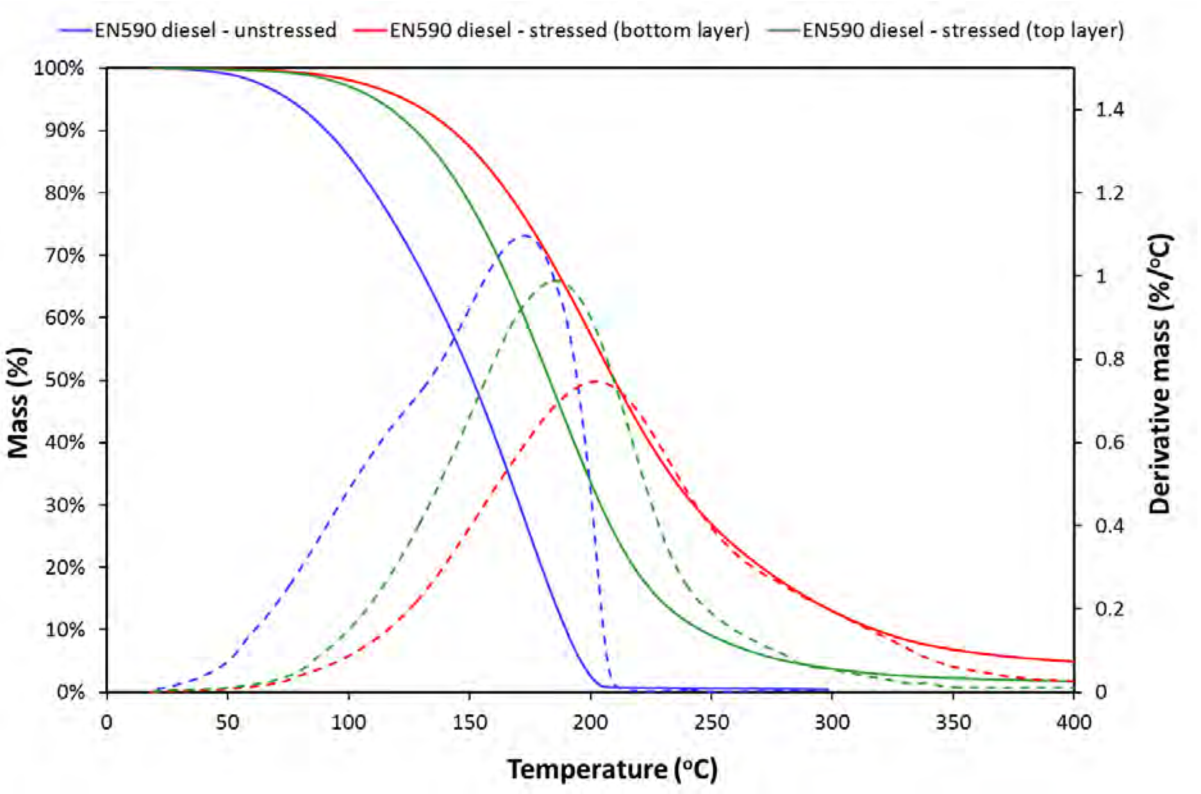

Figure 6.5: Thermograms of the two layers of stressed (red (bottom) and green (top)) and unstressed (blue) EN590 diesel. Experiments were conducted under nitrogen at a heating rate of 10°C/min. Solid lines – mass loss curves; dashed lines – derivatives

Figure 6.5 presents thermograms of stressed and unstressed E590 diesel. It is apparent that, as with the commercial diesel, stressed and unstressed EN590 diesels have different volatilities; with stressed EN590 diesel displaying lower volatility (shifting of thermogram to the right). Furthermore the shift is greater for the bottom layer (peak shift of 29°C for the bottom layer and 12°C for the top layer). This suggests that the bottom layer contained higher molecular weight species which had precipitated from the bulk fuel. This is consistent with the darker colour of this layer. Furthermore this layer has a much longer tail than the top layer. No tail can be seen in the neat EN590 diesel which has a sharp end point. Note that the neat EN590 diesel was blended from three petroleum streams which explains the non-Gaussian nature of the derivative curve.

The top layer had a residue of 0.1% at 600°C but the residue for the bottom layer was a noticeable 0.9% . This may be the result of the presence of carbonaceous materials but may also be the result of charring that occurs when these high molecular weight species are pyrolysed under nitrogen. Not only is there a shift in the peak maximum of the derivative for top and bottom layers but a shoulder can be seen to develop at higher temperatures.

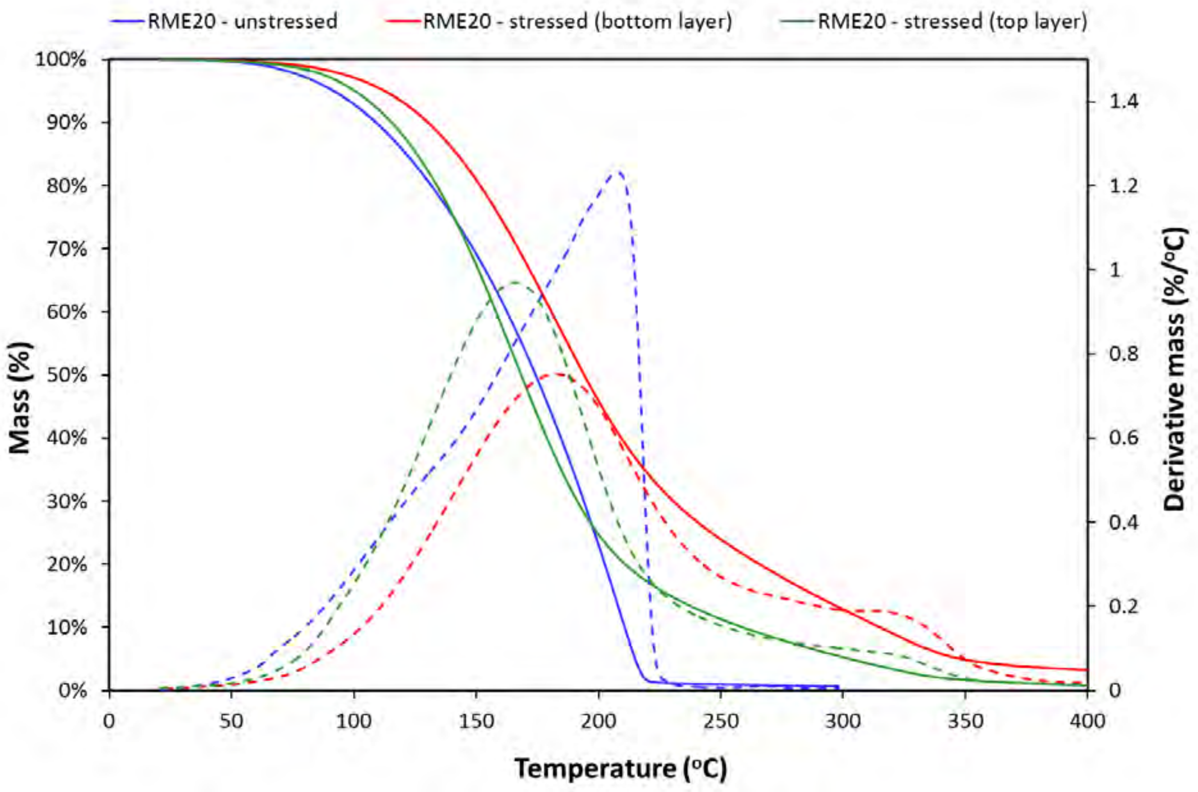

Figure 6.6: Thermograms of the two layers of stressed (red (bottom) and blue (top)) and unstressed (green) RME20, compared with unstressed RME20. Experiments were conducted under nitrogen at a heating rate of 10°C/min

Figure 6.6 clearly indicates that stressed and unstressed RME20 have very different thermal behaviour under an inert atmosphere. A number of interesting features can be seen. Firstly the maximum in the derivative peak for RME20 has shifted to 210°C. RME20 if a 4:1 EN590 diesel:RME blend. RME is less volatile than EN590 which explain the shift. In both the top and bottom layer a larger shoulder from 225-350°C can be observed. This shoulder can be seen to form, but not to the same extent, when the neat RME20 is heated. It is ascribed to pyrolysis reactions [99]. Such a shoulder in the heating of FAME has been noted by other authors [84, 100].

The size of this shoulder is greater for the bottom layer and for both is greater than the shoulder that develops in EN590 diesel when stressed. It is suggested that the bulk of the compounds that are volatile at the temperatures, associated with the shoulder, are FAME-derived. Interestingly the maximum in the derivative actually drops. Furthermore if one looks closely at the top layer one sees that the early part of the mass loss curve is very similar to the neat fuel. These two results would suggest that in combination with EN590 diesel, it is the FAME components that are more likely to be oxidised.

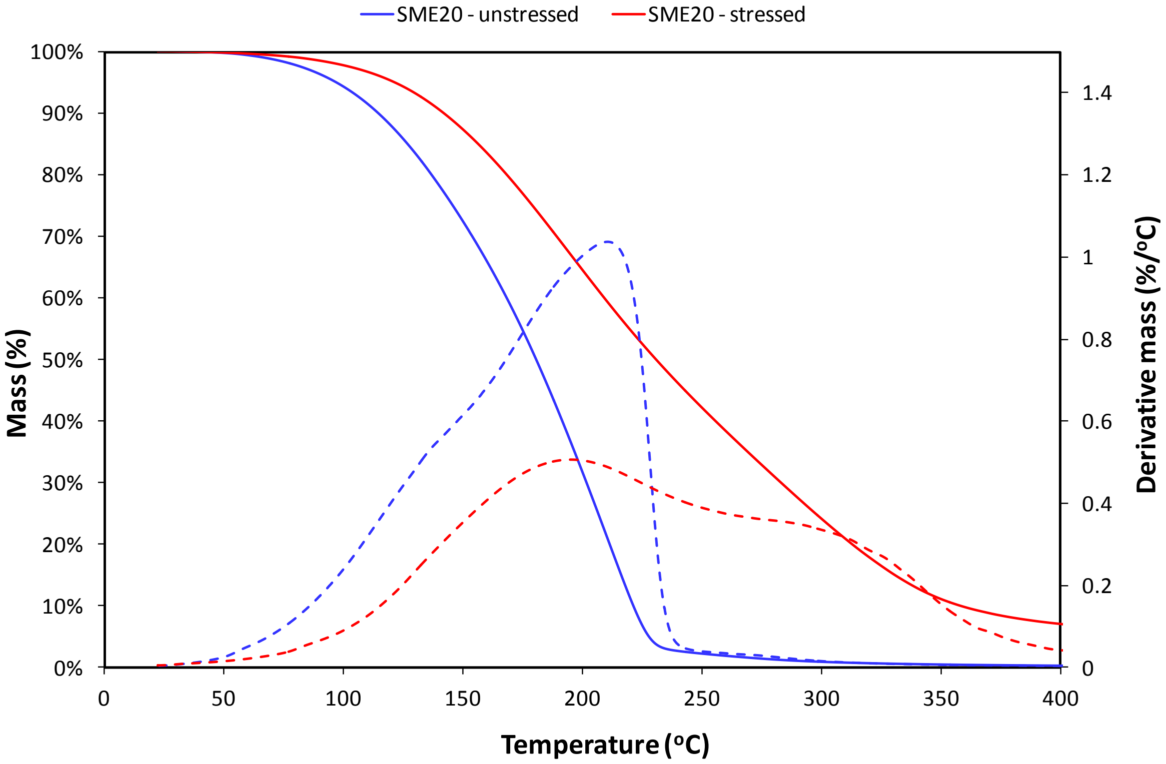

Figure 6.7: Thermograms of unstressed (green) and stressed (red) SME20. Experiments were conducted under nitrogen at a heating rate of 10°C/min

According to Figure 6.7, stressed SME20 has similar features to the bottom layer of RME20. However, these features were more pronounced, *i.e.* the size of the shoulder was larger. A 4% residue remained at 600°C. The mass remaining at the onset of the shoulder was approximately 40% which would suggest that at least part of the stressed compounds is EN590 diesel derived. Nonetheless, if one looks at the neat fuel one sees that even in nitrogen some degradation takes place.

If one compares this neat fuel to the previous neat fuels one sees that the mass does not immediately reach zero after the bulk of the fuel has evaporated. The shoulder that forms on heating the SME20 is larger than that that forms when RME20 was heated. Focke *et al.* performed similar studies on neat sunflower, soybean and canola FAME and found the residual mass to be in the order sunflower > soybean > canola [84]. Since canola is edible rapeseed, this result is consistent with what was seen in this study. The extent of pyrolysis increases with increasing unsaturation. SME has a much higher degree of unsaturation and importantly *bis*-allylic structures. These are capable of cross-linking and are the likely pre-cursors of higher molecular weight species, formed on heating.

6.3.2 Oxidative TGA of stressed fuels

In the figures that follow, the peaks in the DTG thermograms indicate the temperature at which the most rapid volatilisation of the samples occurred which can be attributed to elementary processes such as combustion, sublimation or simply desorption [68].

The mass spectrometer used in this study detects fluctuations in vapour pressures emanating from the TGA. In this study the evolved gases that were of interest were the combustion products, H_2O and CO_2. This would permit comparison with the work of Venketaraman and Eser [10]. Note that TGA-MS analysis was conducted on the test fuels and the CO_2 profiles as well as H_2O profiles highlighted no peaks or significant deviations from the curves baselines.

This was helpful as it indicated that any combustion process resulting from stressed fuels could be attributed to combustion of fuel deposits and not the actual fuel. Inspection of the figures that follow reveals that the initial mass loss for each fuel is not associated with CO_2 evolution which is indicative of evaporation. A similar absence of CO_2 evolution was noted when neat fuels were heated. None of the unstressed fuels had reached their auto-ignition temperature before they had fully evaporated.

Figure 6.8 displays the oxidative mass loss when stressed commercial diesel was heated in air. The mass loss curve is very similar to that when stressed commercial diesel was heated in nitrogen. The bulk of the mass loss is associated with fuel evaporation. Only near 300°C when there is a small residue remaining (associated with a small shoulder in the DTG curve), do we see a slight increase in the CO_2 pressure which is associated with the burning of this last residue.

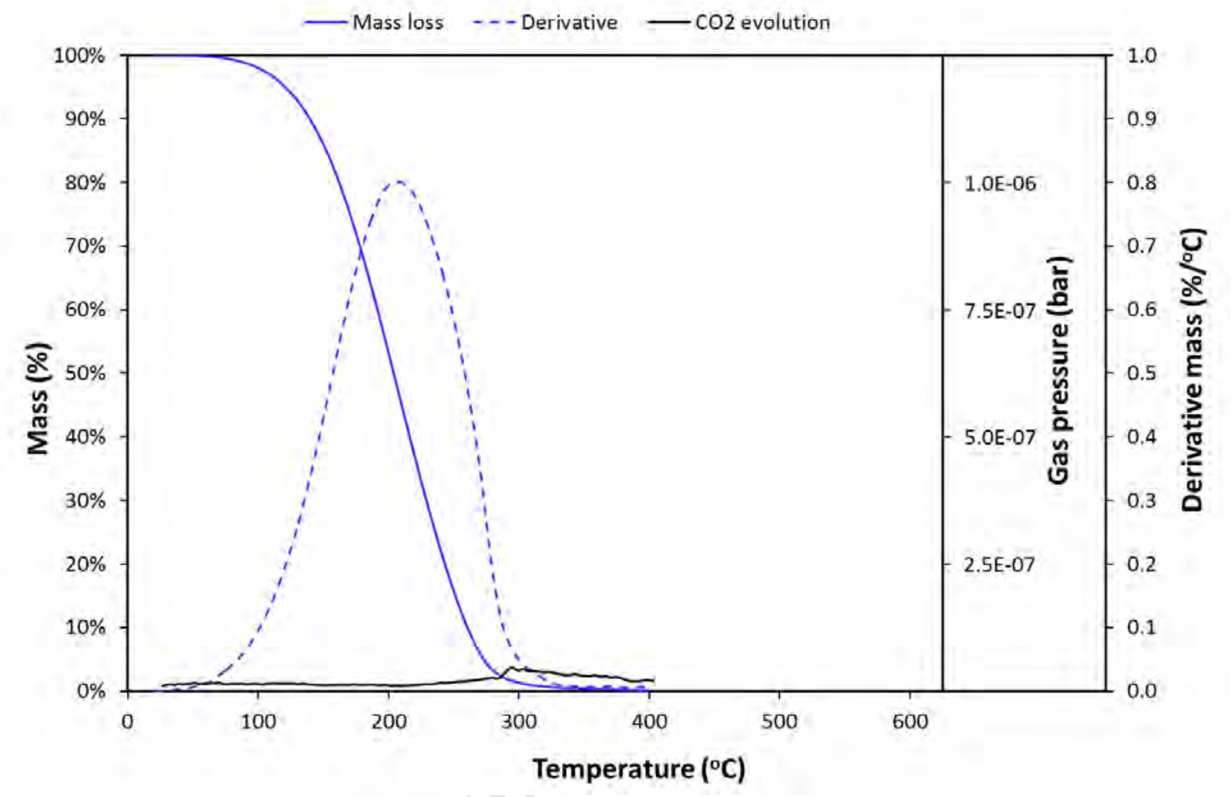

Figure 6.8: Mass loss, DTG and CO_2 evolution curves of stressed commercial diesel. Experiments were conducted under air at a heating rate of 10^oC/min

Figure 6.9 presents the evaporation and combustion of stressed EN590 diesel in air. Many of the features, such as the shoulder, that were noted for the TGA curve in nitrogen are still present. The large spike in CO_2 may be rapid combustion of occluded fuel within a deposit. Although at a somewhat higher temperature, Venkateraman and Eser observed two spikes in the CO_2 profile of high temperature fuel deposits which they attributed to the oxidation of capsules of volatiles trapped within the layers of ordered PAHs [10].The initial H_2O level is higher because of water in the synthetic air. The first CO_2 is associated with the combustion of the first deposit-like material. It coincides with the shoulder in the DTG curve. The peak in the DTG curve near 200^oC is likely evaporation since at this temperature the diesel should be below its auto-ignition temperature.

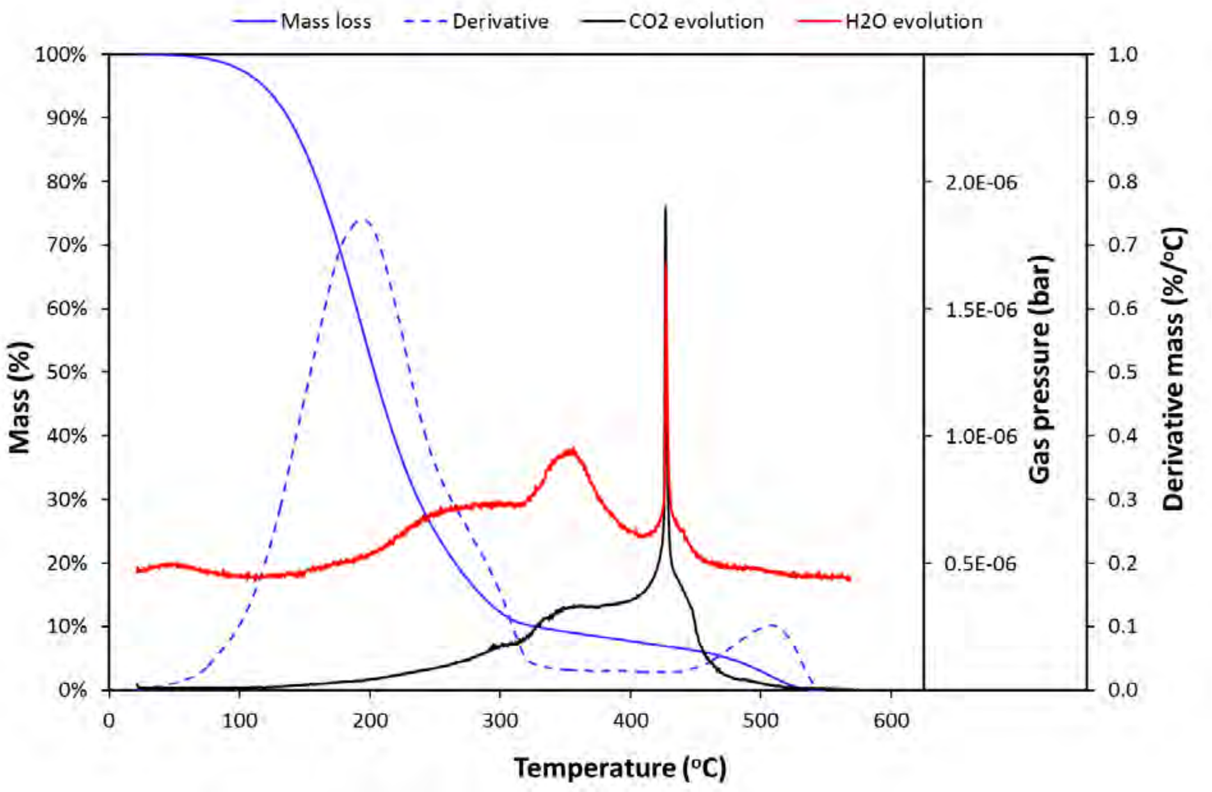

Figure 6.9: Mass loss, DTG and CO_2 evolution curves of stressed EN590 diesel (lower layer). Experiments were conducted under air at a heating rate of 10^oC/min

Figure 6.10 is similar to Figure 6.9. The rapid combustion event should again be noted. Again the CO_2 curve has two peaks and a shoulder near 300°C . What should be noted is that as the temperature rises the ratio of H_2O to CO_2 drops indicating that the deposit becomes more carbonaceous in nature. This is especially apparent if one compares the ratio of (H_2O less its base line) to ($CO_{2)}$ less its baseline) of the two sharp peaks of the gas evolution curves.

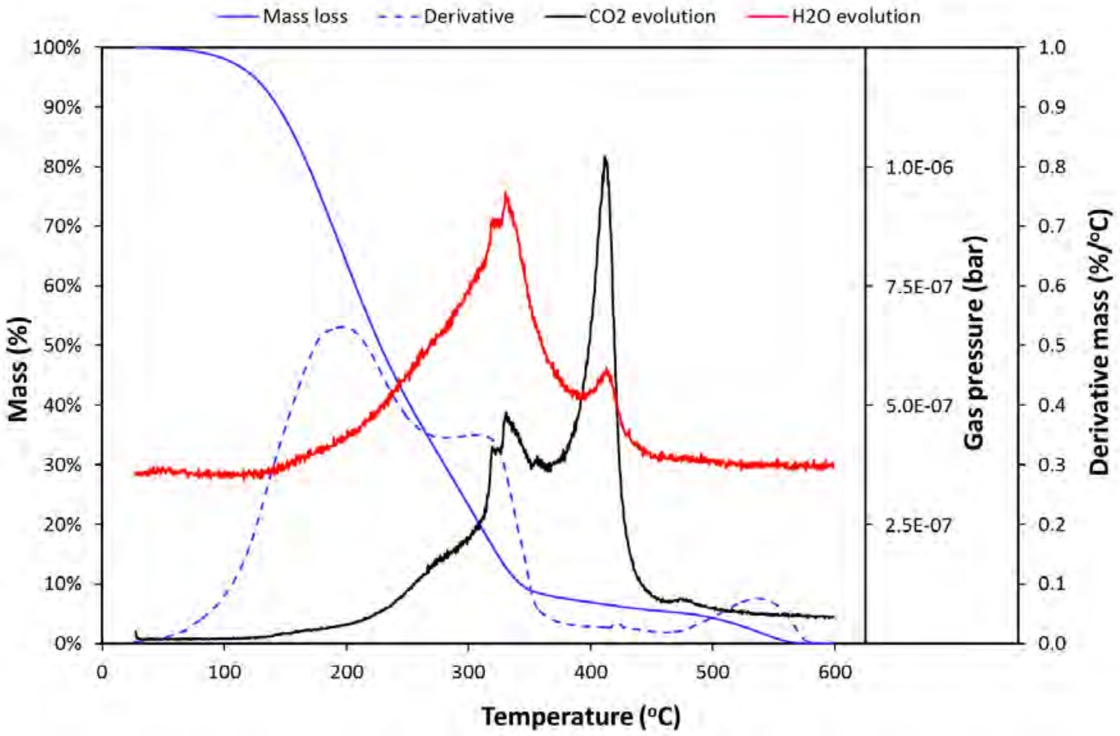

Figure 6.10: Mass loss, DTG and CO_2 evolution curves of stressed RME20 diesel (lower layer). Experiments were conducted under air at a heating rate of 10^oC/min

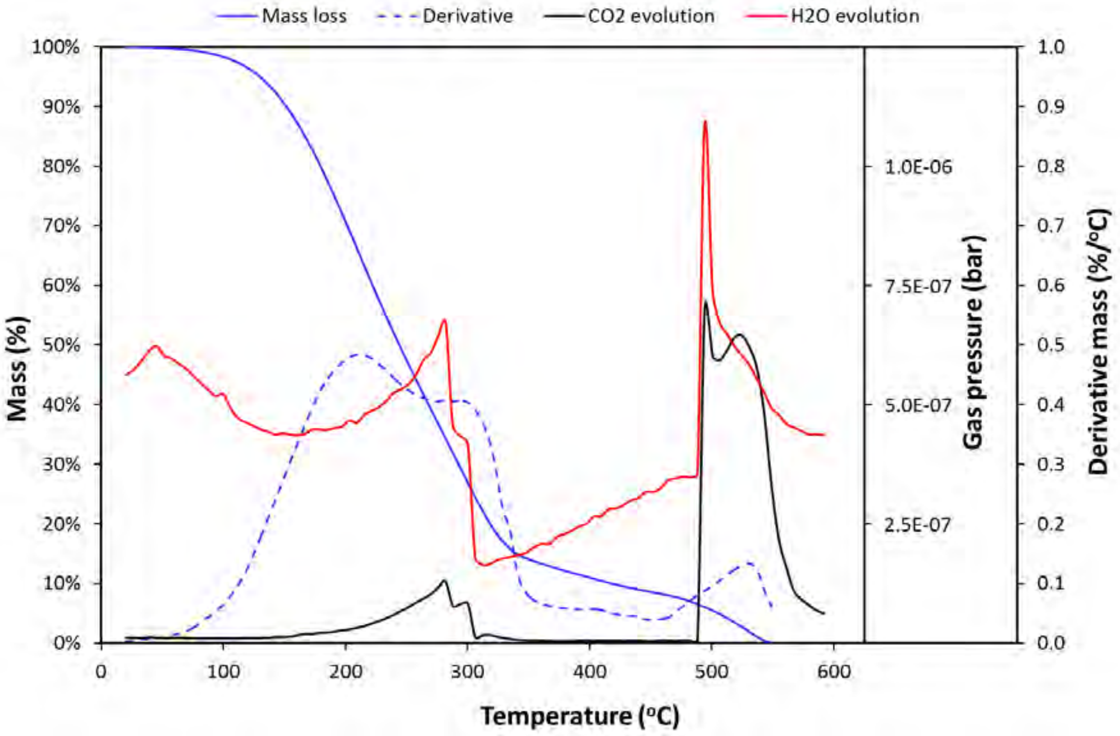

Figure 6.11: Mass loss, DTG and CO_2 evolution curves of stressed RME20 diesel (lower layer). Experiments were conducted under air at a heating rate of 10^oC/min

Unfortunately a catastrophic failure of the MS prevented meaningful mass spectrometric data being collected for the evaporation and oxidation of stressed SME20. Part-way through this final set of experiments the detector was observed to lose pressure. Unfortunately appropriate repairs could not be affected to allow the run to be repeated.

Nonetheless many similar features were observed in the mass loss curves. These can be identified in Figure 6.11. The size of the shoulder has increased compared to that of RME20 and EN590 diesel.

6.4 FTIR investigation of the fuels

Changes in the fuels were assessed by investigating FTIR spectra of the stressed fuels and comparing them to the neat fuels. Figure 6.12 provides a comparison of neat and stressed commercial diesel. What is apparent is the relative simplicity of the neat fuel spectrum. Upon oxidation, the presence of a new absorbance at 1680 cm^{-1} can be observed. These are associated with the formation of C=O groups (ketones and carboxylic acids) and the formation of conjugated double bonds [101].

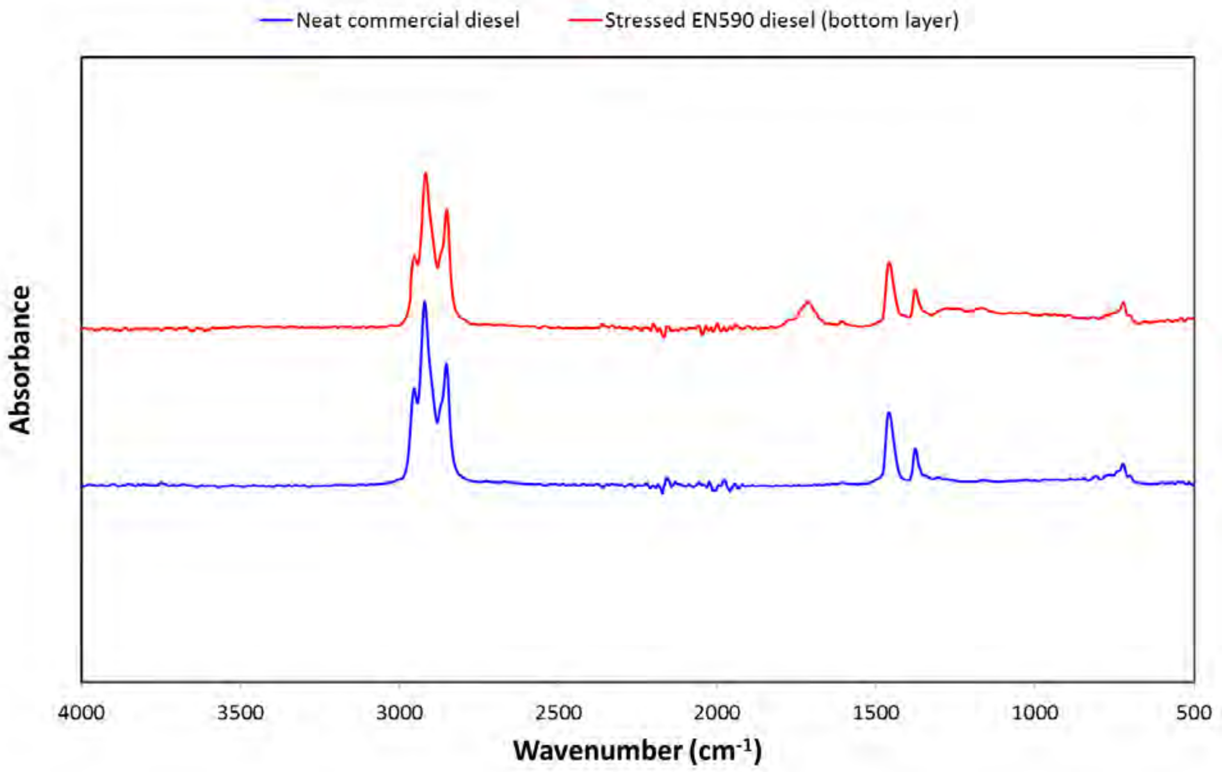

Figure 6.12: FTIR spectra of neat commercial diesel and stressed commercial diesel

There is also a slight shift in the baseline of the absorbance spectrum in the region 3500-3000 cm^{-1}. This would be associated with the formation of alcohols. Furthermore more complex bands appear in the region 1300-800 cm^{-1}.

In Figure 6.13 the formation of bands at 3500-3000, 1776, and 1705 cm^{-1} can be seen. These are characteristic of thermo-oxidative products. The band at 3500-3000 cm^{-1} is associated with the formation of OH groups [101]. The band at 1705 cm^{-1} is characteristic of carbonyl groups. Bands in the region 1400-1000 cm^{-1} which are likely due to C-OR (where R = C, O or H) bonds have also appeared. The size of these bands relative to the aliphatic bands is larger than with commercial diesel. The presence of alcohols, aldehydes and carboxylic acids have been demonstrated by ion chromatography after the stressing of methyl linoleate [59].

No distinct difference between the two layers, formed when EN590 diesel was stressed, could be seen. It can be seen by the fact that the band at 1590 cm^{-1} (due to C=C stretching in aromatic compounds is very weak that the aromatic compound of this diesel was low.

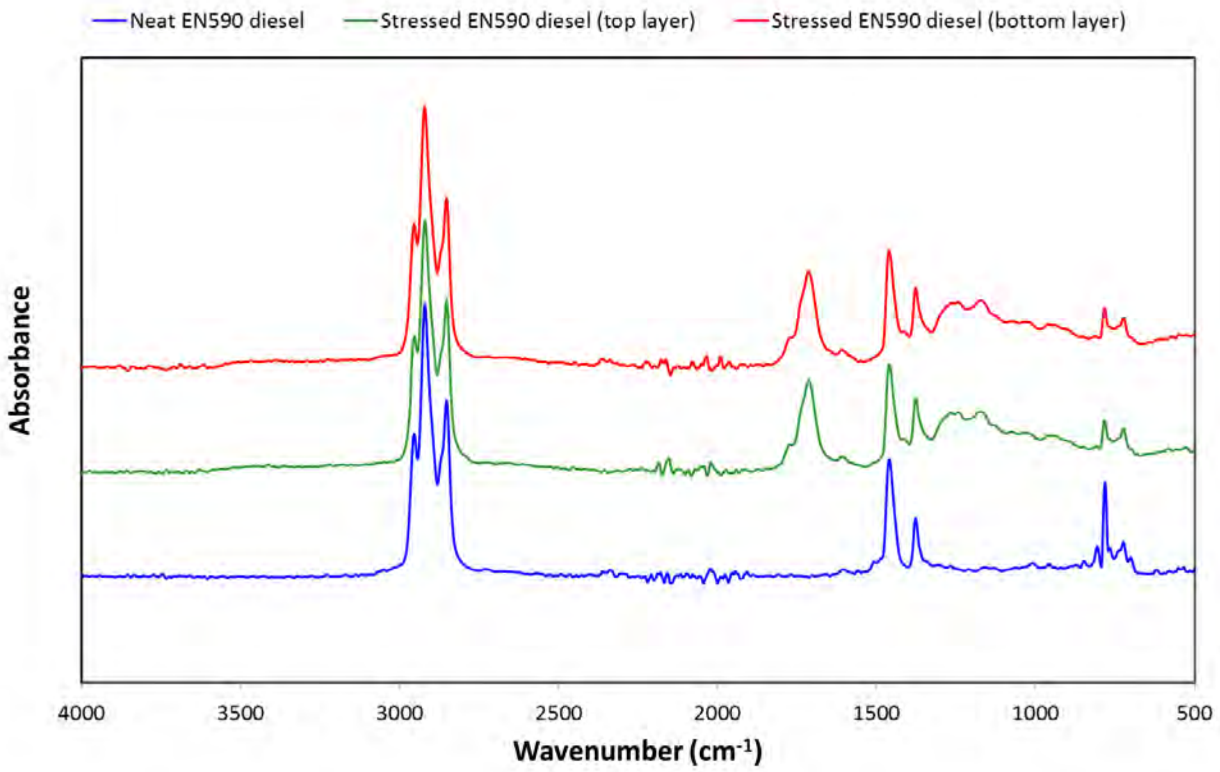

Figure 6.13: FTIR spectra of neat EN590 diesel and the two layers of stressed EN590 diesel

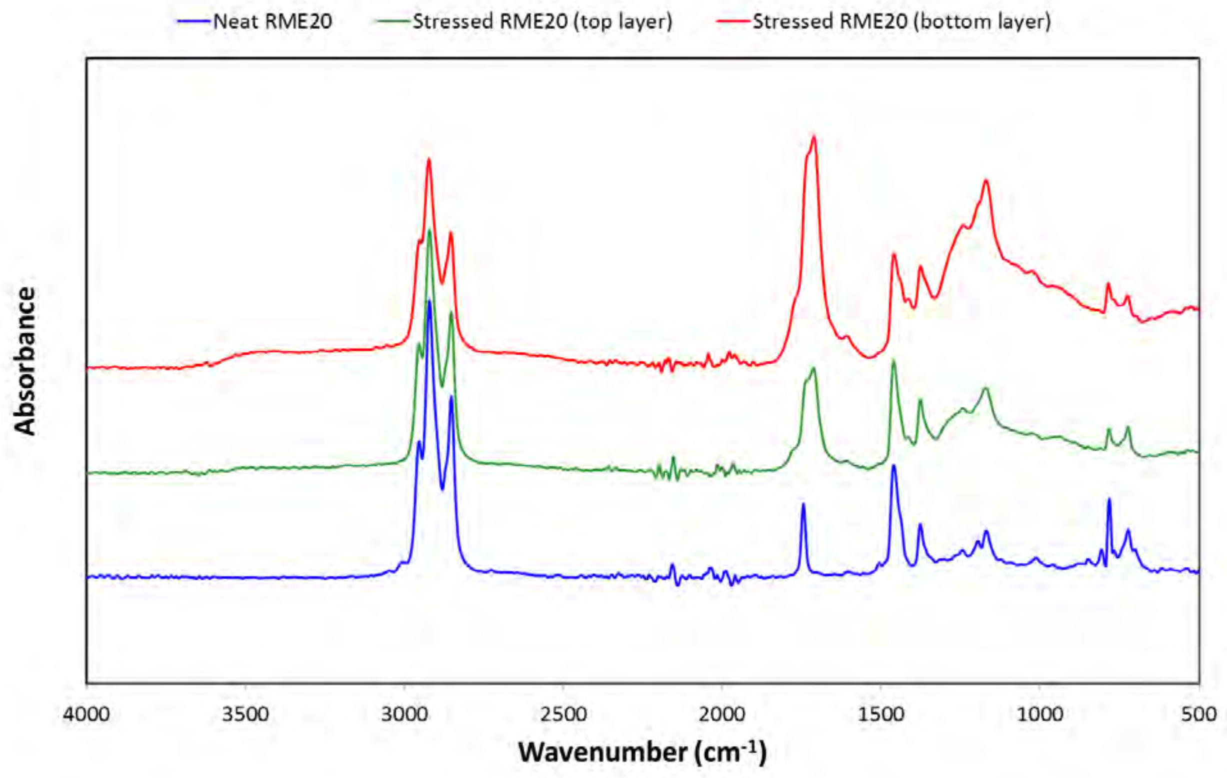

Figure 6.14: FTIR spectra of neat RME20 diesel and stressed RME20 (top and bottom layers)

Again the growth of bands due to OH (3500-3000 cm^{-1}, C=O (1775 cm^{-1} (seen as a shoulder) and 1708 cm^{-1}) and C-OR (1400-cm^{-1}) can clearly be seen. Furthermore the extent of this growth is greatest for the lower layer which is consistent with this layer being stressed to a greater extent. Note that the C=O (at 1747 cm^{-1}) and C-OR stretches are present in the original fuel because these groups are present in fatty acid methyl esters. Conjugated dienes, acids and alcohols are not, hence their absence from the spectrum for the neat fuel. It can be seen that the extent of stressing in the lower layer is greater than the top layer, evidenced by the greater size of the new peaks.

Figure 6.15 indicates the presence of similar groups in stressed SME20. Interestingly the size of these bands is similar to the lower layer of the RME20, suggesting a similar nature.

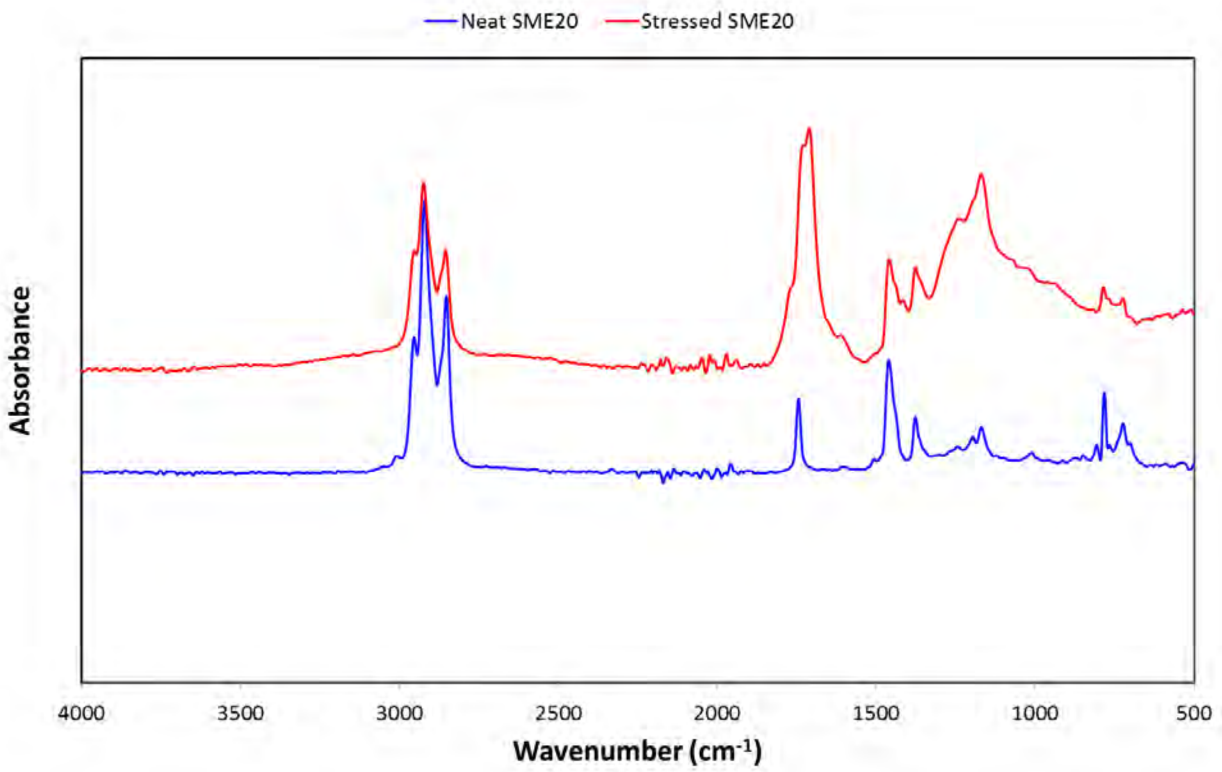

Figure 6.15: FTIR spectra of neat SME20 diesel and stressed SME20

6.5 ESI-MS evaluation of soluble precursor deposits

The methanol extract of thermally stressed diesel fuels in air-saturated conditions was isolated to enable positive ESI-MS investigation. Methanol was shaken with the fuels to perform the extraction so that extraction could take place from both fuel layers where two layers existed. The reason for investigating the polar component of thermally stressed fuels was to analyse the evolution (pre and post stress) of high molecular weight polar species and to identify possible deposit precursors and their molecular weight distribution. ESI (+) MS results of the methanol fractions for all diesel samples are presented in the following section with digital images of the methanol extracts (pre and post-stress) in appendix C.

6.5.1 Unstressed commercial diesel

Unstressed commercial diesel ESI (+) MS spectrum, indicated by Figure 6.16, is akin to unstressed EN590 diesel (Figure 6.18) but has a relatively greater distribution of species in the m/z 450-1000 range.

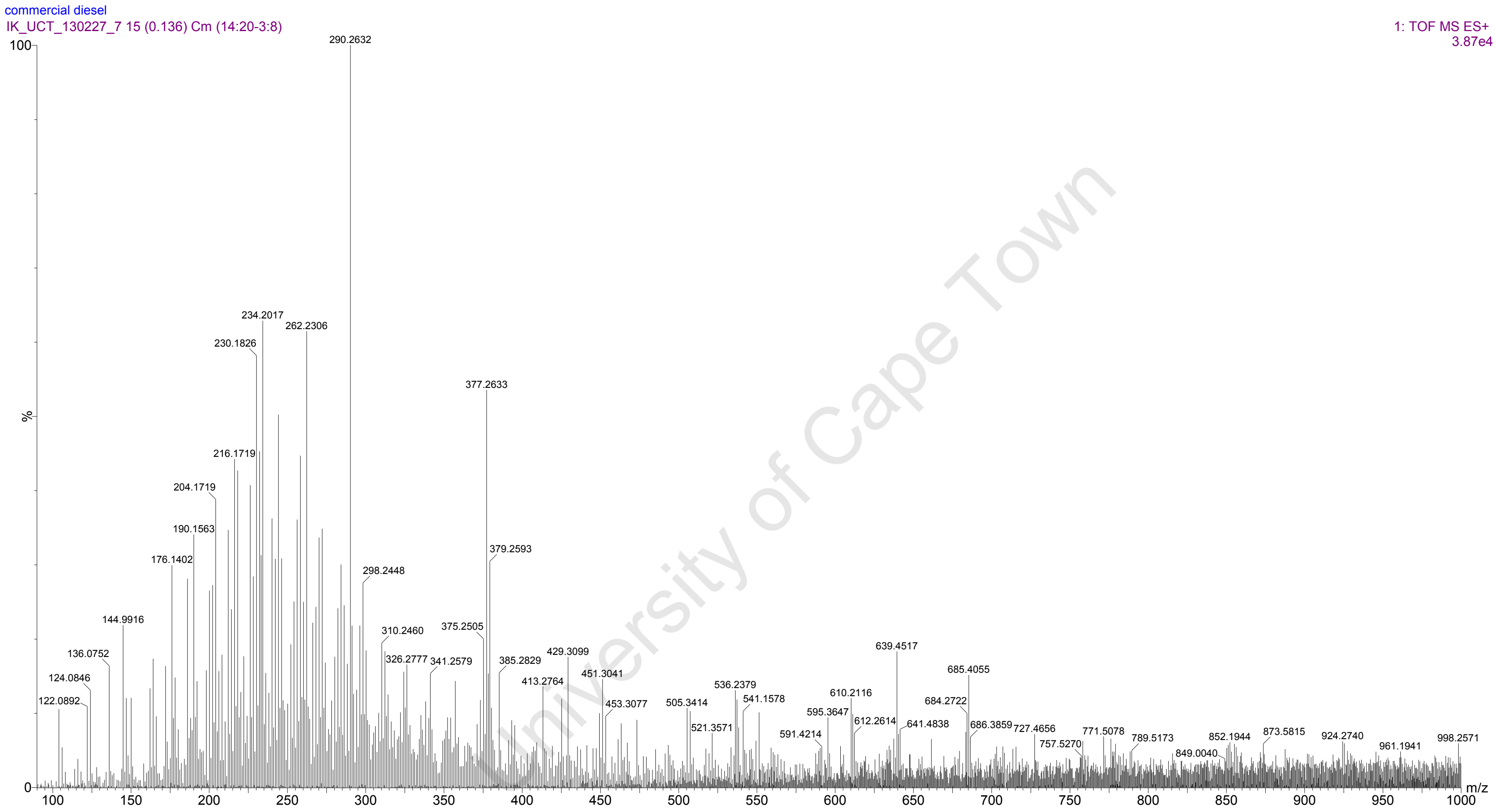

Figure 6.16: ESI (+) MS in the m/z 100-1000 for the methanol fraction of unstressed commercial diesel

Table 6.1: Possible homologous series in pre-stress commercial diesel

Homologous series (-CH_2-)						
A	B	C	D	E	F	G
144	122	162	268	166	202	206
160	136	176	282	180	216	220
172	150	190	296	194	230	234
186	164	204	310	208	244	248
200	178	218	324	222	258	262
214		232	338	236	272	276
228		246	352	250	286	290
242		260		264	300	
256		274		278	314	
270		288		292	328	
284		302		306	342	
298		316		320		
312		330				
326						
340						

The majority of species are concentrated in the m/z <300 range. The peaks at 290, 377 and likely 639 are associated with polar additives. The commercial diesel spectrum shows considerably more $[M + H]^+$ ions in ESI-MS spectra than EN590 diesel. This is because this is a real additised fuel rather than a blend of middle distillate solvents. Two homologous series analogous to the ones Commodo *et al.* [74] found in ESI (+) MS spectra of unstressed Jet A-1 are identified and correspond to A and B in Table 6.1

6.5.2 Stressed commercial diesel

Comparison of unstressed (Figure 6.16) and stressed (Figure 6.17) ESI (+) MS spectra of commercial diesel reveals that stressed commercial diesel, as expected, has a higher concentration of high molecular mass polar compounds. The number of species within the m/z 550-1000 range is greater than EN590 diesel. Nonetheless, the main peaks in stressed commercial diesel are still below m/z 550. Even numbered homologous series in unstressed commercial diesel are replaced by odd numbered homologous series in stressed commercial diesel

.

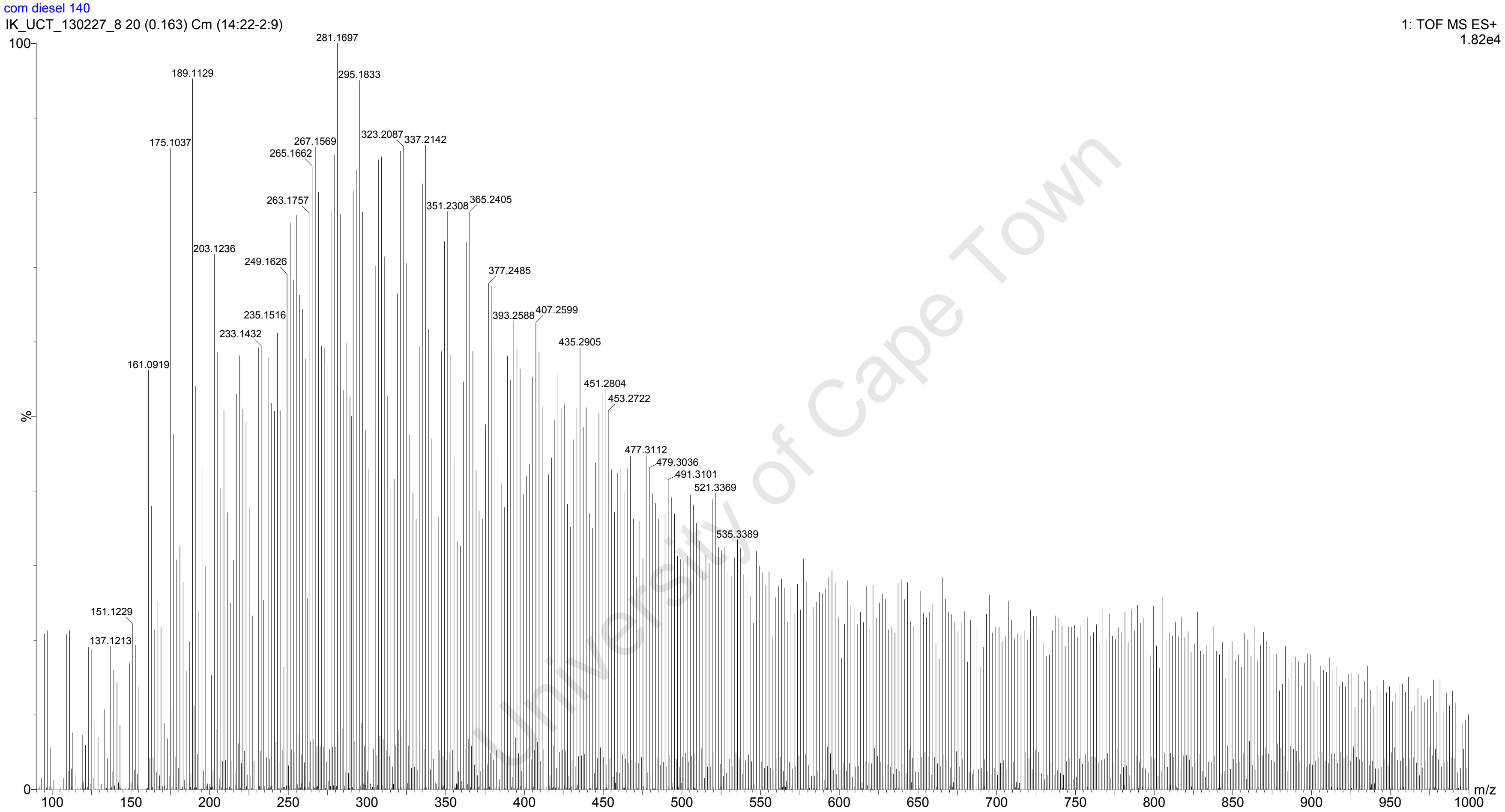

Figure 6.17: ESI (+) MS in the m/z 100-1000 of the methanol fraction of stressed commercial diesel

The decrease in the species at 290 vs that at 377 amu, suggests it may be an anti-oxidant.

Table 6.2: Possible homologous series in post-stress commercial diesel

Homologous series ($-CH_2-$)				
V	W	X	Y	Z
235	237	243	213	219
249	251	257	245	233
263	265	271	259	247
277	279	285	287	261
291	293	299	301	275
305	307	313	315	289
319	321	327	329	303
333	335	341	343	317
347	349	355	357	331
361	363	369	371	345
375	377	383	385	359
389	391	397	399	373
403	405	411	413	387
				401
				415

Series X is likely associated with paraffinic alcohols ($C_nH_{2n-1}OH$). Alternatively it may arise from the addition of a keto-group to series A in the original fuel. The addition of an alcohol will cause a shift in the homologous series for the neat fuels by 17 amu (16 for O + 1 for H^+). Keto groups cause a shift of 15 amu (16 for O, -2 for H abstracted, +1 for H^+). Because di-alcohols and keto-alcohols can form one rapidly obtains a host of new species. Such dimer diols and diketones were observed in field ionisation mass spectrometry performed on stressed jet fuel [63]. The reason it appears as an odd-numbered sequence is that the species are protonated. Careful inspection reveals two peaks in the series (observed as a darkening in the spectrum in Figure 6.17. These are indicative of cross-linking reactions and likely indicate oxygenated dimers and trimers.

The effect is that the peak in the ESI-MS spectra moves to higher M_w, *i.e* from 234 (additive at 290 is ignored) to 281. This is a shift of 47, which would be the result of 2 alcohol groups and one ketone group to the molecules (+47 = 3 x 16 (O) – 2 (H abstraction) + 1 (H^+)). It can thus be seen that significant levels of oxygen have been incorporated. Ogawa *et al.* [59] reported a range of polyoxygenated species in their studies on FAME model compounds.

6.5.3 Unstressed EN590 diesel

Below is the ESI (+) MS spectrum (Figure 6.18) of the methanol fraction of unstressed EN590 diesel.

Table 6.3 illustrates possible homologous series emanating from the spectrum.

Table 6.3: Possible homologous series (identified by 14 m/z ($-CH_2-$) increments) in unstressed EN590 diesel

Homologous series ($-CH_2-$)							
A	B	C	D	E	F	G	H
335	263	351	275	397	489	431	234
349	277	365	289	411	503	445	248
363	291	379	303	425		459	262
377	305		317			473	276
	319						290
	333						
	347						

The very large response species could not be identified but are likely additives. The maximum possibly belongs in the homologous series which starts at m/z 234 and increases in alkyl groups ($-CH_2-$) until m/z 290, although it is more likely there are more than one species with m/z 290 present. Other possible but unidentified homologous series are listed from A-G. Species at m/z 144 and 158 were also found in [74]. These may correspond with methyl isoquinoline and ethyl isoquinoline respectively.

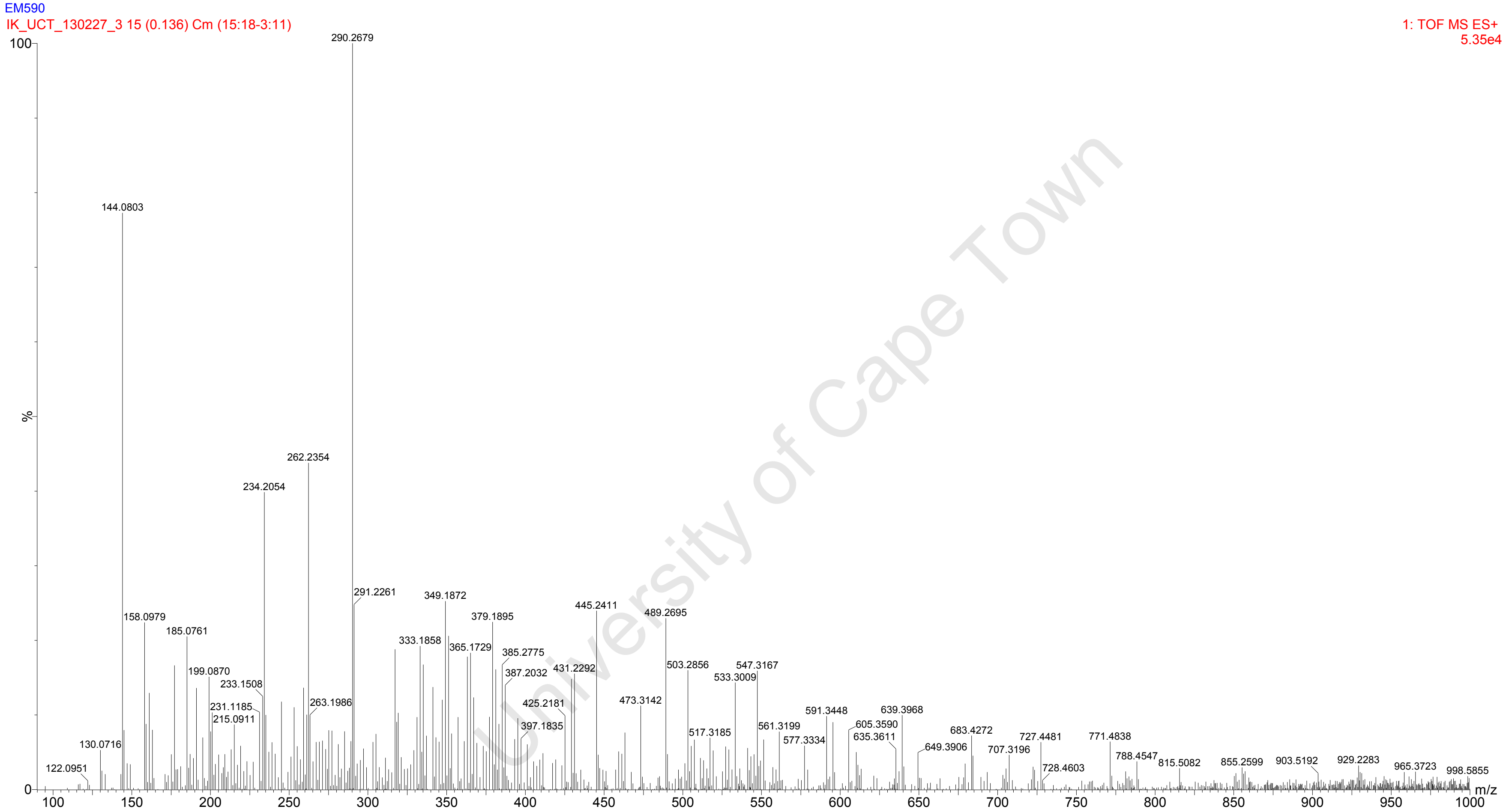

Figure 6.18: ESI (+) MS profile in the m/z 100-1000 of the methanol fraction of unstressed EN590 diesel.

6.5.4 Stressed EN590 diesel

Below is the ESI (+) MS spectrum (Figure 6.19) of the methanol fraction of stressed EN590 diesel while Table 6.4 illustrates possible homologous series emanating from the spectrum.

The ESI (+) MS spectrum of stressed EN590 diesel is fundamentally different to the unstressed EN590 diesel spectrum and to a greater degree than stressed JET-A1 [74] (Note that this was stressed for a shorter time period (2 h) but at a higher temperature (160^{o}C) in excess oxygen). Figure 6.19 shows that the stressed EN590 diesel produced an array of polar species in the m/z 100-1000 range

Table 6.4: Possible homologous series, by (identified by 14 m/z (-CH$_2$-) increments) increments, of post-stressed EN590

Homologous series (-CH$_2$-)									
V		W		X		Y		Z	
197	351	195	349	185	339	193	347	219	373
211	365	209	363	199	353	207	361	233	387
225	379	223	377	213	367	221	375	247	401
239	393	237	391	227	395	235	389	261	415
253	407	251	405	241	409	249	403	275	429
267	421	265	419	255	423	263	417	289	443
281	435	279	433	269	437	277	431	303	457
295	449	293	447	283	451	291	445	317	
309	463	307	461	297	465	305	459	331	
323	477	321	475	311	479	319	473	345	
337		335		325		333		359	

Table 6.3 and Table 6.4, one can see that a number of series (*e.g.* A and V) differ by 16 amu. This is consistent with the addition of one oxygen atom. Series W and Y are 2 and 4 mass units less than series V. This is consistent with the formation of alkenes and dienes which would occur with the elimination of peroxide groups, formed during oxidation. Again the presence of high molecular weight species suggests cross-linking.

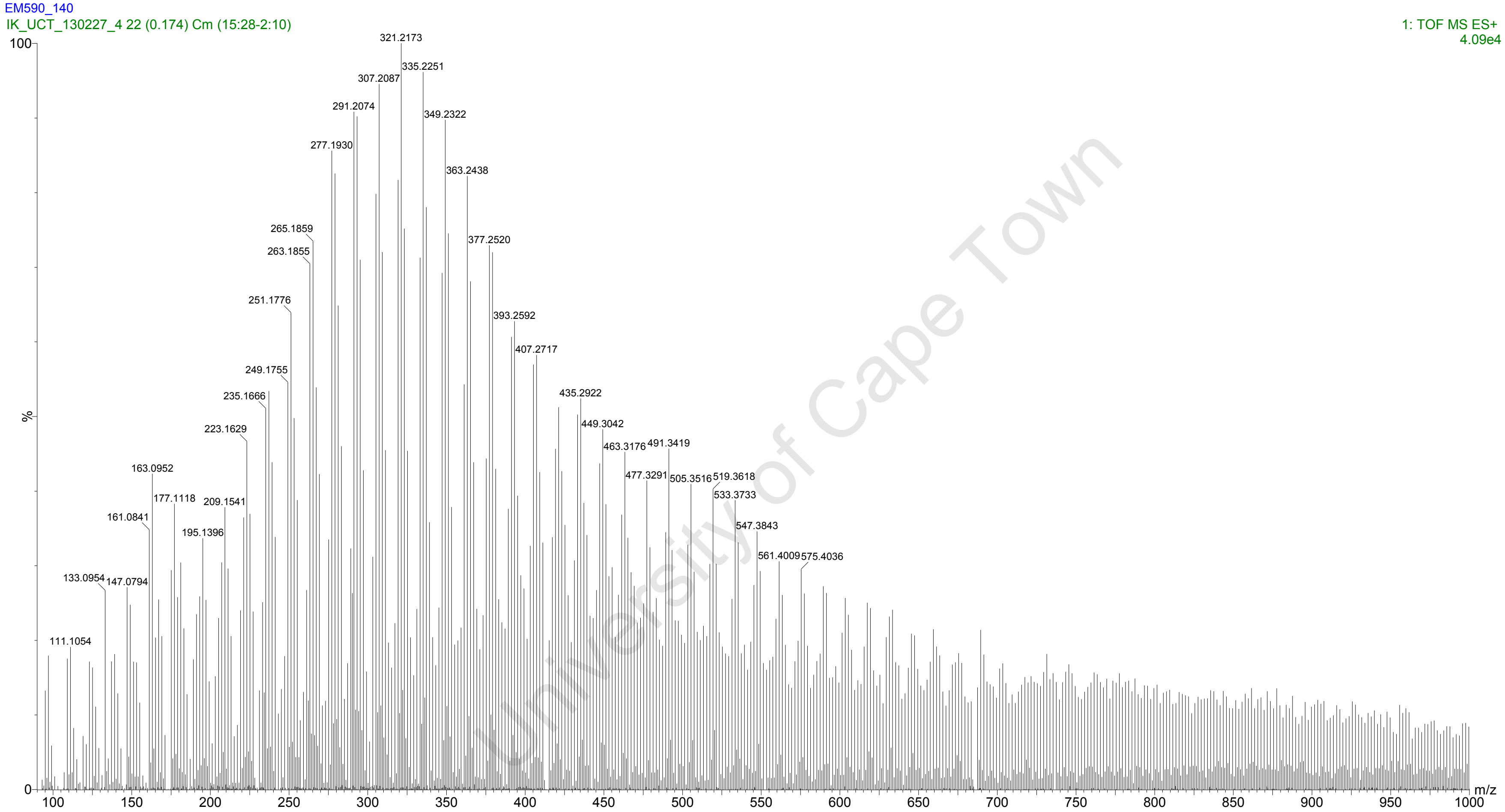

Figure 6.19: ESI (+) MS profile in the m/z 100-1000 for the methanol fraction of stressed EN590 diesel

The formation of dimers or trimers was difficult to identify due to the complexity of spectra. The peak maximum for EN590 diesel was higher than that for commercial diesel. This is consistent with commercial diesel being more volatile (see QCM total pressure data and TGA curves).

6.5.5 Unstressed RME20

The spectrum of RME20 is depicted by Figure 6.20 while Table 6.5 highlights possible homologous series that were found in the spectrum. In order to identify the peaks that are due to the biodiesel portion (RME) in the blend, ESI (+) MS was conducted on pure RME (B100) biodiesel. The B100 spectrum of RME highlights that the major peaks are at m/z 293 (methyl linoleneate), m/z 295 (methyl linoleate), m/z 297 (methyl oleate), m/z 309, 331, 341 and 379. The higher peaks are due to additives in the biodiesel. The peak at m/z 290 which was the dominant peak in the spectrum of EN590 diesel is also present in the spectrum RME20 but is very small in comparison to the largest peak in the RME20 spectrum which is given by the molecular ion $[M + H]^{n+}$ at m/z 379.

Table 6.5: Possible homologous series in unstressed RME20

Homologous series			
A	B	C	D
307	277	281	311
321	291	295	325
335	305	309	339
349	319	323	353
363	333	337	367
377	347	351	381
391	361	365	395
	375	379	409
		393	

This is likely the result of the ability of ESI (+) MS in characterising species that with different ionisation propensity. Although RME biodiesel made up only 20% of the RME20 blend, the polar species in its composition ionise better than the molecules in EN590 diesel.

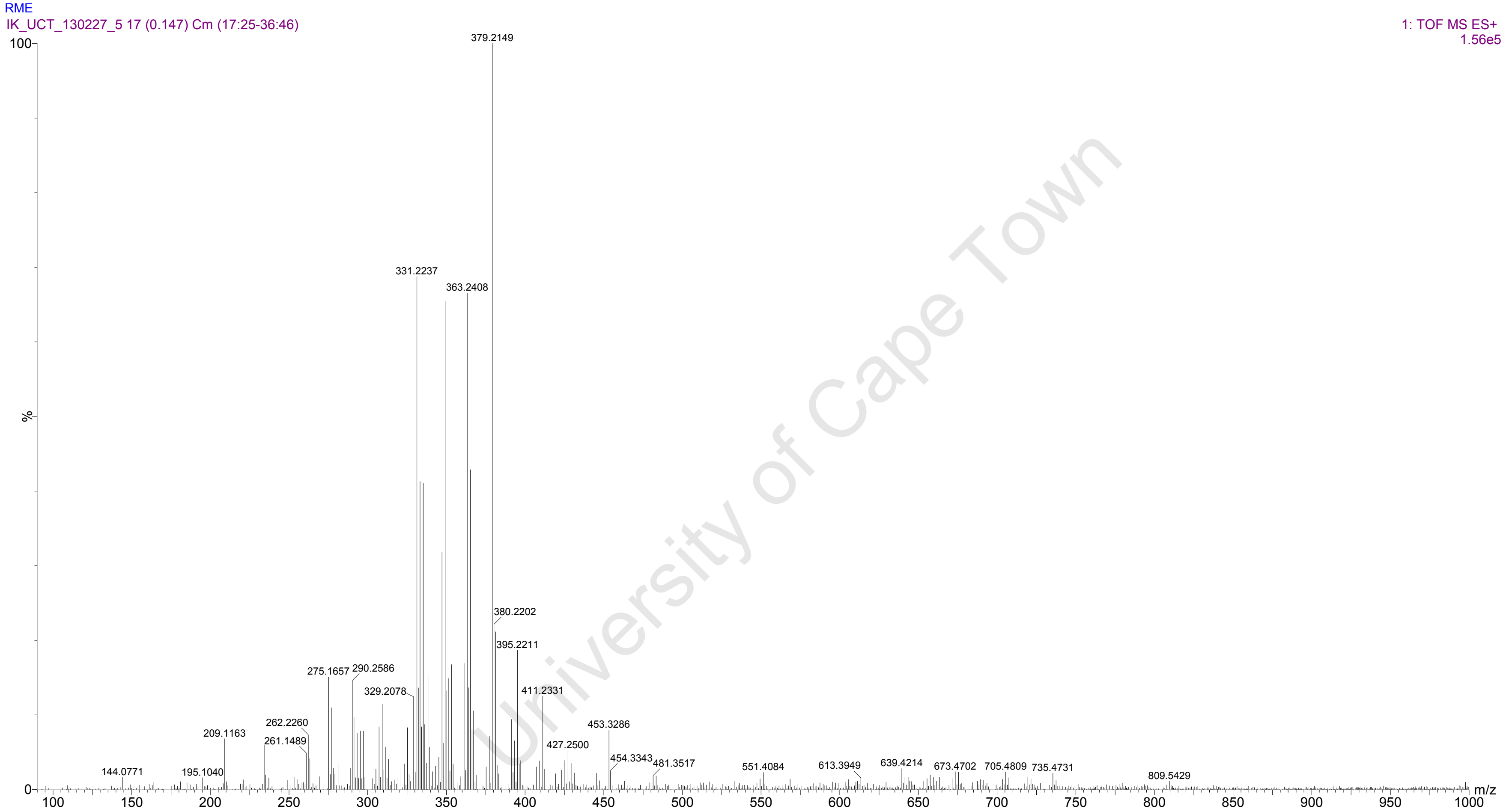

Figure 6.20: Expanded positive ESI-MS profile in the range m/z 100-1000 for unstressed RME20 methanol fraction

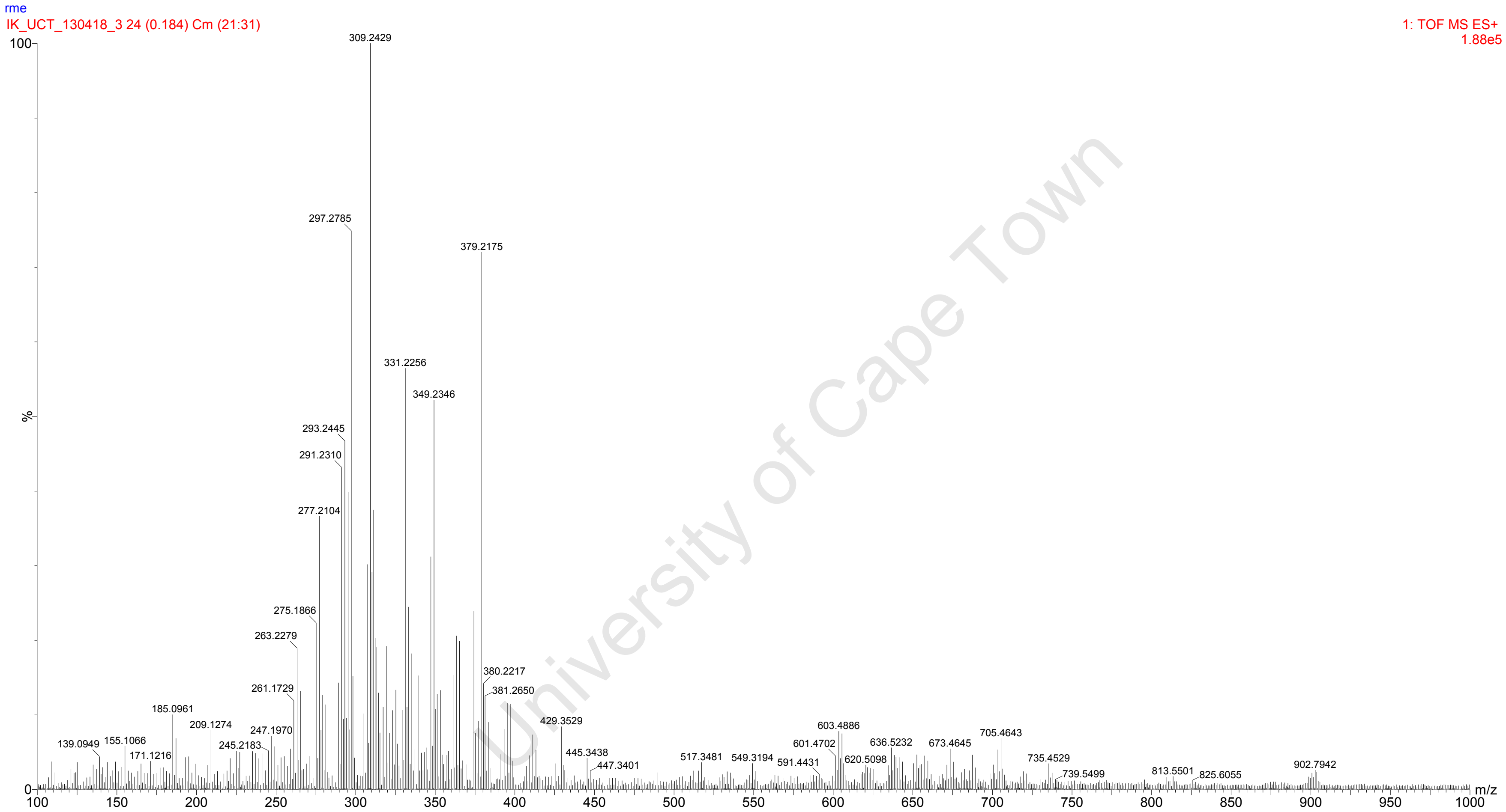

Figure 6.21: ESI (+) MS spectrum of unstressed neat RME in the range of m/z 100-1000

6.5.6 Stressed RME20

There appear to be fewer peaks in the spectrum of RME20 than in both stressed EN590 diesel and commercial diesel. This, however, is because the spectra are normalised to the most intense peak. The concentration of major peaks lay in the m/z 250-550. Possible homologous series are presented in Table 6.6.

Comparison of homologous series in stressed and unstressed reveals some matches: W with A, X with C and Z with D.

Table 6.6: Possible homologous series that were found in stressed RME20

Homologous series ($-CH_2-$)			
W	X	Y	Z
237	281	509	339
251	309	523	353
265	323	537	367
279	337	551	381
293	351	565	395
307	365	579	409
321	379	593	423
335	393	607	437
349	407	621	451
363	421	635	465
367	435		479
391	449		493
405	463		507
	477		521
	491		535
			549

What is apparent is a consistent repeating pattern at high molecular weight. It is suggested that these are the result of dimerization and trimerisation of the FAME esters.

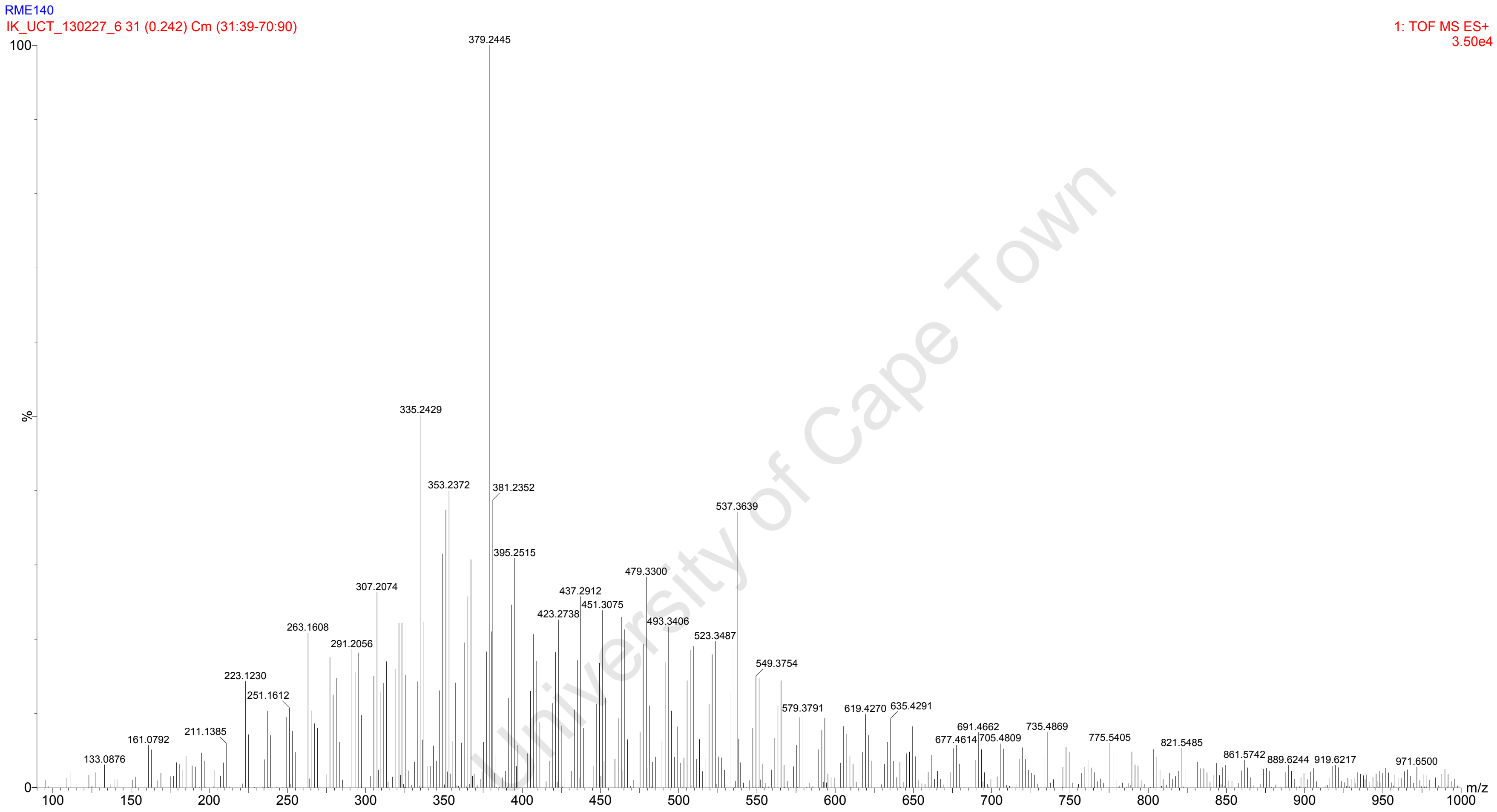

Figure 6.22: ESI (+) MS profile in the m/z 100-1000 for methanol fraction of stressed RME20

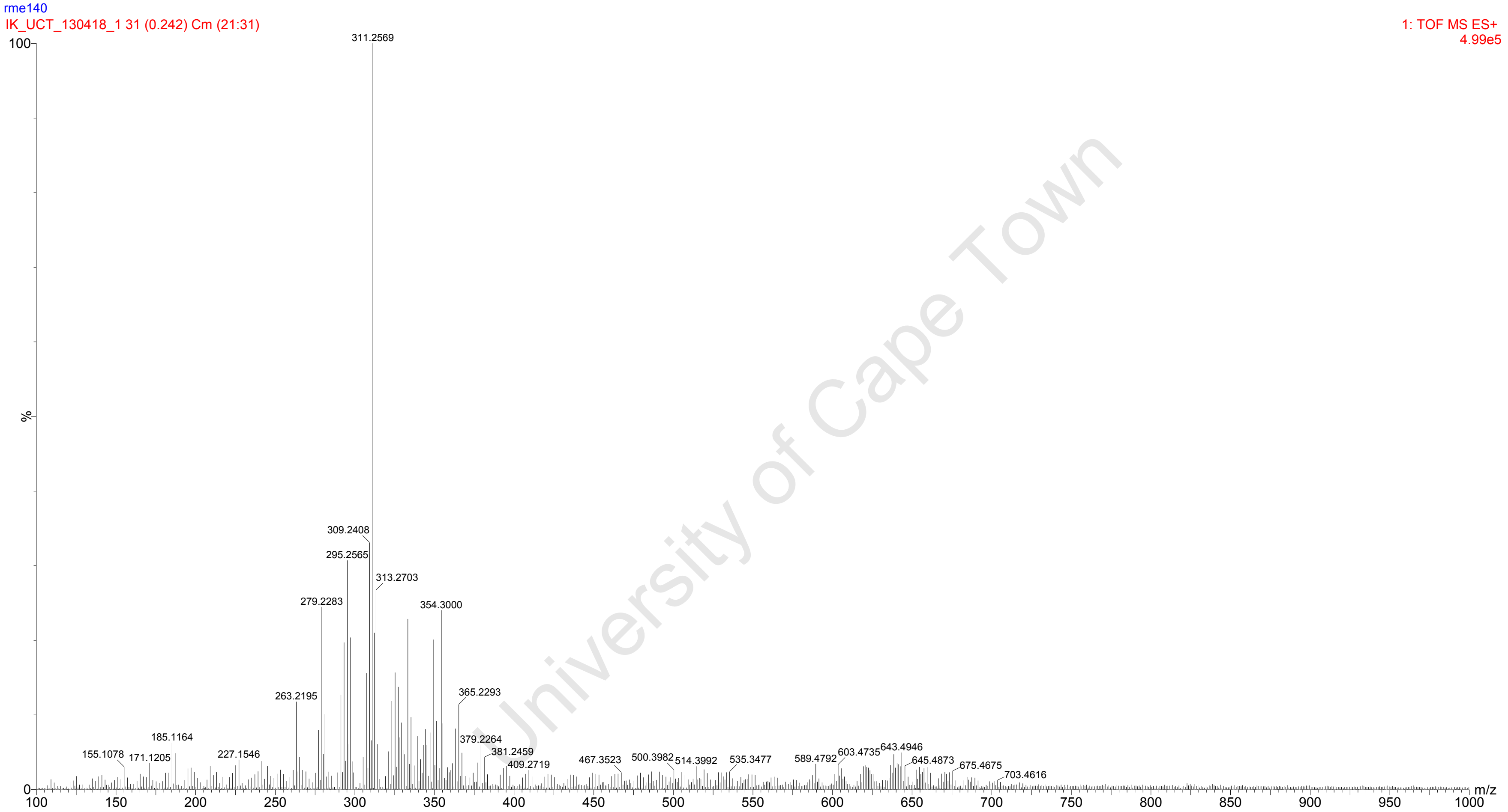

Figure 6.23: ESI (+) MS spectrum of stressed neat RME in the range of m/z 100-1000

The peak heights in the dimerisation region (600-650) are larger than those in the trimerisation region (900-975). This is to be expected since dimers need to be formed, prior to trimers being formed. Some can also be seen to be present in the neat RME. It should be noted that dimerisation involve a doubling of mass but will involve the inclusion of at least one oxygen (+16) and usually more, see Figure 2.9. Ogawa *et al.* report the average addition of three oxygen atoms on dimerisation (an ether crosslink and two ketones allylic to the crosslink) [59].

6.5.7 SME20 unstressed

In order to ascertain the contribution of SME polar species when blended with EN590 diesel, ESI (+) MS was conducted on pure SME. The main peaks in that spectrum are m/z 263, 291, 293 (methyl linolinate), 295 (highest intensity peak; likely to be methyl linoleate), 335, 349, 365 and 379. In the spectrum of SME20 the main peaks are represented at m/z 293, 295, 309, 331, 333, 335, 349, 351, 365 and 379. The peaks above 330 are associated with additives in the RME.

It is apparent that the largest peaks in the blend (Figure 6.24) correlate well with the main peaks in neat SME.

Possible homologous series that were identified in unstressed SME20 are shown in Table 6.7.

Table 6.7: Possible homologous series in unstressed SME20

Homologous series (-CH_2-)					
A	B	C	D	E	F
281	261	297	307	369	333
295	275	311	321	383	347
309	289	325	335	397	361
--	303	339	349	411	
351	317	353	363	425	
365	331	367	377		
375		381			
		395			
		409			

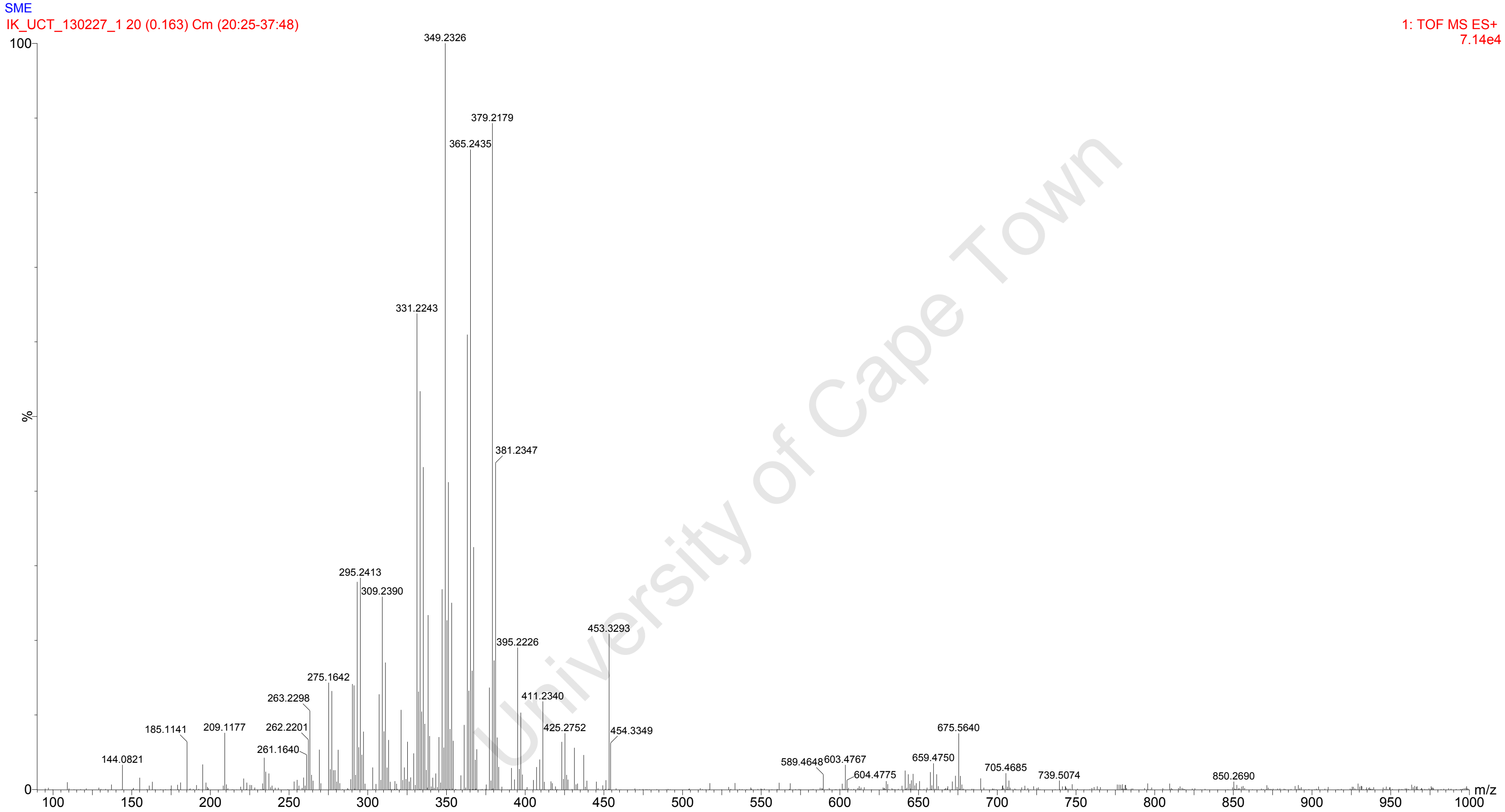

Figure 6.24: ESI (+) MS in the m/z 100-1000 for the methanol fraction of unstressed SME20.

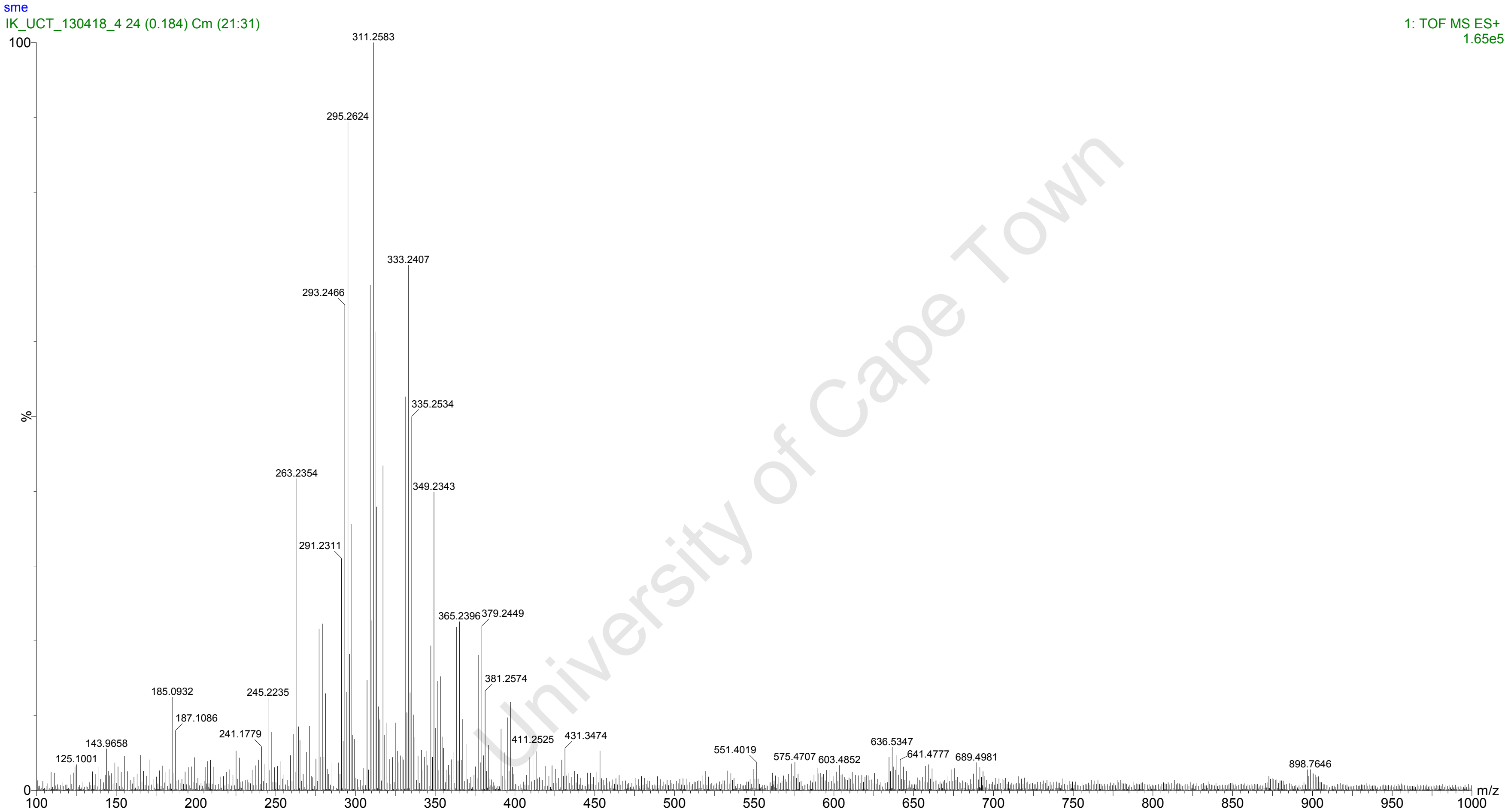

Figure 6.25: ESI (+) MS spectrum of unstressed neat SME in the range of m/z100-1000

6.5.8 SME20 stressed

The spectrum of stressed SME20 may be found in Figure 6.26. The stressed SME20 has a greater amount of polar species than unstressed SME 20. This is similar to RME20. The main peak in stressed SME20 is again m/z 379, which was also the main peak in stressed RME20. This is highly likely an additive. Possible homologous series in stressed SME20 are illustrated in Figure 6.27.

Possible matches of the homologous series are A with X, D with W and F with V. The concentration of polar species in stressed SME20 beyond m/z 500 is greater than what was witnessed in stressed RME20 relative to peak 379, suggesting greater oxidation of SME20. It can also be seen that the peaks between the repeating peaks are larger for SME20. This is not surprising since SME has a higher proportion of alkene and diene esters than RME. Dimerisation is clearly visible in the spectrum for stressed neat SME.

Table 6.8: Possible homologous series in unstressed SME20

Homologous series (CH_2)					
U	V	W	X	Y	Z:
255	249	265	239	439	549
269	263	279	253	453	463
283	277	293	281	467	577
297	291	307	295	481	591
311	305	321	309	495	605
325	319	335	323	509	619
339	333	349	337	523	633
353	347	363	351	537	647
7	361	377	365		661
381	375	391	379		
395	389	405	393		
409	403	419	407		
423		433	421		
437		447	435		
451		461	449		
465		475	463		
479		489	477		
493			491		

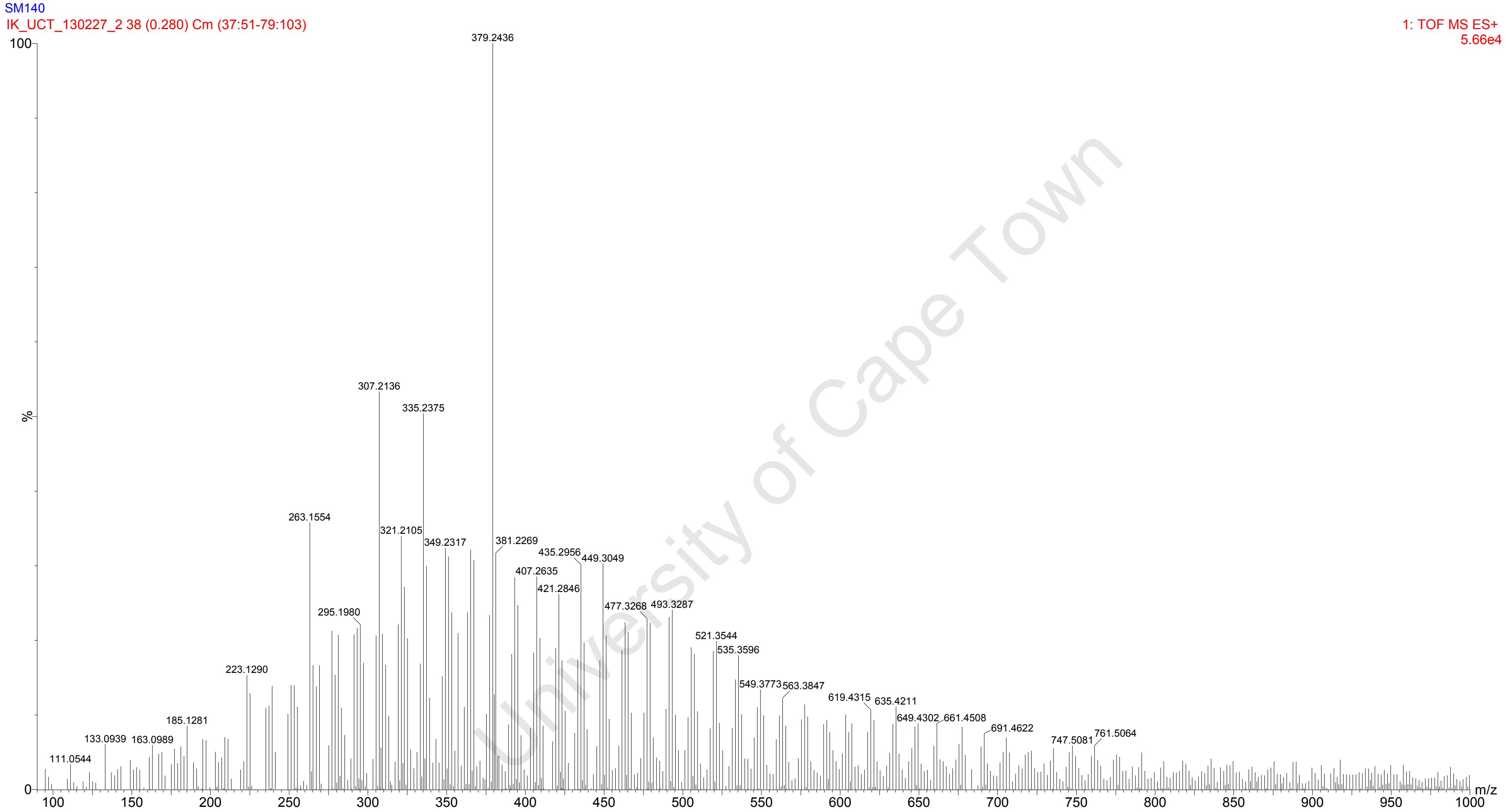

Figure 6.26: ESI (+) MS in the m/z 100-1000 for methanol fraction of stressed SME20

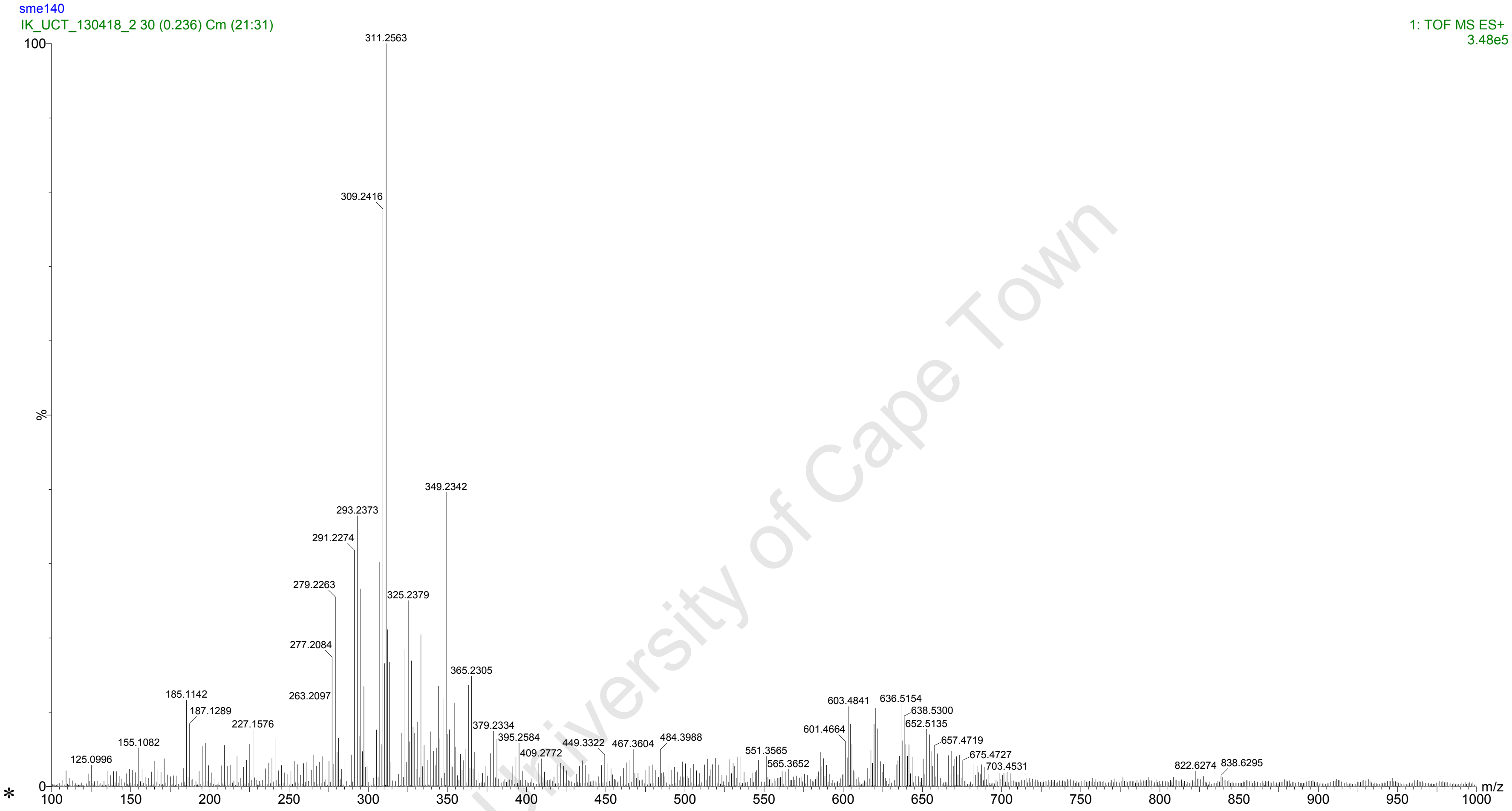

Figure 6.27: ESI (+) MS spectrum of stressed neat SME in the range of m/z100-1000

6.6 Discussion

The darkening of the fuels on stressing is associated with the formation of strong chromophores. These are likely conjugated dienes and keto-alkenes. Evidence for ketone can be found in the FTIR and ESI-MS spectra. Upon stressing, both EN590 diesel and RME20 form two layers with the lower layer showing more reaction by TGA-MS and FTIR.

Below is a comparison of the thermogravimetric properties of the stressed fuels.

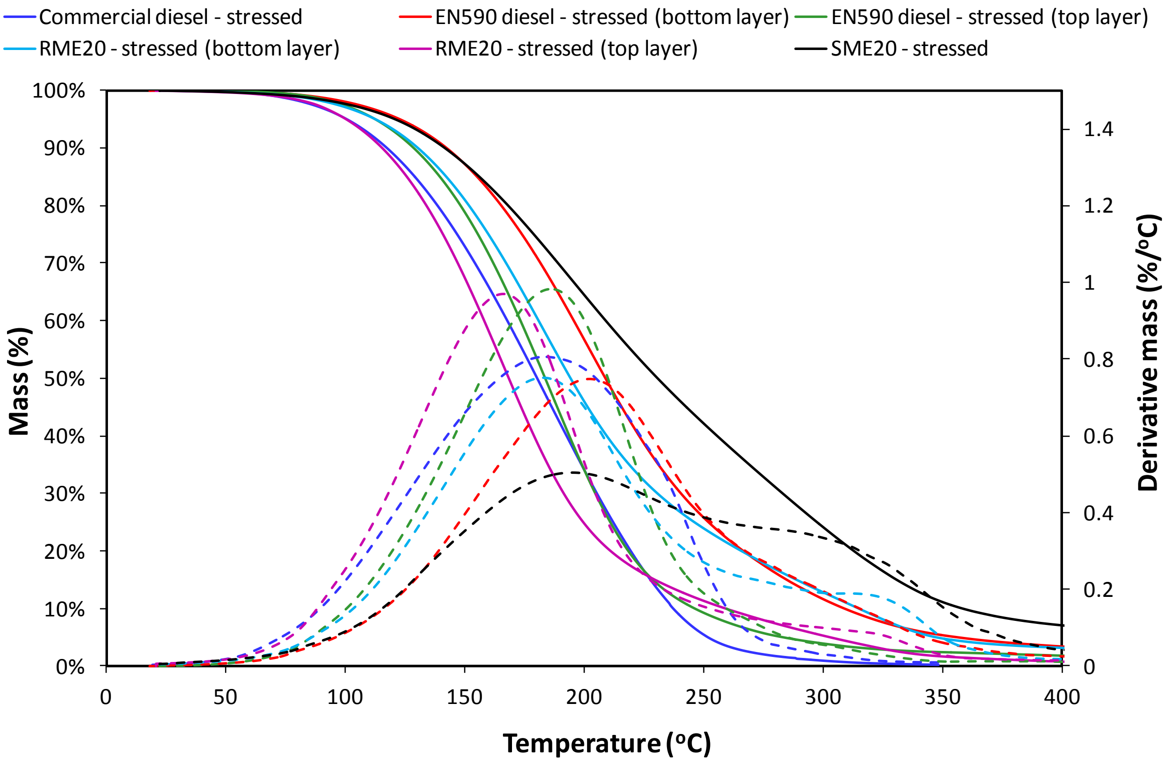

Figure 6.28: Comparison of the thermograms to various stressed fuels. Experiments were conducted under nitrogen at a heating rate of 10^{o}C/min

The curves are summarised by the data in Table 6.9. The comparison of the stressed fuels in Figure 6.28 has some interesting features. One can see that the SME20 curve (far to the right) is consistent with this fuel being the least stable and most oxidised. Of interest is a comparison of the two EN590 layers with the RME20 layers. It can be seen that the position of the peaks in the RME layers are at lower temperatures than the EN590 diesel layers. In particular the top RME20 layer has a peak very similar to the unstressed EN590. It should however, be borne in mind that the size of the top layer is smaller for RME20 than for EN590 diesel. In all samples there is the development of a small shoulder on the derivative peak from 300°C onwards. This is most noticeable in the DTG curve. The height of the DTG step is twice as large for SME20 as it is for the bottom layer of RME20.

Table 6.9: Summary statistics decomposition/evaporation of stressed fuels in nitrogen

Fuel	**DTG peak unstressed fuel (°C)**	**DTG peak stressed bottom layer* (°C)**	**DTG peak stressed top layer (°C)**
Commercial diesel	149	183	
EN590 diesel	173	186	202
RME20	210	170	183
SME20	210	194	

* where there is only one layer this is reported here

If one were to rank the fuels/layers based on the mass remaining at 300°C one would find the order commercial diesel < EN590 (top layer) < RME20 (top layer) << EN590 (top layer) ≈ RME20 (top layer) << SME20.

It is evident that the size of the tail and hence the size of the step in the DTG curve is largest for SME20. The height of the DTG step is twice as large for SME20 as it is for the bottom layer of RME20. Chien *et al.,* [99]ascribed the mass loss when biodiesel was heated to volatilisation and pyrolysis [99]. This shoulder is associated with these pyrolysis processes.

When the fuels were heated in air, a peak was noted above 500°C for all fuels except the commercial diesel. It is suggested that this is the combustion of carbonaceous material within the stressed fuels, although it may also arise from the combustion of products that arise from the pyrolysis of deposit precursors during heating. The area under these peaks is consistent with the extent of stressing, inferred from visual inspection. No lower layer was seen in the stressed commercial diesel which may explain the absence of such a peak.

The CO_2 evolution from commercial diesel was very small suggesting evaporation. In the case of stressed EN590, RME20 and SME20 two mass loss events are followed by carbon dioxide and water evolution. This suggests combustion events as surmised above, although some carbon dioxide evolution could be associated with CO_2 release from ester functionalities. EN590 diesel had a minor broad peak at 320°C and a major distinct peak at 402°C. The H_2O profile of the curve of EN590 diesel mirrors its carbon profile in that the peaks occur at similar temperatures. The water that comes off at these temperatures is associated with combustion of the deposits. The CO_2 profile of RME20 had two distinct peaks. The first occurred at around 295°C while the second major peak near 365°C. Close inspection of the curve revealed a third minor peak at around 520°C. The peak shape is similar to the TGA derivative curve, although the first peak is more significant in the derivative curve.

If one subtracts the baseline from the water and the CO_2 evolution curves one sees that the CO_2 curve grows relative to H_2O curve at elevated temperatures. This is consistent with a lower H/C ratio in the components that are decomposing at this temperature. This can be seen as a narrowing of the gap between the CO_2 and H_2O curves in the earlier oxidative thermograms. At 370^{o}C for stressed EN590 the ratio of water:CO_2 (less the base line values) is 1 which indicates a H:C of 2:1 whereas by 475^{o}C the H:C ratio is 1:1. A 2:1 ratio is indicative of a deposit that is very similar to a saturated paraffin or alcohol while a lower H:C ratio indicates an increase in unsaturation (including aromaticity) and/or the introduction of carbonyl groups. For RME20 the ratio was 1.8 (350^{o}C), 1.1 (375^{o}C) and 0.8 (475^{o}C). Notwithstanding the noise in the CO_2 and H_2O data the trend is clear with the material that burns at a higher temperature has a lower H:C ratio.

Venketaraman and Eser [10] suggest that carbonaceous species bonded to oxygen functional groups are the most reactive and are most likely to oxidise/combust earliest. Deposits formed in the flask reactor were formed under excess oxygen conditions and it is suggested that the deposits formed therein were associated with significant levels of oxygen. This is consistent with their gum-like nature, observed by TEM. This would explain why oxidation of fuel deposits in this study commenced at lower temperatures than HDPI deposits which have lower oxygen and hydrogen content. Venketaraman and Eser [10] attributed high temperature of combustion of HDPI deposits (occurring from 610 to 720°C) and n-hexadecane (740°C) deposits to combustion of ordered polyaromatics structures.

FTIR spectra and ESI-MS data suggest the formation of oxygenated species. This was inferred by the formation of odd-numbered (w.r.t. mass) homologous series when commercial diesel and EN590 were stressed. The neat fuels had even-numbered series. Because FAME blends contain oxygen containing species, the primary sequences in both the neat and stressed fuels were dominated by odd-numbered masses. The species formed differ in polarity from the base fuels. Furthermore ESI-MS data suggest the formation of high molecular weight species.

FTIR spectra of stressed fuels are compared in Figure 6.29. The spectra are for the lower layers where two layers were formed. There is a strong similarity between the shape and size of the peaks of the lower layer formed from RME20 and the stressed SME20. This result would suggest that once the concentration of polar groups have increased to a critical level, this causes phase separation with a more dense layer, concentrated in polar species, forming. In the case of SME20 the upper layer had disappeared after the duration of the experiment.

The high molecular mass and polarity of these species would make it difficult for the base fuels to retain them in solution.

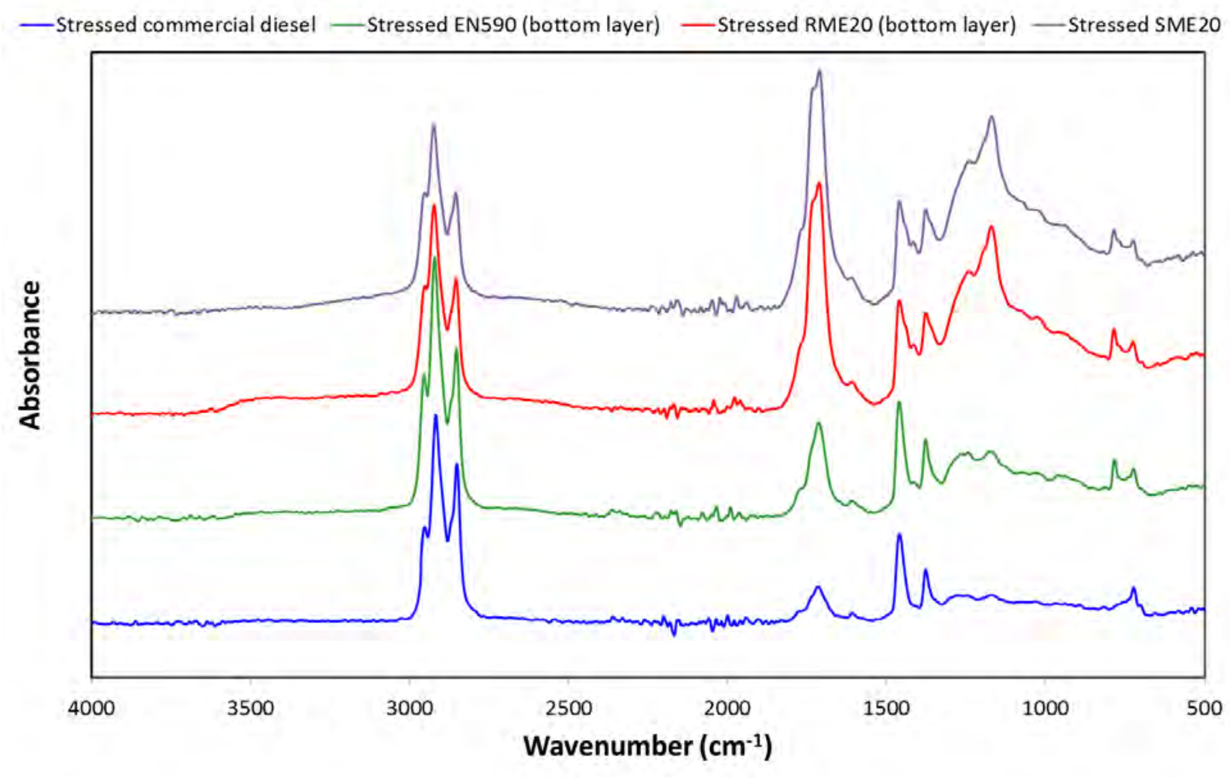

Figure 6.29: Comparison of the FTIR spectra of stressed fuels

Stressing diesel fuel leads to the formation of higher molecular weight species. The molecular weight distribution varies depending on the test fuel, however all stressed diesel fuels portrayed species with significantly higher molecular weight distribution than stressed jet fuel. Although ESI (+) MS shows strong capability as a diagnostic tool for tracking evolution of polar species in fuels, biodiesel blends showed that it is biased towards particular molecules. When biodiesel was blended with EN590 diesel, the peaks that had the greatest intensity in the spectrum emanated from the biodiesel component of the blend, even though, in both cases, the biodiesel component only accounted for 20%. This is not surprising given the presence of oxygen in the FAME constituent molecules.

6.7 Conclusions

Visual inspections, TGA thermograms, FTIR spectra and ESI-MS all suggest that SME20 experiences greater reaction under oxidative stressing and is thus less stable at elevated temperatures with flowing oxygen than RME20, EN590 diesel and commercial diesel. The order of stability is commercial diesel > EN590 diesel > RME20 > SME20. These results are in agreement with those obtained from the QCM, even though that study was performed under oxygen-limited conditions. The species that were formed were higher in molecular mass and polar in nature containing increased levels of oxygen.

The analysis of reactor deposits suggests that TGA may be used to monitor the oxidative degradation of fuels, in particular those containing FAME. While beyond the scope of this study, it is possible that TGA thermograms could be used with stressing experiments of different duration to provide kinetic data for the analysis of oxidation. This could be coupled with FTIR information, *e.g.* the growth of C=O bands. Importantly TGA could provide a handy method of tracking high molecular weight species by concentrating on the mass of sample that decomposes above 300^{o}C.

7 Closed bomb reactor deposits

7.1 Results and discussion

Test fuels were stressed inside a reactor bomb at 250°C for 24h at a pressure of 10 atm. The temperature was selected to fall within the range of temperatures at the tip of a diesel injector [78], while the reactor vessel was charged with oxygen to facilitate the deposition process. A charging pressure of 10bar was selected because it was sufficient for the duration of the experiment, *i.e.* there would still be oxygen present in the reactor bomb after the fuel degradation process. Below are images of reactor bomb vessels as well as their lids.

7.2 Visual observations

7.2.1 Commercial diesel

Figure 7.1: Deposits derived from closed bomb degradation of commercial diesel at 250 °C for 24h at a pressure of 10bar: left) the reactor lid vessel body and b) the reactor lid

Commercial diesel formed very little deposits on its reactor surfaces (see Figure 7.1). Fouling on both the reactor lid and the reactor vessel body was less than observed for any of the other fuels. Not only was the quantity of deposit reduced, but the deposits were visibly lighter in colour. This result shows that even at elevated temperatures and the addition of a metallic surface, commercial diesel still displayed the highest thermo-oxidative stability.

7.2.2 EN590 diesel

Figure 7.2: Deposits derived from closed bomb degradation of EN590 diesel at 250 °C for 24h at a pressure of 10bar: left) the reactor lid vessel body and b) the reactor lid

Figure 7.2 shows the emptied vessel (after the stressed liquid fuel had been removed) and sealing lid of a reactor bomb, in which EN590 was reacted for 24h at 250°C in the presence of 10 bar oxygen. It is apparent that carbonaceous deposits formed on the surfaces of the reactor vessel as well as the reactor lid. In the reactor vessel the deposits primarily formed in bottom half of the reactor. This is not surprising as the fuel resided and occupied the bottom half of the cylindrical reactor vessel and as such readily deposited on the adjacent vessel walls. Deposition on the sealing lids likely results from cracked fuel components where the lid provides a condensation surface for the gaseous components. Keck *et al.* [48] provide a mechanism to explain deposit formation in diesel injector tips. Their proposed mechanism is likely to be similar to the mechanism that governed the formation of deposits inside the reactor bomb walls.

7.2.3 RME20 and SME20

As can be seen in Figure 7.3 and Figure 7.4, fouling on reactor vessels of both RME20 and SME20 was significantly worse than commercial diesel. Comparison with Figure 7.2 suggests similar type of deposits to EN590 diesel. These experiments were repeated several times and similar deposits were observed.

Figure 7.3: Deposits derived from closed bomb degradation of RME20 at 250 °C for 24h at a pressure of 10bar: left) the reactor lid vessel body and b) the reactor lid

Figure 7.4: Deposits derived from closed bomb degradation of SME20 at 250 °C for 24h at a pressure of 10bar: left) the reactor lid vessel body and b) the reactor lid

7.3 Transmission electron microscopy

Deposits generated on the walls of the reactor after degradation of diesel fuels were scraped off, ultra-sonicated in an ethanol solution and then viewed under a TEM. The micrographs of deposits from each fuel are depicted below.

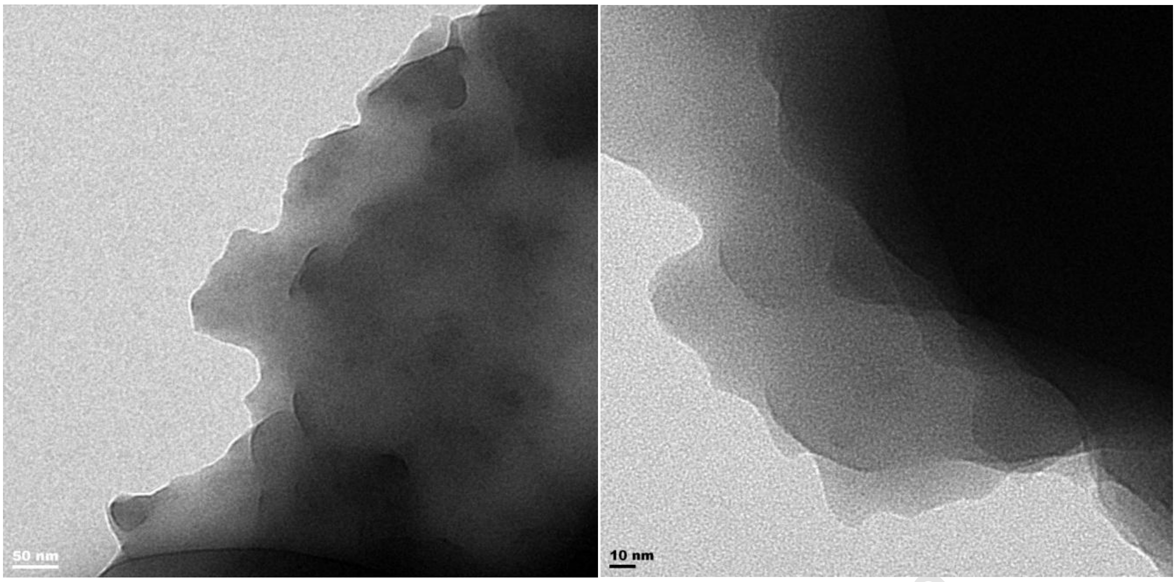

Figure 7.5: TEM micrographs of deposits formed from stressing commercial diesel in a closed bomb reactor; left) lower magnification image and right) higher magnification image

Figure 7.5 illustrates that the deposits formed from commercial diesel had no regular structure. Figure 7.6 shows two TEM micrographs of EN590 diesel deposits at different magnifications. The microstructure of deposits formed in the bomb reactor appears to be similar to EN590 diesel deposits, formed in the flask reactors. The structures appear to be amorphous with no regular diffraction patterns visible [10].

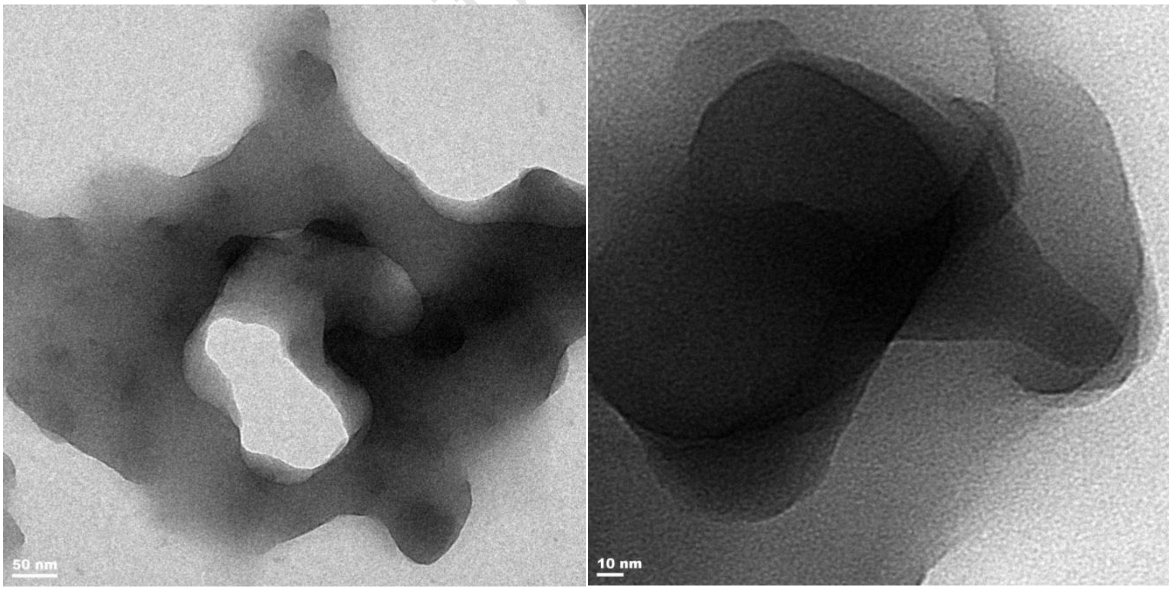

Figure 7.6: TEM micrographs of deposits formed from stressing EN590 diesel in a closed bomb reactor; left) lower magnification image and right) higher magnification image

The microstructure of RME20-derived deposits are shown in Figure 7.7. The microstructure of deposits from both these fuels produced familiar amorphous hybrid deposits with physical characteristics akin to EN590 diesel bomb reactor deposits.

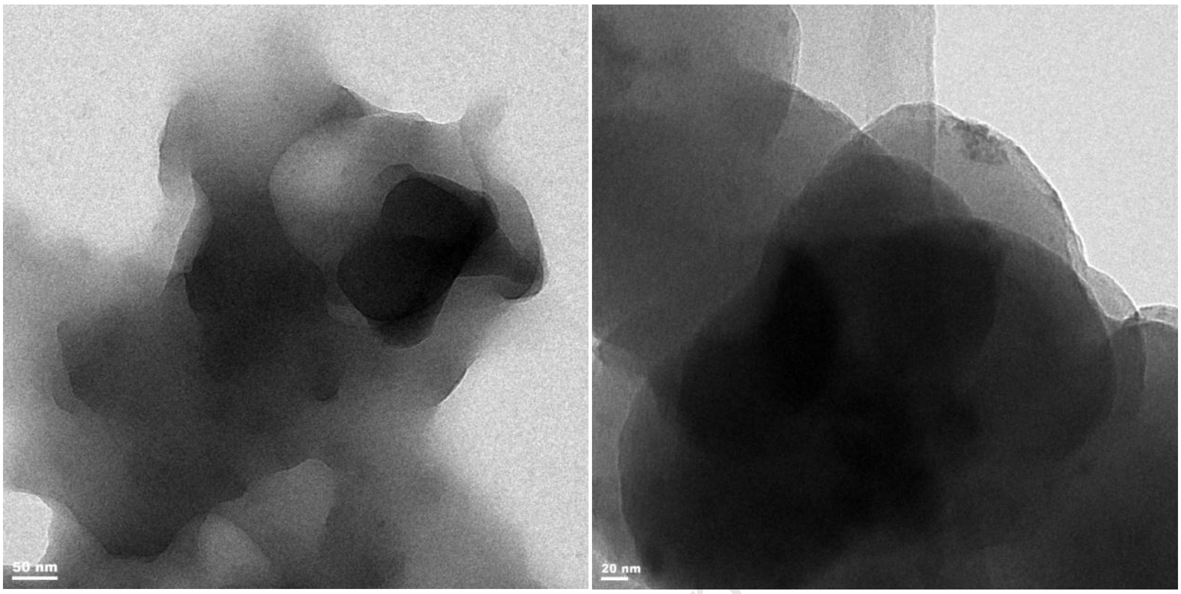

Figure 7.7: TEM micrographs of deposits formed from stressing RME20 in a closed bomb reactor; left) lower magnification image and right) higher magnification image

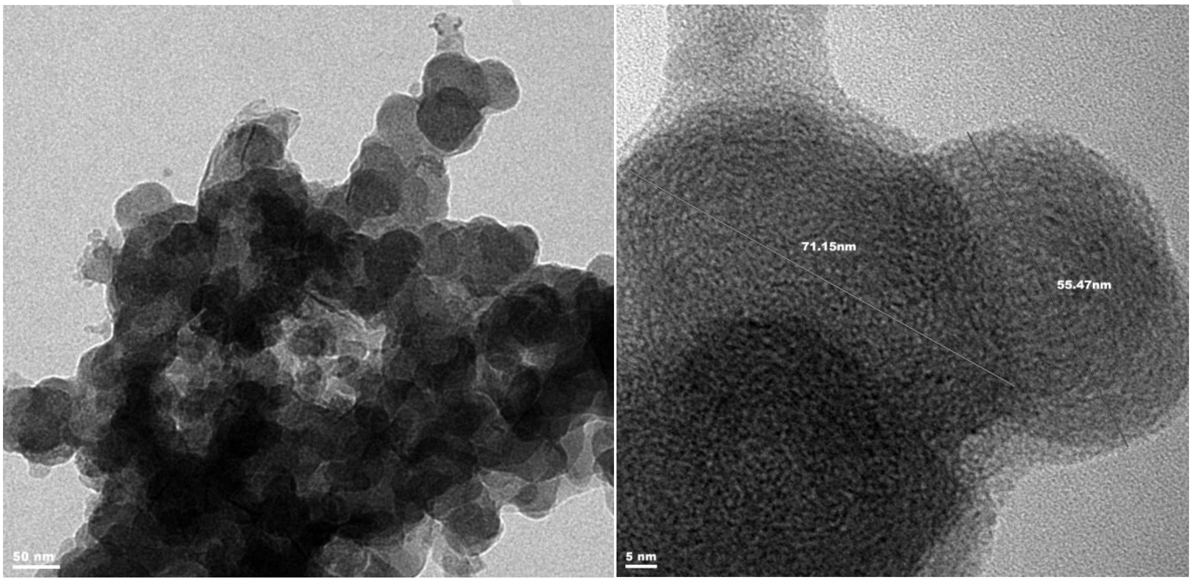

Figure 7.8: TEM micrographs of deposits formed from stressing SME20 in a closed bomb reactor; left) lower magnification image and right) higher magnification image

SME20, on the other hand, produced deposits with a very different microstructure. Closer inspection of Figure 7.8 reveals that SME20 deposits have smaller primary particles when compared to particles of other fuels. Diameters are less than 100 nm. Furthermore these particles configure into agglomerates in a manner that is similar to carbonaceous soot. Figure 7.8b reveals the presence of diffraction patterns as can be seen in the particle on the right. The patterns, however, are not perfectly circular suggesting a disordered structure. These are similar to those for HDPI deposits, reported by Venketaraman and Eser [10].

7.4 TGA-MS

Deposits were collected by filtration on Munktell filter paper. Because of their gummy nature, they could not be removed from the filter paper, so TGA analysis was performed with the deposits on the filter. The TGA data for the filter paper may be found in Appendix E.

Thermogravimetric analysis was performed in oxidative mode. Samples were heated at 10°C/min in synthetic air and the mass loss and CO_2 evolution signals were captured. A small amount of the mass loss can be ascribed to the filter paper but as indicated in the Appendix, none of the CO_2 signal is due to the filter paper.

The purpose of oxidative TGA was to assess the structural nature of the deposits by looking at the temperatures at which deposit combustion occurs.

7.4.1 Deposit oxidation

Figure 7.9 illustrates the combustion of reactor bomb deposits derived from commercial diesel. A number of features stand-out. The residue is non-zero since that reflects the filter. The initial rapid drop in H_2O is because it was a very humid day and the initial moisture level reflects air in the TGA furnace when it initially closed. The initial mass loss has a peak at 130°C. This is lower than the original commercial diesel but much higher than the boiling point of hexane (66°C). If hexane were present the initial mass would not be stable because hexane is volatile. This material which evaporates near 130°C is likely to be fuel-derived but because it has a lower evaporation temperature than the neat fuel, it is indicative of cracking to smaller molecules. The CO_2 curve mimics all the features in the DTG curve, except the initial mass loss, even down to the small rise at 235°C. The H_2O profile is similar to the CO_2 profile except that its peak is earlier. This suggests that the H:C ratio of the deposits are declining as the material is heated. This is consistent with the material that is burning becoming progressively more unsaturated and aromatics. Note also the H_2O peak also has the small but sharp increase at 235°C. The reason that the DTG curve is closer to the CO_2 rather than the H_2O profile is because the loss of 1 carbon atom is six times as heavy as 2 hydrogen atoms.

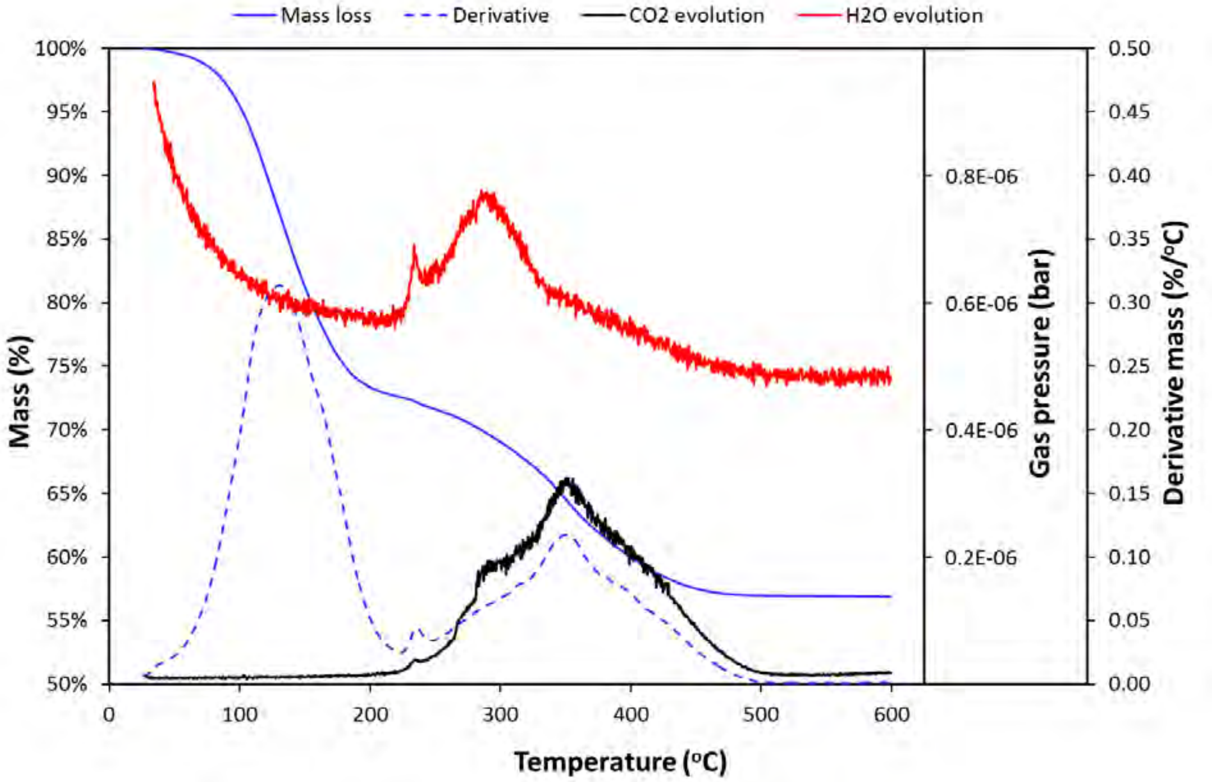

Figure 7.9: Oxidative mass loss, and H_2O and CO_2 profiles of fuel deposits derived from thermo-oxidative stressing of commercial diesel inside the reactor bombs charged with 10 bar oxygen pressure and at 250°C for 24h

Figure 7.10 illustrates what happens to deposits from the oxidative stressing of EN590 diesel when heated in air. Again there is a highly volatile fuel-derived component. The CO_2 curve has two peaks, only one of which is matched in the H_2O profile. The second CO_2 evolution has a much smaller H_2O shoulder associated which can just be seen against the background. This too, suggests the deposits have a range of H:C ratios with the more condensed fraction burning at higher temperatures.

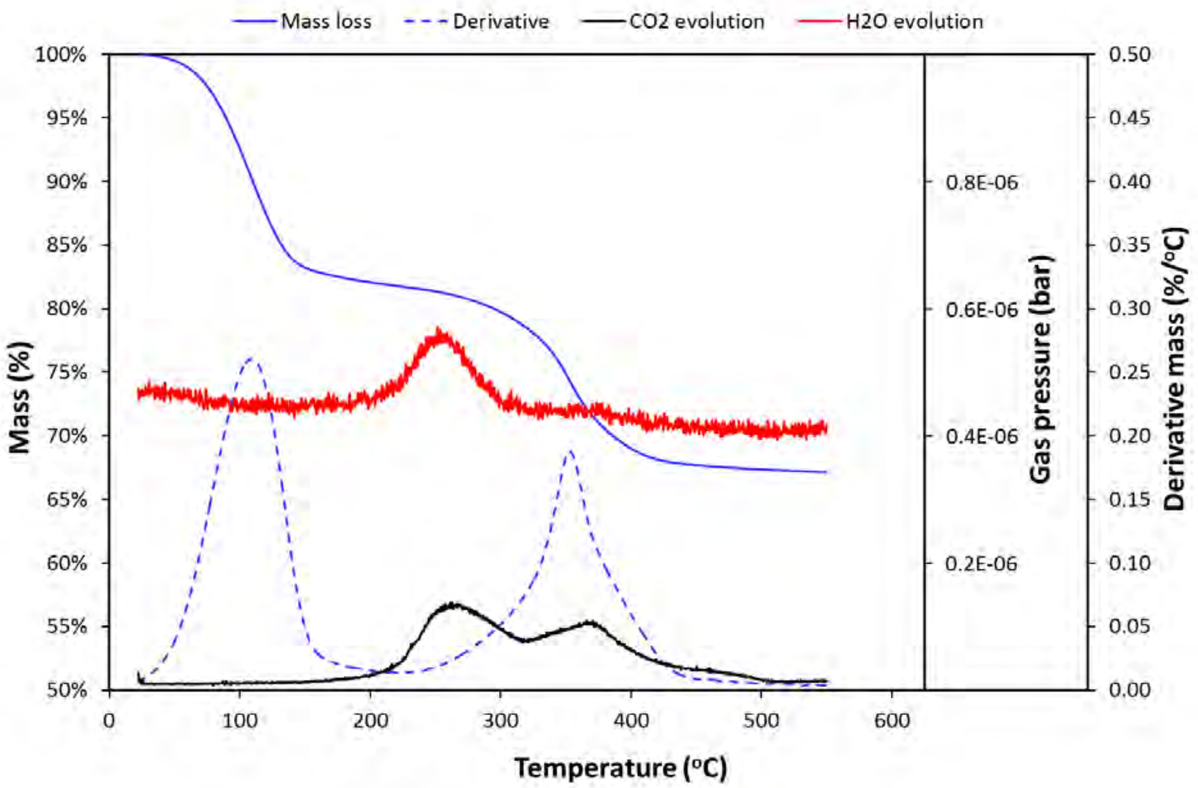

Figure 7.10: Oxidative mass loss, and H_2O and CO_2 profiles of fuel deposits derived from thermo-oxidative stressing of EN590 diesel inside the reactor bombs charged with 10 bar oxygen pressure and at 250°C for 24h

Figure 7.11 shows a comparison between the evolved gas profiles of deposits formed from the stressing of RME20. The correlation between the DTG curve and the CO_2 profile is striking. It can be seen that the DTG curve has two major peaks: one for volatile material and one for the carbonaceous deposits but that the latter has two shoulders. Careful perusal of the DTG curves for EN590 and commercial diesel reveals the presence of two shoulders in those curves too. There are two peaks in the H_2O profile at similar temperatures to the main CO_2 evolution peak and one of its shoulders. However, the height of the second H_2O peak is similar to the first unlike CO_2 in which the second peak is much larger. Again this demonstrates the increasing degree of unsaturation. The absence of H_2O for the last shoulder suggests that the material is very unsaturated and likely implies the presence of condensed aromatic rings.

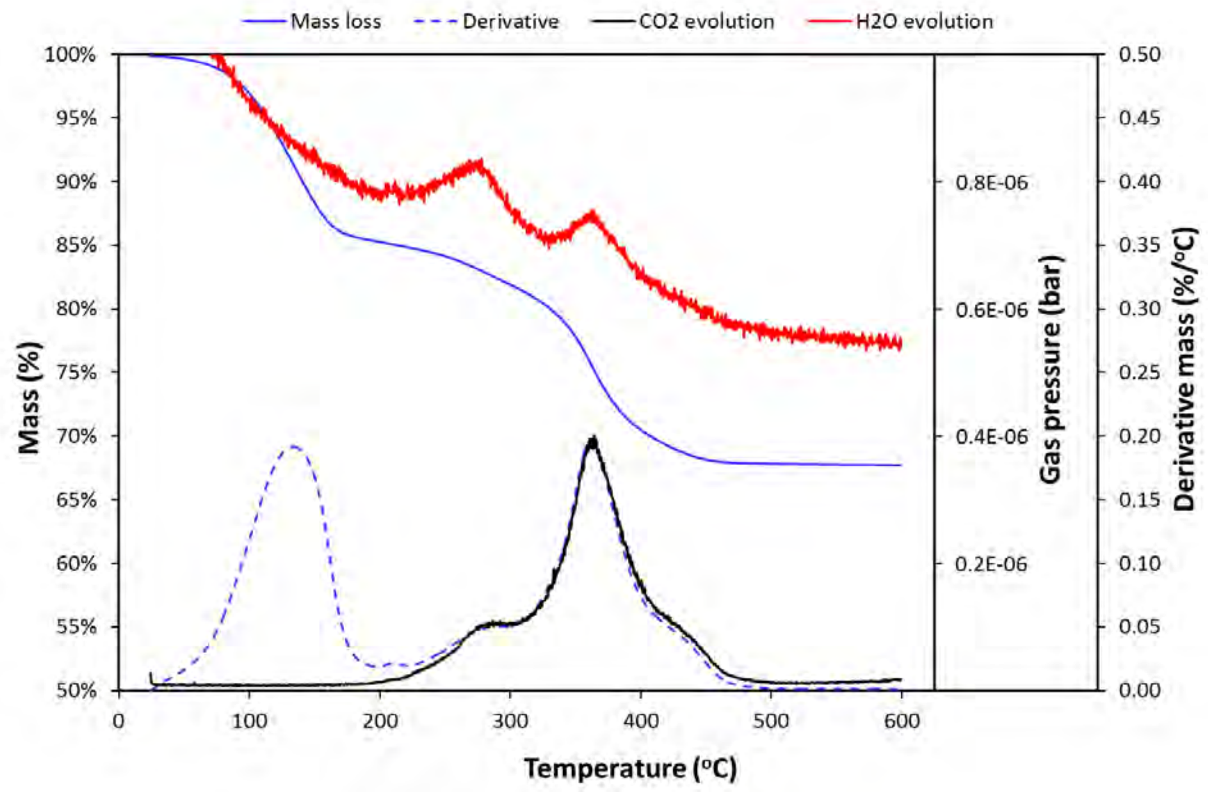

Figure 7.11: Oxidative mass loss, and H_2O and CO_2 profiles of fuel deposits derived from thermo-oxidative stressing of RME20 inside the reactor bombs charged with 10 bar oxygen pressure and at 250°C for 24h

Figure 7.12 shows the oxidative mass loss curve for SME20. Again, a number of common features are present: the low temperature mass loss and the second mass loss which consists of a main peak and two shoulders. In the case of SME20, the shoulder in the DTG curve on the higher temperature side becomes more significant. It also extends to slightly higher temperatures than RME20 deposits. As with the other deposits the quantity of water evolved declines relative to CO_2 as the temperature rises. It should be noted that the larger size of the first mass loss compared to the other fuel deposits does not necessarily imply that there is more cracked material and may merely be an artefact that the filter became clogged more easily, not allowing this light material to be filtered away.

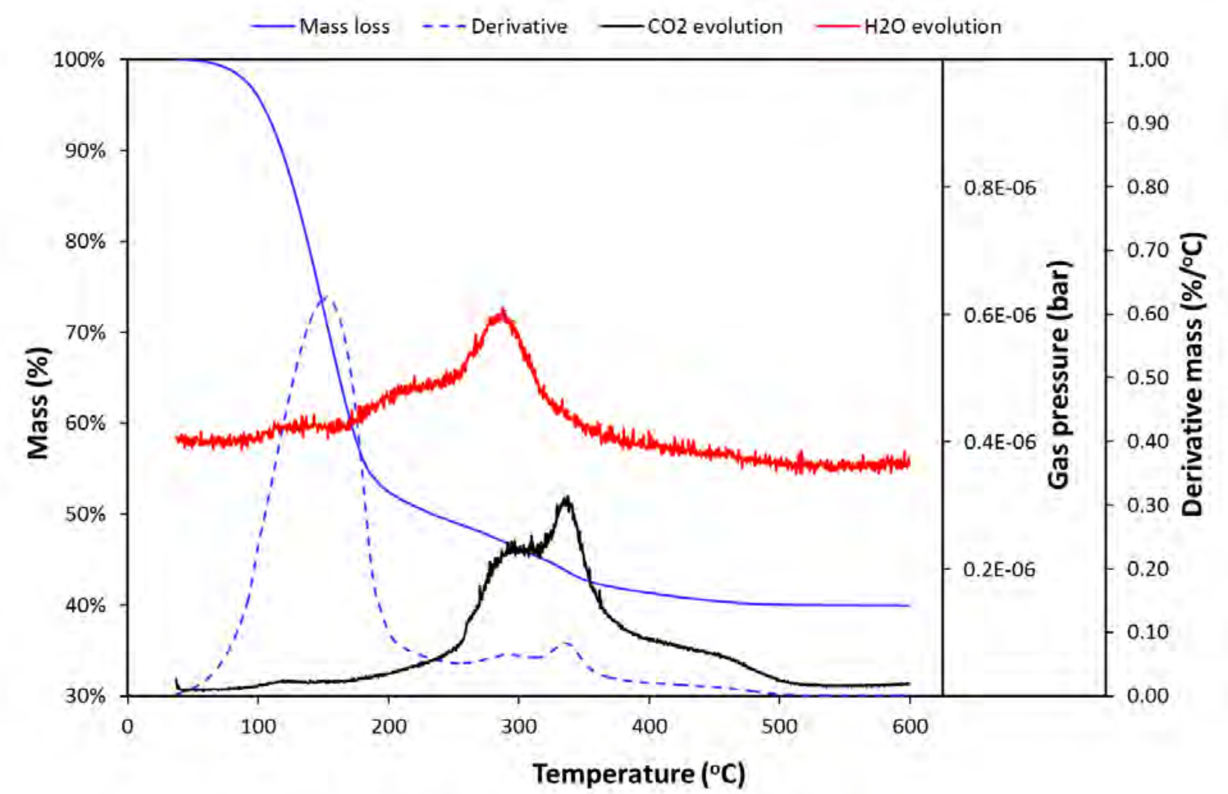

Figure 7.12: Oxidative mass loss, and H_2O and CO_2 profiles of fuel deposits derived from thermo-oxidative stressing of SME20 inside the reactor bombs charged with 10 bar oxygen pressure and at 250°C for 24h

7.5 Discussion

All mass loss curves contain initial mass loss in the region 100-200°C. This is ascribed to the evaporation of residual fuel in the deposits. The evaporation temperature is lower than the original fuels which is consistent with cracking having taken place.

Comparison of EN590 diesel and commercial diesel images shows fouling on walls of the sand bath reactors. One might assume that EN590 diesel, which endured significantly more fouling, would form deposits with much greater resistance to combustion. Results show that is not the case.

The DTG curve shape is matched very closely in the CO_2 profile. In all cases the DTG profile has a peak near 350°C which was consistent across all fuels. This peak also has two characteristic shoulders. The first shoulder starts near 260°C for all four fuels. The relatively low oxidation temperature of these deposits suggests that they are associated with oxygen moieties [10]. Although images of EN590 diesel sand bath reactors (Figure 7.2) revealed fouling, akin to those of automobile diesel injectors in the study by Quigley *et al.* [102], the combustibility of these deposits formed in the current study was higher, *i.e.* they burnt at lower temperatures. TGA-MS of diesel injector deposits was conducted by Venketaram and Eser [10]. The injector deposits had much higher thermal-oxidative stability than EN590 diesel sand bath deposits. It is likely that under injector conditions higher levels of carbonisation are achieved. Nonetheless, comparison of the H_2O to CO_2 profiles reveals that the deposits of all fuels have a range of H:C ratios with the lower H:C ratio components burning at higher temperatures. The last CO_2 shoulder is associated with little H_2O which suggests that there are polyaromatic rings in this component. The relative importance of this shoulder is greatest for SME20.

Altin and Eser [12] also noted the major CO_2 evolution on metal surfaces (Inconel 600 and Inconel X) to be between 250 and 450^{o}C when jet fuel was stressed. These measurements were made using a carbon analyser. In fact the Inconel X CO_2 profile appeared to have a central peak and two shoulders as obtained here. These authors suggested that the low temperature peaks possibly contained significantly more hydrogen. This has been confirmed to be the case in this study. Some of the deposits studied by Gül *et al.*, also had the characteristic two shoulders and a main peak in their TPO profile, despite having been produced at temperatures above 400^{o}C [7].

It should be noted that, although the deposits' thermal profiles are similar across the fuels, the quantity of deposits are not necessarily slow. Nonetheless the similarity of profiles suggest a similar progression of deposit formation.

7.6 Conclusions

The set of conditions in the sand bath reactor (250°C, 10 bar oxygen pressure for 24 h) led to fouling of the reactor vessels in all test fuels. Reactor vessel fouling was lowest for commercial diesel and greatest for SME20.

TEM micrographs elucidated the microstructure of fuel deposits and revealed that they were primarily amorphous in nature for commercial diesel, EN590 diesel and RME20 stressing. Some structure was noted in SME20 deposits, as indicated by the interference patterns that are visible. This would suggest that the greatest carbonisation had occurred in this sample.

Consistent with the visual and TEM observation was the observation that the deposits formed from SME20 has a greater fraction burning at higher temperatures (the final shoulder in the DTG curve was more prominent. This is consistent with more carbonised deposits, *i.e.* deposits containing less hydrogen and oxygen. It has been demonstrated that oxidative TGA with MS detection can provide information consistent with microscopy that is indicative of the degree of carbonisation of the deposit. The relationship between the DTG curves and the

CO_2 profile was striking and much stronger than what was observed for flask deposits. It should, however, be noted that the bulk of flask deposits burnt at lower temperatures and had much higher hydrogen content and likely less condensed structures.

8 Fuel degradation in a flow reactor

8.1 Results and discussion

A flow reactor was used for two reasons: 1) to stress diesel fuels under thermal-oxidative conditions similar to those used in the sand bath reactor and 2) to ascertain whether zinc (in solution with fuel) affects the depositing behaviour of fuels. Fuels were doped with 10ppm zinc neodecanoate because such doping has been shown to accelerate deposition [82, 83].

Table 8.1 indicates that no deposits that were discernible by digital microscope. No SEM and TEM analysis on the tubes were performed. TGA-MS analysis of small segments of the tubes yielded negligible mass loss while the MS detected no significant rise in CO_2 pressure. Figure 8.1 is an image highlighting the typical appearance of sectioned reactor tubes post-stress. A small amount of yellow staining can be observed.

Table 8.1: Fuels tested and deposit character

Fuel	Visible deposits (Microscope)	Gravimetric evidence of deposits (TGA-MS)
EN590 diesel	No	Negligible mass loss, no CO_2 peak
RME20	No (yellow stains)	Negligible mass loss, no CO_2 peak
SME20	No (yellow stains)	Negligible mass loss, no CO_2 peak
Commercial diesel	No	Negligible mass loss, no CO_2 peak
EN590 (10ppm zinc)	No	Negligible mass loss, no CO_2 peak
SME20(10ppm zinc)	No (yellow stains)	Negligible mass loss, no CO_2 peak

All post stress sample tubes exhibited negligible mass loss during oxidative TGA analysis. No significant CO_2 evolution was observed. Figure 8.2 presents an example thermogram and CO_2 profile of a sectioned (3mm disk) reactor tube which ran EN590 10ppm zinc fuel. From this example it is noticeable that the tube experienced a very small mass loss up to 600°C. The total sample size was 84.301 mg. The observed mass loss of 0.096 is equivalent to 81 µg which while small is detectable by the sensitive balance of the Q5000IR. However, at least half of this is associated with the loss of volatile components which is likely fuel. Compare Figure 6.5. The accompanying carbon evolution is very close to background because the mass of evolved compounds must be small as a result of the small mass of decomposable material. There may well be a slight rise in CO_2 above 200°C which could be associated with fuel combustion but this could also be an artefact.

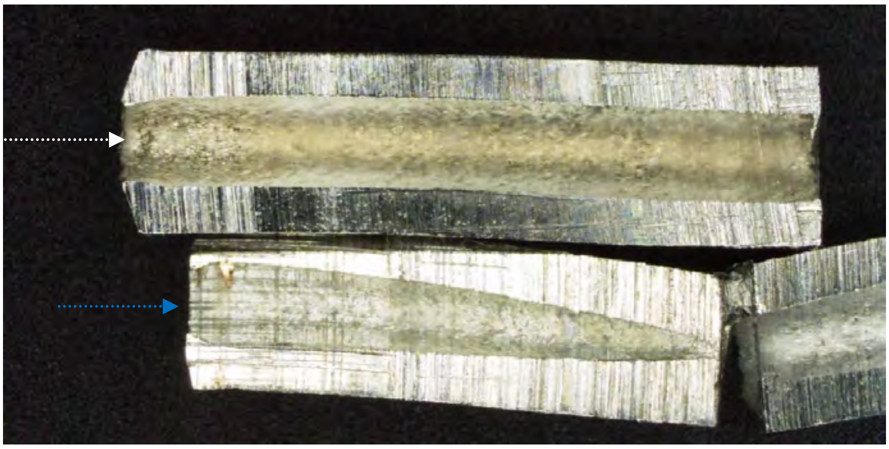

Figure 8.1: Digital microscope image of sectioned flow reactor tubes which contained (a) (white arrow) SME20 doped with 10ppm zinc and (b) (blue arrow) EN590 diesel and were stressed for 24 hours in a flow reactor at 250°C with fuel line pressure of 10 bar

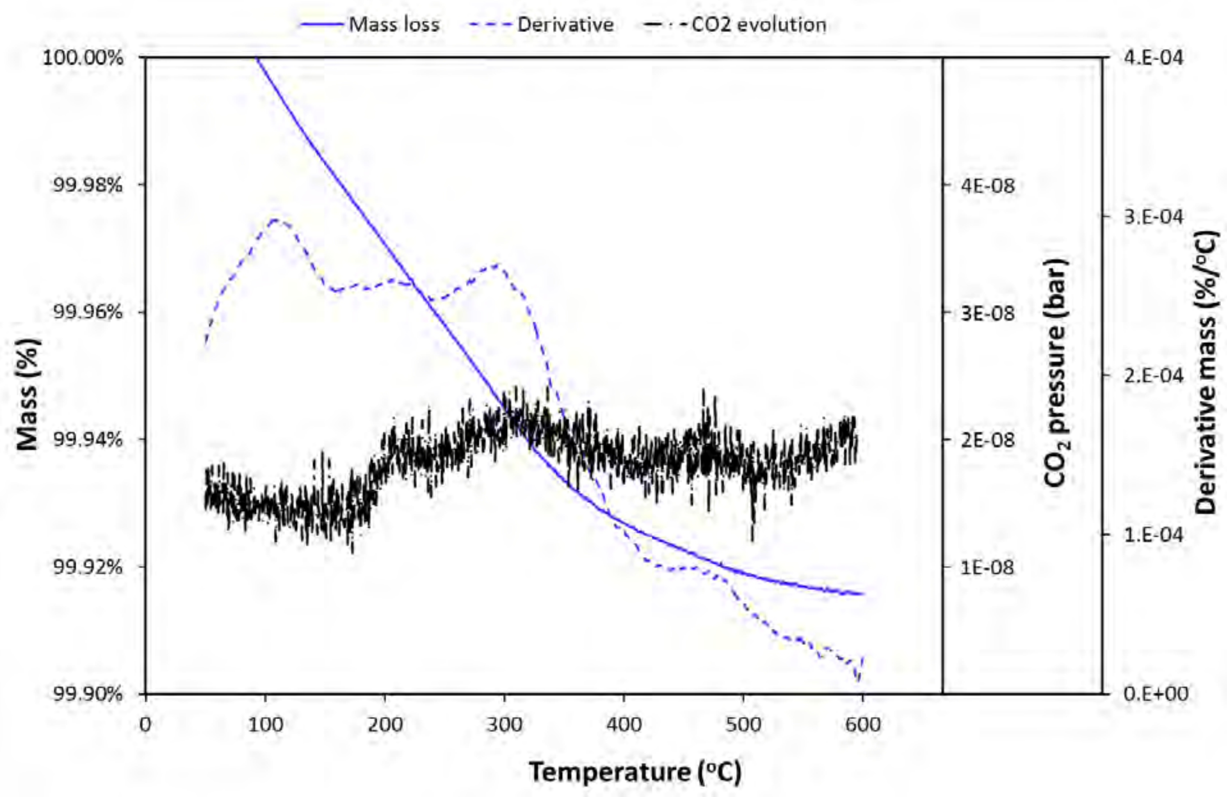

Figure 8.2: Mass loss and CO_2 evolution of reactor tube exposed to EN590 diesel doped with 10 ppm zinc

8.2 Conclusions

Thermal stressing of all fuels in the flow reactor did not produce deposits on the same scale as closed bomb reactor experiments. The influence of zinc on deposit formation in fuels was also inconclusive. TGA-MS is not sensitive to formation of very thin deposits. The bulk of the small mass loss observed was likely absorbed fuel. A much heavier segment of tube would be required which would be beyond the mass that the TGA could measure. An alternative approach would be to perform the analysis in an instrument capable of taking larger samples such as a LECO RC612 carbon analyser. This instrument is capable of quantifying carbon and hydrogen present in any deposit. From the CO_2 and H_2O formed, mass loss is inferred.

It should also be noted that 250^{o}C was the furnace temperature and not the fuel temperature. In the closed bomb experiments, fuel reached this temperature because the system is under thermal equilibrium but when passing through the furnace, fuel at the centre does not reach the final temperature for a significant fraction of time before it passes out of the reactor. More importantly the residence time of fuel in the reactor was only of the order of 7-8 min unlike the hours spent in the closed bomb. It should be noted that flow reactors are more commonly used to study pyrolysis processes at higher reaction temperatures.

In order to increase the residence time it is possible to recirculate the fuel through the flow reactor. Such an experiment has not been reported before and would require rig modification. As such it was deemed beyond the scope of this study.

9 Conclusions

"Follow the evidence to where it leads, even if the conclusion is uncomfortable."- Steven James, The Knight

It has been demonstrated that the extraction solvent has a significant impact on the quantity of SOF extracted from diesel soot and the chemical nature of this soot. Increasing solvent polarity led to an increase in the quantity of SOF. This is because many of the components in the SOF such as aromatic esters are polar and have a natural affinity for polar solvents, unlike paraffinic hydrocarbons which did not extract these species at all.

It is evident when comparing the characterisation in this study and previous studies that the importance of PAHs in the SOF of diesel soot has declined. This is ascribed to the use of cleaner diesel with lower PAHs and the replacement of mineral oil based lubricants with those based on synthetic stocks. Such lubricants are likely to reduce the loading on diesel particulate filters significantly. What has increased is the importance of esters, including phthalates. Since these are potential endocrine disruptors, this may warrant future studies. These esters are likely derived from synthetic lubricating oils which contain such compounds as additives.

PAHs were best extracted by acetone whereas methanol was better for the extraction of esters. This would suggest that the SOF is best characterised by a sequential extraction procedure of these two solvents.

A significant discrepancy between SOF and VOF, as determined by TGA, was observed. It is suggested that this is due to the presence of species which were not extracted by the organic solvents used. Likely candidates are sulfates, sulfurous and sulphuric acids derived from sulfur-containing diesel. This indicates that both methods are required for the full characterisation of soot. Thermogravimetric analysis also revealed that the soot formed consists of a multitude of carbonaceous forms. This was evidenced by three peaks in both the DTG and CO_2 evolution curves when the soot was burnt in oxygen. These are likely material of increasing carbonisation.

Stressing diesel fuel under thermo-oxidative conditions can lead to the formation of deposits. All experiments and analysis techniques pointed to thermo-oxidative stability which followed the trend commercial diesel > EN590 reference diesel > RME20 and SME20. The low stability of the last two is ascribed to the presence of double bonds in the backbone of their constituent fatty acid methyl esters. The higher concentration of such bonds in SME20 explains why it has the lowest stability. The rate of oxygen uptake is not a predictor of stability under the reactor conditions measured in this study. This was ascribed to different oxidative mechanisms being important for different fuels.

It has been demonstrated that a number of techniques and experimental methodologies can be used to discriminate between fuels. In particular QCMs can be used to accurately assess the deposit-forming potential of diesel fuels. This has not previously been demonstrated for diesels which contain FAME.

Stressing fuels leads to a variety of changes. These include colour changes which can be used to differentiate between stressed and unstressed fuel. These changes are likely the result of the formation of conjugated chromophores. Furthermore oxygen containing groups (C-OH and C=O) were also formed as evidenced by FTIR spectra.

Thermogravimetric analysis (TGA) can also be used to differentiate between stressed and unstressed fuels. Stressing was observed to raise the temperature at which a fuel volatilised. Furthermore significant quantities of high molecular weight species (as inferred from high decomposition temperatures) were observed. The presence of these species was most noticeable in SME20 followed by RME20. Oxidative TGA revealed the presence of a carbonaceous residue which burnt above 500^{o}C. Again SME20 was shown to have the lowest stability.

Moreover when TGA is connected to MS, the oxidative stability of carbonaceous deposits of the stressed fuel can be ascertained. The MS also permits observation of water formed as stressed fuel is thermally interrogated in the TGA and consequently assist in elucidating carbonaceous deposits associated with hydrogen. This was especially useful for characterising deposits formed under more severe conditions. TGA-MS data demonstrated the likely occurrence of cracking as well as the formation of deposits of varying H:C ratios. Material with lower H:C ratios was observed to burn at higher temperatures.

ESI (+) MS was shown adequate in tracking the formation of soluble macromolecular species during fuel oxidation. Preferential ionisation of particular molecules however restricts the technique to qualitative analyses. Notwithstanding the technique showed that there is no direct association between number of soluble macromolecular polar species formed during fuel oxidation and solid deposits formed. The data revealed that stressing caused the formation of high molecular weight species which were inferred to contain oxygen. The formation high molecular weight polar species is consistent with the formation of two phases upon extended stressing of diesel fuel.

TEM imaging suggested that deposits were formed from the liquid phase as demonstrated by the spherical nature of the deposits seen under electron microscopy. The structure in the SME20 deposits at elevated temperatures may, however, hint at a different formation mechanism, *e.g.* by reaction of cracked fuel products.

It has been demonstrated that a number of techniques provide complementary information about the relative stability of different fuels. In particular the application of thermogravimetric analysis and ESI-MS to diesel stability has been demonstrated.

10 Recommendations and further work

There are plenty of recommendations on how to get out of trouble cheaply and fast. Most of them come down to this: Deny your responsibility.-Lyndon B. Johnson

Based on findings of this dissertation the following recommendations have been made.

- If one is to perform Soxhlet extraction of diesel soot, it is best performed using glass thimbles, particularly when emphasis is on SOF determination.
- Extraction of PAHs and esters such as phthalates from diesel soot matrix is best achieved using polar solvents. Furthermore extraction of phthalates with polar oxygenated solvents will be most effective during Soxhlet extraction.
- It is recommended that sequential extraction using acetone followed by methanol be performed to provide an accurate value of SOF. This will maximise PAH and ester extraction. A final toluene extraction may be required to remove any residual paraffins. Further extraction of sulfurous acids should also be considered. This will allow better correlation between SOF and VOF.
- In ascertaining the microstructure of diesel soot, it is advisable to perform TEM and discount SEM as TEM provides micrographs that can enable distinction of soot's complex microstructure and the hierarchal components (primary particles, agglomerates etc.). SEM's resolving power is insufficient for fine microstructure analysis and should only be used in tandem with EDS to enable elemental analysis.
- Sampling of soot from an exhaust pipe of a vehicle should be conducted with great care as to avoid introduction of exhaust pipe components into the soot sample. A future study would require the direct sampling of soot from the exhaust stream. The quantity of soot obtained from a dilution tunnel limited the amount of testing that could be performed.

10.1 Further work

Based on the findings the following is suggested work that could advance and expand on this study.

- Extraction of diesel soot was conducted with six solvents. Many other solvents could be used to extract soot. Polar nitrogen containing solvents (e.g. acetonitrile, pyridine etc.) for example could be benchmarked against polar oxygenated solvents in extraction PAHs and/or phthalates. A wider range of solvents would allow a correlation between extraction and solubility parameters to be probed. Such studies could also encompass mixed solvents. GCxGC could be considered for the characterisation of the extracts.

- As other authors have shown, a more accurate quantity of the SOF is obtained by two subsequent extractions i.e. extraction of a soot sample with one solvent followed by extraction with another solvent. This procedure could be tested and the resulting SOF could be benchmarked against the VOF obtained from the TGA. Such benchmarking should also include the aqueous extraction of sulfurous compounds. The hypothesis that some of the VOF results from pyrolysis processes, as proposed by Leifeld [94], could be tested by performing TGA-MS and looking for pyrolysis signatures, notably CO.
- Although the microstructure of diesel soot from a commuter bus and a bench engine was observed using TEM, the process involved ultrasonicating the soot samples in ethanol. This process potentially modifies the hierarchal components of soot as well as its microstructure. This hypothesis could be tested by comparing the microstructure of soot sampled directly onto a TEM grid (located at the exhaust of a bench engine) via a process known as thermophoresis, to the microstructure of soot that endures ultrasonication in ethanol.
- During oxidative thermal analysis of soot (via TGA-MS), the only gases that were monitored were CO_2 and H_2O. Inert atmosphere TGA-MS could be used to track other gases or volatiles that develop or desorb from the soot matrix during thermal treatment. Of particular importance would be cracked alkenes. Furthermore Ar should be used as an inert medium so that CO can be identified.
- The SMORS mechanism suggests that fuel stability is depressed by inherent fuel phenols. Diesel fuel could be doped with phenols and degraded in reactors (QCM, flask, fluidised sand bath and flow reactor) under their respective conditions. This could be useful in evaluating the effect phenols have on carbonaceous deposit formation in fuels under thermal oxidative conditions.
- Testing the effect that zinc has on fuel stability could be extended to other reactors namely, the QCM, flask reactor and fluidised reactor. Furthermore reactions in a flow reactor could be done at a higher fuel temperature to accelerate deposition.
- In sand bath experiments, the reactor bomb could be modified to permit determination of headspace oxygen pressure pre and post an experiment. This would enable one to relate the quantity of carbonaceous deposits formed to oxygen consumption (one would perceptibly vary the initial oxygen pressure in the bomb prior across several experiments).
- Speeding up deposit formation by using elevated temperatures may cause cracking. An alternative would be to do longer testing at lower temperatures. The flow reactor (configured in a closed loop system) could be used to simulate fuel that recirculates from the tank to the diesel injector equipment and back to the tank. Fuel that is exposed to fuel injectors and recirculated back to the tank can experience temperatures above 100°C. The recirculated fuel can also be characterised using

continuous FTIR or UV-Vis flow cells to provide kinetic information about the formation of deposition products.

- TGA-MS data should be compared with data obtained from an instrument such as a carbon analyser.
- The use of MALDI-MS for the characterisation of deposits should be investigated. This result may be compared to ESI-MS. Furthermore size exclusion chromatography could be used to monitor dimerization and trimerisation.
- Oxidative TGA can be extended to obtain oxidation kinetic parameters, *e.g.* activation energy, of the stressed fuels and/or carbonaceous deposits of the fuels.
- Negative ESI (-) MS could be performed on methanol fractions of stressed fuels, from the flask reactor, to give a more complete picture of all possible polar soluble macromolecular species that are formed during thermal oxidative stressing of fuel. ESI (-) MS would highlight proton donating species such as acids, which are one of the main products of fuel oxidation.
- Finally the test fuel matrix could be extended to include neat RME and SME (B100), and a variety of blend concentrations.

11 List of references

[1] B. R. Stanmore, J. F. Brilhac and P. Gilot, “The oxidation of soot: a review of experiments, mechanisms,” *Carbon,* vol. 39, p. 2247–2268, 2001.

[2] D. L. Poster, M. M. Schantz, L. C. Sander and S. A. Wise, “Analysis of polycyclic aromatic hydrocarbons (PAHs) in environmental samples: a critical review of gas chromatographic (GC) methods,” *Anal. Bioanal. Chem.,* vol. 386, pp. 859-881, 2006.

[3] R. Ballesteros, “Determination of PAHs in diesel particulate matter using thermal extraction and solid phase micro-extraction,” *Atmos. Env.,* vol. 43, pp. 655-662, 2009.

[4] D. Todorović and Z. Zdravkovski, “Development of a trap for fuel exhaust particulate matter under driving conditions and GC-MS method for their analysis,” *Macedonian J. Chem. & Chem. Eng.,* vol. 30, pp. 97-106, 2011.

[5] E. Borras, L. A. Tortajada-Genaro, M. Vázquez and B. Zielinska, “Polycyclic aromatic hydrocarbon exhaust emissions from different reformulated diesel fuels and engine operating conditions,” *Atmos. Env.,* vol. 43, p. 5944–5952, 2009.

[6] B. D. Batts and A. Z. Fathoni, “A literature review on fuel stability studies with particular emphasis on diesel oil,” *Energy & Fuels,* vol. 5, pp. 2-21, 1991.

[7] O. Gül, L. Rudnick and H. Schobert, “Morphology of carbon deposits as a function of coal-derived jet fuel chemical composition,” *Prepr. Pap.-Am. Chem. Soc., Div. Fuel Chem.,* vol. 29, no. 2, pp. 773-775, 2004.

[8] O. Altin and S. Eser, “Carbon deposit formation from thermal stressing of petroleum fuels,” *Prepr. Pap. - Am. Chem. Soc., Div. Fuel Chem.,* vol. 49, pp. 764-766, 2004.

[9] A. Birgel, N. Ladommatos, P. Aleiferis, S. Zülch, N. Milovanovic, V. Lafon, A. Orlovic, P. Lacey and P. Richards, “Deposit formation in the holes of diesel injector nozzles: A critical review,” *SAE 2008-01-2383,* 2008.

[10] R. Venkataraman and S. Eser, “Characterization of deposits formed on diesel injectors in field test and form thermal oxidative degradation of n-hexadecane in a laboratory reactor,” *Chem. Cent. J.,* vol. 25, p. 25, 2008.

[11] O. Altin and S. Eser, “Analysis of solid deposits from thermal stressing of a JP-8

fuel on different tube surfaces in a flow reactor," *Ind. Eng. Chem. Res.,* vol. 40, pp. 596-603, 2001.

[12] O. Altin and S. Eser, "Characterization of carbon deposits from jet fuel on Inconel 600 and Inconel X surfaces," *Ind. Eng. Chem. Res.,* vol. 39, pp. 642-645, 2000.

[13] H. N. Sharma, L. Pahalagedara, A. Joshi, S. L. Suib and A. B. Mhadeshwar, "Experimental study of carbon black and diesel engine soot oxidation kinetics using thermogravimetric analysis," *Energy & Fuels,* vol. 26, pp. 5613-5625, 2012.

[14] T. Nishiyama and N. Emori, "Commercialisation of a diesel particulate filter (DPF)," *Komatsu Technical Report,* vol. 48, pp. 23-28, 2002.

[15] A. Stanislaus, A. Marafi and M. S. Rana, "Recent advances in the science and technology of ultra low sulfur diesel (ULSD) production," *Catalysis Today,* vol. 153, p. 1–68, 2010.

[16] S. C. Gad and C. P. Chengelis, Acute toxicology testing, 2nd ed., Amsterdam, NL: Elsevier, 1998.

[17] J. Bacha, J. Freel , A. Gibbs, L. Gibbs, G. Hemighaus, K. Hoekman and J. Horn, Diesel fuels technical review, San Ramon, CA, USA: Chevron, 2007.

[18] SAPIA, Petrol and diesel in South Africa and the impact on air quality, Johannesburg, RSA: SAPIA, 2008, pp. 81-122.

[19] S. Gad, Diesel Fuel, Acute Toxicology Testing, 2005, p. 19.

[20] "Fuel regulations USA," [Online]. Available: http://www.dieselnet.com/standards/us/fuel.php#sulfur. [Accessed February 2012].

[21] "Fuel regulations: European Union," [Online]. Available: http://www.dieselnet.com/standards/eu/fuel.php. [Accessed February 2012].

[22] A. Keskin, A. Yasar, M. Guru and D. Altiparmak, "Usage of methyl ester of tall oil fatty acids and resinic acids as alternative diesel fuel," *Energy Conservation & Management,* vol. 51, pp. 2863-2868, 2010.

[23] R. Caprotti, S. Takaharu and D. Masahiro, "Impact of diesel fuel additives on vehicle performance," *SAE 2008-01-1600,* 2008.

[24] M. Matzke, U. Litzow, A. Jess, R. Caprotti and G. Balfour, "Diesel lubricity requirements of future fuel injection equipment," *SAE Int. J. Fuels Lubr.,* vol. 2,

pp. 273-286, 2009.

[25] R. H. Barbour, D. J. Rickeard and N. G. Elliott, “Understanding diesel lubricity,” *SAE Transactions,* vol. 109, pp. 1556-1566, 2000.

[26] S. Grgelewicz, M. Stankiewicz, F. A. Oko and I. Surawska, “Esters of dicarboxylic acids as additives for lubricating oils,” *Tribol. Int.,* vol. 39, pp. 560-564, 2006.

[27] M. Maricq, “Chemical characterization of particulate emissions from diesel engines: A review,” *Aer. Sci.,* vol. 38, p. 1079–1118, 2007.

[28] H. Burtscher, “A review on physical characterization of soot,” *Aerosol Sci.,* vol. 36, p. 896–932, 2005.

[29] M. S. Celnik, M. Sander, A. Raj, R. H. West and M. Kraft, “Modelling soot formation in a premixed flame using an aromatic-site soot model and an improved oxidation rate,” *Proc. Combust. Inst.,* vol. 32, pp. 639-646, 22 January 2010.

[30] I. Glassman and R. A. Yetter, Combustion, 4th ed., Burlington, MA, USA: Academic Press, 2008.

[31] A. Clague, J. Donnet, T. Wang and J. Peng, “A comparison of diesel engine soot with carbon black,” *Carbon,* vol. 37, pp. 1553-1565, 1999.

[32] A. Oberlin, “High resolution TEM studies of carbonization and graphitization,” in *Chemistry and physics of carbon*, vol. 22, P. Thrower, Ed., New York, NY, USA, Dekker, 1989.

[33] M. Lapuerta, F. J. Martos and J. M. Herrerosa, “Effect of engine operating conditions on the size of primary particles composing diesel soot agglomerates,” *Aer. Sci.,* vol. 38, pp. 455-466, 2007.

[34] M. Lapuerta, R. Ballesteros and F. J. Martos, “A method to determine the fractal dimension of diesel soot agglomerates,” *J. Coll. Interf. Sci.,* vol. 303, p. 149–158, 2006.

[35] S. Collura, N. Chaoui, B. Azambre, G. Finqueneisel, O. Heintz, A. Krzton, A. Koch and J. V. Weber, “Influence of the soluble organic fraction on the thermal behaviour, texture and surface chemistry of diesel exhaust,” *Carbon,* vol. 43, p. 605–613, 2005.

[36] M.-L. Yu and R. A. Hites, “Identification of organic compounds on diesel engine soot,” *Anal. Chem.,* vol. 53, pp. 951-954, 1981.

[37] D. H. Phillips, “Polycyclic aromatic hydrocarbons in the diet,” *Mutation Research,* vol. 443, p. 139–147, 1999.

[38] G. Lyons, “Polyaromatic Hydrocarbons (PAHs),” August 1997. [Online]. Available: http://www.wwf.org.uk/filelibrary/pdf/mu_32.pdf. [Accessed July 2012].

[39] N. Saim, J. R. Dean, M. P. Abdullah and Z. Zakaria, “Extraction of polycyclic aromatic hydrocarbons from contaminated soil using Soxhlet extraction, pressurised and atmospheric microwave-assisted extraction, super critical fluid extraction and accelerated solvent extraction,” *J. Chrom. A,* vol. 791, p. 361–366, 1997.

[40] M. O. Jonker and A. A. Koelmans, “Extraction of polycyclic aromatic hydrocarbons from soot and sediment: solvent evaluation and implications for sorption mechanism,” *Environ. Sci. Technol,* vol. 36, pp. 4107-4113, 2002.

[41] R. Romero, R. Sienra and P. Richter, “Efficient screening method for determination of polycyclic aromatic hydrocarbons (PAHs) in airborne particles,” *Atmos. Env.,* vol. 36, p. 2375–2381, 2002.

[42] Japanese Environmental Agency, “Strategic Programs on Environmental Endocrine Disruptors '98,” 1998. [Online]. Available: http://www.env.go.jp/en/chemi/ed/bda_speed96.pdf. [Accessed 11 June 2012].

[43] “Phthalates: Toxicity and Exposure Assessment for Children’s Health,” 2007. [Online]. Available: http://www.epa.gov/teach/chem_summ/phthalates_summary.pdf. [Accessed October 2012].

[44] T. Murahashi, S. Sasaki and T. Nakajima, “Determination of endocrine disruptors in automobile exhaust particulate matter,” *J. Health Sci.,* vol. 49, pp. 72-75, 2003.

[45] M. Diaby, M. Sablier, A. Le Negrate, M. El Fassi and J. Bocquet, “Understanding carbonaceous deposit formation resulting from engine oil degradation,” *Carbon,* vol. 47, pp. 355-366, 2009.

[46] J. Barker, P. Richards, D. Pinch and B. Cheeseman, “Temperature programmed oxidation as a technique for understanding diesel fuel system deposits,” *SAE Int. J. Fuels Lubr.,* vol. 3, pp. 85-99, 2010.

[47] J. Barker, P. Richards, C. Snape and W. Meredith, “Diesel injector deposits – an issue that has evolved with engine technology,” *SAE 2011-01-1923,* 2011.

[48] J. Keck, "DI-Diesel Engine - Injection Nozzle Coking," 2008. [Online]. Available: http://cdm.unfccc.int/filestorage/U/6/0/U60DS3HTCQF9PW1J2KGXB5E7IML48A/Additional%20information%3A%20Annex%201.pdf?t=NEF8bWp5ZndufDChRLgBY2BZozpTClxvb1fW. [Accessed February 2013].

[49] P. Aksoy, O. Gul, R. Cetiner, D. A. Fonseca, M. Sobkowiak, S. Falcone-Miller, B. D. Miller and B. Beaver, "Insight into the mechanisms of middle distillate fuel oxidative degradation. Part 2: On the relationship between jet fuel thermal oxidative deposit, soluble macromolecular oxidatively reactive species, and smoke point," *Energy & Fuels,* vol. 23, p. 2047–2051, 2009.

[50] C. G. Kabana, S. Botha, C. Schmucker, C. Woolard and B. Beaver, "Oxidative stability of middle distillate fuels. Part 1: Exploring the soluble macromolecular oxidatively reactive species (SMORS) mechanism with jet fuels," *Energy & Fuels,* vol. 25, p. 5145–5157, 2011.

[51] D. Hardy and M. Wechter, "Characterization of Soluble Macromolecular Oxidatively Reactive Species (SMORS) from middle distillate diesel fuels: Their origin and role in instability," *Energy Fuels,* vol. 8, pp. 782-787, 1994.

[52] M. Sobkowiak, J. Griffith, B. Wang and B. Beaver, "Insight into the mechanisms of middle distillate fuel oxidative degradation. Part 1: on the role of phenol, indole, and carbazole derivatives in the thermal oxidative stability of Fischer-Tropsch/Petroleum jet fuel blends," *Energy Fuels,* vol. 23, pp. 2041-2046, 2009.

[53] A. R. Mohan, PhD Dissertation: Metal organic chemical vapor deposition of environmental barrier coatings for the inhibition of solid deposit formation from heated jet fuel, State College, PA, USA, The Pennsylvania State University: Pennsylvania State University, 2011.

[54] A. Bouaid, M. Martinez and J. Aracil, "Long storage stability of biodiesel from vegetable and used frying oils," *Fuel,* vol. 87, pp. 2355-2373, 2007.

[55] G. Knothe and R. O. Dunn, "Dependence of oil stability index of fatty compounds on their structure and concentration and presence of metals," *J. Am. Oil Chem. Soc.,* vol. 80, pp. 1021-1026, 2003.

[56] R. O. Dunn, "Effect of antioxidants on the oxidative stability of methyl soyate (biodiesel)," *Fuel Process Technol.,* vol. 86, pp. 1071-1085, 2005.

[57] G. Knothe, "Some aspects of biodiesel stability," *Fuel Process technol.,* vol. 88, pp. 669-677, 2007.

[58] S. Jain and M. Sharma, "Prospects of biodiesel from Jatropha in India: a review,"

Renew. Sustainable Energy Rev., vol. 14, pp. 761-771, 2010.

[59] T. Ogawa, S. Kajiya, S. kosaka, I. Tajima, M. Yamamoto and M. Okada, “Analysis of oxidative deterioration of biodiesel fuel,” *SAE Technical Paper Series 2008-01-2502,* 2008.

[60] G. Knothe, “Analysis of oxidized biodiesel by 1H-NMR and effect of contact area with air,” *Eur. J. Lipid Sci. Technol.,* vol. 108, pp. 493-500, 2006.

[61] H. L. Fang and R. L. McCormick, “Spectroscopic study of biodiesel degradation,” *SAE Technical Paper Series 2006-01-3300,* 2006.

[62] M. Husnawan, H. H. Masjuki, T. M. I. Mahlia and M. G. Saifullah, “Thermal analysis of cylinder head carbon deposits from single cylinder diesel engine fueled by palm oil–diesel fuel emulsions,” *Appl. Energy,* vol. 86, p. 2107–2113, 2009.

[63] F. R. Mayo and B. Y. Lan, “Gum and deposit formation from jet turbine and diesel fuels at 130 degrees celcius,” *Ind. Eng. Chem. Prod. Res. Dev.,* vol. 25, pp. 333-348, 1986.

[64] A. R. Mohan and S. Esir, “Analysis of carbonaceous solid deposits from thermal oxidative stressing of Jet-A fuel on iron- and nickel-based alloy surfaces,” *Ind. Eng. Chem. Res.,* vol. 49, p. 2722–2730, 2010.

[65] S. Zabarnick, “Studies of jet fuel thermal stability and oxidation using a quartz crystal microbalance and pressure measurements,” *Ind. Eng. Chem. Res,* vol. 33, pp. 1348-1354, 1994.

[66] E. Klavetter, S. Martin and K. Wessendorf, “Monitoring jet fuel thermal stability using a quartz crystal microbalance,” *Energy Fuels,* vol. 7, pp. 582-588, 1993.

[67] ASTM D7739-11: Standard practice for thermal oxidative stability measurement via quartz crystal microbalance, West Conshohocken, PA, USA: ASTM International, 2011.

[68] A. W. Coats and J. P. Redfern, “Thermogravimetric Analysis A Review,” *Analyst,* vol. 88, pp. 906-924, 1963.

[69] J. McCarty and H. Wise, “Hydrogenation of surface carbon on alumina-supported nickel,” *J. Catal.,* vol. 57, pp. 406-416, 1979.

[70] P. Marecot, A. Akhachane, C. Micheaud and J. Barbier, “Deactivation by coking of supported palladium catalysts. Effect of time and temperature,” *Appl. Catal. A: Gen.,* vol. 169, pp. 189-196, 1998.

[71] K. Wanner and G. Höfner, Eds., Mass spectrometry in medicinal chemistry, Weinheim, DE: WILEY-VCH, 2007, pp. 14-15.

[72] K. Qian, K. E. Edwards, J. H. Diehl and L. A. Green, "Fundamentals and applications of electrospray ionization mass spectrometry for petroleum characterization," *Energy & Fuels,* vol. 18, pp. 1784-1791, 2004.

[73] C. Dass, "Electrospray ionization," in *Fundamentals of contemporary mass spectrometry*, Hoboken, NJ, USA, John Wiley & Sons, 2007.

[74] M. Commodo, I. Fabris, C. P. T. Groth and O. L. Gulder, "Analysis of aviation fuel thermal oxidative stability by electrospray ionization mass spectrometry (ESI-MS)," *Energy & Fuels,* vol. 25, pp. 2142-2150, 2011.

[75] C. E. Rostad, "Screening of polar components of petroleum products by electrospray ionization mass spectrometry," *Energy & Fuels,* vol. 19, pp. 992-997, 2005.

[76] C. A. Hughey, C. L. Hendrickson, R. P. Rodgers and A. G. Marshall, "Elemental composition analysis of processed and unprocessed diesel fuel by electrospray ionization Fourier Transform ion cyclotron resonance mass spectrometry," *Energy & Fuels,* vol. 15, pp. 1186-1193, 2001.

[77] R. R. Catharino, H. M. S. Milagre, S. A. Saraiva and C. M. Garcia, "Biodiesel typification and quality control by direct infusion electrospray ionization mass spectrometry fingerprinting," *Energy & Fuels,* vol. 21, p. 3698–3701, 2007.

[78] J. Byatt-Smith, R. Day, O. Harlen, J. Lister, S. L. Smith, C. P. Please, R. Stone, S. D. Howison and A. Fowler, *Temperature of diesel fuel spray at injector nozzle hole exit,* Aus: Perkins Technologies, 1996.

[79] R. Caprotti, A. Breakspear, O. Graupner and T. Klaua, "Detergency requirements of future diesel injection systems," *SAE Technical Paper Series 2005-01-3901,* 2005.

[80] R. Caprotti, A. Breakspear, O. Greipner, T. Klaua and O. Kohnen, "Diesel injector deposits potential in future fueling systems," *SAE Technical Paper Series 2006-01-3359,* 2006.

[81] M. Ikemoto, K. Omae, K. Nakai, R. Ueda, N. Kakehashi and K. Sunami, "Injection nozzle coking mechanism in common-rail diesel engine," *SAE Technical Paper Series 2011-01-1818,* 2011.

[82] A. Velaers, S. De Goede, R. Burnham and C. Woolard, "Injector fouling performance and solubility of GTL diesel doped with zinc," *SAE Int. J. Lubr.,* vol.

6, no. 1, pp. 276-288, 2013.

[83] R. Barbour, R. Quigley, D. Browne and A. Panesar, “A comparison of Peugeot DW10 dynamometer and vehicle engine performance,” in *8th International Colloquiom on Fuels*, Esslingen, 2011.

[84] W. Focke, I. Van der Westhuizen, A. Lofté Grobler, T. Ntshoane, J. Reddy and A. Luyt, “The effect of synthetic antioxidants on the oxidative stability of biodiesel,” *Fuel,* vol. 94, pp. 227-233, 2012.

[85] K. Oukebdane, F. Portet-Koltalo, N. Machoura, F. Dionnet and P. L. Desbène, “Comparison of hot Soxhlet and accelerated solvent extractions,” *Talanta,* vol. 82, p. 227–236, 2010.

[86] NIST/EPA/NIH Mass Spectral Library, Gaithersburg, MD, USA: National Institute of Standards and Technology, 2008.

[87] P. C. Sadek, The HPLC solvent guide, 2nd ed., New York, NY, USA: John Wiley & Sons, 2002, pp. 10-300.

[88] A. S. G.A. Stratakis, “Thermogravimetric analysis of soot emitted by a modern diesel engine run on catalyst-doped fuel,” *Combustion and Flame ,* vol. 132, pp. 157-169, 2003.

[89] S. Collura, “Influence of the soluble organic fraction on the thermal behaviour, texture and surface chemistry of diesel exhaust,” *Carbon,* no. 43, p. 605–613, 2005.

[90] J. Rodríguez-Fernandez, F. Oliva and R. A. Vazquez, “Characterization of the Diesel Soot Oxidation Process through an Optimized Thermogravimetric Method,” *Energy Fuels,* 2011.

[91] D. Su, R. Jentoft, J. Müller, D. Rothe, E. Jacob, C. Simpson, Z. Tomovic', K. Müllen, A. Messerer, U. Poschl, R. Niessner and R. Schlogl, “Microstructure and oxidation behaviour of Euro IV diesel engine soot: a comparative study with synthetic model soot substances,” *Catal. Today,* vol. 90, pp. 127-132, 2004.

[92] C. M. Hansen, Hansen solubility parameters: A user's handbook, 2nd ed., Boca Raton, FL, USA: CRC Press, 2007.

[93] K. Mannistu, H. Yarranton and J. Masliyah, “Solubility modelling of asphaltenes in organic solvents,” *Energy Fuels,* vol. 11, pp. 615-622, 1997.

[94] J. Leifeld, “Thermal stability of black carbon characterised by oxidative

differential scanning calorimetry," *Org. Geochem.,* vol. 38, pp. 112-127, 2007.

[95] S. Japar, A. Szkariat, R. Gorse, E. Heyerdahl, R. Johnson, J. Rau and J. Huntzicker, "Comparison of solvent extraction and thermal-optical carbon analysis methods: application to disel vehicale exhaust aerosol," *Environ. Sci. Technol.,* pp. 231-234, 1984.

[96] M. A. Fazal, A. S. M. A. Haseeb and H. H. Masjuki, "Biodiesel feasibility study: An evaluation of material compatibility; performance; emission and engine durability," *Renewable & Sustainable Energy Reviews,* vol. 15, pp. 1314-1324, 2011.

[97] G. Knothe, "Dependence of biodiesel fuel properties on the structure of fatty acid alkyl esters," *Fuel Process Technol.,* vol. 86, pp. 1059-1070, 2005.

[98] M. Frenklach, "Reaction mechanism of soot formation in flames," *Phys. Chem. Chem. Phys.,* vol. 4, pp. 2028-2037, 2002.

[99] Y. Chien, M. Lu, M. Chai and F. Boreo, "Characterization of biodiesel and biodiesel particulate matter by TG, TG-MS and FTIR," *Energy Fuels,* vol. 23, pp. 202-206, 2009.

[100] R. Umer, A. Farooq, J. Amer and N. Haq, "Jatropha Curcas seed oil as a viable source for biodiesel," *Pak. J. Bot.,* vol. 42, pp. 575-582, 2010.

[101] B. Stuart, "Infrared Spectroscopy: Fundamentals and Applications," New York, NY, USA, 2004.

[102] R. Quigley, R. Barbour and E. Fahey, "A study of the internal diesel injector deposit phenomenon," in *Proceedings of Fuels: conventional and future energy for automobiles, 8th International Colloquium*, Esslingen, DE, 2011.

[103] E. G. Hammond, L. A. Johnson and C. Su, "Soybean oil," 2005. [Online]. Available: http://uqu.edu.sa/files2/tiny_mce/plugins/filemanager/files/4281709/84607_28.pdf . [Accessed March 2013].

12 Appendices

12.1 APPENDIX A – Soot extracts

12.1.1 SOF data

Table 12.1: The mean SOF of six solvents and their corresponding standard deviations (N=5)

Solvent	Mean SOF (wt %)	Standard deviation of the mean (%)	Coefficient of variation (%)
Dichloromethane	4.10	0.34	8.3
Methanol	4.76	0.18	3.8
Acetone	4.36	0.24	5.5
Toluene	2.53	0.24	9.5
Cyclohexane	1.69	0.23	13.6
Hexane	0.95	0.21	22.1

Table 12.2: Chemical speciation of the hexane extract of commuter bus soot

Retention time	**Area**	**Area (%)**	**% Match**	**Name**	**Class**
3.663	3348472	5.17%	95	n-Decane	PARAFFIN
3.683	1045557	1.61%	95	1,3,5-Trimethylbenzene	MONOAROMATIC
3.7	357945	0.55%	90	1,2,3-Trimethyl benzene	PARAFFIN
3.783	246467	0.38%	86	2,5-Dimethylnonane	PARAFFIN
3.842	444363	0.69%	72	Malonic acid, heptadecyl 4-methylpent-2-yl ester	ESTER
3.882	523615	0.81%	94	2,6-Dimethylnonane	PARAFFIN
3.942	267703	0.41%	75	2,6,11-Trimethyldodecane	PARAFFIN
3.985	874395	1.35%	92	1,2,4-Trimethylbenzene	MONOAROMATIC
4.017	153277	0.24%	91	2,9-Dimethyldecane	PARAFFIN
4.06	485926	0.75%	91	(4-Methylpentyl)cyclohexane	CYCLOPARAFFIN
4.091	65875	0.10%	67	Sulfurous acid, cyclohexylmethyl tridecyl ester	UNCLASSIFIED
4.146	898207	1.39%	70	o-Vinyltoluene	MONOAROMATIC
4.194	211092	0.33%	83	4-Methyl-dodecan-1-ol	OTHER OXYGENATE
4.239	1059252	1.63%	96	m-Diethylbenzene	MONOAROMATIC
4.276	3105086	4.79%	95	3-n-Propyltoluene	MONOAROMATIC
4.34	7159440	11.05%	92	p-Ethylethylbenzene	MONOAROMATIC
4.408	356463	0.55%	71	Decalin	CYCLOPARAFFIN
4.432	1236319	1.91%	97	2-Propyltoluene	MONOAROMATIC
4.542	2688513	4.15%	96	3-Ethyl-o-xylene	MONOAROMATIC
4.574	2439364	3.76%	96	1-Isopropyl-3-methylbenzene	MONOAROMATIC
4.639	5344056	8.25%	96	1,3-Dimethyl-2-ethyl benzene	MONOAROMATIC
4.716	2062161	3.18%	94	2,9-Dimethyldecane	PARAFFIN
4.794	217623	0.34%	83	1-Isobutyl-4-methylbenzene	MONOAROMATIC
4.847	1153892	1.78%	92	3-Ethyl-o-xylene	MONOAROMATIC
4.977	3154572	4.87%	93	1,2,3,4-Tetramethylbenzene	MONOAROMATIC
5.017	3167217	4.89%	96	1,2,4,5-Tetramethylbenzene	MONOAROMATIC
5.143	566135	0.87%	72	p-Toluic acid, 5-tridecyl ester	ESTER
5.193	211257	0.33%	85	1,3-Diethyl-5-methylbenzene	MONOAROMATIC
5.242	1342766	2.07%	88	2-Allyltoluene	MONOAROMATIC
5.275	96181	0.15%	85	1-Sec-butyl-4-methylbenzene	MONOAROMATIC
5.339	2471415	3.81%	82	1,2-Dimethyl-3-ethylbenzene	MONOAROMATIC
5.396	308448	0.48%	86	1-Methyl-3,5-diethylbenzene	MONOAROMATIC
5.433	373360	0.58%	90	2,3-Dimethylundecane	PARAFFIN
5.482	651518	1.01%	94	Tetralin	HYDROCYCLIC AROMATIC
5.548	316819	0.49%	91	1-Sec-butyl-4-methylbenzene	MONOAROMATIC
5.642	204983	0.32%	88	1-Methyl-2-pentylcyclohexane	CYCLOPARAFFIN
5.675	164950	0.25%	64	Tricyclo[4.3.0.0(7,9)]non-3-ene, 2,2,5,5,8,8-hexamethyl-	UNCLASSIFIED
5.727	2169804	3.35%	96	n-Dodecane	PARAFFIN
5.767	2150664	3.32%	92	Naphthalene	PAH
5.8	101090	0.16%	72	4,6-Dimethylindane	HYDROCYCLIC AROMATIC
5.839	374762	0.58%	94	2,6-Dimethylundecene	PARAFFIN
5.884	142096	0.22%	82	1-Ethyl-3-isopropylbenzene	MONOAROMATIC
5.916	46454	0.07%	75	2,4-Dimethylcyclohexanol,	OTHER OXYGENATE
5.98	127239	0.20%	83	2-Methyl-1-decanol,	OTHER OXYGENATE
6.024	233275	0.36%	77	1,2,4-Triethylbenzene	MONOAROMATIC
6.1	87643	0.14%	76	Oxalic acid, allyl pentadecyl ester	ESTER

6.164	273688	0.42%	79	(1,3-Dimethylbutyl)cyclohexane	CYCLOPARAFFIN
6.231	276219	0.43%	88	2,7-Dimethylundecane	PARAFFIN
6.288	144393	0.22%	86	4-Methyldodecane	PARAFFIN
6.337	278758	0.43%	75	2,3,6-Trimethyldecane	PARAFFIN
6.4	489130	0.75%	94	2,7,10-Trimethyldodecane	PARAFFIN
6.444	90982	0.14%	83	4,7-Dimethylindane	HYDROCYCLIC AROMATIC
6.506	166899	0.26%	79	6-Methyltetralin	HYDROCYCLIC AROMATIC
6.552	34350	0.05%	63	2,4,4,6-Tetramethyl-6-phenyl-2-heptene	UNCLASSIFIED
6.603	111224	0.17%	66	4-Ethylbenzoic acid, 6-ethyl-3-octyl ester	UNCLASSIFIED
6.683	1128450	1.74%	93	2-Methyl-n-tridecane	PARAFFIN
6.746	186969	0.29%	75	5-Methyltetralin	HYDROCYCLIC AROMATIC
6.835	422289	0.65%	92	2-Methylnaphthalene	PAH
6.932	23226	0.04%	75	Oxalic acid, decyl propyl ester	ESTER
6.987	162721	0.25%	87	1-Methylnaphthalene	PAH
7.008	77187	0.12%	72	2,6-Dimethyltetralin	HYDROCYCLIC AROMATIC
7.051	25226	0.04%	65	2,5-Octadiene, 3,4,5,6-tetramethyl	UNCLASSIFIED
7.141	308359	0.48%	82	Dodecyl pentanoate	ESTER
7.202	232542	0.36%	82	Butyric acid, 4-pentadecyl ester	ESTER
7.259	97121	0.15%	89	3-Ethylundecane	PARAFFIN
7.324	96728	0.15%	83	3-Methyltridecane	PARAFFIN
7.35	132721	0.20%	83	2,6,11-Trimethyldodecane	PARAFFIN
7.421	176800	0.27%	92	Propanoic acid, 2-methyl-, 3-hydroxy-2,4,4-trimethylpentyl ester	ESTER
7.482	19431	0.03%	74	(1-Butylhexyl)cyclohexane	CYCLOPARAFFIN
7.533	19090	0.03%	81	1-Hexyl-3-methylcyclopentane	CYCLOPARAFFIN
7.586	662838	1.02%	97	n-Tetradecane	PARAFFIN
7.65	48842	0.08%	63	Oxalic acid, butyl neopentyl ester	UNCLASSIFIED
7.716	23528	0.04%	65	Pentobarbituric acid	UNCLASSIFIED
7.832	39947	0.06%	74	1,2-Dimethylnaphthalene	PAH
7.875	10198	0.02%	87	2-Methylbutyl pentanoate	ESTER
7.943	53841	0.08%	65	1,3-Dimethylnaphthalene	UNCLASSIFIED
7.992	71322	0.11%	71	6-Ethylundecane	PARAFFIN
8.022	26415	0.04%	82	5-Methylnonane	PARAFFIN
8.08	100172	0.15%	91	2,8-Dimethylundecane	PARAFFIN
8.129	55226	0.09%	91	3,8-Dimethylundecane	PARAFFIN
8.185	26827	0.04%	85	3,7-Dimethylnonane	PARAFFIN
8.248	16258	0.03%	71	2,3,5-Trimethyldecane	PARAFFIN
8.292	10476	0.02%	81	3-Ethyl-4-methylheptane	PARAFFIN
8.375	12913	0.02%	77	Oxalic acid, allyl pentadecyl ester	ESTER
8.384	12651	0.02%	82	Sulfurous acid, 2-ethylhexyl isohexyl ester	SULFATE/SULFITE/SULFONE
8.437	158099	0.24%	93	n-Pentadecane	PARAFFIN
8.508	40966	0.06%	76	3-Methyltridecane	PARAFFIN
8.533	15498	0.02%	75	1,1-Dimethylcyclohexane	CYCLOPARAFFIN
8.598	7970	0.01%	75	Sulfurous acid, decyl hexyl ester	SULFATE/SULFITE/SULFONE
8.659	31452	0.05%	88	2,8-Dimethylundecane	PARAFFIN
8.708	24600	0.04%	87	n-Tridecane	PARAFFIN
8.8	43089	0.07%	83	Sulfurous acid, hexyl pentyl ester	SULFATE/SULFITE/SULFONE
8.848	173255	0.27%	93	5-Methylpentadecane	PARAFFIN
8.905	40597	0.06%	80	2,3,6,7-Tetramethyloctane	PARAFFIN
8.953	54435	0.08%	86	3-Ethyl-2,7-dimethyloctane	PARAFFIN

9.008	74288	0.11%	88	3,7-Dimethylnonane	PARAFFIN
9.134	17564	0.03%	70	6-Methyl-1-octene	PARAFFIN
9.187	47044	0.07%	80	Propanoic acid, 2-methyl-, 1-(1,1-dimethylethyl)-2-methyl-1,3-propanediyl ester	ESTER
9.244	663054	1.02%	93	n-Hexadecane	PARAFFIN
9.275	90831	0.14%	74	Di-n-dodecyl phthalate	ESTER
9.392	5793	0.01%	73	Sulfurous acid, cyclohexylmethyl isobutyl ester	SULFATE/SULFITE/SULFONE
9.442	11205	0.02%	82	Sulfurous acid, 2-ethylhexyl hexyl ester	SULFATE/SULFITE/SULFONE
9.501	5374	0.01%	81	Sulfurous acid, butyl isohexyl ester	SULFATE/SULFITE/SULFONE
9.581	50168	0.08%	88	2,8-Dimethylundecane	PARAFFIN
9.581	75759	0.12%	88	2,8-Dimethylundecane	PARAFFIN
9.631	6425	0.01%	83	n-Valeric anhydride	ESTER
9.672	19079	0.03%	85	4,5-Dimethyloctane	PARAFFIN
9.733	19906	0.03%	81	Oxalic acid, allyl nonyl ester	ESTER
9.79	9377	0.01%	83	3,7-Dimethylnonane	PARAFFIN
9.817	7394	0.01%	82	(2-Ethylbutyl)benzene	MONOAROMATIC
9.887	27437	0.04%	85	3,7-Dimethyldecane	PARAFFIN
9.949	16462	0.03%	81	6-Ethyl-2-methyloctane	PARAFFIN
10.008	116176	0.18%	91	2,6,10,15-Tetramethylheptadecane	PARAFFIN
10.041	23814	0.04%	86	2,7-Dimethyloctane	PARAFFIN
10.092	11913	0.02%	67	Sulfurous acid, butyl isohexyl ester	SULFATE/SULFITE/SULFONE
10.168	39469	0.06%	76	5-Isobutylnonane	PARAFFIN
10.19	38670	0.06%	85	Oxalic acid, allyl pentadecyl ester	ESTER
10.243	39302	0.06%	86	n-Tridecane	PARAFFIN
10.317	49529	0.08%	83	5-Methyldodecane	PARAFFIN
10.369	93039	0.14%	88	5-Methyldodecane	PARAFFIN
10.423	14523	0.02%	85	3,3,4-Trimethyldecane	PARAFFIN
10.475	36305	0.06%	85	2,8-Dimethylundecane	PARAFFIN
10.523	124290	0.19%	91	3-Methylheptadecane	PARAFFIN
10.692	12264	0.02%	76	1,1-Dimethylcyclohexane	CYCLOPARAFFIN
10.735	153258	0.24%	91	2,6,10,15-Tetramethylheptadecane	PARAFFIN
10.767	14518	0.02%	76	Oxalic acid, allyl tridecyl ester	ESTER
11.022	9310	0.01%	85	2,8-Dimethylundecane	PARAFFIN
11.256	110648	0.17%	88	1,2-Benzenedicarboxylic acid, bis(2-methylpropyl) ester	ESTER
11.32	29386	0.05%	77	Sulfurous acid, decyl 2-propyl ester	SULFATE/SULFITE/SULFONE
11.35	6578	0.01%	75	2,4-Dimethyl-2,3-pentanediol	OTHER OXYGENATE
11.428	80824	0.12%	88	2,6,10,15-Tetramethylheptadecane	PARAFFIN
11.539	75274	0.12%	80	Sulfurous acid, decyl 2-propyl ester	SULFATE/SULFITE/SULFONE
11.581	15460	0.02%	84	3,7-Dimethylnonane	PARAFFIN
11.71	46703	0.07%	84	3,7-Dimethylundecane	PARAFFIN
11.751	24047	0.04%	87	3-Ethyl-2-methylhexane	PARAFFIN
11.85	29882	0.05%	86	2,8-Dimethylundecane	PARAFFIN
11.899	149681	0.23%	83	2-Methylicosane	PARAFFIN
12.012	10832	0.02%	78	2-Ethyl-1-decene	PARAFFIN
12.085	92746	0.14%	88	2,3,5,8-Tetramethyldecane	PARAFFIN
12.317	18197	0.03%	77	Sulfurous acid, hexyl nonyl ester	SULFATE/SULFITE/SULFONE
12.54	19918	0.03%	74	Oxalic acid, 2-ethylhexyl hexyl ester	ESTER
12.602	49747	0.08%	79	Heneicosane	PARAFFIN

13.039	11240	0.02%	71	Sulfurous acid, isohexyl 2-pentyl ester	SULFATE/SULFITE/SULFONE
13.119	42915	0.07%	75	2,3,4-Trimethyldecane	PARAFFIN
13.15	106878	0.16%	87	2-Methylicosane	PARAFFIN
13.319	82383	0.13%	87	2,6,10,15-Tetramethylheptadecane	PARAFFIN
13.78	64521	0.10%	70	Sulfurous acid, decyl 2-propyl ester	SULFATE/SULFITE/SULFONE
13.899	48328	0.07%	75	2-Methyldecane	PARAFFIN
13.945	138500	0.21%	84	10-Methylnonadecane	PARAFFIN
14.301	75722	0.12%	84	2,6,10,15-Tetramethylheptadecane	PARAFFIN
14.87	57445	0.09%	85	2,3,5,8-Tetramethyldecane	PARAFFIN
15.014	115254	0.18%	86	2,6,10,15-Tetramethylheptadecane	PARAFFIN
15.224	48268	0.07%	75	1,2-Benzenedicarboxylic acid, diisooctyl ester	ESTER
15.366	39816	0.06%	78	3,7-Dimethyldecane	PARAFFIN
15.506	27862	0.04%	78	4-Methyl-1-undecene	PARAFFIN
15.876	100025	0.15%	83	2,3,5,8-Tetramethyldecane	PARAFFIN
16.01	223855	0.35%	83	2,6,10,15-Tetramethylheptadecane	PARAFFIN

Table 12.3: Chemical speciation of the cyclohexane extract of commuter bus soot

Retention time	Area	Area (%)	% Match	Name	Class
3.517	32847	0.18%	88	2,5,6-Trimethyldecane	PARAFFIN
3.578	40820	0.22%	92	4-Ethyl-2,2,6,6-tetramethylheptane	PARAFFIN
3.609	133021	0.73%	78	1-Propylbenzene	AROMATIC
3.665	65781	0.36%	90	2,7-Dimethyloctane	PARAFFIN
3.71	251894	1.38%	95	m-Ethyltoluene	AROMATIC
3.757	231441	1.26%	76	m-Methylethylbenzene	AROMATIC
3.836	160366	0.88%	90	1,3,5-Trimethylbenzene	AROMATIC
3.891	19725	0.11%	88	Sulfurous acid, isobutyl pentyl ester	SULFATE/SULFITE/SULFONE
3.967	125316	0.68%	85	o-Methylethylbenzene	AROMATIC
3.99	512914	2.80%	96	2,2,4,6,6-Pentamethylheptane	PARAFFIN
4.043	64321	0.35%	78	3,7-Dimethyl-1-octene	PARAFFIN
4.182	1256773	6.87%	73	1,3,5-Trimethylbenzene	AROMATIC
4.278	25097	0.14%	82	2,2-Dimethyldecane	PARAFFIN
4.326	30842	0.17%	85	2,8-Dimethylundecane	PARAFFIN
4.387	85325	0.47%	75	sec-Butylbenzene	AROMATIC
4.417	31436	0.17%	86	4-Methyloctane	PARAFFIN
4.474	93421	0.51%	90	3,3,5-Trimethylheptane	PARAFFIN
4.543	100319	0.55%	72	2,2,6-Trimethyldecane	PARAFFIN
4.588	258817	1.41%	91	o-Ethyltoluene	AROMATIC
4.622	88806	0.49%	83	p-Cymene	AROMATIC
4.693	102094	0.56%	90	Butylcyclohexane	CYCLOPARAFFIN
4.723	66137	0.36%	79	4,5-Dimethylnonane	PARAFFIN
4.803	106617	0.58%	81	Indane	HYDROCYCLIC AROMATIC
4.848	31108	0.17%	85	Oxalic acid, isobutyl pentyl ester	ESTER
4.894	60090	0.33%	82	3-Ethyl-2,7-dimethyloctane	PARAFFIN
4.947	196346	1.07%	89	1,3-Diethylbenzene	AROMATIC
5	528017	2.88%	95	m-Propyltoluene	AROMATIC
5.044	46044	0.25%	87	4-Methyldecane	PARAFFIN
5.089	1359841	7.43%	91	p-Diethylbenzene	AROMATIC
5.211	303166	1.66%	85	sec-Butylbenzene	AROMATIC
5.273	39294	0.21%	91	2,2-Dimethyldecane	PARAFFIN
5.37	439610	2.40%	95	1,2-Dimethyl-3-ethylbenzene	AROMATIC
5.415	463345	2.53%	96	2-Ethyl-1,3-dimethylbenzene	AROMATIC
5.507	939721	5.13%	96	1,3-Dimethyl-2-ethylbenzene	AROMATIC
5.574	54459	0.30%	80	tert-Butylbenzene	AROMATIC
5.643	667783	3.65%	95	n-Dodecane	PARAFFIN
5.73	62363	0.34%	78	1-Isobutyl-4-methylbenzene	AROMATIC
5.792	204969	1.12%	83	1,2-Dimethyl-3-ethylbenzene	AROMATIC
5.851	73168	0.40%	73	Malonic acid, 2-ethylbutyl heptyl ester	ESTER
5.958	76425	0.42%	81	trans-Decalin, 2-methyl-	CYCLOPARAFFIN
5.985	459123	2.51%	96	Prehnitene	AROMATIC
6.039	645488	3.53%	95	1,2,4,5-Tetramethylbenzene	AROMATIC
6.131	15652	0.09%	80	Oxalic acid, isohexyl neopentyl ester	ESTER
6.175	31377	0.17%	74	cis-Decalin, 2-syn-methyl-	CYCLOPARAFFIN
6.239	116362	0.64%	76	(1,1-Dimethyldodecyl)benzene	AROMATIC
6.307	54615	0.30%	90	1-Methyl-3,5-diethylbenzene	AROMATIC
6.352	242722	1.33%	91	4-Methylindane	HYDROCYCLIC AROMATIC
6.418	67809	0.37%	78	2,4,6-Trimethyloctane	PARAFFIN
6.492	288802	1.58%	89	4-Methylindane	HYDROCYCLIC

					AROMATIC
6.499	292577	1.60%	88	1,3-Dimethyl-5-ethylbenzene	AROMATIC
6.59	143863	0.79%	74	3,5-Diethyltoluene	AROMATIC
6.69	454786	2.48%	91	Tetralin	HYDROCYCLIC AROMATIC
6.816	53250	0.29%	85	1-Sec-butyl-4-methylbenzene	AROMATIC
6.992	12176	0.07%	63	1-Propyl-1,2,3,4-tetrahydronaphthalene	UNCLASSIFIED
7.043	30946	0.17%	70	2,2-Dimethylindane	HYDROCYCLIC AROMATIC
7.096	1432812	7.83%	79	Naphthalene	PAH
7.142	45535	0.25%	76	1-Ethyl-4-isopropylbenzene	AROMATIC
7.268	15135	0.08%	90	Oxalic acid, butyl propyl ester	ESTER
7.299	13389	0.07%	65	1,2,3,4,5-Pentamethylbenzene	UNCLASSIFIED
7.481	17278	0.09%	70	(3-Neopentyl-4-pentenyl)benzene	AROMATIC
7.675	16556	0.09%	75	4-Ethylbenzoic acid, undec-2-enyl ester	ESTER
7.715	25405	0.14%	86	Pentylcyclohexane	CYCLOPARAFFIN
7.844	29783	0.16%	88	3,7-Dimethylnonane	PARAFFIN
7.927	27349	0.15%	64	1-Ethyl-1-methylindane	UNCLASSIFIED
8	27926	0.15%	86	Sulfurous acid, 2-ethylhexyl hexyl ester	SULFATE/SULFITE/SULFONE
8.093	48322	0.26%	86	3-Ethyl-2,7-dimethyloctane	PARAFFIN
8.185	12891	0.07%	74	6-Methyl-tetralin	HYDROCYCLIC AROMATIC
8.326	12424	0.07%	65	1,2,3,4,5-Pentamethylbenzene	UNCLASSIFIED
8.509	220861	1.21%	93	n-Tridecane	PARAFFIN
8.656	93890	0.51%	89	2-Methylnaphthalene	PAH
8.87	38180	0.21%	80	1-Methylnaphthalene	PAH
8.925	7097	0.04%	78	[1-(2-Phenylethyl)-2-propenyl]benzene	AROMATIC
8.997	16849	0.09%	73	tert-Butyl butyrate	ESTER
9.159	22867	0.12%	83	Oxalic acid, cyclohexyl isobutyl ester	ESTER
9.223	155166	0.85%	78	1-Methyloctyl butyrate	ESTER
9.283	15309	0.08%	78	3,3,4-Trimethylheptane	PARAFFIN
9.36	23619	0.13%	87	Sulfurous acid, 2-ethylhexyl hexyl ester	SULFATE/SULFITE/SULFONE
9.448	27527	0.15%	81	2,2,6,6-Tetramethylheptane	PARAFFIN
9.492	15028	0.08%	86	3,7-Dimethylnonane	PARAFFIN
9.561	124671	0.68%	93	Propanoic acid, 2-methyl-, 3-hydroxy-2,4,4-trimethylpentyl este	ESTER
9.742	9040	0.05%	89	Oxalic acid, allyl butyl ester	ESTER
9.843	291399	1.59%	96	n-Tetradecane	PARAFFIN
10.434	12534	0.07%	92	Sulfurous acid, isobutyl pentyl ester	SULFATE/SULFITE/SULFONE
10.499	14661	0.08%	77	Icosylcyclohexane	CYCLOPARAFFIN
10.574	26520	0.14%	90	2,8-Dimethylundecane	PARAFFIN
10.648	25610	0.14%	75	3,7-Dimethylnonane	PARAFFIN
10.733	18491	0.10%	90	Butanoic acid, 1,1-dimethylethyl este	ESTER
10.884	14186	0.08%	81	3,7-Dimethylnonane	PARAFFIN
11.033	20978	0.11%	94	2,2-Dimethyl-propyl 2,2-dimethyl-propanesulfinyl sulfone	SULFATE/SULFITE/SULFONE
11.106	152649	0.83%	92	4,7-Dimethylundecane	PARAFFIN
11.2	13413	0.07%	84	2,2-Dimethyl-propyl 2,2-dimethyl-propanesulfinyl sulfone	SULFATE/SULFITE/SULFONE
11.223	21412	0.12%	79	2,4-Dimethylheptane	PARAFFIN
11.446	32030	0.17%	83	Oxalic acid, isohexyl neopentyl	ESTER

				ester	
11.509	15410	0.08%	82	4,7-Dimethylundecane	PARAFFIN
11.656	28968	0.16%	81	Oxalic acid, dineopentyl ester	ESTER
11.715	90112	0.49%	91	5-Methyldodecane	PARAFFIN
11.789	24410	0.13%	84	Sulfurous acid, decyl pentyl este	SULFATE/SULFITE/SULFONE
11.866	30241	0.17%	86	5-Isobutylnonane	PARAFFIN
11.95	24625	0.13%	85	3,7-Dimethyldecane	PARAFFIN
12.184	39366	0.22%	92	Propanoic acid, 2-methyl-, anhydride	ESTER
12.303	579842	3.17%	95	n-Hexadecane	PARAFFIN
12.358	19530	0.11%	83	3-Ethyl-2,7-dimethyloctane	PARAFFIN
12.444	22575	0.12%	78	Sulfurous acid, isohexyl pentyl ester 79	ESTER
12.603	18199	0.10%	86	2,2-Dimethyl-propyl 2,2-dimethyl-propane-thiosulfinate	SULFATE/SULFITE/SULFONE
12.806	41826	0.23%	85	2,3,3-Trimethyloctane	PARAFFIN
12.883	10849	0.06%	84	n-Valeric anhydride	ESTER
12.95	14944	0.08%	90	2,2-Dimethyl-propyl 2,2-dimethyl-propane-thiosulfinate	SULFATE/SULFITE/SULFONE
13.022	18037	0.10%	85	5-Methyl-5-propylnonane	PARAFFIN
13.088	50425	0.28%	83	(5-Methyloctyl)benzene	AROMATIC
13.259	36593	0.20%	88	3,7-Dimethylnonane	PARAFFIN
13.342	30466	0.17%	81	5-Methyl-5-propylnonane	PARAFFIN
13.438	95267	0.52%	90	3,8-Dimethylundecane	PARAFFIN
13.717	9989	0.05%	92	2,2-Dimethyl-propyl 2,2-dimethyl-propane-thiosulfinate	SULFATE/SULFITE/SULFONE
13.788	16563	0.09%	89	3,7-Dimethylnonane	PARAFFIN
13.833	12339	0.07%	79	Sulfurous acid, isohexyl pentyl ester	ESTER
13.899	18191	0.10%	86	3,7-Dimethylnonane	PARAFFIN
13.977	100062	0.55%	87	3-Ethyl-3-methyldecane	PARAFFIN
14.047	11900	0.07%	86	2,6,6-Trimethyloctane	PARAFFIN
14.126	9932	0.05%	86	Oxalic acid, dineopentyl ester	ESTER
14.198	7305	0.04%	84	Oxalic acid, isohexyl neopentyl ester	ESTER
14.5	74882	0.41%	89	2,8-Dimethylundecane	PARAFFIN
14.533	14815	0.08%	87	Vinyl crotonate	ESTER
14.619	11234	0.06%	84	Oxalic acid, dineopentyl ester	ESTER
14.675	3889	0.02%	88	2,2-Dimethyl-propyl 2,2-dimethyl-propane-thiosulfinate	SULFATE/SULFITE/SULFONE
14.875	11778	0.06%	81	2,6,6-Trimethyloctane	PARAFFIN
14.979	3768	0.02%	93	2,2-Dimethyl-propyl 2,2-dimethyl-propanesulfinyl sulfone	SULFATE/SULFITE/SULFONE
15.083	5390	0.03%	91	2,2-Dimethyl-propyl 2,2-dimethyl-propane-thiosulfinate	SULFATE/SULFITE/SULFONE
15.158	16610	0.09%	77	Phthalic acid, cyclobutyl isobutyl ester	ESTER
15.204	37919	0.21%	83	5-Methyldodecane	PARAFFIN
15.258	11245	0.06%	80	Isovaleric acid, isobutyl ester	ESTER
15.317	6994	0.04%	82	Pentanoic acid, 3-butenyl ester	ESTER
15.402	102972	0.56%	89	2,3,7-Trimethyldecane	PARAFFIN
15.655	16467	0.09%	85	Sulfurous acid, 2-ethylhexyl isohexyl ester	SULFATE/SULFITE/SULFONE
15.8	95471	0.52%	85	5,7-Dimethylundecane	PARAFFIN
15.858	8004	0.04%	84	4-Methyl-1-hexanol	OTHER OXYGENATE
15.905	17141	0.09%	83	4,4-Dimethylundecane	PARAFFIN
16.194	174237	0.95%	90	2,3,6-Trimethyldecane	PARAFFIN

16.643	13843	0.08%	76	2-Isopropyl-5-methyl-1-hexanol	OTHER OXYGENATE
16.695	79178	0.43%	86	2,3,5,8-Tetramethyldecane	PARAFFIN
16.766	28936	0.16%	79	Undecylcyclohexane	PARAFFIN
16.817	7843	0.04%	91	2,6,10,15-Tetramethylheptadecane	PARAFFIN
17.232	126285	0.69%	89	5-Methyloctadecane	PARAFFIN
17.468	19451	0.11%	81	Tetradecylcyclohexane	PARAFFIN
17.562	172268	0.94%	91	2,6,10,15-Tetramethylheptadecane	PARAFFIN
17.951	68511	0.37%	87	2,6,10,15-Tetramethylheptadecane	PARAFFIN
18.175	94391	0.52%	82	10-Methylnonadecane	PARAFFIN
18.458	46291	0.25%	77	5-Methylhenicosane	PARAFFIN
18.753	95225	0.52%	86	2,3,7-Trimethyldecane	PARAFFIN
19.459	16894	0.09%	70	Oxalic acid, isohexyl propyl ester	ESTER
20.083	64949	0.35%	83	2,6,10,15-Tetramethylheptadecane	PARAFFIN

Table 12.4: Chemical speciation of the toluene extract of commuter bus soot

Retention time	**Area**	**Area (%)**	**% Match**	**Name**	**Class**
3.238	2258537	3.61%	94	Cumene	AROMATIC
3.277	75649	0.12%	89	2,6-dimethyl octane	PARAFFIN
3.292	153208	0.24%	84	Oxalic acid, allyl nonyl ester	ESTER
3.34	50068	0.08%	88	2,6-dimethyl octane	PARAFFIN
3.546	64838	0.10%	90	5,6-dimethyl undecane	PARAFFIN
3.608	43518	0.07%	85	2,2,6,6-Tetramethylheptane	PARAFFIN
3.636	836895	1.34%	94	n-Propylbenzene	AROMATIC
3.69	97355	0.16%	88	2-Methylnonane 88	PARAFFIN
3.738	1631829	2.61%	98	m-Ethyltoluene	AROMATIC
3.784	714515	1.14%	93	o-Ethyltoluene	AROMATIC
3.863	677483	1.08%	92	1,2,4-Trimethylbenzene	AROMATIC
3.982	432890	0.69%	93	1,2,3-Trimethylbenzene	AROMATIC
4.059	83460	0.13%	71	Phenyl butyrate	ESTER
4.207	2430549	3.88%	91	1,3,5-Trimethylbenzene	AROMATIC
4.403	156746	0.25%	74	sec-Butylbenzene	AROMATIC
4.487	64924	0.10%	86	2,3,6-Trimethyloctane	PARAFFIN
4.575	86274	0.14%	77	tert-Butylbenzene	AROMATIC
4.603	1180550	1.89%	96	1,2,3-Trimethylbenzene	AROMATIC
4.667	239345	0.38%	86	Bicyclopentadiene 86	CYCLOPARAFFIN
4.707	58361	0.09%	78	Isopropylcyclohexane	CYCLOPARAFFIN
4.732	44496	0.07%	84	Oxalic acid, allyl pentadecyl ester	ESTER
4.816	805461	1.29%	80	Indane	HYDROCYCLIC AROMATIC
4.901	94337	0.15%	72	Benzyl alcohol	OTHER OXYGENATE
4.958	1133025	1.81%	96	m-Diethylbenzene	AROMATIC
5.01	3357578	5.36%	97	3-n-Propyltoluene	AROMATIC
5.099	8063836	12.88%	93	p-Diethylbenzene	AROMATIC
5.221	1350378	2.16%	96	2-Propyltoluene	AROMATIC
5.282	30275	0.05%	86	2,2,6,6-Tetramethylheptane	PARAFFIN
5.376	2902504	4.64%	96	3-Ethyl-o-xylene	AROMATIC
5.421	2840511	4.54%	96	1,3-Dimethyl-2-ethyl benzene	AROMATIC
5.511	6271597	10.02%	96	1,2-Dimethyl-3-ethyl benzene	AROMATIC
5.579	235279	0.38%	86	p-Cymene	AROMATIC
5.646	797276	1.27%	97	Tridecane	PARAFFIN
5.733	211871	0.34%	81	1-Isobutyl-4-methylbenzene	AROMATIC
5.796	991282	1.58%	95	3-Ethyl-o-xylene	AROMATIC
5.852	90867	0.15%	71	3-Methyl-2-phenylbutane	AROMATIC
5.985	3405784	5.44%	97	1,2,4,5-Tetramethylbenzene	AROMATIC
6.04	4373658	6.98%	96	1,2,3,4-Tetramethylbenzene	AROMATIC
6.236	274248	0.44%	82	1-Sec-butyl-4-methylbenzene	AROMATIC
6.305	203574	0.33%	91	3,5-Diethyltoluene	AROMATIC
6.352	1311106	2.09%	94	4-Methylindane	HYDROCYCLIC AROMATIC
6.413	150702	0.24%	72	2-Methyl-2-phenylpentane	AROMATIC
6.492	1403428	2.24%	93	4-Methylindane	HYDROCYCLIC AROMATIC
6.496	1052625	1.68%	91	1,2-Dimethyl-3-ethyl benzene	AROMATIC
6.591	435891	0.70%	85	1,3-Diethyl-5-methylbenzene	AROMATIC
6.687	721723	1.15%	87	Tetralin	HYDROCYCLIC AROMATIC
6.811	235372	0.38%	93	1-Sec-butyl-4-methylbenzene	AROMATIC
6.983	62958	0.10%	58	Succinamic acid, N-isochroman-1-ylmethyl	UNCLASSIFIED

7.043	94445	0.15%	63	1-Methyl-2-(1-methyl-2-propenyl)benzene	UNCLASSIFIED
7.089	3877790	6.19%	90	Naphthalene	PAH
7.142	155998	0.25%	84	3,5-Dimethylcumene	AROMATIC
7.293	132622	0.21%	82	1-Ethyl-2,4,5-trimethylbenzene	AROMATIC
7.423	18526	0.03%	61	Benzene, (1-isopropyl-2-methylpropyl)	UNCLASSIFIED
7.479	37833	0.06%	71	Benzenepropanoic acid, decyl ester	ESTER
7.508	12409	0.02%	70	1-Ethyl-1-methylpropylbenzene	AROMATIC
7.574	10451	0.02%	63	Oxalic acid di-n-butyl ester	UNCLASSIFIED
7.673	67929	0.11%	65	1-Ethyl-1-methylpropylbenzene	UNCLASSIFIED
7.708	18248	0.03%	86	Isopropylcyclohexane	ESTER
7.839	42723	0.07%	80	Oxalic acid, allyl nonyl ester	HYDROCYCLIC AROMATIC
7.923	82295	0.13%	72	1,6-Dimethylindane	HYDROCYCLIC AROMATIC
7.998	45150	0.07%	82	3-Ethyl-2,7-dimethyloctane	PARAFFIN
8.091	75789	0.12%	73	Oxalic acid, allyl nonyl ester	ESTER
8.18	53274	0.09%	78	5-Methyltetralin	HYDROCYCLIC AROMATIC
8.324	35563	0.06%	74	m-tert-Butyltoluene	AROMATIC
8.369	13243	0.02%	62	1-Ethyl-1-methylindan	UNCLASSIFIED
8.402	5303	0.01%	76	1-Methyl-3-nonylcyclohexane	CYCLOPARAFFIN
8.503	281085	0.45%	83	4,7-Dimethylundecane	PARAFFIN
8.649	283512	0.45%	93	2-Methylnaphthalene	PARAFFIN
8.702	16846	0.03%	85	2,2,3-Trimethylbutane	PARAFFIN
8.792	1433	0.00%	89	Di-n-butyl sulphate	SULFATE/SULFITE/SULFONE
8.864	90536	0.14%	95	1-Methylnaphthalene	PAH
8.922	30463	0.05%	64	2,6-Dimethyltetralin	UNCLASSIFIED
8.991	11467	0.02%	72	Oxalic acid, isobutyl neopentyl ester	ESTER
9.1	3882	0.01%	78	Sulphuric acid dibutyl ester	SULFATE/SULFITE/SULFONE
9.155	26115	0.04%	81	Oxalic acid, allyl octyl ester	ESTER
9.215	120747	0.19%	74	n-Hexyl isobutanoate	ESTER
9.271	14344	0.02%	76	tert-Pentyl pentanoate	ESTER
9.356	24114	0.04%	86	Sulfurous acid, 2-ethylhexyl isohexyl ester	SULFATE/SULFITE/SULFONE
9.442	22591	0.04%	82	2,2,6,6-Tetramethylheptane	PARAFFIN
9.489	12922	0.02%	79	Oxalic acid, dineopentyl ester	ESTER
9.556	103596	0.17%	85	Butyl butanoate	ESTER
9.749	18907	0.03%	83	Vinyl 2-methylacrylate	ESTER
9.837	225956	0.36%	94	4,7-Dimethylundecane	PARAFFIN
9.925	15956	0.03%	87	Oxalic acid, dineopentyl ester	ESTER
9.999	8934	0.01%	91	2-Methylpropanoic anhydride	ESTER
10.113	11502	0.02%	67	1-Ethyl-4,4-dimethyl-2,5-dioxoimidazolidine	UNCLASSIFIED
10.242	4161	0.01%	72	Di-n-butyl sulphate	SULFATE/SULFITE/SULFONE
10.258	3962	0.01%	66	(2E)-5-Methyl-2-heptene	UNCLASSIFIED
10.279	12703	0.02%	71	1,2-Dimethylnaphthalene	PAH
10.341	9824	0.02%	54	4,6-Ditert-butyl-1,3-benzenediol	UNCLASSIFIED
10.414	11953	0.02%	68	Ethyl 2-hydroxypentanoate	UNCLASSIFIED
10.441	15077	0.02%	70	Sulfurous acid, butyl undecyl ester	SULFATE/SULFITE/SULFONE
10.49	22672	0.04%	64	Oxalic acid, cyclohexyl isobutyl ester	UNCLASSIFIED
10.568	22452	0.04%	82	Oxalic acid, dineopentyl ester	ESTER

10.636	23315	0.04%	75	5-Isobutylnonane	PARAFFIN
10.728	10741	0.02%	87	Sulfurous acid, isobutyl pentyl ester	SULFATE/SULFITE/SULFONE
11.036	4053	0.01%	83	S-Neopentyl 2,2-dimethyl-1-propanesulfinothioate	SULFATE/SULFITE/SULFONE
11.099	46050	0.07%	90	2,8-Dimethylundecane	PARAFFIN
11.219	10493	0.02%	84	Oxalic acid, dineopentyl ester	ESTER
11.513	11595	0.02%	76	Sulfurous acid, isobutyl pentyl ester	SULFATE/SULFITE/SULFONE
11.658	12068	0.02%	80	2,2-Dimethyl-propyl 2,2-dimethyl-propanesulfinyl sulfone	SULFATE/SULFITE/SULFONE
11.708	68652	0.11%	87	2,7-Dimethylundecane	PARAFFIN
11.783	10295	0.02%	89	S-Neopentyl 2,2-dimethyl-1-propanesulfinothioate	SULFATE/SULFITE/SULFONE
11.857	14628	0.02%	76	Oxalic acid, isohexyl neopentyl ester	ESTER
11.944	11470	0.02%	84	2,2-Dimethyl-propyl 2,2-dimethyl-propanesulfinyl sulfone	SULFATE/SULFITE/SULFONE
12.219	92946	0.15%	75	Phthalic acid, isobutyl 2-methoxyethyl ester	ESTER
12.298	312152	0.50%	78	2,3,3-Trimethyloctane	PARAFFIN
12.807	30512	0.05%	88	Oxalic acid, isobutyl neopentyl ester	ESTER
12.358	11012	0.02%	72	1,2,4-Benzenetricarboxylic acid, 1,2-dimethyl ester	ESTER
12.807	95586	0.15%	75	2,3,3-Trimethyloctane	PARAFFIN
12.95	9786	0.02%	86	Propanoic acid, 2-methyl-, anhydride	ESTER
13.014	7550	0.01%	83	Oxalic acid, dineopentyl ester	ESTER
13.09	31424	0.05%	82	5-Methyl-1-phenyloctane	AROMATIC
13.257	26841	0.04%	83	5-Methyl-5-propylnonane	PARAFFIN
13.364	10688	0.02%	68	1,2,4-Benzenetricarboxylic acid, 1,2-dimethyl ester	UNCLASSIFIED
13.432	55986	0.09%	89	4,7-Dimethylundecane	PARAFFIN
13.5	26623	0.04%	79	Oxalic acid, butyl neopentyl ester	ESTER
13.695	21040	0.03%	77	Butyric acid, crotyl ester 77	ESTER
13.783	27325	0.04%	79	Butanoic acid, 1,1-dimethylethyl ester	ESTER
13.893	12525	0.02%	81	Sulfurous acid, isohexyl pentyl ester	SULFATE/SULFITE/SULFONE
13.97	92045	0.15%	87	5-Methyldodecane	PARAFFIN
14.041	7170	0.01%	76	Oxalic acid, dineopentyl ester	ESTER
14.13	7267	0.01%	95	2,2-Dimethyl-propyl 2,2-dimethyl-propanesulfinyl sulfone	SULFATE/SULFITE/SULFONE
14.197	9586	0.02%	76	Butanoic acid, 1,1-dimethylethyl ester	ESTER
14.495	63756	0.10%	90	2,8-Dimethylundecane 89	PARAFFIN
14.614	13696	0.02%	74	(1,3,3-Trimethylnonyl)benzene	AROMATIC
14.762	5205	0.01%	80	(2Z)-4-Methyl-2-pentanone o-benzyloxime	OTHER NITROGENOUS
14.905	9638	0.02%	92	2,2-Dimethyl-propyl 2,2-dimethyl-propane-thiosulfinate	SULFATE/SULFITE/SULFONE
15.16	40627	0.06%	87	Phthalic acid, 6-ethyl-3-octyl butyl ester	ESTER
15.201	24420	0.04%	81	Decane, 3-ethyl-3-methyl-	PARAFFIN
15.242	5699	0.01%	87	Propanoic acid, 2-methyl-, anhydride	ESTER
15.312	5829	0.01%	90	2,2-Dimethyl-propyl 2,2-dimethyl-propane-thiosulfinate	SULFATE/SULFITE/SULFONE

15.401	35833	0.06%	86	5-Isobutylnonane	PARAFFIN
15.533	4849	0.01%	86	5-Isobutylnonane	PARAFFIN
15.651	8786	0.01%	86	2,2-Dimethyl-propyl 2,2-dimethyl-propanesulfinyl sulfone	SULFATE/SULFITE/SULFONE
15.797	76716	0.12%	89	Sulfurous acid, hexyl octyl ester	SULFATE/SULFITE/SULFONE
15.85	5538	0.01%	91	Propanoic acid, 2-methyl-, anhydride	ESTER
15.959	24503	0.04%	87	Phthalic acid, cyclobutyl heptyl ester	ESTER
16.19	37706	0.06%	84	2,3,6-Trimethyldecane	PARAFFIN
16.3	6769	0.01%	88	Oxalic acid, dineopentyl ester	ESTER
16.692	35129	0.06%	82	3-Ethyl-3-methyldecane	PARAFFIN
16.75	8481	0.01%	79	Oxalic acid, isohexyl propyl ester 79	ESTER
16.817	6006	0.01%	88	Oxalic acid, dineopentyl ester 88	ESTER
16.907	33902	0.05%	87	Oxalic acid, isohexyl neopentyl ester 87	ESTER
17.008	5594	0.01%	83	Hexadecanal cyclic ethylene acetal	OTHER OXYGENATE
17.104	12667	0.02%	84	Sulfurous acid, nonyl 2-propyl ester 84	SULFATE/SULFITE/SULFONE
17.229	61696	0.10%	87	Sulfurous acid, hexyl pentadecyl ester	SULFATE/SULFITE/SULFONE
17.275	5041	0.01%	79	Butanoic acid, anhydrid	ESTER
17.325	8376	0.01%	82	Butyric acid, crotyl ester	ESTER
17.559	38281	0.06%	89	2,8-Dimethylundecane	PARAFFIN
17.948	48640	0.08%	77	2,8-Dimethylundecane	PARAFFIN
18.172	28615	0.05%	81	Oxalic acid, isohexyl neopentyl ester	ESTER
18.453	44156	0.07%	89	Sulfurous acid, hexyl pentadecyl ester	SULFATE/SULFITE/SULFONE
18.749	55700	0.09%	84	6-Ethyl-2-methyloctane	PARAFFIN
19.061	67358	0.11%	80	Sulfurous acid, decyl 2-propyl ester	SULFATE/SULFITE/SULFONE
19.294	27189	0.04%	70	Sulfurous acid, butyl nonyl ester	SULFATE/SULFITE/SULFONE
19.534	66530	0.11%	78	1,2-Benzenedicarboxylic acid, ditridecyl ester	ESTER
19.823	32228	0.05%	75	3,4-Dimethylundecane	PARAFFIN
19.89	29514	0.05%	57	2-Phenyleicosane	UNCLASSIFIED
20.078	60000	0.10%	68	Sulfurous acid, pentadecyl 2-propyl ester	SULFATE/SULFITE/SULFONE
20.223	23555	0.04%	63	Oxalic acid, isohexyl propyl ester	ESTER
20.321	20138	0.03%	77	Sulfurous acid, butyl isohexyl ester	SULFATE/SULFITE/SULFONE
20.768	22370	0.04%	71	3-Methyleicosane	PARAFFIN

Table 12.5: Chemical speciation of the acetone extract of commuter bus soot

Retention time	**Area**	**Area (%)**	**% Match**	**Name**	**Class**
3.701	9287	0.18%	95	Cumene	AROMATIC
3.747	19044	0.38%	77	Propanedioic acid, dibutyl ester	ESTER
3.828	6420	0.13%	74	Dibutyl malonate	ESTER
3.882	4730	0.09%	91	Dibutyl sulphate	SULFATE/SULFITE/SULFONE

4.037	5565	0.11%	98	2,2-Dimethyl-propyl 2,2-dimethyl-propanesulfinyl sulfone	SULFATE/SULFITE/SULFONE
4.17	187470	3.71%	77	n-Undecane	PARAFFIN
4.274	6325	0.13%	93	Oxalic acid, butyl cyclobutyl ester	ESTER
4.307	4027	0.08%	93	Oxalic acid, dibutyl ester	ESTER
4.443	6268	0.12%	94	Dipentyl sulphate	SULFATE/SULFITE/SULFONE
4.508	5579	0.11%	97	Oxalic acid, butyl cyclobutyl ester	ESTER
4.578	28700	0.57%	97	Valerophenone	OTHER OXYGENATE
4.794	29433	0.58%	84	Indane	HYDROCYCLIC AROMATIC
4.884	11329	0.22%	93	2,2,4-Trimethylhexane	PARAFFIN
4.942	63251	1.25%	86	1,4-Diethylbenzene	AROMATIC
4.994	241456	4.78%	94	3-Propyl-toluene	AROMATIC
5.076	586475	11.61%	90	1,2-Diethylbenzene	AROMATIC
5.208	70086	1.39%	89	Secondary butylbenzene	AROMATIC
5.267	10104	0.20%	94	Oxalic acid, butyl propyl ester	ESTER
5.365	132184	2.62%	90	2-Ethyl-p-xylene	AROMATIC
5.409	198894	3.94%	94	1,3-Dimethyl-2-ethyl benzene	AROMATIC
5.501	499062	9.88%	96	1,2-Dimethyl-3-ethyl benzene	AROMATIC
5.567	3092	0.06%	81	p-Toluic acid, tridec-2-ynyl ester	ESTER
5.638	192185	3.80%	93	n-Dodecane	PARAFFIN
5.789	42334	0.84%	85	1,4-Dimethyl-2-ethyl benzene	AROMATIC
5.98	215705	4.27%	94	1,2,4,5-Tetramethylbenzene	AROMATIC
6.034	235177	4.66%	95	Durene	AROMATIC
6.229	13084	0.26%	80	2,5-Pyrrolidinedione, 1-[(4-methylbenzoyl)oxy]	OTHER NITROGENOUS
6.348	131039	2.59%	90	4-Methylindane	HYDROCYCLIC AROMATIC
6.41	13878	0.27%	77	Benzoic acid, 4-methyl-, [3-(4-methylbenzoyloxy)-5-methylphenyl] ester	ESTER
6.483	76620	1.52%	88	5-Methylindane	HYDROCYCLIC AROMATIC
6.508	82124	1.63%	85	2-Ethyl-p-xylene	AROMATIC
6.586	15760	0.31%	64	Adipic acid, di(4-heptyl) ester	UNCLASSIFIED
6.675	22880	0.45%	74	Benzene, (1,1-dimethylbutyl)	AROMATIC
6.81	17831	0.35%	83	1,2-Benzenediol, o-(4-methylbenzoyl)	ESTER
7.088	806803	15.97%	83	Naphthalene	PAH
7.527	19364	0.38%	71	2-Furancarboxylic acid, 2-tetrahydrofurylmethyl ester	ESTER
7.923	5410	0.11%	78	tert-Butyl butyrate	ESTER
8.504	27341	0.54%	89	3,7-Dimethylnonane	PARAFFIN
8.651	117644	2.33%	91	Naphthalene, 2-methyl-	PAH
8.864	26728	0.53%	80	1-Methylnaphthalene	PAH
8.983	8112	0.16%	77	1,5-Dimethyl-2-phenyl-1-pyrrolin-3-one	OTHER NITROGENOUS
9.223	29735	0.59%	82	1-(2-Hydroxy-1-methylethyl)-2,2-dimethylpropyl 2-methylpropanoate	ESTER
9.558	49148	0.97%	87	Butyl 2-methylpropanoate	ESTER
9.748	11573	0.23%	84	2Z)-8-Methyl-2-decene	PARAFFIN
9.839	135679	2.69%	94	4,7-Dimethylundecane	PARAFFIN
10.563	10843	0.21%	89	2,2-Dimethyl-propyl 2,2-dimethyl-propanesulfinyl sulfone	SULFATE/SULFITE/SULFONE
11.101	14490	0.29%	86	6-Ethyl-2-methyldecane	PARAFFIN
11.642	7167	0.14%	96	Oxalic acid, allyl butyl ester	ESTER
11.783	2178	0.04%	93	Oxalic acid, allyl isobutyl ester	ESTER

11.859	6944	0.14%	92	Oxalic acid, butyl propyl ester	ESTER
12.177	8620	0.17%	92	Propanoic acid, 2-methyl-, anhydride	ESTER
12.225	9136	0.18%	90	Oxalic acid, butyl isobutyl ester	ESTER
12.298	125594	2.49%	88	4,7-Dimethylundecane	PARAFFIN
12.358	6988	0.14%	92	2,2-Dimethyl-propyl 2,2-dimethyl-propanesulfinyl sulfone	SULFATE/SULFITE/SULFONE
12.801	13793	0.27%	85	Sulfurous acid, isobutyl pentyl ester	SULFATE/SULFITE/SULFONE
12.944	16738	0.33%	86	Oxalic acid, dineopentyl ester	ESTER
13.017	9912	0.20%	89	Oxalic acid, butyl propyl ester	ESTER
13.433	36252	0.72%	86	Sulfurous acid, 2-ethylhexyl hexyl ester	SULFATE/SULFITE/SULFONE
13.894	21056	0.42%	83	tert-Butyl butyrate	ESTER
14.115	9341	0.18%	88	Oxalic acid, allyl butyl ester	ESTER
14.198	7156	0.14%	86	Oxalic acid, butyl propyl ester	ESTER
14.313	10729	0.21%	87	Oxalic acid, allyl butyl ester	ESTER
14.494	52927	1.05%	89	3,7-Dimethylundecane	PARAFFIN
15.018	8970	0.18%	92	2,2-Dimethyl-propyl 2,2-dimethyl-propanesulfinyl sulfone	SULFATE/SULFITE/SULFONE
15.159	34349	0.68%	81	1,2-Benzenedicarboxylic acid, diheptyl ester	ESTER
15.399	18079	0.36%	84	4,7-Dimethylundecane	PARAFFIN
15.962	8208	0.16%	83	Phthalic acid, hexyl heptyl ester	ESTER
16.189	16263	0.32%	81	3,7-Dimethylnonane	PARAFFIN
16.904	7888	0.16%	84	5-Methyl-5-propylnonane	PARAFFIN
17.556	11823	0.23%	82	5-Isobutylnonane	PARAFFIN
18.171	6824	0.14%	81	Oxalic acid, isohexyl neopentyl ester	ESTER
18.75	32175	0.64%	80	Oxalic acid, dineopentyl ester	ESTER
18.933	7721	0.15%	75	Phthalic acid, butyl hexyl ester	ESTER
19.017	10270	0.20%	72	Phthalic acid, cyclobutyl tridecyl ester	ESTER
19.062	21300	0.42%	73	Didodecyl phthalate	ESTER
19.122	10575	0.21%	78	Phthalic acid, cyclobutyl heptyl ester	ESTER
19.183	5596	0.11%	82	Phthalic acid, cyclobutyl tridecyl ester	ESTER
19.294	8406	0.17%	73	Phthalic acid, dodecyl nonyl ester	ESTER
19.342	3880	0.08%	84	Phthalic acid, 4-bromophenyl heptyl ester	ESTER
19.533	5206	0.10%	75	Phthalic acid, cyclobutyl tridecyl ester	ESTER
19.649	2850	0.06%	67	Glycine, N-(4-ethylbenzoyl)-, hexyl ester	UNCLASSIFIED
19.767	3915	0.08%	66	2-tert-Butyl-4-(1,1,3,3-tetramethylbutyl)pheno	UNCLASSIFIED
19.817	12877	0.25%	63	Oxalic acid, octyl propyl ester	UNCLASSIFIED
20.108	6667	0.13%	70	3,4-Bis(methoxycarbonyl)benzoic acid	ESTER
20.318	13117	0.26%	58	Oxalic acid, dineopentyl ester	UNCLASSIFIED

Table 12.6: Chemical speciation of the methanol extract of commuter bus diesel soot

Retention time	Area	Area (%)	% Match	Name	Class
3.56	7863	0.46%	98	Oxalic acid, butyl cyclobutyl ester	ESTER
3.703	27101	1.59%	87	1-Ethyl-2-methylbenzene	AROMATIC
3.748	18846	1.11%	77	1-Ethyl-3-methylbenzene	AROMATIC
3.827	10921	0.64%	74	1-Methyl-4-ethylbenzene	AROMATIC
3.879	5251	0.31%	93	Dibutyl sulfate	SULFATE/SULFITE/SULFONE
3.95	6156	0.36%	90	Acetophenone	OTHER OXYGENATE
3.958	3023	0.18%	86	Cumene	AROMATIC
4.167	179804	10.58%	86	n-Decane	PARAFFIN
4.183	54467	3.20%	86	1,3,5-Trimethylbenzene	AROMATIC
4.349	20059	1.18%	81	Butanedioic acid, monopropargyl ester	ESTER
4.578	11809	0.69%	89	p-Ethyltoluene	AROMATIC
4.799	10374	0.61%	83	Indane	HYDROCYCLIC AROMATIC
4.882	9936	0.58%	77	2,2-Dimethyl-3-ethylpentane	PARAFFIN
4.942	8344	0.49%	77	Benzoic acid, 3-methyl-, 2-oxo-2-phenylethyl ester	ESTER
4.993	27045	1.59%	91	sec-Butylbenzene	AROMATIC
5.03	4461	0.26%	90	Propanoic acid, 2-methyl-, 2-methylpropyl ester	ESTER
5.077	39380	2.32%	78	3-n-Propyltoluene	AROMATIC
5.091	25984	1.53%	76	tert-Butylbenzene	AROMATIC
5.194	19208	1.13%	82	Oxalic acid, isobutyl neopentyl ester	ESTER
5.308	10697	0.63%	96	Dipentyl sulfate	SULFATE/SULFITE/SULFONE
5.367	19400	1.14%	76	Isoamylbenzene	AROMATIC
5.407	16018	0.94%	81	m-Toluic acid, cyclobutyl ester	ESTER
5.499	43324	2.55%	87	4-Ethyl-m-xylene	AROMATIC
5.636	243274	14.31%	97	n-Undecane	PARAFFIN
5.792	27865	1.64%	85	1,2-Benzenediol, O-(4-methylbenzoyl)-O'-propoxycarbonyl-	ESTER
5.978	26146	1.54%	79	p-Toluic acid, cyclobutyl ester	ESTER
6.033	22088	1.30%	81	o-Toluic acid, cyclobutyl ester	ESTER
6.345	4750	0.28%	81	1-Methylindane	HYDROCYCLIC AROMATIC
6.491	9661	0.57%	79	4-Methyl-1-pentanoylbenzene	OTHER OXYGENATE
6.686	4205	0.25%	72	Fumaric acid, heptyl 2-phenylethyl ester	ESTER
7.092	107345	6.32%	83	Naphthalene	PAH
7.1	63936	3.76%	77	5,7-Dimethylundecane	PARAFFIN
7.55	108137	6.36%	94	6-Methylheptyl acrylate	ESTER
8.501	4345	0.26%	91	Oxalic acid, bis(isobutyl) ester	ESTER
8.649	12467	0.73%	77	2-Methylnaphthalene	PAH
8.972	8994	0.53%	80	Phthalic acid, monoethyl ester	ESTER
9.21	11131	0.65%	79	1,2,3-Propanetriol, diacetate	ESTER
9.558	15966	0.94%	87	n-Butyl butanoate	ESTER
9.745	3291	0.19%	92	Oxalic acid, dicyclobutyl ester	ESTER
9.836	53797	3.17%	89	4,7-Dimethylundecane	PARAFFIN
10.563	4028	0.24%	88	Sulfurous acid, isobutyl pentyl ester	ESTER

11.101	7640	0.45%	90	2,2-Dimethyl-propyl 2,2-dimethyl-propanesulfinyl sulfone	SULFATE/SULFITE/SULFONE
11.942	2457	0.14%	87	Oxalic acid, allyl isobutyl ester	ESTER
12.177	6050	0.36%	92	Isobutryic anhydride	ESTER
12.298	120387	7.08%	74	Didodecyl phthalate	ESTER
12.939	7992	0.47%	83	Oxalic acid, isobutyl pentyl ester	ESTER
13.431	22667	1.33%	86	2,2-Dimethyl-propyl 2,2-dimethyl-propanesulfinyl sulfone	SULFATE/SULFITE/SULFONE
13.895	13803	0.81%	90	Oxalic acid, allyl butyl ester	ESTER
14.493	22341	1.31%	89	Sulfurous acid, 2-ethylhexyl hexyl ester	ESTER
15.158	36477	2.15%	87	Phthalic acid, cyclobutyl isobutyl ester	ESTER
15.399	10911	0.64%	85	5-Methyl-5-propylnonane	PARAFFIN
15.65	2819	0.17%	79	2-Methylheptanoic acid	OTHER OXYGENATE
15.711	13461	0.79%	56	1,2,4-Benzenetricarboxylic acid, trihexyl ester	UNCLASSIFIED
15.958	16666	0.98%	85	Phthalic acid, hexyl heptyl ester	ESTER
16.189	13984	0.82%	79	6-Ethyl-2-methyloctane	PARAFFIN
16.902	25140	1.48%	85	Oxalic acid, isohexyl neopentyl ester	ESTER
16.95	12550	0.74%	79	Tetrahydrofurfuryl acrylate	ESTER
17	8449	0.50%	78	n-Butyric acid anhydride	ESTER
17.075	9920	0.58%	76	3-Butoxy propanoic acid	OTHER OXYGENATE
17.117	12620	0.74%	66	Oxalic acid, neopentyl propyl ester	ESTER
17.559	13156	0.77%	83	Sulfurous acid, 2-ethylhexyl isohexyl ester	SULFATE/SULFITE/SULFONE
17.775	5184	0.31%	69	Sulfurous acid, hexyl nonyl ester	UNCLASSIFIED
18.116	3928	0.23%	66	Sulfurous acid, cyclohexylmethyl dodecyl ester	UNCLASSIFIED

Table 12.7: Chemical speciation of the dichloromethane extract of commuter bus diesel soot (own analysis)

Retention time	**Area**	**Area (%)**	**% Match**	**Name**	**Class**
3.414	35570	5.62%	88	2,4,4-Trimethyl-1-hexene	PARAFFIN
3.518	5731	0.91%	85	Butanoic acid, 3-methylbutyl ester	ESTER
3.563	8112	1.28%	96	Oxalic acid, butyl cyclobutyl ester	ESTER
3.882	5031	0.80%			UNCLASSIFIED
3.736	12415	1.96%	92	Dibutylsulfate	SULFATE/SULFITE/SULFONE
4.033	5607	0.89%	98	2,2-Dimethyl-propyl 2,2-dimethyl-propanesulfinyl sulfone	SULFATE/SULFITE/SULFONE
4.273	7123	1.13%			UNCLASSIFIED
4.383	10689	1.69%	98	Oxalic acid, allyl butyl ester	ESTER
4.443	6617	1.05%	93	Acetic acid, butoxyhydroxy-, butyl ester	ESTER
4.553	7532	1.19%	96	Oxalic acid, dibutyl ester	ESTER
4.883	10400	1.64%	91	2,2,3-Trimethylnonane	PARAFFIN
4.883	10400	1.64%			UNCLASSIFIED
4.967	11813	1.87%			UNCLASSIFIED
5.067	15459	2.44%			UNCLASSIFIED
5.198	6232	0.99%			UNCLASSIFIED
5.271	15586	2.46%			UNCLASSIFIED
5.386	14646	2.32%			UNCLASSIFIED
5.502	8304	1.31%			UNCLASSIFIED
5.775	8161	1.29%			UNCLASSIFIED
5.839	9882	1.56%			UNCLASSIFIED
5.992	8149	1.29%			UNCLASSIFIED
7.096	6434	1.02%	88	Butanoic acid, 1,1-dimethylethyl ester	ESTER
9.219	51117	8.08%	78	1-(2-Hydroxy-1-methylethyl)-2,2-dimethylpropyl 2-methylpropanoate	ESTER
9.557	55379	8.76%	87	3-Hydroxy-2,4,4-trimethylpentyl 2-methylpropanoate	ESTER
9.838	4832	0.76%	89	Butanoic acid, 1,1-dimethylethyl ester	ESTER
11.102	7992	1.26%	85	Butanoic acid, 1,1-dimethylethyl ester	ESTER
12.177	6928	1.10%	85	Tetrahydrofurfuryl acrylate	ESTER
12.299	56080	8.87%	80	2,8-Dimethylundecane	PARAFFIN
12.317	29238	4.62%	80	2,8-Dimethylundecane	PARAFFIN
12.802	11836	1.87%	74	Phthalic acid, cyclobutyl tridecyl ester	ESTER
13.096	9012	1.43%			UNCLASSIFIED
13.431	23091	3.65%	86	3-Ethyl-2,7-dimethyloctane	PARAFFIN
13.692	10756	1.70%			UNCLASSIFIED
13.933	9139	1.45%			UNCLASSIFIED
14.108	4550	0.72%			UNCLASSIFIED
14.2	10140	1.60%			UNCLASSIFIED
14.495	22981	3.63%	84	Butanoic acid, 1,1-dimethylethyl ester	ESTER
14.525	10684	1.69%	87	Isobutyl acrylate	ESTER
14.883	18380	2.91%	81	Phthalic acid, cyclobutyl isobutyl ester	ESTER
15.16	10875	1.72%			UNCLASSIFIED
15.398	16287	2.58%	75	2,2,3-Trimethyldecane	PARAFFIN
15.45	7775	1.23%			UNCLASSIFIED

15.708	8288	1.31%			UNCLASSIFIED
15.959	8055	1.27%	74	Phthalic acid, butyl hexyl ester	ESTER
15.45	3775	0.60%			UNCLASSIFIED
15.708	5288	0.84%			UNCLASSIFIED

Table 12.8: Instrumental parameters used for GC-MS analysis at the University of Stellenbosch

Instrument	Agilent 6890N GC with CTC CombiPAL Autosampler and Agilent 5975B MS
Column	Restek 12723-127, Rtx-5Sill MS w/Integra Guard MS Column (fused silica) with a temperature range: -60 °C to 330 °C and dimensions of 30m (axial length), 0.25 mm (internal diameter) and 0.25µm (film thickness).
Gas	Helium
GC injection program	
Injection temperature	280 °C
Injection mode	Splitless
Injection volume	1µl
GC pressure program	
Flow control mode	Pressure
Pressure	47.5 kPa
Total flow	53.7 mL/min
Column flow	50.0 mL/min
Purge flow	50.0 mL/min
Linear velocity (helium, carrier gas)	36 cm/sec

Column oven temperature program		
Rate	Final temperature (°C)	Hold time (min)
-	40	2
15	170	5
10	280	5

MS program				
Start time (min)	End time (min)	Acquisition mode	Start m/z	End m/z
5.20	31.67	Scan	40	550

MS parameters		
Ion source temperature (°C)	Interface temperature (°C)	Solvent cut off time (min)
240	280	5

12.2 APPENDIX B – FAME composition

Table 12.9: Fatty acid composition of rapeseed oil and soybean oil [103]

Oil Type	Fatty acid composition (%)						
	16:0	18:0	18:1	18:2	18:3	20:1	22:1
Rapeseed	4.0	1.5	17.0	13.0	9.0	14.5	41.0
Soybean	11.4	4.2	26.1	50.3	6.9	0.0	0.0

12.3 Appendix C – Flask reactor stressing

12.3.1 Thermal analysis repeatability

Repeat thermogravimetric analysis revealed that mass loss behaviour of stressed and neat fuels was highly repeatable. Curves lie within 2.5°C of each other. This is illustrated below.

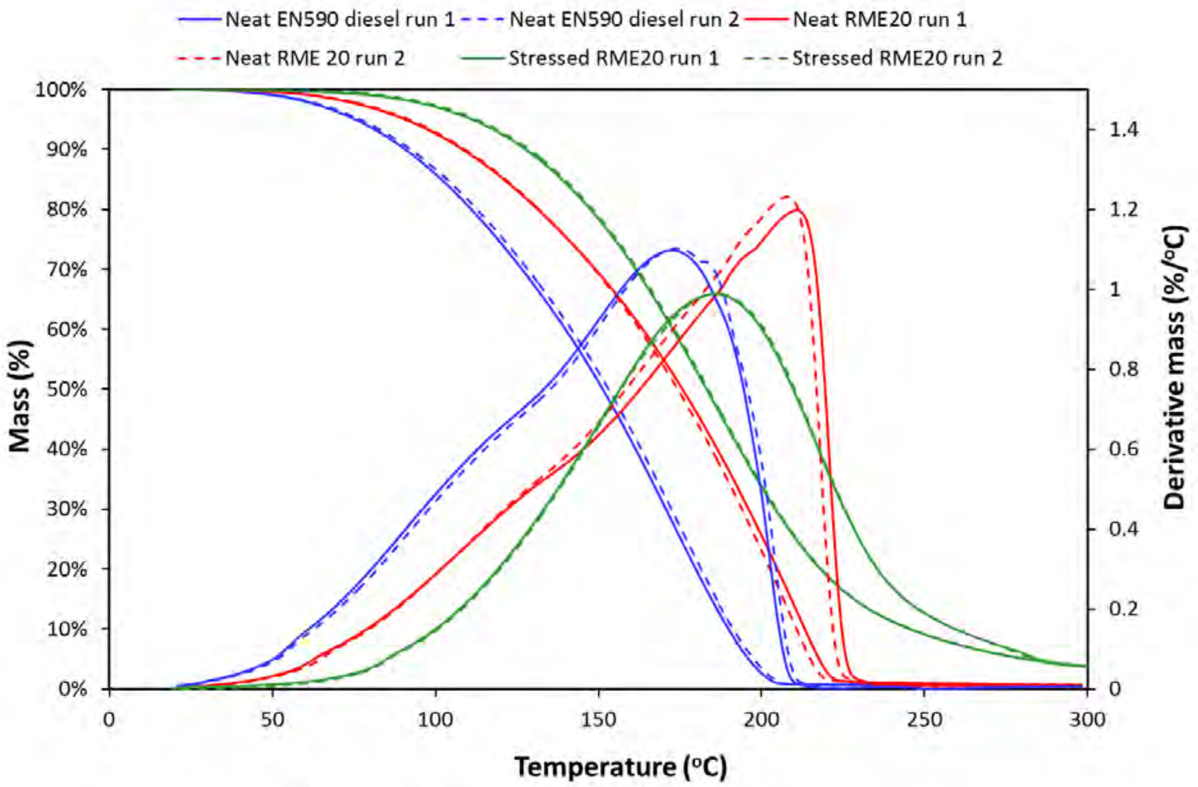

Figure 12.1: Repeat thermograms for the evaporation/decomposition of neat EN590 diesel and RME20 and stressed EN590 diesel (top layer). Experiments were conducted under nitrogen at a heating rate of 10°C/min.

12.3.2 Methanol extracts

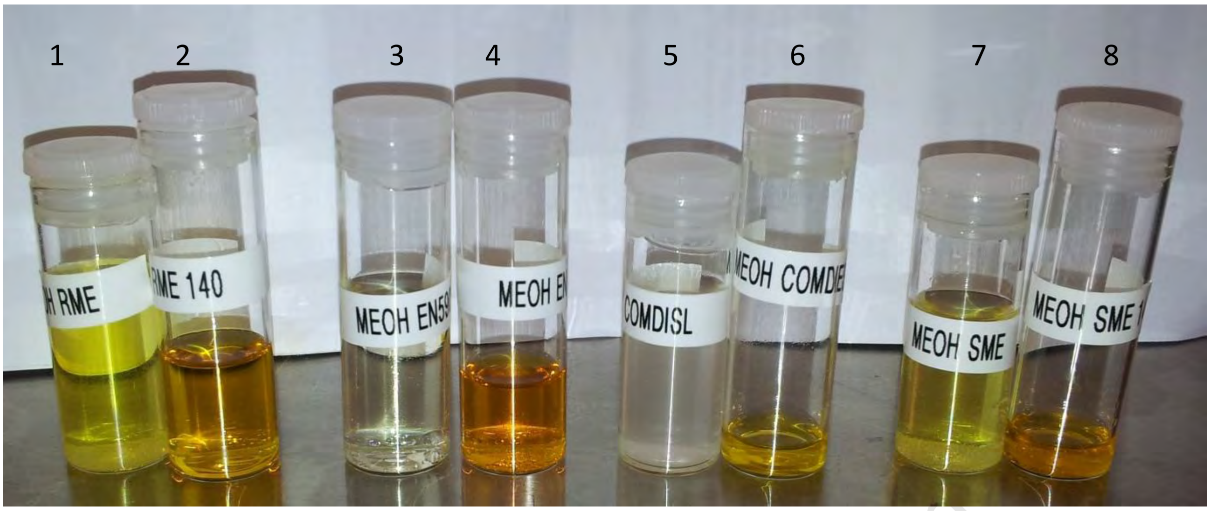

Figure 12.2: Methanol fractions of stressed and unstressed fuel. Methanol was added to both unstressed and stressed fuels (at a ratio of fuel: methanol of 5:2) in order to facilitate extraction of the polar fractions. (1) unstressed RME20, (2) stressed RME20, (3) unstressed EN590 diesel, (4) stressed EN590 diesel, (5) unstressed commercial diesel, (6) stressed commercial diesel, (7) unstressed SME20 and (8) stressed SME20.

12.3.3 ESI-MS

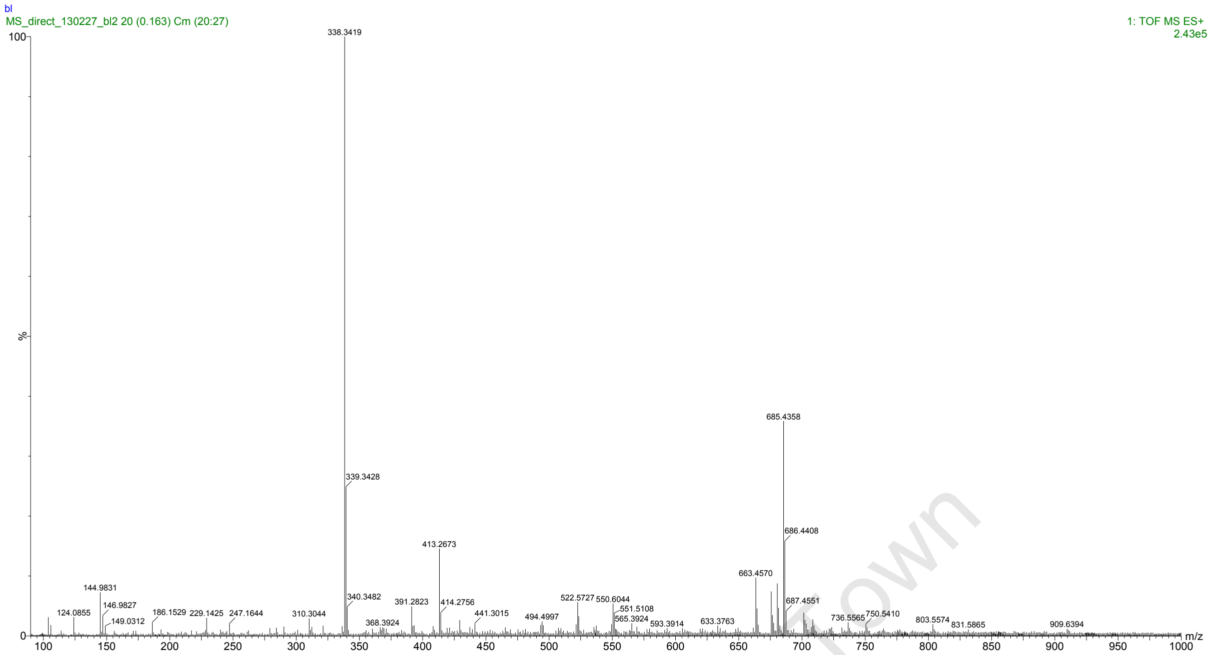

Figure 12.3: Expanded positive ESI-MS spectrum profile in the m/z 100-1000 range for a blank injection

The ESI-MS spectrum of the blank injection is relatively clean with about four main contamination peaks. The most distinct contamination peak is at m/z 338.34 with three other minor peaks at m/z 685.4, m/z 339.3, m/z 686.4 and 413.2 m/z.

12.4 Appendix D - Cellulose vs glass thimbles for efficient Soxhlet extraction

Initial extraction of commuter bus soot was conducted using high purity cellulose extraction thimbles from Sigma Aldrich (see Figure 12.4). They were employed for extraction for their apparent high purity which translates to reliable and reproducible results. During extraction of commuter bus soot with cellulose thimble, it was noticed that the SOF volumes that were determined from the various solvents were erratic and inconsistent.

One of the main reasons that led to poor SOF results being obtained was that the cellulose thimble interacted significantly with the atmosphere. Subsequent to an extraction process the thimble (containing sample) was air dried under the fumehood for 1h to evaporate the extraction solvent. This was followed by drying the thimble (with sample) in an oven at 50°C for 24h. After drying the cellulose thimble in an oven, the thimble was reweighed and it was at this point during this process that it was evident that the thimble interacted with the atmosphere. The mass of the thimble on the microbalance would increase and then reach a maximum. It is suggested that this is associated with the absorption of water. Similar behaviour was seen with plain cellulose thimbles. This was tested by immersing the cellulose thimble in two low boiling point solvents (methanol and dichloromethane) and subsequently drying in an oven at 50°C for 24h. To negate this shortcoming of cellulose thimbles, glass thimbles were used. Extractions with glass thimbles resulted in no variation in mass.

Figure 12.4: (left) Cellulose thimble; (right) glass thimble

12.5 Appendix E – TGA of Munktell filter paper

Oxidative TGA-MS was conducted on the Munktell^{TM} glass fibre filter which was used to collect the deposits. The primary purpose of this was to ascertain whether the glass fibre filter releases CO_2 during its oxidation in the mentioned temperature region. A secondary reason was to determine whether the glass fibre loses mass during thermal analysis up to 700°C. This was to establish the influence the filter had on the thermograms of deposit oxidation. Figure 12.5 shows that the filter experienced a small mass loss, *i.e.* at 300°C 2.3% mass had been lost and by 700°C the filter had lost 3.4% of its mass. The same mass loss was observed when nitrogen was used as atmosphere.

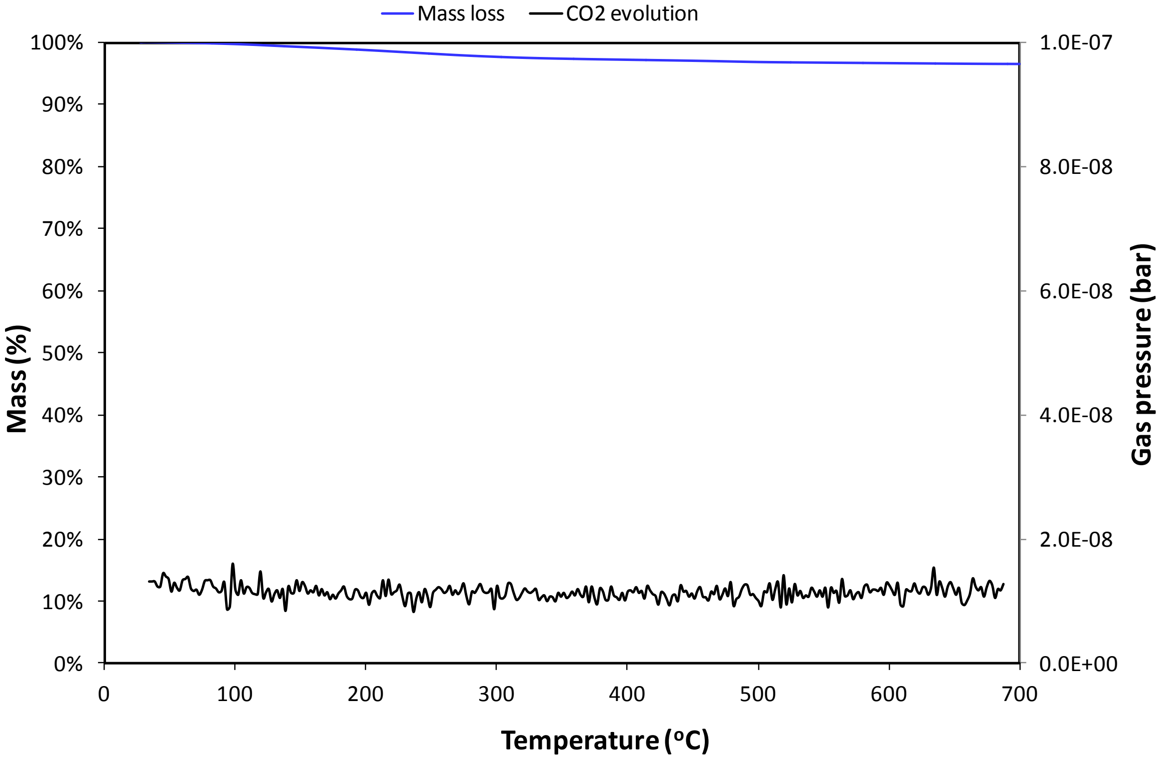

Figure 12.5: Oxidative TGA-profile curve of the glass fibre filter used to collect sand bath reactor deposits

The CO_2 profile reveals that the mass loss is not associated with CO_2 evolution under oxidative conditions. It is suggested that it results from the desorption of bonded water on the glass surface.